The Dissertation Committee for Ruohan Gao Certifies that this is the approved version of the following dissertation:

Storage, fractionation and melt-crust interaction of basaltic magmas at oceanic and continental settings

Committee:

John C. Lassiter, Supervisor

Jaime D. Barnes

James E. Gardner

Marc A. Hesse

Staci Loewy

David A. Clague

Storage, fractionation and melt-crust interaction of basaltic magmas at oceanic and continental settings

by

Ruohan Gao, B.N.S.

Dissertation

Presented to the Faculty of the Graduate School of

The University of Texas at Austin

in Partial Fulfillment

of the Requirements

for the Degree of

Doctor of Philosophy

The University of Texas at Austin

August 2016

Dedication

This dissertation is dedicated to my parents Shijun Gao and Ying Liang, and my husband Jie Xu.

Acknowledgements

First and foremost, I am especially grateful to my advisor, John Lassiter, who has taught me the right attitude and skills to become a geochemist and a scientific writer, through our weekly to daily meetings in the past six years. I could not have completed this dissertation without his guidance, inspiration, and support. I also appreciate the efforts of the rest of my dissertation committee, David Clague, Jaime Barnes, James Gardner, Staci Loewy, and Marc Hesse, whose constructive suggestions have provided invaluable insight and help to my research.

My experience at UT has been enriched and delighted by association with many wonderful fellow students, research scientists and staffs at Jackson School. I thank my group members Benjamin Byerly, Rudra Chartterjee, Ed Marshall, Gabrielle Ramirez and Leslie Bruce, for all the inspiring discussions, and the assistance and accompany they provided in lab works. I thank the excellent lab managers in our department: Staci Loewy, Donggao Zhao, Alison Koleszar, Toti Larson, Nathaniel Miller, Zhaoping Yang and Shuangquan Zhang. I could not have accomplished the analytical works without their guidance and assistance. I would also like to express my gratitude to our best graduate coordinator, Philip Guerrero, who has always been patient and helpful with my every question.

My graduate research projects were financially supported by the National Science Foundation in the form of grants EAR-1301621 and EAR-1321937, and by the Jackson School of Geosciences in the form of graduate student assistantships and summer researching founding.

Finally, I would like to thank my family. My parents have always provided encouragement and support to my decisions in every way that they could. Without them I would not have been who I am today. I could not have make this achievement without the love and support from my husband, Jie. I am very lucky to have him sharing my mood, taking care of me, and brightening my life.

Storage, fractionation and melt-crust interaction of basaltic magmas at oceanic and continental settings

Ruohan Gao, Ph.D.

The University of Texas at Austin, 2016

Supervisor: John C. Lassiter

This study uses phenocrysts and xenoliths to examine storage, fractionation and melt-crust interaction of basaltic magmas. Gabbroic xenoliths from Hualalai Volcano, Hawaii include fragments of lower oceanic crust (LOC) cumulates. Oxygen and Sr isotope compositions of these gabbros indicate minimal hydrothermal alteration. Magmas from fast ridges fractionate on average at shallower and less variable depths and undergo more homogenization than those from fast ridges. These features suggest a long-lived shallow magma lens exists at fast ridges, which limits the penetration of hydrothermal circulation into the LOC. Anorthitic plagioclases in these LOC gabbros therefore unlikely derive from hydrous melting or hydrothermal replacement. The strongly positive correlation between plagioclase anorthite content and whole rock Re concentration of Hualalai LOC gabbros may place further constraints on the origin of anorthitic plagioclase at mid-ocean ridges.

Most Hualalai xenoliths represent Hualalai melt-derived cumulates. MELTS modeling and equilibration temperatures suggest Hualalai shield-stage-related gabbros crystallized within local LOC. Therefore, a deep magma reservoir existed within or at the base of the LOC during the shield stage of Hualalai Volcano. Melt–crust interaction

between Hawaiian melts and Pacific crust partially overprinted Sr, Nd, and Pb isotope compositions of LOC-derived gabbros. The modified isotope compositions of Pacific LOC (and likely lithospheric mantle) are similar to Hawaiian rejuvenated-stage lavas. Although minor assimilation of Pacific crust by Hawaiian melts cannot be excluded, the range of oxygen isotope compositions recorded in Hawaiian magmas cannot be generated by assimilation of the *in situ* LOC.

The Papoose Canyon (PC) monogenetic eruption sequence in the Big Pine volcanic field, California displays temporal-compositional variations indicating mixing of two distinct melts. PC phenocrysts and xenoliths derive from melt that is more fractionated and enriched than PC lavas. Pressure constraints suggest these phenocrysts and xenoliths crystallized at mid-crust depths. PC lavas also show evidence of crustal contamination. Therefore, PC phenocrysts and xenoliths likely derive from early PC melts that ponded, fractionated and assimilated continental crust in mid-crustal sills, which were mixed with more primitive melts as the eruption began. The temporal-compositional trends thus reflect gradual exhaustion of these sills over time.

Table of Contents

List of Tables

List of Figures

Introduction

Basalt is the most common volcanic rock type on Earth, which is formed by partial melting of Earth's mantle (Yoder & Tilley, 1962). In particular, oceanic crust that covers about 60 percent of Earth's surface is primarily composed of basaltic lavas and cumulates. Two thirds of oceanic crust are formed by mafic and ultramafic cumulates that derive from fractionation of basaltic melts in magma sills at mid-ocean ridges. Investigating the magma plumbing system and fractionation process at mid-ocean ridges is important for understanding the mechanism of lower oceanic crust (LOC) accretion.

On the other hand, geochemists often use compositional variations in basalts as a tool to study the composition and evolution of Earth's mantle (e.g., Hart, 1988; Sun & McDonough, 1989). However, basalts represent only indirect probes of mantle composition. The composition of erupted lava is also affected by magmatic processes during melt generation and transportation. For example, mixing, fractional crystallization, and assimilation in crustal reservoirs can significantly damp out small-scale heterogeneities, and overprint source signatures in mantle-derived magmas. Therefore, understanding the history of magma storage, fractionation, and melt-crust interaction is also necessary when using basaltic lavas as a probe of Earth's mantle.

In the following chapters, the fractional crystallization products of basaltic magmas (xenoliths and phenocrysts) are used as tools to investigate magma storage, fractionation, and melt-crust interaction at a variety of tectonic settings. I focus on xenoliths and phenocrysts because signature of magma ponding, fractionation, and crustal contamination may be better preserved in these melt "crystal cargos" than in bulk lavas.

I examined a suite of gabbroic and ultramafic xenoliths from the c.a. 1800-1801 Kaupulehu flow of Hualalai Volcano, Hawaii. A subset of gabbroic xenoliths derives

from ancient Pacific LOC beneath the Hawaiian Islands (~110 Ma; Waggoner, 1993; Clague, 1987). Strontium and O isotope composition of these LOC-derived gabbros are examined to evaluate the extent of hydrothermal alteration of the *in situ* LOC, which then provides constraints on the magma plumbing systems and models of LOC formation at mid-ocean ridges ("gabbro glacier" versus "multiple sills"). I use the mineral major element, trace element, and Sr-Nd-Pb-Hf-Os isotope compositions of the LOC xenoliths to examine the fingerprints of melt-crust interaction between Hawaiian magmas and Pacific LOC recorded in these rocks.

Most Hualalai xenoliths are fractional crystallization products of Hualalai shield- and post-shield-stage magmas (e.g., Clague, 1987). I used mineralogical and compositional constraints on the fractionation pressures of Hualalai-related gabbros, and estimated the depth(s) of storage for Hualalai shield-stage magmas. I examined the Os and O isotope compositions of LOC- and Hualalai-derived xenoliths to evaluate the effects of melt–crust interaction in the evolution of Hawaiian magmas.

I also investigated the origin of temporal compositional variations in a continental basaltic monogenetic vent sequence, the Papoose Canyon (PC) eruption sequence in Big Pine Volcanic Field (BPVF), California. Compositional variations in monogenetic vent eruption sequence have been proposed to either reflect source heterogeneity or crustal contamination (e.g., Blondes et al., 2008; Erlund et al., 2010). Major element, trace element, and Sr-Nd-Pb-O isotope variations in olivine and clinopyroxene phenocrysts and ultramafic xenoliths provide new constraints on the pre-eruptive magma storage, fractionation, and crustal assimilation history at PC vent. Such insight allows us to test crust versus mantle origins for the observed temporal-compositional trends.

Chapter 1: Geochemical investigation of Gabbroic Xenoliths from Hualalai Volcano: Implications for lower oceanic crust accretion and Hualalai Volcano magma storage system[1]

ABSTRACT

The patterns of axial hydrothermal circulation at mid-ocean ridges both affect and are influenced by the styles of magma plumbing. Therefore, the intensity and distribution of hydrothermal alteration in the lower oceanic crust (LOC) can provide constraints on LOC accretion models (e.g., "gabbro glacier" vs. "multiple sills"). Gabbroic xenoliths from Hualalai Volcano, Hawaii include rare fragments of *in situ* Pacific lower oceanic crust. Oxygen and strontium isotope compositions of 16 LOC-derived Hualalai gabbros are primarily within the range of fresh MORB, indicating minimal hydrothermal alteration of the *in situ* Pacific LOC, in contrast to pervasive alteration recorded in LOC xenoliths from the Canary Islands. This difference may reflect less hydrothermal alteration of LOC formed at fast ridges than at slow ridges. Mid-ocean ridge magmas from slow ridges also pond on average at greater and more variable depths and undergo less homogenization than those from fast ridges. These features are consistent with LOC accretion resembling the "multiple sills" model at slow ridges. In contrast, shallow magma ponding and limited hydrothermal alteration in LOC at fast ridges are consistent with the presence of a long-lived shallow magma lens, which limits the penetration of hydrothermal circulation into the LOC.

Most Hualalai gabbros have geochemical and petrologic characteristics indicating derivation from Hualalai shield-stage and post-shield-stage cumulates. These xenoliths provide information on the evolution of Hawaiian magmas and magma storage systems. MELTS modeling and equilibration temperatures constrain the crystallization pressures

[1]The content of this chapter was published in 2016 in *Earth and Planetary Science Letters* 442, 162-172.

of 7 Hualalai shield-stage-related gabbros to be ~2.5–5 kbar, generally consistent with inferred local LOC depth. Therefore a deep magma reservoir existed within or at the base of the LOC during the shield stage of Hualalai Volcano. Melt–crust interaction between Hawaiian melts and *in situ* Pacific crust during magma storage partially overprinted clinopyroxene Sr and Nd isotope compositions of LOC-derived gabbros. Although minor assimilation of Pacific crust by Hawaiian melts cannot be excluded, the range of oxygen isotope compositions recorded in Hawaiian lavas and cumulates cannot be generated by assimilation of the *in situ* LOC gabbros, which have relatively uniform and MORB-like $\delta^{18}O$ values. To first order, the isotopic heterogeneity observed in Hawaiian melts appears to derive from the heterogeneous plume source(s), rather than assimilation of local oceanic crust.

1.1 INTRODUCTION

Hydrothermal circulation at mid-ocean ridges is intimately linked to the processes of oceanic crust accretion. Axial hydrothermal circulation drives cooling and crystallization of axial magmas. In addition, the distribution of magmas in the crust, in particular the presence or absence of a long-lived shallow axial magma chamber, influences the depth and degree of axial hydrothermal circulation. Hydrothermal alteration of newly formed oceanic crust dominates the heat and mass exchange between the Earth's lithosphere and hydrosphere. However, the intensity and distribution of hydrothermal circulation in gabbro cumulates, the thickest layer of oceanic crust, is still poorly constrained.

The ca. 1800-1801 Kaupulehu flow of Hualalai Volcano, Hawaii contains abundant dunite, wehrlite and gabbro, and rare websterite and anorthosite xenoliths (Jackson et al., 1981; Clague, 1987; Kauahikaua et al., 2002). A small subset of the

gabbros appears to be Pacific lower oceanic crust (LOC) layer-3 gabbros (Clague, 1987; Lassiter and Hauri, 1998). These gabbros can be used to examine the hydrothermal alteration history of LOC, and provide constraints on the mechanism of LOC accretion. The majority of Hualalai gab- bros are cumulates derived from Hualalai shield- and post-shield- stage melts (Clague, 1987). These gabbros can be used to investigate the Hualalai magma plumbing system and the role of crustal assimilation in the evolution of Hawaiian magmas.

In this study, we report mineral major and trace element and Sr–Nd–O isotope variations in a suite of 28 Hualalai gabbros, including 16 samples with chemical characteristics indicative of derivation from *in situ* Pacific LOC and 12 samples related to the shield and post-shield stages of Hualalai magmatism. Strontium and oxygen isotope data of LOC-derived gabbros are used to evaluate the extent of hydrothermal alteration of the *in situ* LOC, providing constraints on different models of LOC formation. We examine mineralogical and compositional constraints on the fractionation pressures of Hualalai-related gabbros to constrain the depth(s) of magma storage, and examine compositional variations in LOC- and Hualalai-derived gabbros to evaluate the effects of melt–crust interaction in the evolution of the *in situ* LOC and Hawaiian magmas.

1.2 BACKGROUND

Hawaiian volcanoes commonly evolve through four stages that are characterized by different lava types, magma supply rates and inferred degrees of mantle melting (Clague, 1987). Magma supply rates and degree of melting increase as the volcano moves towards the center of the plume, and then decrease as the Pacific plate moves away from the plume (e.g., Frey et al., 1990). Small volumes of alkalic basalt are primarily erupted during the pre-shield stage. Large volumes of tholeiitic basalt dominate the following

shield stage. The post-shield stage is characterized by a return to mostly alkalic basalt and associated differentiated lavas. Finally, some Hawaiian volcanoes erupt small volumes of alkalic basalt, basanite and nephelinite during a rejuvenated stage, usually following a hiatus in activity at the end of the post-shield stage (Clague, 1987).

Hawaiian lavas also display significant temporal and spatial variability in isotopic composition. Post-shield and rejuvenated-stage lavas typically have more depleted isotopic compositions than shield-stage lavas (e.g. Chen and Frey, 1985). In addition, recent Hawaiian volcanoes display systematic spatial-compositional variations that define two parallel linear trends. "Loa trend" volcanoes typically have more "enriched" Sr–Nd isotopic compositions compared to "Kea trend" volcanoes, and are also characterized by higher $^{208}Pb/^{204}Pb$ at a given $^{206}Pb/^{204}Pb$ (Abouchami et al., 2005). In addition, olivine in "Loa trend" lavas have $\delta^{18}O$ values that extend as high as +6.1‰, beyond the range of fresh MORB or most mantle peridotites. Olivine in "Kea trend" lavas have $\delta^{18}O$ values as low as +4.3‰ (Eiler et al., 1996).

The chemical characteristics of "Loa trend" lavas likely reflect ancient recycled oceanic crust and sediments entrained in the Hawaiian plume source (e.g. Eiler et al., 1996; Lassiter and Hauri, 1998). In contrast, several different origins have been proposed for the "Kea trend" lavas, including incorporation of depleted upper mantle asthenosphere (e.g. Chen and Frey, 1985), lower Pacific crust or lithospheric mantle (e.g. Eiler et al., 1996), and recycled lithosphere within the Hawaiian plume itself (e.g. Lassiter and Hauri, 1998). Evaluation of the role of local crust/lithospheric mantle is difficult because the composition of the *in situ* Pacific crust and lithospheric mantle is not well characterized. Furthermore, the extent to which Hawaiian magmas pond and crystallize within the oceanic crust/lithospheric mantle during different stages of Hawaiian volcanism is unclear.

Hualalai Volcano is located on the west coast of the Big Island of Hawaii (Fig. 1.1). Post-shield alkali basalts cover most of the subaerial portion of Hualalai Volcano. Shield-stage tholeiitic basalts are exposed along the submarine northwest rift zone. The 1800–1801 Huehue and the slightly older Kaupulehu alkali basalt lava flows contain abundant mafic and ultramafic xenoliths that are interpreted as Hualalai cumulates and *in situ* Pacific LOC (Clague, 1987). These xenoliths provide new constraints on the composition and evolution of the local LOC, and on the evolution of Hawaiian volcano magma storage systems.

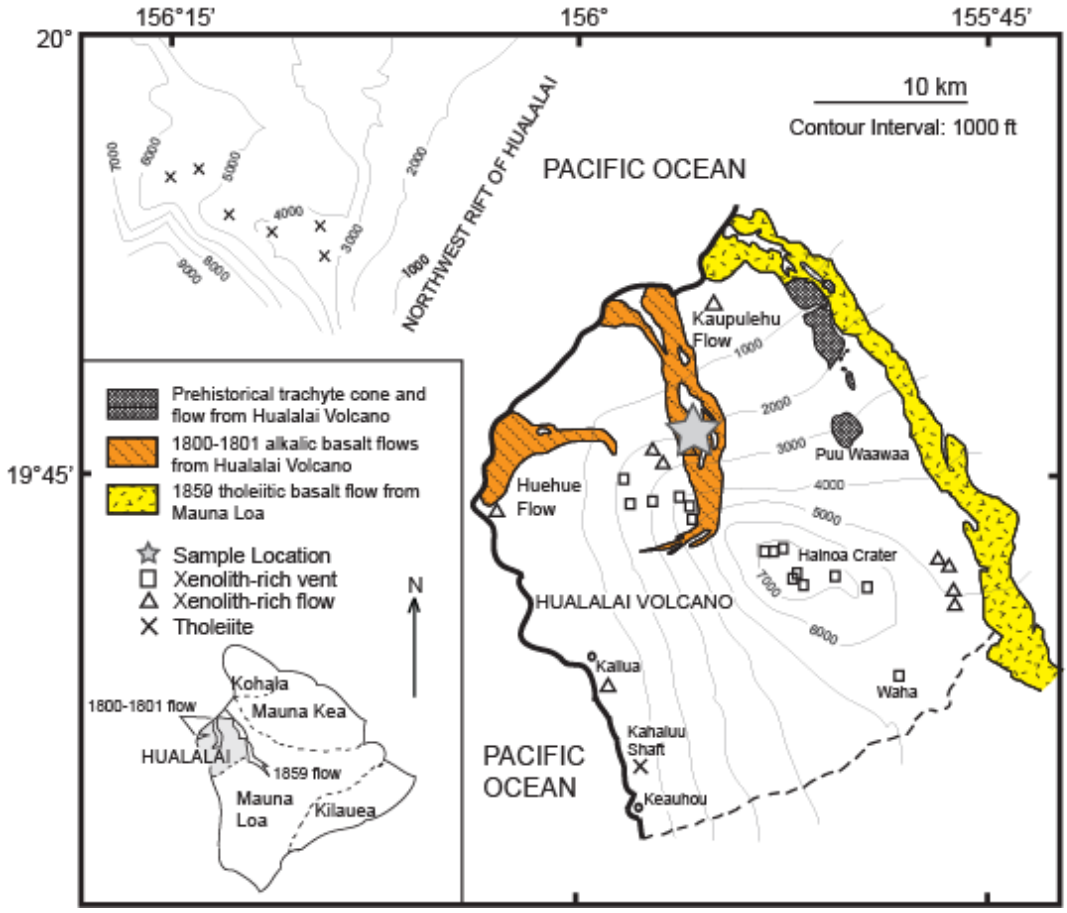

Figure 1.1 Simplified map of Hualalai Volcano

Star marks location where gabbroic xenoliths were collected (modified from Clague, 1987). Inset shows the location of Hualalai Volcano on the Big Island of Hawaii.

1.3 SAMPLES AND METHODS

We examined 28 gabbroic xenoliths from the c.a. 1800-1801 Kaupulehu alkalic basalt flow of Hualalai Volcano. Seventeen of the analyzed samples were collected by Dale Jackson and Mel Beeson in 1963 and 1965; these samples are housed in the Jackson Collection at the Smithsonian National Museum of Natural History. Eleven additional samples were collected by David Clague and Wendy Bohrson in 1983 and 1984, or by Clague between 1987 and 1996. Previous studies have shown that a small population of Hualalai gabbros (<<1%) has low, MORB-like $^{87}Sr/^{86}Sr$ (e.g., Clague and Chen, 1986; Clague, 1987; Lassiter & Hauri, 1998). These samples also have depleted LREE (light rare earth element) and Sm/Yb<1. We selected samples with low $^{87}Sr/^{86}Sr$ and/or low Sm/Yb, thought to derive from the *in situ* LOC beneath the Hawaiian Islands. Samples analyzed also include the more abundant non-LOC gabbros with higher $^{87}Sr/^{86}Sr$ and/or higher Sm/Yb, which appear to derive from Hualalai shield and post-shield stage magmas.

The gabbroic xenoliths generally have modal mineral abundances ranging from 40-60% plagioclase, 35-55% clinopyroxene, and ~2% spinel. Some gabbros also contain up to 10% orthopyroxene and 20% olivine (point counting from this study and data from Jackson et al., 1981). These gabbros can be classified into three distinct populations based on their different mineralogy and chemical characteristics. Group-1 and 2 gabbros contain both clinopyroxene and orthopyroxene, whereas group-3 gabbros lack orthopyroxene. Group-1 and 2 gabbros are distinguished by clinopyroxene Sm/Yb ratios (Fig. S1.1). Most samples are relatively fresh with only minor alteration (likely iddingsite) on olivine and Fe-oxidation on pyroxene grain boundaries or surfaces. 88Kap-2, 92Kap-3, 63Kap-15, 65-100-110, 65-115-10, 63Kap-7 and 65-60-17 show greater surface alteration. Clinopyroxene in some samples exhibits orthopyroxene exsolution

reflecting sub-solidus cooling. In some samples, the presence of highly irregular grain boundaries may indicate incipient partial melting. Planar fluid inclusion arrays in minerals indicative of annealed fractures are also present in some xenoliths.

Mineral major element compositions for clinopyroxene, orthopyroxene, and plagioclase were measured by EPMA at the USGS and University of Texas at Austin (UT Austin). Clinopyroxene trace element compositions were measured by LA-ICP-MS (UT Austin). Strontium and neodymium isotopes were measured by TIMS. Neodymium and samarium concentrations were measured by isotope dilution using TIMS. Oxygen isotope ratios were measured by laser fluorination. All isotopic analyses were performed at UT Austin. Refer to Appendix A1.1 for more method details.

1.4 RESULTS

Major element mineral compositions are presented in Appendix Tables S1.1 through S1.3. Clinopyroxene Mg# [molar Mg/(Mg+Fe)*100] varies from 73 to 87, and negatively correlates with clinopyroxene TiO_2 content (Fig. S1.1). Plagioclase anorthite contents (An) range from 57 to 98. Core-rim variation of An is up to 6, but neither cores nor rims are systematically more anorthitic. For some samples, clinopyroxene Mg# variation among grains is up to 2, and plagioclase An variation is up to ~10. However, intra-sample heterogeneity is small compared to inter-sample heterogeneity. Group-1 and 2 gabbros have systematically lower clinopyroxene TiO_2 contents and extend to higher Mg# than group-3 gabbros. Group-2 and 3 gabbros have similar plagioclase K_2O contents, whereas group-1 gabbros have systematically lower K_2O contents that the other two groups (Fig. S1.2).

Clinopyroxene trace element abundances are presented in Supplemental Table S1.4. Clinopyroxene from group-2 and 3 gabbros have high LREE concentrations ([La] =

0.9 – 2.2 ppm) and concave-down REE patterns (La/Sm = 0.34-0.81, Sm/Yb > 1.6, Fig. 1.2a). In contrast, clinopyroxene from group-1 gabbros have lower LREE concentrations ([La] = 0.01-1 ppm). They also have depleted LREE/MREE (La/Sm = 0.09-0.56), and flat to slightly depleted MREE-HREE patterns (e.g., Sm/Yb < 1; Fig. 1.2a). Group-1 gabbros are also more depleted in other highly incompatible trace elements (e.g., Sr, Zr and Hf).

Radiogenic and stable isotope data are presented in Table 1.1. Both group-2 and 3 gabbros have enriched Sr-Nd isotopic compositions ($^{87}Sr/^{86}Sr$ = 0.70356-0.70377, ε_{Nd}= 4.0-8.3) similar to Hawaiian lavas (Fig. 1.3). Group-1 gabbros have depleted Sr-Nd isotopic compositions ($^{87}Sr/^{86}Sr_{plag}$ = 0.70255-0.70287, $\varepsilon_{Nd,\ cpx}$ = 6.6-10.9), which resemble East Pacific Rise (EPR) MORBs. Several group-1 gabbros have higher $^{87}Sr/^{86}Sr$ in clinopyroxene than in plagioclase. In contrast, clinopyroxene and plagioclase from group-2 and 3 gabbros are in isotopic equilibrium.

Clinopyroxene and plagioclase $\delta^{18}O$ values correlate well with each other with $\Delta_{plag\text{-}cpx}$ = +0.7 ± 0.2‰ (Fig. 1.5 inset). Most group-1 gabbros have $\delta^{18}O$ values in a narrow range ($\delta^{18}O_{plag}$ values = +5.7 to +6.2‰, $\delta^{18}O_{cpx}$ values = +4.9 to +5.3‰), except one sample with a $\delta^{18}O_{plag}$ value of +5.3‰. Oxygen isotope compositions of group-2 gabbros show more variation ($\delta^{18}O_{plag}$ values = +5.1 to +6.3‰, $\delta^{18}O_{cpx}$ values = +4.3 to +5.5‰). Group-3 gabbros span a narrow range of oxygen isotope compositions ($\delta^{18}O_{plag}$ values = +6.1 to +6.2‰, $\delta^{18}O_{cpx}$ values = +5.2 to +5.6‰).

Sample	$^{87}Sr/^{86}Sr$	Sm (ppm)	Nd (ppm)	$^{143}Nd/^{144}Nd$	ε_{Nd}	$\delta^{18}O$(‰)	$^{87}Sr/^{86}Sr$	$^{143}Nd/^{144}Nd$	ε_{Nd}	$\delta^{18}O$(‰)
	Clinopyroxene						*Plagioclase*			
Group-1 MORB										
63Kap-3	0.70265			0.513104	9.1	5.1	0.70262	0.513018	7.4	5.7
65Kap-14d	0.70256			0.513171	10.4	5.3	0.70255			
63Kap-13	0.70268			0.513179	10.6	5.1	0.70266			5.9
65Kap-13	0.70261			0.513071	8.4	5.3	0.70261			6.0
65Kap-14a	0.70256			0.513118	9.4	5.3	0.70255			5.7
65-61-26	0.70295	1.64	4.94	0.512968	6.4	4.9	0.70282	0.512951	6.1	5.8
65-61-26 dup				*0.512966*	6.4		*0.70284*			
65-60-32	0.70308	2.07	4.49	0.513134	9.7	5.8	0.70272	0.513138	9.8	6.2
65-7-133	0.70293	1.16	2.59	0.513109	9.2	5.1	0.70257	0.513065	8.3	5.8
65-7-133 dup				*0.513102*	9.1		*0.70255*			
65-86-64	0.70348	1.60	4.60	0.512998	7.0	5.1	0.70271	0.512998	7.0	5.7
65-86-64 dup				*0.512989*	6.8		*0.70270*			
83Kap-8	0.70295	0.63	1.21	0.513143	9.9		0.70270			5.3
83Kap-9	0.70267	0.50	0.87	0.513192	10.8		0.70266			5.7
87Kap-10	0.70294	0.45	1.57	0.512977	6.6		0.70280			5.7
94Kap-7	0.70260	0.10	0.19	0.513109	9.2		0.70254			5.7
96Kap-7	0.70275			0.513168	10.3		0.70265			5.8
88Kap-2	0.70289			0.513021	7.5					5.8
87Kap-14	0.70265			0.513195	10.9					5.8
Group-2 Shield										
63Kap-15	0.70360			0.512933	5.8		0.70358	0.512974	6.6	5.2
65-115-10	0.70376			0.512867	4.5		0.70377	0.51291	5.3	5.7
65-60-17	0.70359			0.513064	8.3	5.4	0.70359			6.3
84-1801-5	0.70376			0.512873	4.6					
87Kap-11	0.70364			0.512845	4	4.9				
92Kap-1	0.70331			0.512897	5.1					6.1
92Kap-3	0.70359			0.512910	5.3	5.3				
Group-3 Post-shield										
63Kap-7	0.70364			0.512907	5.2	5.6	0.70363	0.512911	5.3	6.1
65-86-92	0.70359			0.512937	5.8	5.4	0.70357			6.0
65-86-92 dup				*0.512933*	5.8		*0.70358*			
65-109-146abc	0.70358			0.512917	5.4	5.2	0.70356	0.512917	5.4	6.1
65-109-146abc dup				*0.512924*	5.6		*0.70357*			
65-60-221	0.70368			0.512900	5.1		0.70364			
65-100-110	0.70357			0.512927	5.6		0.70356			

Table 1.1: Sr- Nd-, and oxygen-isotope compositions of Hualalai gabbroic xenoliths.

For $\delta^{18}O$ values, averages of duplicate measurements are presented in this table. Duplicate data are reported in Supplemental Table S1.6.

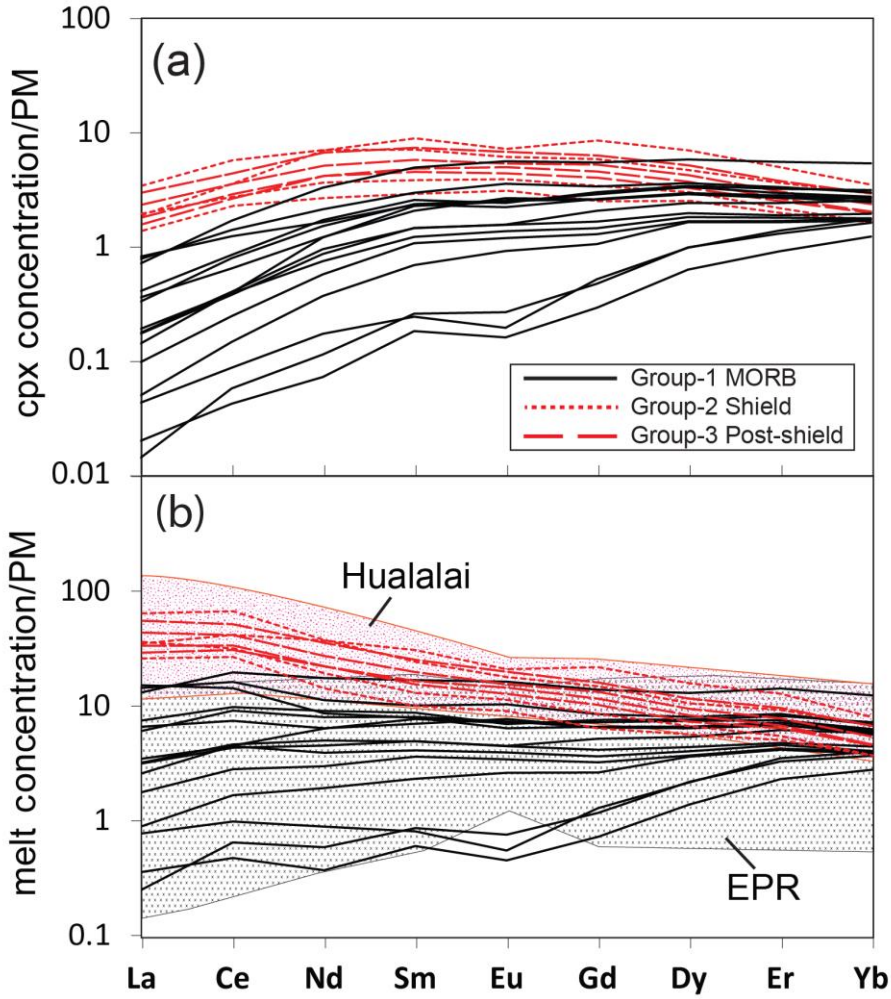

Figure 1.2 REE patterns of clinopyroxene from Hualalai xenoliths and equilibrium melts.

(a) Measured clinopyroxene REE concentrations of the Hualalai gabbroic xenoliths normalized to primitive mantle (McDonough & Sun, 1995). (b) Calculated melt REE concentrations in equilibrium with clinopyroxene from the Hualalai gabbroic xenoliths assuming no trap melt in the xenoliths. REE clinopyroxene-melt K_d values used were calculated using BIGD (see supplement for more details). Fields of Hualalai lavas and EPR basalts are shown for comparison (data from GeoRoc and PetDB).

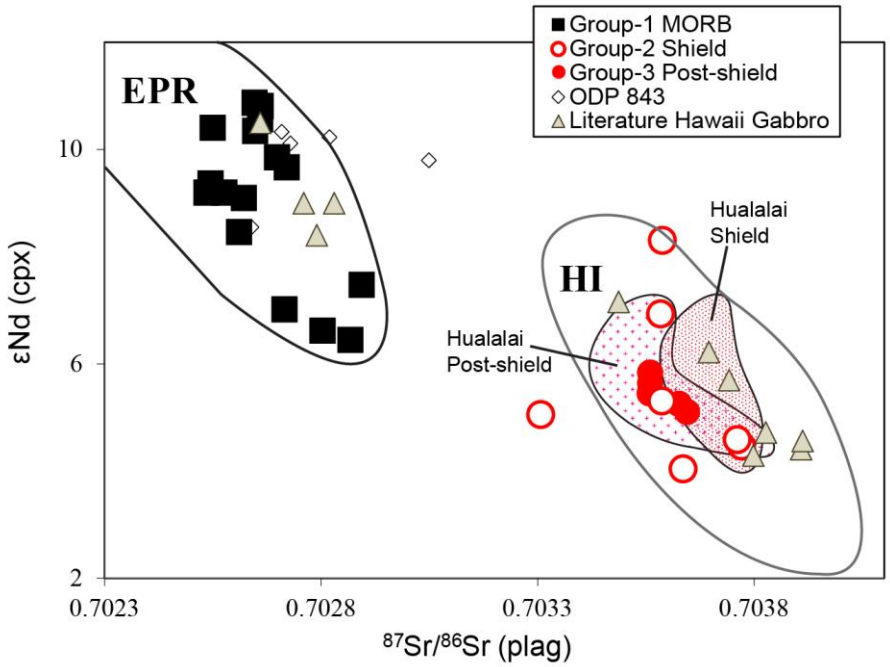

Figure 1.3 Clinopyroxene ε_{Nd} vs. plagioclase $^{87}Sr/^{86}Sr$.

Plagioclase $^{87}Sr/^{86}Sr$ are plotted because Sr-isotopes in some clinopyroxene have been partially reset by melt-crust interaction (see 1.5.3.2 for more discussion). Fields of Hawaiian lavas and EPR MORB are shown for comparison (data are from GeoRoc and PetDB). Also shown are whole rock Sr-Nd isotope data for basalts from PDP 843 to the west of Hawaii (King et al., 1991), and previously reported whole rock Sr-Nd isotope data from the Hualalai gabbros (e.g., Lassiter & Hauri, 1998).

1.5 DISCUSSION

1.5.1 Origins of Hualalai gabbros

Group-1 gabbros have Sr-Nd isotope compositions that starkly differ from Hualalai and other Hawaiian lavas but overlap with EPR MORB (Fig. 1.3). Assuming no trapped melt, the REE concentrations of melts in equilibrium with clinopyroxene from group-1 gabbros were calculated using measured clinopyroxene REE concentrations and estimated cpx-melt partition coefficients (see supplement for details). From this calculation, the melts in equilibrium with group-1 gabbros have MORB-like flat to LREE-depleted patterns (Fig. 1.2b). These characteristics suggest group-1 gabbros derive from layer-3 gabbros of the Pacific oceanic crust beneath the Hawaiian Islands as previously proposed (e.g., Clague, 1987).

The presence of orthopyroxene in group-2 gabbros suggests they derive from tholeiitic melts (Bohrson & Clague, 1988; Fodor & Galar, 1997). The clinopyroxene REE compositions of group-2 gabbros are in equilibrium with melts that have LREE-enriched REE patterns similar to Hualalai lavas (Fig. 1.2b). The Sr-Nd isotope compositions of the group-2 gabbros plot primarily within the field of Hawaiian lavas (Fig. 1.3). Group-2 gabbros therefore are most likely related to Hualalai tholeiitic shield stage magmas.

Clinopyroxene from group-3 gabbros are also in equilibrium with melts that have LREE-enriched patterns resembling Hualalai lavas (Fig. 1.2b). The Sr-Nd isotope compositions of group-3 gabbros cluster closely within the field of Hualalai alkalic post-shield stage lavas (Fig. 1.3). In addition, the absence of orthopyroxene in group-3 gabbros suggests they derive from alkalic basalts (Fodor & Galar, 1997). Together, these features suggest that group-3 gabbros likely derive from Hualalai alkalic post-shield stage magmas. In the following discussion, we assign group-1, 2 and 3 gabbros as derived from

in situ Pacific LOC, Hualalai tholeiitic shield stage magmas and Hualalai alkalic post-shield stage magmas, respectively.

1.5.2 Hydrothermal circulation in LOC

Hydrothermal circulation at mid-ocean ridges plays a critical role in heat and mass transfer between Earth's lithosphere and hydrosphere. Near-axis hydrothermal circulation removes a significant portion of the heat from crystallization and cooling of the plutonic LOC (e.g., Phipps Morgan & Chen, 1993; Maclennan et al., 2005). Interaction with hydrothermal fluids can also substantially modify the chemical and isotopic composition of altered oceanic crust (e.g., Gregory & Taylor, 1981; Alt & Teagle, 2000). The strength and distribution of near-axis hydrothermal circulation remains a matter of debate. Different studies have proposed pervasive hydrothermal circulation through the entire LOC (e.g., Bosch et al., 2004), focused hydrothermal circulation within fracture zones in the LOC (e.g., Coogan et al., 2006), and hydrothermal circulation that only penetrates the upper oceanic crust (e.g., Manning et al., 1996). The strength and distribution of hydrothermal circulation in LOC can be evaluated by examining geochemical signatures of hydrothermal alteration in LOC rocks.

Oxygen and strontium isotopes are sensitive tracers of hydrothermal alteration. Unaltered oceanic crust spans a narrow range of O and Sr isotope compositions [$\delta^{18}O_{MORB} \approx +5.4$ to $+5.8‰$ (Eiler, 2001); $^{87}Sr/^{86}Sr_{NMORB} \approx 0.7022$-$0.7032$ (Sun & McDonough, 1989)]. Low temperature hydrothermal alteration results in higher $\delta^{18}O$ values than NMORB, whereas high temperature hydrothermal alteration results in lower $\delta^{18}O$ values. Alteration also increases the $^{87}Sr/^{86}Sr$ of oceanic crust because seawater has $^{87}Sr/^{86}Sr$ significantly higher than fresh MORB [$^{87}Sr/^{86}Sr_{seawater} \approx 0.709$ (e.g., Burke et al., 1982)]. Previous studies of ophiolites and fault-uplifted seafloor oceanic crust sections

have documented high $\delta^{18}O$ values (whole rock $\delta^{18}O_{wr} \approx +5$ to +12.5‰) and $^{87}Sr/^{86}Sr$ (up to 0.7085) in pillow basalt and upper sheeted dikes, suggesting low-T hydrothermal alteration in the upper oceanic crust (e.g., Gregory & Taylor, 1981; Alt &Teagle, 2000). In contrast, lower sheeted dike and gabbro layers have low average $\delta^{18}O$ values ($\delta^{18}O_{wr} \approx$ +1.5 to +11.5‰, $\delta^{18}O_{plag} \approx$ +2.5 to +12.5‰; e.g., Gregory & Taylor, 1981) and are interpreted to have undergone high-T hydrothermal alteration.

In contrast to typical observations from ophiolitic gabbros, most of the Hualalai LOC gabbros span a narrow range of plagioclase oxygen isotope compositions (Fig. 1.4a, $\delta^{18}O_{plag}$ values = +5.7 to +6.2‰). Clinopyroxene from these gabbros have $\delta^{18}O_{cpx}$ values ranging from +4.9‰ to +5.3‰. Clinopyroxene $\delta^{18}O$ values correlate well with plagioclase $\delta^{18}O$ values ($\Delta_{plag\text{-}cpx}$ = +0.7 ± 0.2‰, Fig. 1.5 inset). Plagioclase-clinopyroxene fractionation is ~0.5‰ for rapidly quenched gabbroic magmas, and $\Delta_{plag\text{-}cpx}$ increases during cooling of the system (Gregory & Taylor, 1981). The observed $\Delta_{plag\text{-}cpx}$ is consistent with equilibrium fractionation at temperatures ~1150±60°C (Kyser et al., 1981). If these values are corrected back to $\Delta_{plag\text{-}cpx}$ = 0.5‰, the Hualalai LOC gabbros would have $\delta^{18}O_{plag}$ values ≈ +5.6 to +6.2‰ and $\delta^{18}O_{cpx}$ values ≈ +5.1 to +5.4‰ (assuming ~50:50 plagioclase/clinopyroxene). Considering analytical uncertainties, these values are within the range of primary magmatic $\delta^{18}O_{plag}$ values of +5.7 to +6.2‰ and $\delta^{18}O_{cpx}$ values of +5.2 to 5.7‰ in equilibrium with NMORB (Gregory & Taylor, 1981; Eiler, 2001). Previous studies have observed large variations in $\delta^{18}O$ values (up to 3‰) over short (mm) length-scales adjacent to micro hydrothermal veins in ophiolitic LOC gabbros (Coogan et al., 2007). Analyses of plagioclase and clinopyroxene separates could potentially overlook such small-scale alteration. However, hydrothermal micro veins were not observed in Hualalai LOC gabbros. Whole rock $\delta^{18}O$ values in the Hualalai LOC gabbros (+5.9 to +6.2‰; Lassiter & Hauri, 1998) are also primarily consistent with

NMORB (+5.3 to +5.9‰; Eiler, 2001). The oxygen isotope compositions of both the gabbroic whole rocks and mineral separates suggest minimal hydrothermal alteration.

Strontium isotopes in Hualalai LOC gabbros also appear to record minimal interaction with seawater. Both plagioclase and whole rock Sr isotope compositions of group-1 gabbros [$^{87}Sr/^{86}Sr_{plag}$ = 0.70254-0.70284; $^{87}Sr/^{86}Sr_{wr}$ = 0.70256-0.70279 (Lassiter & Hauri, 1998)] are within the range of fresh NMORB (Fig. 1.4b). Although clinopyroxene in a few LOC gabbros have higher $^{87}Sr/^{86}Sr$ than in plagioclase, there is no correlation between $\delta^{18}O$ values and $^{87}Sr/^{86}Sr$ (Fig. 1.5), as is typically observed in hydrothermally altered oceanic crust basalts and gabbros (e.g., Hart et al., 1999). Instead, the higher clinopyroxene $^{87}Sr/^{86}Sr$ ratios more likely reflect minor interaction between Hawaiian magmas and *in situ* LOC (see Section 1.5.4.2). The combined Sr and O isotope data from the Hualalai LOC gabbros suggest much less hydrothermal alteration than typically observed in ophiolitic or fault-uplifted seafloor gabbros.

The absence of an alteration signature in the Hualalai LOC gabbroic xenoliths does not necessarily preclude alteration in other portions of the LOC not sampled by these xenoliths. Some LOC gabbros from ophiolitic sections also appear to have unaltered O and Sr isotope compositions. However, the majority of LOC gabbros in many ophiolites show significant shifts in $\delta^{18}O$ values and/or $^{87}Sr/^{86}Sr$ from fresh oceanic crust values. Gabbros from the Oman ophiolite do not show a significant decrease in alteration signatures with increasing depth (Fig. 1.4). Although focused fluid flow near fractures has been proposed for portions of the Oman ophiolite, alteration is still observed in most gabbros far from fracture zones (Coogan et al., 2006). These features suggest pervasive hydrothermal alteration from diffuse fluid flow throughout the entire LOC. The Hualalai LOC gabbros span a range of compositions (e.g., cpx Mg# = 76–86) and 2-pyroxene equilibration temperatures (954-1065 °C, calculated temperatures are reported

in Table S1.5.), which suggests they likely represent a random sampling of the *in situ* LOC at various depths. If the *in situ* LOC beneath the Hawaii Islands displayed the same distribution of alteration signatures as is observed in ophiolites, it would be unlikely for alteration signatures to be missing from the LOC gabbroic xenoliths.

The hydrothermal alteration in ophiolitic and fault-uplifted seafloor gabbros may reflect alteration associated with their uplift and exposure, which we refer to as secondary hydrothermal alteration. Isotope tracers (O, Sr) in ophiolitic gabbros exhibit larger shifts from fresh MORB values than in fault-exposed seafloor gabbros (Alt & Teagle, 2000), which likely reflect more intensive secondary hydrothermal alteration associated with the thrusting and emplacement of ophiolites. Recent studies of *in situ* LOC samples (from ODP 1256D) show that the intensity of hydrothermal alteration decreases sharply with increasing depth within the uppermost ~100 m of the gabbro layer (Gao et al., 2012; Höfig et al., 2014). The minimal hydrothermal circulation recorded in the Hualalai LOC gabbros may therefore be more representative of *in situ* LOC than tectonically exhumed gabbros.

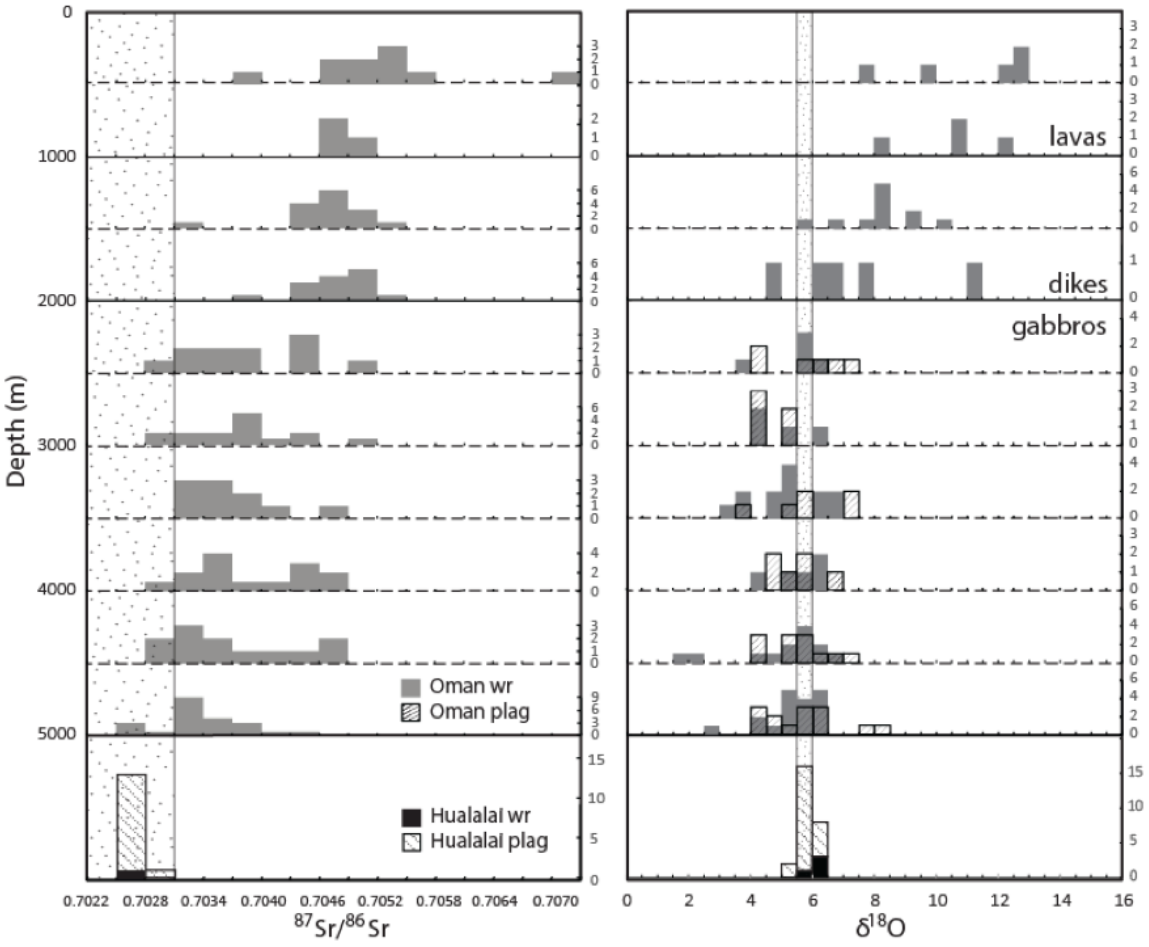

Figure 1.4 O and Sr isotope compositions of Hualalai group-1 gabbros compared to the Oman ophiolite.

Data of the Oman ophiolite is compiled from Gregory & Taylor (1981), McCulloch et al. (1980), Stakes & Taylor (1992), Bosch et al. (2004), Kawahata et al. (2001), Lanphere et al. (1981) and Coogan et al. (2006). Shaded fields of Sr and O isotope compositions of unaltered NMORB are plotted for reference.

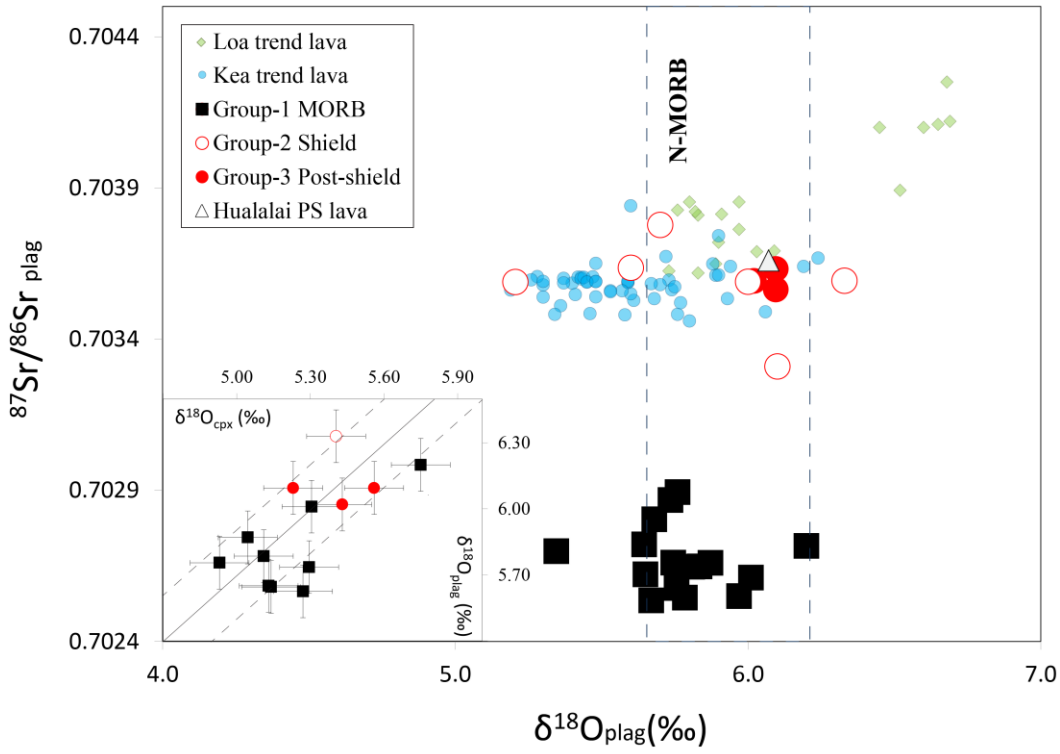

Figure 1.5 $^{87}Sr/^{86}Sr$- $\delta^{18}O$ in Hualalai gabbroic xenoliths and Hawaiian lavas.

For LOC gabbros, plagioclase $^{87}Sr/^{86}Sr$ ratios are plotted as they are more resistant to melt-rock interaction (see 5.3.2 for more discussion). Plagioclase $^{87}Sr/^{86}Sr$ and clinopyroxene $^{87}Sr/^{86}Sr$ are indistinguishable for Hualalai-related group-2 and -3 gabbros. Therefore, we plot clinopyroxene $^{87}Sr/^{86}Sr$ ratios for group-2 and -3 samples for which plagioclase $^{87}Sr/^{86}Sr$ was not measured. Because most Hawaiian lava $\delta^{18}O$ data are measured in olivine phenocrysts (data from Eiler et al., 1996), we plotted plagioclase $\delta^{18}O$ values in equilibrium with measured olivine given the fractionation factor $\Delta_{plag\text{-}ol}$= 0.7‰ (Eiler, 2001). Inset shows the correlation between plagioclase $\delta^{18}O$ and clinopyroxene $\delta^{18}O$ of Hualalai gabbroic xenoliths. Fractionation lines of $\Delta_{plag\text{-}cpx}$ = 0.7±0.2‰ are plotted for reference.

1.5.3 Implications for LOC accretion

Hydrothermal alteration recorded in the Hualalai LOC gabbros may place constraints on the mechanism of LOC accretion. Two endmember models have been proposed. The "gabbro glacier" model proposes that magmas are fed from the underlying mantle to a shallow, long-lived melt lens at the dike-gabbro boundary. Crystallization of gabbroic cumulates takes place in the shallow melt lens, and LOC is formed by downward advection of these cumulates (e.g., Phipps Morgan & Chen, 1993; Quick and Denlinger, 1993). In contrast, the "multiple sills" model proposes multiple magma sills injected into LOC at various depths and times, with LOC produced by crystallization of these magma sills followed by dominantly horizontal flow of the solid gabbro away from the ridge axis (e.g. Kelemen et al, 1997). Hybrid models combine these two end members, with the top part of the LOC formed in a shallow melt lens and the rest formed in lower magma sills (e.g., Maclennan et al., 2005).

Heat released from magma crystallization at mid-ocean ridges is primarily removed by near-axis hydrothermal circulation (e.g., Phipps Morgan & Chen, 1993). Different LOC accretion models make different predictions regarding the strength and distribution of this circulation. The "gabbro glacier" model predicts near-axis hydrothermal circulation primarily focused above the shallow melt lens (e.g., Phipps Morgan & Chen, 1993; Maclennan et al., 2004, 2005). In contrast, the "multiple sills" or hybrid models predict deep and intensive near-axis hydrothermal cooling throughout the LOC. Otherwise, the latent heat from sills injected at various depths would trigger remelting of the LOC instead of crystallization (e.g., Maclennan et al., 2004; Thelssen-Krah et al., 2011). Both models permit but do not require focused off-axis hydrothermal circulation penetrating the LOC along fracture zones after melt lenses have solidified. Although the relationship between hydrothermal alteration of off-axis LOC and LOC

accretion is complex, in general, greater deep hydrothermal alteration is expected for the "multiple sills" model (e.g., Maclennan et al., 2005).

The range of compositions and equilibrium temperatures spanned by Hualalai LOC gabbros (see Section 1.5.2) suggests they do not derive from a single locality. Assuming they represent a random sampling of the *in situ* LOC, we can calculate the probability that hydrothermally altered portions of the lower crust would not be sampled if present. For example, given 16 random samples of LOC material (the number of Hualalai LOC gabbroic xenoliths), if 5% by volume of the *in situ* LOC is altered, the probability that this material would not be sampled is ~44% [$P=(1-x)^N$]. If 20% of the LOC is altered, the probability of not sampling altered regions decreases to ~3%. Therefore, the absence of alteration signatures in the LOC xenoliths suggests volumetrically minor hydrothermal alteration of the LOC beneath Hualalai, which is difficult to reconcile with the "multiple sills" model.

LOC gabbroic xenoliths have been reported or suggested for several other localities, including Jasper Seamount (Gee et al., 1991), the Canary Islands (e.g., Schmincke et al., 1998), Davidson Seamount (Davis et al., 2007), and Flores Island, Azores (Franca et al., 2008). However, Sr and O isotope compositions have only been reported for LOC xenoliths from several Canary Islands (Vance et al., 1989; Hoernle, 1998; Hansteen & Troll, 2003). The majority of these xenoliths have $^{87}Sr/^{86}Sr$ shifted to higher values than Atlantic NMORB at a given $^{143}Nd/^{144}Nd$ (cf. Fig. 5 in Hoernle, 1998). Sr-isotope enrichments are most pronounced in Gran Canaria xenoliths. Furthermore, four Gran Canaria xenoliths have lower $\delta^{18}O_{wr}$ values ($\delta^{18}O_{wr}$ = +3.4 to +5.1‰; Hansteen & Troll, 2003) than fresh NMORB. These features suggest pervasive high-T hydrothermal alteration of *in situ* LOC beneath the Canary Islands, in contrast to what is

observed at Hualalai. The pervasive hydrothermal alteration observed in the Canary Island LOC xenoliths is compatible with the "multiple sills" model.

The oceanic crust beneath the Hawaiian Islands was formed at the EPR, a fast spreading ridge, whereas the crust beneath the Canary Islands was formed at the Mid-Atlantic Ridge (MAR), a slow spreading ridge. Oceanic crust at slow ridges is generally more fractured than at fast ridges (e.g., Phipps Morgan et al., 1987), which can provide conduits for fluid infiltration and hydrothermal alteration (e.g., Alt et al., 2010). More data from additional xenolith localities is needed to determine if LOC formed at fast ridges is consistently less altered than LOC formed at slow ridges. However, cooling rates in LOC gabbros from fast ridges decrease significantly with depth in the upper kilometer of the gabbro layer, as estimated from the Ca-in-olivine geospeedometer. In contrast, LOC gabbros at slow ridges display no variation in cooling rates with depth, and cool substantially faster than those at fast ridges. The cooling rate profiles are consistent with more extensive deep hydrothermal circulation and associated cooling at slow ridges (Coogan et al., 2007). In addition, as discussed below, several other observations are consistent with different magma plumbing systems at fast and slow ridges.

Shallow melt lenses have been consistently detected by seismic imaging beneath fast ridges (e.g., Hooft et al., 1997). In contrast, crustal melt lenses are only occasionally detected beneath slow spreading ridges in the Atlantic Ocean (e.g., Sinha et al., 2006). These geophysical observations are consistent with petrologic models that suggest shallower magma ponding at fast ridges. For example, Michael & Cornell (1998) shows that melts fractionate fast ridges at shallower depths than at slow ridges. Magma fractionation also appears to occur within a narrower range of depths at fast ridges than at slow ridges (Michael & Cornell, 1998). MORB glasses from fast ridges also have higher average Cl/K ratios than those from slow ridges. These features indicate assimilation of

shallow, hydrothermally altered materials with elevated Cl/K during shallow magma ponding and fractionation at fast ridges (Michael & Cornell, 1998).

Correlations between MORB isotopic heterogeneity and spreading rate also suggest different magma plumbing systems at fast and slow ridges. Sr isotope heterogeneity at individual ridge segments decreases with decreasing average Mg# (Rubin et al., 2009). In addition, both average Mg# and Sr isotopic heterogeneity correlate with ridge spreading rate, with fast ridges possessing lower average Mg# and less isotopic heterogeneity than slow ridges. Similar correlations are also observed for Nd isotopes. We compiled MORB Nd isotope data from 10 mid-ocean ridge segments as well as samples from ODP Sites 843 and 1256D (see supplement for details). As shown in Fig. S1.3, ε_{Nd} variability is negatively correlated with ridge spreading rate. The lower average Mg# and isotopic heterogeneity at fast ridges is consistent with greater mixing and homogenization of discrete magma batches coupled with protracted fractional crystallization in long-lived magma chambers. Combined with the observation that magmas at fast ridges fractionate on average at shallower depths than at slow ridges (Michael & Cornell, 1998), these features are consistent with the presence of a shallow, long-lived magma chamber, through which most magmas pass prior to eruption. In contrast, the greater isotopic heterogeneity at slow ridges may reflect greater preservation of primary magma heterogeneity due to direct tapping of discrete melt batches from multiple sills intruded at various depths.

Taken collectively, the geochemical and geophysical observations at slow ridges are consistent with the thermal and petrologic predictions of the “multiple sills” model. Fractional crystallization in a long-lived shallow magma chamber is significant at fast ridges. In principle, hybrid models where magmas pond and fractionate in multiple sills over a range of depths and then feed into a shallow melt lens prior to eruption are

consistent with the petrologic observations. However, magma crystallization requires sufficient removal of latent heat, often through hydrothermal cooling (Maclennan et al., 2004, 2005). Therefore, the limited hydrothermal alteration observed in the LOC beneath the Hawaiian Islands, although not conclusive, favors the "gabbro glacier" model. Future studies of LOC xenoliths from additional localities may place further constraints on the distribution of hydrothermal alteration in LOC, and may provide a new avenue to study the processes of LOC accretion.

1.5.4 Magma storage system of Hualalai Volcano and melt-crust interaction

1.5.4.1 Evidence for LOC shield-stage magma reservoir of Hualalai Volcano

The depths of magma storage may affect the evolution of Hawaiian magmas in several ways. For example, pressure affects the liquid line of descent and volatile degassing processes. In addition, the effects of assimilation or melt/wallrock interaction will vary depending on whether melts pond within the volcanic edifice, oceanic crust, or upper mantle. The magma plumbing systems of Hawaiian volcanoes evolve as magma supply rates change (e.g., Clague 1987; Bohrson, 2007 and references therein). The high magma supply during the shield stage provides the thermal impetus to maintain a shallow-level magma reservoir within the volcanic edifice. During the post-shield stage, decreasing magma supply leads to solidification of the shallow magma reservoir. The presence of LOC gabbroic xenoliths in Hualalai post-shield stage lavas and the crystallization sequence of Mauna Kea post-shield lavas suggest deep magma reservoirs exist within or beneath the LOC during the post-shield stage, possibly close to the Moho (Clague, 1987; Frey et al., 1990). However, whether a deep magma reservoir is also present during the shield stage is a matter of debate. Several studies propose that a deep magma reservoir coexists with the shallow reservoir during the shield stage (e.g., Clague,

1987; Bohrson & Clague, 1988; Vazquez et al., 2007). Other studies suggest there is only one magma reservoir during the shield stage, and this reservoir deepens during the shield to post-shield transition (e.g., Frey et al., 1990; Shamberger & Hammer, 2006).

The depths of origin of shield-stage gabbros can be used to infer the depth of the Hualalai shield stage magma reservoir(s), because the gabbros are most likely cumulates derived from these crystallized reservoirs. We evaluate the crystallization depths of Hualalai shield gabbros using (1) MELTS thermodynamic modeling (Ghiorso & Sack, 1995); (2) comparison of equilibration temperature in shield gabbros and LOC gabbros; and (3) comparison with previous estimates for depth of origin of Hualalai gabbroic and ultramafic xenoliths. Each of these approaches provides an independent, if imprecise, assessment of magma fractionation pressure. Taken together, they provide a consistent picture of the Hualalai volcano shield-stage plumbing system.

Isobaric fractional crystallization of a primitive tholeiite melt was modeled using MELTS over a pressure range of 2-8 kbar. Crystallization depths of Hualalai shield gabbros were then constrained by comparing observed mineralogy and composition with model-predicted crystallization sequences and mineral compositions at various pressures. We used the primitive Hualalai tholeiite KK-14-5 (Bohrson & Clague, 1988) and an initial water content of 0.4 to 0.7 wt.% as the initial melt composition for the MELTS modeling (Table S1.8). MELTS models were initiated at the NNO or QFM oxygen buffer and allowed to proceed unbuffered.

Over the range of initial water content and oxygen fugacity investigated, all models were able to produce all the major mineral phases present in shield gabbros, and show two consistent results: (1) as pressure increases, the temperature at which plagioclase arrives at the liquidus decreases, and as a result of earlier pyroxene fractionation the An content of the first plagioclase crystallized decreases with increasing

pressure; (2) the onset of orthopyroxene fractionation occurs at higher temperature with increasing pressure, resulting in higher Mg# of the first-crystallized orthopyroxene (Fig. 1.6; more discussion of the MELTS modeling is presented in supplement). The mineral compositions observed in shield gabbros (plagioclase An up to 70, orthopyroxene Mg# up to 87) require fractionation within the pressure range of ~2.5-5 kbar. This range is consistent with pressure constraints (1-5 kbar) of Shamberger & Hammer (2006) based on clinopyroxene geobarometry. This pressure range corresponds to a depth of ~11-18 km, which is within the local oceanic crust (Moore, 1987; Clague, 1987). This depth interval overlaps with but is slightly shallower than crystallization depths previously estimated for Hualalai shield ultramafic xenoliths by Bohrson & Clague (1988) (~13-28 km).

Comparison of equilibration temperatures between Hualalai shield-stage and LOC gabbros also provides indirect evidence that these two xenolith types derive from similar depths. Hualalai shield gabbros record 2-pyroxene equilibration temperatures [942-1075°C; precision ~±25°C; (Brey & Kohler, 1990)] similar to temperatures recorded in the LOC gabbros (954-1065°C). MELTS modeling suggests crystallization of group-2 gabbros at temperatures higher than 1075°C. Lamellar exsolution textures are observed in pyroxene from some group-2 gabbros. Therefore, the 2-pyroxene temperatures recorded by group-2 gabbros likely reflect subsolidus cooling. In contrast, the Pacific LOC beneath the Hawaiian Islands (Müller et al., 2008) should have cooled to ~400 °C due to conductive cooling over the past ~100 Ma (Pollack et al., 1993), and 2-pyx thermometers in these gabbros should record a pyroxene blocking temperature of ~650 °C (Mitra et al., 1999). However, LOC group-1 gabbros record equilibrium temperatures nearly identical to the range recorded in the shield-stage related gabbros. This likely reflects re-heating of the LOC by Hawaiian magmas.

Given that the equilibration temperatures recorded by the group-2 gabbros likely reflect post-crystallization sub-solidus cooling, and the temperatures in the group-1 gabbros reflect recent reheating of the LOC, it would seem fortuitous for these xenoliths to record such similar temperatures unless they last equilibrated at similar depths. Bohrson & Clague (1988) suggested slightly higher sub-solidus temperatures (~1045-1090°C) for Hualalai shield-stage-related ultramafic xenoliths compared to shield gabbros. Combined with the slightly higher pressure estimates for these ultramafic xenoliths (Bohrson & Clague, 1988), this suggests that Hualalai shield ultramafic xenoliths derive from somewhat deeper depths than shield gabbros. In conclusion, although precise pressure estimates for formation of the shield-related gabbroic and ultramafic xenoliths are difficult, it appears most likely that Hualalai shield stage magmas ponded and fractionated within and/or at the base of the LOC. A deep magma reservoir probably existed during the shield stage of Hualalai Volcanism in addition to the shallow intra-edifice reservoir.

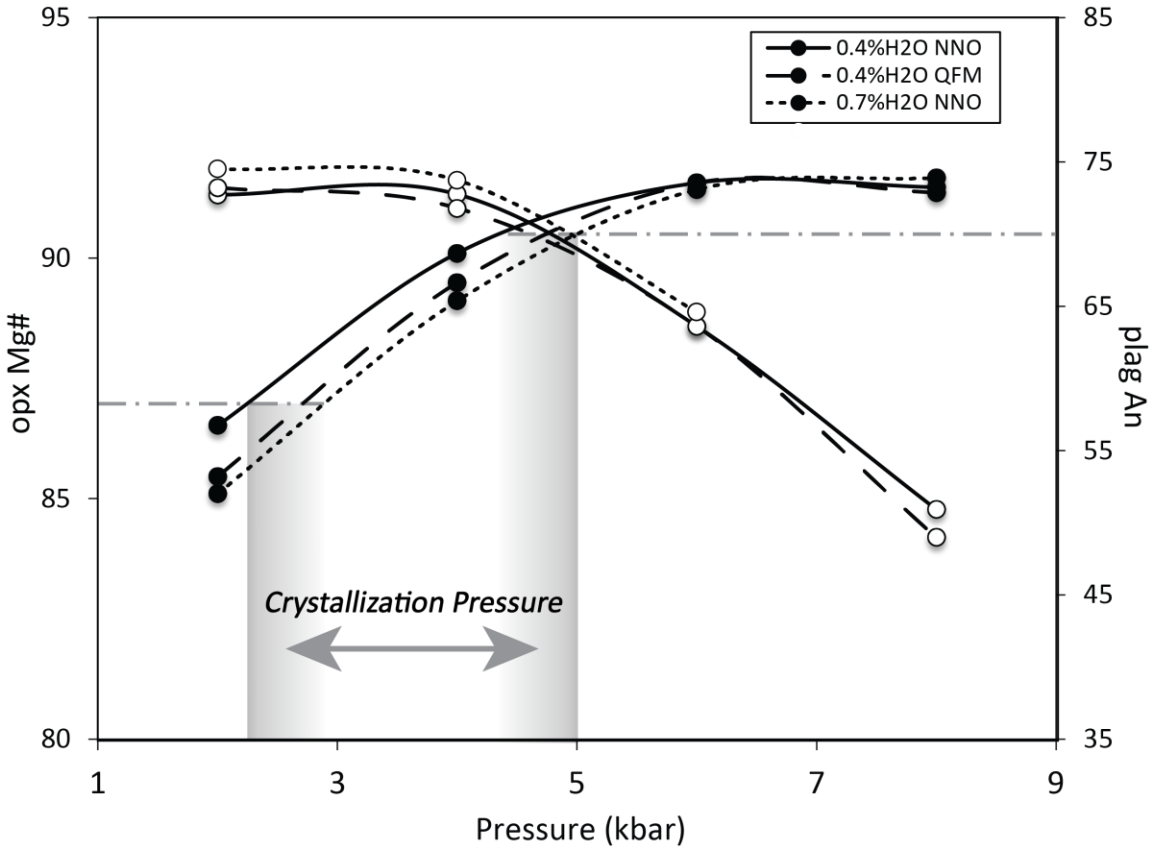

Figure 1.6 MELTS modeling results.

Lines in the figure shows An of the first plagioclase (open circles) and Mg# of the first orthopyroxene (filled circles) predicted by MELTS modeling at different pressures. Initial composition can be found in Table S1.8. The effects of various water contents in the initial melt and different initial oxygen fugacity were assessed and presented. Model-predicted crystallization pressure range of Hualalai shield gabbros is constrained by the highest plagioclase An and orthopyroxene Mg# observed.

1.5.4.2 Effects of melt-crust interaction on in situ LOC

The existence of a magma reservoir within the LOC during shield and post-shield stages of Hawaiian volcanoes provides the opportunity for magmas to interact with the surrounding LOC during magma storage. Several features of group-1 gabbros may record interaction with Hualalai magmas. These features include Sr-isotope disequilibrium between clinopyroxene and plagioclase observed in several samples (Fig. 1.7), and correlations between Sr and Nd isotopes and trace element ratios that trend towards Hualalai magma cumulate compositions (Fig. 1.8).

Whereas clinopyroxene and plagioclase in Hualalai-related group-2 and 3 gabbros have indistinguishable Sr isotopic compositions, clinopyroxene in many group-1 gabbros are out of equilibrium with coexisting plagioclase and extend to more radiogenic compositions (Fig. 1.7a). The extent of Sr isotope disequilibrium ($\Delta^{87}Sr/^{86}Sr_{cpx\text{-}plag}$) correlates with clinopyroxene Sr concentrations and other incompatible trace elements. Clinopyroxene with low incompatible element concentrations (e.g., < 4 ppm Sr) are generally in equilibrium with coexisting plagioclase, whereas incompatible-element-enriched clinopyroxene are not (Fig. 1.7b). Sr isotopic disequilibrium between clinopyroxene and plagioclase has also been observed in gabbros from the Oman ophiolite, which was interpreted to reflect partial exchange with ^{87}Sr-rich seawater-derived hydrothermal fluids (McCulloch et al., 1980). However, the anomalous ^{87}Sr enrichment in clinopyroxene is unlikely to reflect hydrothermal alteration, as there is no oxygen isotope evidence for hydrothermal alteration of the group-1 gabbros (see section 1.5.2).

Both $^{87}Sr/^{86}Sr$ and $^{143}Nd/^{144}Nd$ of group-1 gabbros correlate with insoluble trace elements and ratios such as La/Sm, and trend towards Hualalai magma cumulate compositions (Fig. 1.8). Although clinopyroxene $^{143}Nd/^{144}Nd$ in group-1 gabbros is also

correlated with $^{147}Sm/^{144}Nd$, the slope of the correlation suggests an "age" (170±50 Ma) that is significantly older than local oceanic crust (~100 Ma; Müller et al., 2008). Therefore, rather than reflecting radiogenic ingrowth, these correlations more likely reflect mixing between LOC cumulates and incompatible-element-enriched Hualalai melts.

Interaction between LOC gabbros and Hualalai melts may occur through melt infiltration and reaction along gabbro grain boundaries. As an approximation, this interaction can be modeled as simple binary mixing between gabbro clinopyroxene or plagioclase and Hualalai melts. Such mixing affects Sr isotopes in clinopyroxene to a greater extent than coexisting plagioclase, because clinopyroxene has lower Sr concentrations (Fig. 1.9). The difference in Nd concentrations is smaller between these two mineral phases, so that melt addition has roughly similar effects on plagioclase and clinopyroxene. Mixing models show that the range of both Sr and Nd isotopic variation in LOC gabbros can be generated by addition of less than 5-10% of either shield- or post-shield-stage melts. This amount of melt addition is unlikely to have significantly affected the major element or oxygen isotope compositions of the LOC xenoliths.

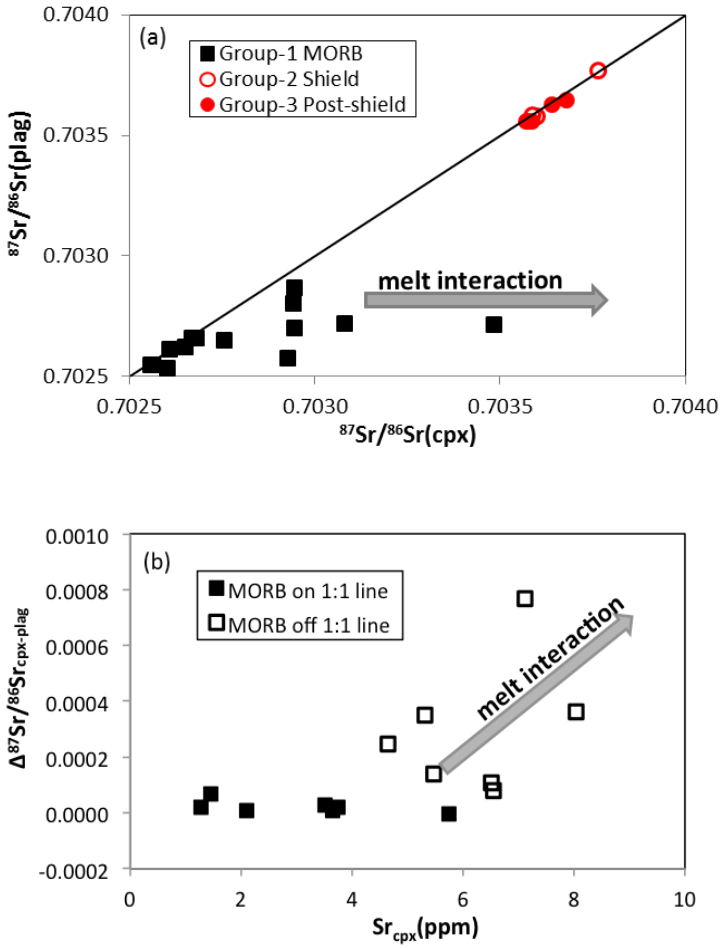

Figure 1.7 Melt-crust interaction signatures.

(a) Comparison of clinopyroxene and plagioclase $^{87}Sr/^{86}Sr$. Several LOC xenoliths have higher clinopyroxene $^{87}Sr/^{86}Sr$ than for plagioclase from the same sample. Shield- and post-shield related gabbros plot close to the 1:1 line, indicating isotopic equilibrium between plagioclase and clinopyroxene in these samples. (b) Correlation between $\Delta^{87}Sr/^{86}Sr_{cpx\text{-}plag}$ in the LOC gabbros and clinopyroxene Sr concentrations. The observed Sr isotope disequilibrium between clinopyroxene and plagioclase most likely reflects melt-crust interaction between Hawaiian melts and in situ LOC.

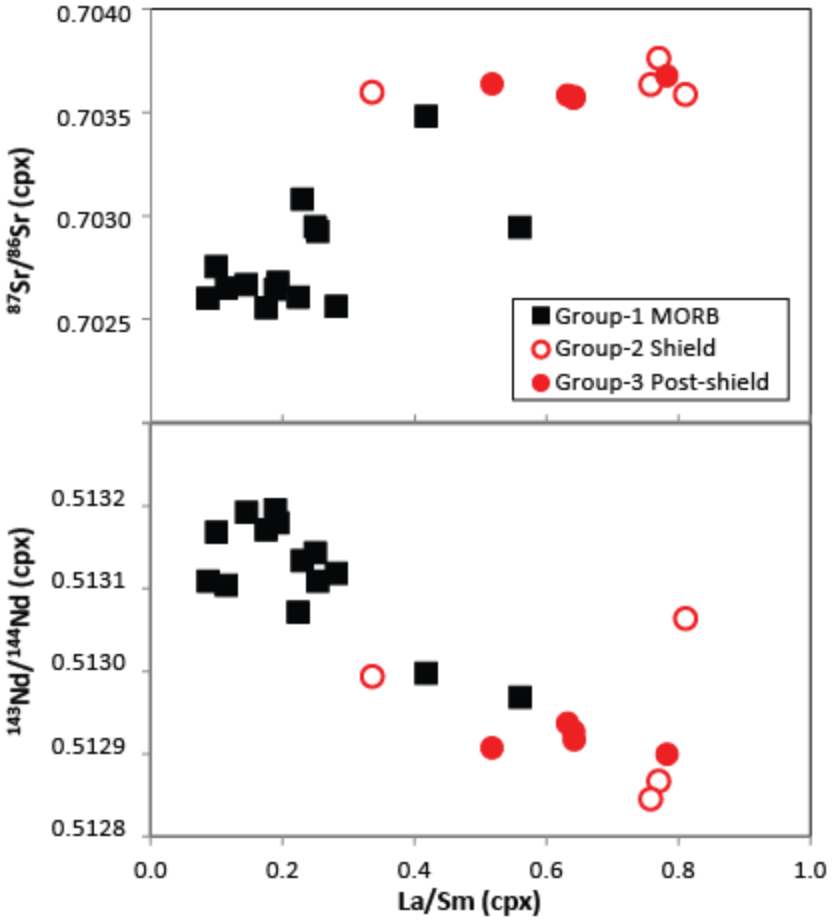

Figure 1.8 Clinopyroxene $^{87}Sr/^{86}Sr$ and $^{143}Nd/^{144}Nd$ versus La/Sm ratios of Hualalai gabbroic xenoliths.

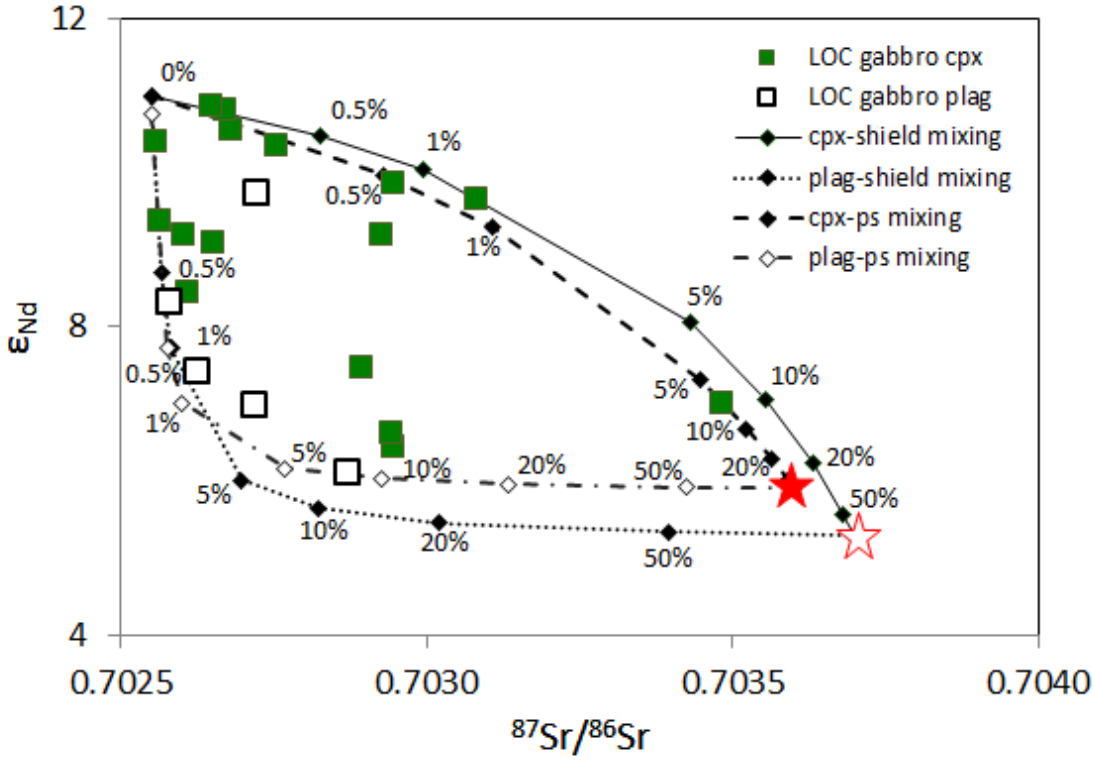

Figure 1.9 Binary mixing model for melt-crust interaction.

Simple binary mixing model as an approximate for the melt-crust interaction processes between Hawaiian magmas and *in situ* LOC. The filled star represents the average Sr-Nd isotopic composition of Hualalai post-shield (PS) stage magmas, whereas the open star marks the average isotopic composition of Hualalai shield stage magmas. Magma and mineral phases Sr/Nd concentrations used for modeling are $[Sr]_{magma,\ shield}$ = 250 ppm, $[Sr]_{magma,\ PS}$ = 450 ppm, $[Sr]_{cpx}$ = 4 ppm, $[Sr]_{plag}$ = 90 pmm; $[Nd]_{magma,\ shield}$ = 20 ppm, $[Nd]_{magma,\ PS}$ = 50 ppm, $[Nd]_{cpx}$ = 1 ppm, $[Nd]_{plag}$ = 0.2 ppm. Magma, clinopyroxene and plagioclase Sr and Nd concentrations are chosen based on literature data compiled from GeoRoc, measurement concentrations in this study, and unpublished data from Nicholas Dygert, respectively.

1.5.4.3 Effects of melt-crust interaction on Hawaiian lavas: the origin of oxygen isotope heterogeneity in Hawaiian lavas

The chemical and isotopic variations in Hawaiian basalts are commonly utilized to infer the origin and length scales of heterogeneities in the Hawaiian plume (e.g., Abouchami et al., 2005). Many studies made the implicit assumption that the compositions of Hawaiian basalts closely track their mantle sources with little modification during transportation and storage in the oceanic crust. However, as discussed in 5.4.1, Hawaiian shield and post-shield stage magmas most likely ponded and fractionated in the lower oceanic crust, prior to eruption or transportation to the intra-edifice magma reservoir. During this ponding, Hawaiian magmas have the potential to assimilate *in situ* LOC. Therefore, the role of crustal contamination in the evolution of Hawaiian magmas needs to be assessed.

Hawaiian lavas display greater oxygen isotope variability than fresh NMORB (Eiler et al., 1996). Several studies have proposed that "Loa trend" lavas inherit their high $\delta^{18}O$ values from ancient recycled oceanic crust or sediment entrained in the Hawaiian plume source (e.g., Eiler et al., 1996, Lassiter & Hauri, 1998). However, the origin of the low $\delta^{18}O$ values of "Kea trend" lavas is still uncertain. Eiler et al. (1996) proposed the low $\delta^{18}O$ values are generated by assimilation of hydrothermally altered *in situ* LOC gabbros. In contrast, Lassiter & Hauri (1998) argued that both the high and low $\delta^{18}O$ values in Hawaiian lavas reflect the presence of ancient recycled oceanic lithosphere in the Hawaiian plume source. More recently, Wang et al. (2003) and Wang and Eiler (2008) proposed that the low $\delta^{18}O$ values in Mauna Kea lavas reflect assimilation of volcanic edifice material that has been altered by meteoric water.

Oxygen isotope data from Hualalai gabbroic xenoliths suggest that assimilation of local LOC cannot generate the range of oxygen isotope compositions observed in

Hawaiian lavas. LOC-derived group-1 gabbros have a narrow range of oxygen isotope compositions similar to fresh NMORB (see section 1.5.2). In contrast, olivine phenocrysts in Hawaiian lavas span a wide range of oxygen isotope compositions ($\delta^{18}O_{ol}$ = +4.3 to +6.1‰; Eiler et al., 1996). For $\Delta^{18}O_{melt\text{-}ol}$ = ~0.5‰ (Eiler, 2001), Hawaiian magmas therefore have $\delta^{18}O$ values extending to both higher and lower values than the *in situ* LOC. Assimilation of the *in situ* LOC cannot generate either the anomalously low or high $\delta^{18}O$ values observed in many Hawaiian melts (Fig. 1.5).

Most group-2 and group-3 gabbros have oxygen isotope compositions at or beyond the upper limit of the range defined by fresh MORB, consistent with the high $\delta^{18}O$ values reported for "Loa trend" lavas including the Hualalai post-shield lava analyzed by Eiler et al. (1996). These Hualalai-related gabbros likely crystallized within or at the base of the LOC (see Section 1.5.4.1). Because assimilation of volcanic edifice material cannot have affected the oxygen isotope composition of cumulates formed within the LOC, the oxygen isotope compositions of these Hualalai cumulates are most likely inherited from the Hawaiian plume source(s). The high $\delta^{18}O$ values in several shield and post-shield stage gabbros are therefore consistent with previous proposals that high $\delta^{18}O$ values in Hawaiian lavas reflect recycled high-$\delta^{18}O$ material in the Hawaiian plume (e.g. Eiler et al., 1996; Lassiter & Hauri, 1998). In addition, although only one Hualalai cumulate with anomalously low $\delta^{18}O$ is reported here, the presence of low $\delta^{18}O$ cumulates, if confirmed, would suggest that low $\delta^{18}O$ values in Hawaiian melts also derive from the Hawaiian plume.

1.6 CONCLUSIONS

Lower oceanic crust (LOC) gabbroic xenoliths reported at several ocean islands and seamounts provide an under-utilized approach to study the compositions and

hydrothermal alteration history of LOC. This information can provide further constraints on LOC accretion models, and the potential influences of melt-crust interaction on the compositions of ocean island basalts. Gabbroic xenoliths from Hualalai Volcano are divided into three groups based on their geochemical and petrologic compositions. Group-1 and 2 gabbros contain clinopyroxene and orthopyroxene, and are consistent with derivation from tholeiitic melts. Group-3 gabbros lack orthopyroxene, and likely derive from alkalic melts. Group-2 and 3 gabbros both have enriched Sr-Nd isotopic compositions similar to Hawaiian lavas, and clinopyroxene REE concentrations in equilibrium with Hualalai-like melts. In contrast, group-1 gabbros have depleted Sr-Nd isotopic compositions that overlap with EPR MORB, and clinopyroxene REE concentrations in equilibrium with MORB-like LREE-depleted melts. The geochemical and petrologic characteristics of group-1, 2 and 3 gabbros suggest they derive from *in situ* Pacific lower oceanic crust, Hualalai tholeiite shield stage magmas and Hualalai post-shield stage magmas, respectively.

In contrast with observations from many ophiolitic and fault-uplifted seafloor LOC gabbros, the O and Sr isotope compositions of group-1 gabbros indicate minimal hydrothermal alteration of *in situ* LOC beneath Hualalai. The higher extents of hydrothermal alteration in ophiolitic and seafloor gabbros may result from "secondary" hydrothermal alteration during faulting and uplift. The minimal hydrothermal alteration recorded in Hualalai LOC xenoliths also contrasts with pervasive alteration recorded in LOC xenoliths from the Canary Islands. These differences may reflect less hydrothermal alteration of LOC formed at fast ridges than at slow ridges. Combined with other lines of geochemical and geophysical evidence (e.g., greater isotopic heterogeneity, the lack of seismic evidence for shallow melt lenses), the high degree of hydrothermal alteration observed in LOC samples from slow ridges suggests the "multiple sills" model of LOC

accretion. In contrast, seismic imaging of shallow melt lenses and reduced isotopic heterogeneity of erupted basalts at fast ridges suggest that magmas in these settings pass through and fractionate within a long-lived shallow melt lens. This long-lived shallow melt lens likely restricts deep penetration of on-axis hydrothermal circulation and cooling of LOC at ridge axes, consistent with the limited hydrothermal alteration of LOC formed at fast ridges.

Group-1 and group-2 gabbros record similar subsolidus 2-pyroxene equilibration temperatures (942 - 1075°C), suggesting derivation from similar depths. MELTS modeling further suggests the crystallization pressures of group-2 gabbros to be ~2.5-5 kbar, roughly consistent with local LOC depth. Therefore, a magma reservoir close to the Moho existed during Hualalai shield stage. Melt-crust interaction between Hawaiian melts and *in situ* Pacific crust during magma storage partially overprinted clinopyroxene Sr and Nd isotopic compositions of group-1 gabbros. Although minor assimilation of Pacific crust by Hawaiian melts cannot be excluded, the range of oxygen isotope compositions recorded in Hawaiian lavas and cumulates cannot be generated by assimilation of the *in situ* LOC gabbros, which have relatively uniform and MORB-like $\delta^{18}O$ values. Therefore, the isotopic variations observed in Hawaiian melts reflect plume source heterogeneity.

ACKNOWLEDGEMENTS

This work was supported in part by NSF grant EAR-1321937 and by the Jackson School of Geosciences, University of Texas at Austin. We thank T.E. Larson, E.M. Marshall, D.O. Breecker, S. Loewy, B.L. Byerly, and R. Chatterjee for laboratory assistance. Some of the xenoliths studied here were collected when DAC and WAB were employed by the U.S. Geological Survey, which supported their fieldwork and

microprobe mineral analyses. DAC is supported through a grant from the David and Lucile Packard Foundation to the Monterey Bay Aquarium Research Institute. Constructive comments by two anonymous reviewers and the editor Tamsin Mather are appreciated and helped improve this manuscript.

Chapter 2: Geochemistry of Mafic and Ultramafic Xenoliths from Hualalai Volcano: Implications for the Origins of Hawaiian Rejuvenated Volcanism

2.1 INTRODUCTION

The Hawaiian Islands are a series of volcanoes developed on the Pacific plate that migrates over a relatively stationary mantle plume (Mogan, 1972). Hawaiian volcanoes commonly evolve through pre-shield stage, shield stage, post-shield stage, and a final rejuvenated stage that usually follows a hiatus in activity after the shield/post-shield stage (Clague & Dalrymple, 1987). Hawaiian lavas display large chemical and isotopic variations, both temporally and spatially. For example, post-shield-stage and rejuvenated-stage lavas usually have more depleted isotopic compositions than shield-stage lavas from the same volcano (e.g., Frey et al., 2005; Fekiacova et al., 2007). There is still no consensus as to whether these variations reflect intrinsic heterogeneity of the mantle plume, mixtures of the plume source with entrained mantle, or contamination by Pacific lithosphere (e.g., Class & Goldstein, 1997; Hofmann & Farnetani, 2013).

In particular, the origin of Hawaiian rejuvenated-stage lavas is highly debated. Because they are characterized by depleted isotopic compositions, many previous studies have proposed that rejuvenated lavas may derive from depleted Pacific lithosphere that has been metasomatized by melts from the Hawaiian plume (e.g., Lassiter et al., 2000; Yang et al., 2003; Dixon et al., 2008). In contrast, recent studies have argued that the rejuvenated lavas are isotopically distinct from Pacific lithosphere, and therefore the rejuvenated lavas sample a depleted source that is widely distributed within the plume itself (e.g., rejuvenated lavas have higher $^{208}Pb/^{204}Pb$ at a given $^{206}Pb/^{204}Pb$ than inferred Pacific lithosphere; Fekiacova et al., 2007; Bizimis, 2013). These debates are largely due

to lack of constraints on the compositions of local Pacific lithosphere beneath the Hawaiian Islands.

The ca. 1800-1801 Kaupulehu flow of Hualalai Volcano, Hawaii contains abundant xenoliths of dunite, wehrlite and gabbro, and rare websterite and anorthosite (Jackson et al., 1981; Clague, 1987; Kauahikaua et al., 2002). According to their Sr-Nd isotope compositions, the majority of these xenoliths are cumulates derived from Hualalai magmas, whereas a small subset of gabbroic xenoliths sample *in situ* Pacific lower oceanic crust (Clague, 1987; Gao et al., 2016). The chemical and isotopic characteristics of these xenoliths can provide critical constraints on the contribution of lithosphere assimilation to the evolution of Hawaiian lava compositions. The lower oceanic crust (LOC) xenoliths provide direct information on the composition of *in situ* lithosphere beneath the Hawaiian Islands. If lithosphere assimilation is significant during magma ponding, signatures of coupled assimilation and fractional crystallization (AFC) is expected to be evident in Hualalai-magma-derived cumulates.

In this study, we report mineral major element, and Sr, Nd, Os and O isotope variations in 12 Hualalai-derived ultramafic (8 dunite and 4 websterite) xenoliths. We also report new Os, Hf and Pb isotope data for a suite of gabbroic xenoliths (both Hualalai- and LOC-derived), which have been previously characterized for chemical and Sr-Nd-O isotope compositions (e.g., Lassiter et al., 1998; Gao et al., 2016a). These new geochemical data are then used to constrain the role of Pacific lithosphere in generating/affecting Hawaiian lava compositions, especially the rejuvenated-stage lavas.

2.2 SAMPLES AND METHODS

The xenoliths examined in this study are from the c.a. 1800-1801 post-shield Kaupulehu alkalic basalt flow of Hualalai Volcano. Ten ultramafic xenoliths (8 dunites

and 2 websterites) were collected by David Clague. Two additional websterites were from the Jackson collection housed at the Simithsonian National Museum of Natural History. Dunites are composed of olivine (~97-99% modal abundance), spinel (~1-2%) and clinopyroxene (<1%). All websterites contain clinopyroxene (~30-45%) and orthopyroxene (~40-60%). Two websterites (63kap-16, 87kap-4) also contain olivine (~15%), and one (63kap-16) contains a small amount of plagioclase (~2%). All ultramafic xenoliths are relatively fresh with no visible alteration. Twenty-eight gabbroic xenoliths were also provided by Clague and Smithsonian Institution. These gabbros include 1-pyroxene (only clinopyroxene) and 2-pyroxene (both clinopyroxene and orthopyroxene) cumulates derived from Hualalai magmas, and 2-pyroxene gabbros from ancient Pacific LOC (Gao et al., 2016a). More detailed sample description of the gabbroic xenoliths can be found in Gao et al. (2016a). These gabbros have been previously characterized for major element, trace element, and Sr-Nd-O isotope compositions (e.g., Clague, 1987; Lassiter et al., 1998; Gao et al., 2016a).

Mineral major element abundances of Hualalai ultramafic xenoliths were measured via EPMA on a JEOL-8200 microprobe using methods outlined in Gao et al. (2016a). Fresh mineral grains were mounted in epoxy and polished for probe analyses. Measurements of secondary standards were accurate to within 5% for Na, Ni and Cr, within 3% for Al, Si and Fe, within 1% for Mg and Ca, and 15% for MnO. The Fe_2O_3 content of spinel was calculated by normalizing all cations to 3.0, assuming Fe was the only multivalent cation, and by partitioning Fe between Fe^{3+} and Fe^{2+} to result in 4.0 oxygens.

For gabbros and websterites, 50-150 mg clinopyroxene separates were processed for Sr, Nd, and Lu-Hf isotope analyses. For dunites, Sr isotopes were measured on 100-150 mg whole rock chips. One websterites was also analyzed for whole rock Sr isotope

composition to check that clinopyroxene isotope compositions comparable to whole rock. Mineral separates and whole rock chips are picked under a binocular microscope to avoid adhered melts and/or surface alteration. Samples were digested following procedures described in Byerly & Lassiter (2012) and Connelly et al. (2006). The separation and analytical procedure, precision and accuracy of Sr, and Nd isotopes were as described in Gao et al. (2016a). AG1-X8 and DGA resins were used to separate Lu and Hf. Lutetium and Hf isotopes were analyzed using a Micromass IsoProbe MC-ICP-MS. The JMC Hf standard was measured between every third samples for standard correction; BRC-2 and BHVO-2 were measured as secondary standards. Average measured $^{176}Hf/^{177}Hf$ of BHVO-2 was 0.283106±0.000046 (2 s.d.), and the accepted value is 0.283109 (GeoReM), and average measured BCR-2 was 0.282867±0.000056 (2 s.d.) with accepted value 0.282878 (GeoReM). Lutetium and Hafnium concentrations were determined by isotope dilution using a mixed ^{176}Lu-^{180}Hf spike.

Lead isotopes were measured on 100-150 mg plagioclase separates. Samples were leached in dilute HF for 5 min before digestion. Both the leachates and leached samples were analyzed for Pb isotope compositions. Lead was separated using AG1-X8, and analyzed as metal loaded with Silica gel on a Triton TIMS. The NBS 981 standard was measured by double spike method regularly, with average measured $^{206}Pb/^{204}Pb$ = 16.933±0.003, $^{207}Pb/^{204}Pb$ = 15.488±0.003, and $^{208}Pb/^{204}Pb$ = 36.688±0.011 (2 s.d.). For comparison, the values reported by Todt et al. (1996) are $^{206}Pb/^{204}Pb$ = 16.9356±0.0007, $^{207}Pb/^{204}Pb$ = 15.4891±0.0009, and $^{208}Pb/^{204}Pb$ = 36.7006±0.0034 (2 s.d.). Average mass fractionation of unspiked NBS 981 was 1.1‰ per AMU. For most samples, instrumental mass fractionation was corrected using a Pb double spike. The other samples were mass fractionation corrected using the average NBS 981 fractionation factor. Double-spike

measurements are within error of mass fractionation corrected values. Pb blanks were lower than 20 pg/g.

Rhenium and Os were separated from bulk xenolith powders following the procedure of Byerly & Lassiter (2012). Fresh samples were carefully polished with aluminum oxide sandpaper to remove any saw marks, and rinsed with DI water. Air dried samples were then wrapped in plastic and crushed with a hammer before being powdered in an alumina ball mill. Os isotopes were measured with the Triton TIMS in negative ion mode, and Re isotopes were analyzed by MC-ICP-MS. The UMD Os standard was measured regularly, averaging a measured $^{187}Os/^{188}Os$ of 0.11382±0.00003 (2 s.d.), which is consistent with value reported by Walker et al. (2005) (0.1137920±0.0000024). Os blank was 160 fg/g. Rhenium and osmium concentrations were determined by isotope dilution using a mixed ^{185}Re-^{190}Os spike. Powder splits of five LOC gabbros were also analyzed for Re concentrations at the University of Bonn.

Oxygen isotopes were analyzed on ~2 mg olivine crystals that were carefully picked under a binocular microscope to avoid visible melt infiltration, inclusions, or surface alteration. Oxygen was extracted by laser fluorination (Sharp, 1990). In house quartz standard Lausanne-1 ($\delta^{18}O$ = 18.1‰), garnet standard UWG-2 ($\delta^{18}O$ = 5.8‰) (Valley et al., 1995) and olivine standard San Carlos ($\delta^{18}O$ = 5.25‰) were measured to ensure accuracy and precision. $\delta^{18}O$ values are reported relative to SMOW, where the $\delta^{18}O$ value of NBS-28 is +9.65‰. Duplicates were run for three samples on different days. All the analyses described above were performed at the University of Texas at Austin.

2.3 RESULTS

Mineral major element compositions of ultramafic xenoliths are reported in Table 2.1. Coexisting olivine, clinopyroxene, and orthopyroxene in individual samples have similar Mg# (molar 100*Mg/(Mg+Fe)), and show no core-rim variation. Websterites have Mg# ranging from 82-86. Clinopyroxene TiO_2 contents of websterites range from 0.25 – 0.31. Dunites have Mg# ranging from 84 to 90. Spinel in dunites have Mg# ranging from 49 to 63 and Cr# varying between 34 and 65. For comparison, gabbroic xenoliths have clinopyroxene Mg# ranging from 73 to 85 (Gao et al., 2016a).

New Sr-Nd-Pb-Hf-Os-O isotope data are reported in Table 2.2. Clinopyroxene from websterites have $^{87}Sr/^{86}Sr$ = 0.70338 – 0.70358 and $^{143}Nd/^{144}Nd$ = 0.51289 – 0.51296. One websterites was also analyzed for whole rock $^{87}Sr/^{86}Sr$ (0.70336), which is consistent with clinopyroxene $^{87}Sr/^{86}Sr$ (0.70338). This suggests that clinopyroxene have isotopic compositions in equilibrium with whole rock. Whole rock $^{87}Sr/^{86}Sr$ ratios of dunite xenoliths range between 0.70355 and 0.70361. For comparison, Hualalai shield-stage lavas have $^{87}Sr/^{86}Sr$ = 0.70366 – 0.70380 and $^{143}Nd/^{144}Nd$ = 0.51285 – 0.51293, whereas post-shield-stage lavas have $^{87}Sr/^{86}Sr$ = 0.70351 – 0.70366 and $^{143}Nd/^{144}Nd$ = 0.51290 – 0.51296 (e.g., Yokose et al., 2005; Yamasaki et al., 2009; Hanano et al., 2010). Websterite xenoliths have $^{143}Nd/^{144}Nd$ within the range of Hualalai lavas, but extend to lower $^{87}Sr/^{86}Sr$. The Sr isotope compositions of dunite xenoliths are within the range of post-shield-stage lavas (Fig. 2.1).

	63-kap-16		87-kap-4		88-kap-1		87-kap-37		96-kap-19	
	opx	*ol*	*cpx*	*opx*	*cpx*	*opx*	*ol*	*sp*	*ol*	*sp*
SiO_2	54.61 (.72)	39.96 (.34)	51.21 (.56)	53.43 (.60)	52.27 (.58)	55.74 (.50)	39.65 (.57)		40.12 (.40)	
Al_2O_3	2.93 (.16)		3.30 (.30)	3.25 (.65)	3.16 (.32)	1.92 (.26)		14.58 (.68)		16.13 (.26)
Na_2O	0.11 (.04)		0.68 (.08)	0.07 (.02)	0.42 (.09)	0.10 (.00)				
MgO	30.82 (1.16)	46.75 (.23)	16.81 (.28)	29.57 (.22)	19.04 (1.42)	31.71 (.01)	47.06 (.26)	10.59 (.34)	48.36 (.30)	12.16 (.04)
CaO	2.62 (1.89)	0.07 (.02)	20.42 (.29)	1.52 (.07)	18.68 (1.49)	1.65 (.06)	0.09 (.03)		0.07 (.02)	
MnO	0.18 (.02)	0.19 (.03)	0.18 (.04)	0.22 (.02)	0.15 (.03)	0.16 (.01)	0.20 (.02)	0.23 (.02)	0.17 (.02)	0.19 (.03)
FeO	8.86 (.52)	14.01 (.11)	6.30 (.03)	11.64 (.26)	5.61 (.20)	9.25 (.33)	13.72 (.22)	19.99 (.27)	12.11 (.27)	17.56 (.50)
Fe_2O_3								16.22 (.70)		11.95 (.24)
TiO2	0.20 (.04)		0.31 (.04)	0.19 (.05)	0.25 (.05)	0.10 (.06)		2.40 (.29)		1.91 (.09)
Cr_2O_3	0.54 (.05)		0.86 (.12)	0.48 (.12)	0.93 (.23)	0.62 (.04)		36.67 (.10)		41.03 (.45)
NiO	0.08 (.03)	0.34 (.02)	0.05 (.04)	0.08 (.02)	0.05 (.02)	0.10 (.03)	0.30 (.03)	0.22 (.01)	0.40 (.02)	0.23 (.03)
Totals	100.96 (.75)	101.33 (.33)	100.12 (.84)	100.46 (.48)	100.56 (.72)	101.36 (.44)	101.02 (.85)	100.90 (.25)	101.26 (.65)	101.17 (1.02)
Mg#	86.2 (.3)	85.7 (.1)	82.8 (.2)	82.1 (.4)	85.9 (.9)	86.0 (.4)	86.1 (.1)	48.8 (1.1)	87.8 (.2)	55.5 (.8)
Cr#								65.4 (1.0)		65.5 (.1)

Table 2.1: Major element compositions of Hualalai ultramafic xenoliths.

Major element contents reported are average of multiple analyses (wt.%). Digits in brackets after concentrations are 1 s.d. of the mineral population for each sample.

	87-kap-42			94-kap-5	87-kap-32		96-kap-20	92-kap-2		87-kap-33	
	cpx	*ol*	*sp*	*ol*	*ol*	*sp*	*ol*	*ol*	*sp*	*ol*	*sp*
SiO_2	50.74 (.56)	39.11 (.36)		39.81 (.53)	39.90 (.22)		39.67 (.55)	39.45 (.41)		39.84 (.15)	
Al_2O_3	4.71 (.44)		32.88			23.40 (1.51)			29.45 (.11)		22.07 (.57)
Na_2O	0.97 (.10)										
MgO	17.24 (1.34)	46.67 (.04)	15.11	47.41 (.24)	48.33 (.09)	14.38 (.18)	49.64 (.17)	45.13 (.11)	13.31 (.04)	45.71 (.09)	12.31 (.23)
CaO	19.10 (1.72)	0.12 (.03)		0.15 (.03)	0.14 (.01)		0.10 (.01)	0.17 (.01)		0.16 (.00)	
MnO	0.14 (.02)	0.22 (.03)	0.15	0.17 (.01)	0.15 (.03)	0.17 (.02)	0.18 (.01)	0.22 (.03)	0.19 (.00)	0.26 (.03)	0.20 (.02)
FeO	5.53 (.43)	14.45 (.31)	16.33	12.55 (.29)	11.25 (.10)	15.52 (.28)	10.50 (.24)	15.73 (.41)	18.56 (.18)	15.49 (.16)	17.87 (.24)
Fe_2O_3			10.84			8.86 (.10)			16.92 (.25)		14.07 (1.20)
TiO_2	0.76 (.22)		2.43			2.56 (.14)			2.63 (.00)		1.62 (.24)
Cr_2O_3	1.16 (.12)		23.39			34.79 (1.34)			20.11 (.10)		32.45 (.64)
NiO	0.06 (.02)	0.26 (.04)	0.27	0.45 (.03)	0.43 (.04)	0.34 (.03)	0.43 (.04)	0.30 (.03)	0.30 (.03)	0.23 (.03)	0.23 (.03)
Totals	100.42 (.22)	100.91 (.07)	101.4	100.57 (.81)	100.27 (.29)	100.02 (.25)	100.53 (.39)	101.08 (.55)	101.46 (.35)	101.74 (.09)	100.83 (.66)
Mg#	84.9 (.2)	85.3 (.3)	62.5	87.2 (.2)	88.5 (.1)	62.5 (.7)	89.5 (.2)	83.8 (.3)	56.3 (.3)	84.2 (.1)	55.4 (.6)
Cr#			34.8			52.7 (2.6)			33.9 (.2)		52.4 (.7)

Table 2.1: Major element compositions of Hualalai ultramafic xenoliths (continue).

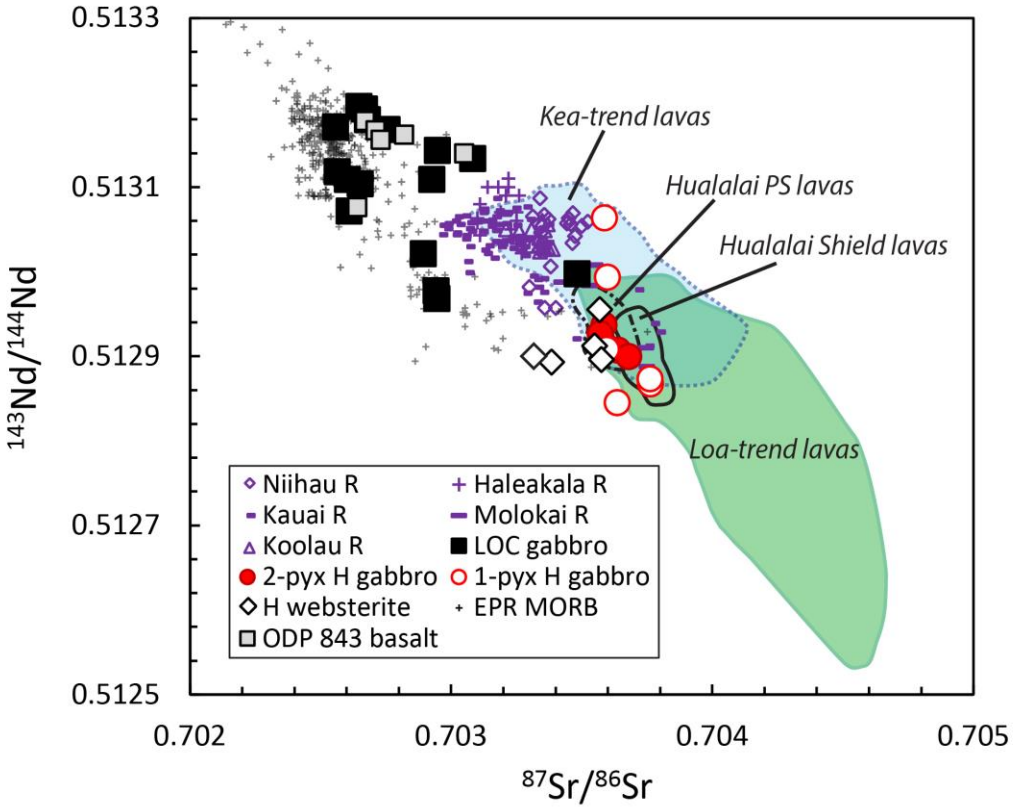

Figure 2.1: Sr-Nd isotope plot.

The clinopyroxene Sr-Nd isotope compositions of Hualalai gabbroic and ultramafic xenoliths are plotted in comparison with Hawaiian lavas, EPR MORBs, and basalts from ODP Site 843 (data compiled from GeoRoc and PetDB). Hawaiian shield and post-shield stage lavas are shown as Kea-trend and Loa-trend fields. The fields of Hualalai shield and post-shield stage lavas are also drawn for comparison. Hawaiian rejuvenated-stage lavas from Niihau, Haleakala, Kauai, Molokai, and Koolau are shown with purple symbols.

Three gabbros with Hualalai-like Sr-Nd isotope compositions (Hualalai-derived cumulate, Gao et al., 2016a) have plagioclase Pb isotope compositions ($^{206}Pb/^{204}Pb$ = 17.974-18.010, $^{207}Pb/^{204}Pb$ = 15.437-15.447, $^{208}Pb/^{204}Pb$ = 37.736-37.755) similar to Hualalai post-shield lavas (e.g., $^{206}Pb/^{204}Pb$ = 17.891-18.011; Hanano et al., 2010). One cumulate gabbro has anomalously high $^{206}Pb/^{204}Pb$ ($^{206}Pb/^{204}Pb$ = 18.327, $^{207}Pb/^{204}Pb$ = 15.421, $^{208}Pb/^{204}Pb$ = 37.772; Fig. 2.2). Most gabbros with depleted, MORB-like Sr-Nd isotope compositions (LOC-derived, Gao et al., 2016a) span a range of plagioclase Pb compositions ($^{206}Pb/^{204}Pb$ = 18.016-18.272, $^{207}Pb/^{204}Pb$ = 15.445-15.497, $^{208}Pb/^{204}Pb$ = 37.610-37.981) that fall between EPR basalts and Hawaiian lavas. The Pb isotope compositions of leachates are reported in Table S2.1. Leachates are more radiogenic than leached samples, and have particularly high $^{207}Pb/^{204}Pb$ ratios. This is consistent with the unleached-leached paring whole rock analyses by Lassiter and Hauri (1998). Similar to the leachates, two LOC-derived gabbros also have high $^{207}Pb/^{204}Pb$ (15.588 and 15.593, respectively) (Fig. 2.2).

Clinopyroxene from most Hualalai-derived 2-pyroxene gabbros have ε_{Hf} ranging from 8.8 to 10.9, whereas one sample has high ε_{Hf} of 20.7. Clinopyroxene from 1-pyroxene gabbros have ε_{Hf} varying between 10.9 and 13.3. Clinopyroxene from LOC-derived gabbros have ε_{Hf} ranging from 11.7 to 18.6, which positively correlates with $^{176}Lu/^{177}Hf$ but displays significant scatter (Fig. S2.1a).

Hualalai-derived xenoliths span a narrow range of Os isotope compositions ($^{187}Os/^{188}Os$ = 0.133 – 0.138; Fig. 2.3), which is similar to Hualalai lavas ($^{187}Os/^{188}Os$ = 0.134 – 0.138), and within the range of "Loa trend" lavas ($^{187}Os/^{188}Os$ = 0.132 – 0.146; e.g., Hauri et al., 1996; Lassiter & Hauri, 1998). LOC gabbros have highly radiogenic Os ($^{187}Os/^{188}Os$ = 0.212-0.634) that positively correlates with $^{187}Re/^{188}Os$ (Fig. S2.1b).

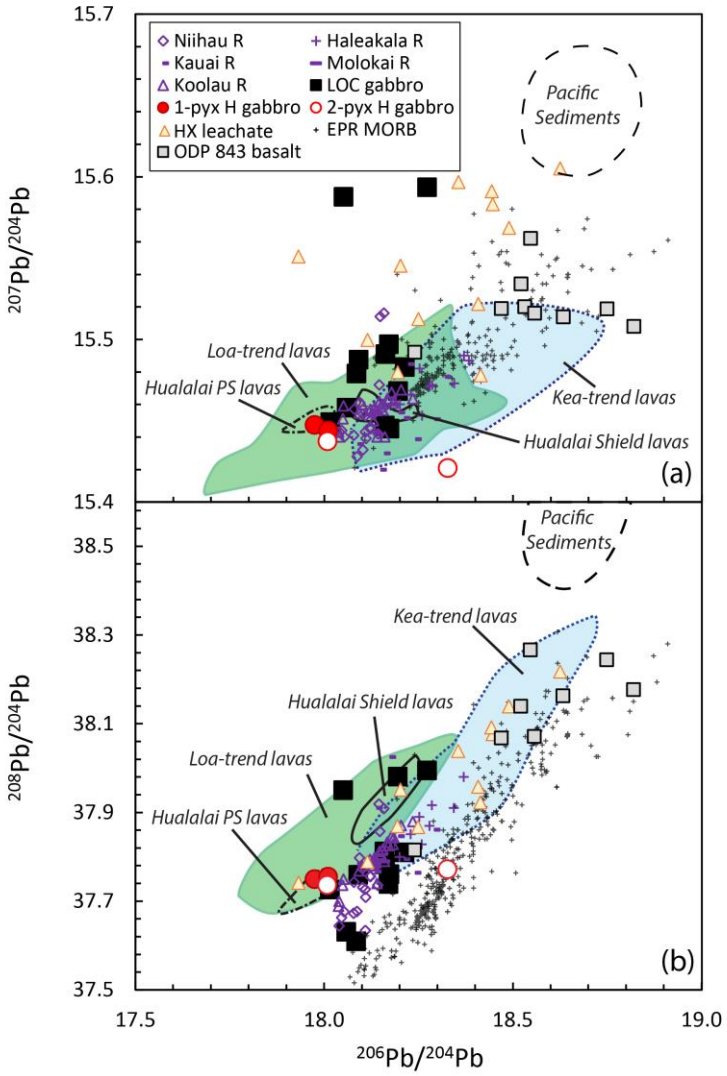

Figure 2.2: Pb isotope plot.

The plagioclase Pb isotope compositions of Hualalai xenoliths are compared with Hawaiian lavas, EPR MORBs, and basalts from ODP Site 843 (data compiled from GeoRoc and PetDB). Hualalai xenolith leachate compositions are also plotted for comparison.

	Rock Type	An (plag)	$^{87}Sr/^{86}Sr$ (cpx/wr)	$^{143}Nd/^{144}Nd$ (cpx)	Lu (cpx)	Hf (cpx)	$^{176}Hf/^{177}Hf$ (cpx)	$^{206}Pb/^{204}Pb$ (plag)	$^{207}Pb/^{204}Pb$ (plag)	$^{208}Pb/^{204}Pb$ (plag)	Δ8/4 (plag)	$\delta^{18}O$ (ol)	Re (wr)	Os (wr)	$^{187}Os/^{188}Os$ (wr)
LOC															
63kap-3	G	86.4						18.090	15.488	37.760	26.1				
65kap-14d*	G	97.7						*18.085*	*15.479*	*37.610*			0.82	24	0.563
63kap-13**	G	85.4			0.1	0.3	0.283223	*18.213*	*15.483*	*37.810*				18	0.395
65kap-13	G	76.9			0.1	0.3	0.283153	18.162	15.491	37.783	19.9		0.16	15	0.285
65kap-14a*	G	97.7						*18.051*	*15.588*	*37.950*			0.83	33	0.634
65kap-14a (dup)													1.00**		
83kap-9	G	83.2						18.171	15.497	37.739	14.3		0.39	25	0.448
83kap-9 (dup)													0.47**	38	
94kap-7*	G	96.8						*18.272*	*15.593*	*37.995*			0.58	19	0.630
94kap-7 (dup)*								*18.316*	*15.584*	*38.002*			0.86**	16	
96kap-7	G	64.5			0.2	0.4	0.283299	18.059	15.458	37.631	17.1				
83kap-8**	G	83.6						*18.173*	*15.445*	*37.761*					
65-7-133	G	78.6			0.2	0.6	0.283236	18.160	15.447	37.812	23.0				
65-60-32	G	70.2			0.4	1.0	0.283087								
88kap-2	G	80.5													
87kap-14	G	61.7			0.2	0.4	0.283248								
87kap-10	G	93.7			0.1	0.2	0.283292								
65-61-26	G	79.3			0.2	0.8	0.283102	18.195	15.468	37.981	35.6		0.31	18	0.370
65-61-26 (dup)													0.34**	24	
65-86-64	G	65.6			0.2	0.4	0.283201	18.016	15.449	37.726	31.8		0.19	25	0.212
65-86-64 (dup)						0.3	0.283177								
Hualalai post-shield															
63kap-7*	G	73.2						*17.974*	*15.447*	*37.750*					
65-86-92	G	83.1			0.1	0.9	0.283080						0.36	1001	0.1340
65-109-146abc	G	79.0			0.1	1.2	0.283148								
65-60-221	G	57.1			0.3	3.3	0.283090								
65-100-110	G	67.5						18.010	15.444	37.755	35.4				

Hualalai shield															
87kap-37	D		0.703605[w]									5.3		393	0.1337
96kap-19	D		0.703548[w]									5.3	0.02	3590	0.1345
87kap-42	D		0.703557[w]									5.1, 5.3	0.19	1752	0.1353
94kap-5	D											5.3		410	0.1341
87kap-32	D		0.703591[w]									5.5	0.05	297	0.1326
96kap-20	D												0.03	648	0.1341
92kap-2	D											5.4		439	0.1345
87kap-33	D		0.703598[w]									5.4	2.16	1070	0.1344
63kap-15	G	61.4			0.2	1.2	0.283357	18.327	15.421	37.772	-1.2		1.21	138	0.1320
63kap-15 (dup)								18.319	15.404	37.725	-4.8				
65-115-10	G	71.4			0.1	2.0	0.283080	18.008	15.437	37.736	33.8		0.08	63	0.1370
65-60-17	G				0.1	1.1	0.283139								
84-1801-5	G	67.9			0.1	0.2	0.283071								
84-1801-5 (dup)						0.2	0.283030								
87kap-11	G	65.4			0.1	0.4	0.283033						0.09	363	0.1360
63kap-16	W		0.703384[c]	0.512893								5.6	0.09	104	0.1356
63kap-16 (dup)			0.703362[w]												
87kap-4	W		0.703550[c]	0.512912								5.3, 5.5	0.42	538	0.1363
65-114-105	W		0.703569[c]	0.512955								5.3, 5.3	0.17	1425	0.1335
88kap-1	W		0.703576[c]	0.512896									1.14	19	0.1385

Table 2.2: Sr-Nd-Pb-Hf-Os-O isotope data of Hualalai mafic and ultramafic xenoliths.

[*] Standard corrected Pb isotope data. [**] Re concentrations measured at University of Bonn. [c] Sr isotopes measured on cpx. [w] Sr isotopes measured on whole rock. G - gabbro, D – dunite, W – websterites. Lu and Hf concentrations are in ppm; Re concentrations are in ppb; Os concentrations are in ppt.

Olivines from the websterite xenoliths have $\delta^{18}O$ values range from +5.3 to +5.6‰. Dunites have olivine $\delta^{18}O$ values range from +5.2 to +5.5‰. Their narrow ranges of oxygen isotope compositions are largely consistent with Hualalai lavas ($\delta^{18}O_{ol}$ = +5.3 to +5.4‰; Eiler et al., 1996).

2.4 DISCUSSION

2.4.1 Effects of crustal storage and melt-crust interaction on Hualalai magmas

The compositional variations of Hawaiian lavas have been widely used to infer heterogeneities within the plume source. However, Hawaiian magmas have transported through and ponded within the Pacific lithosphere (e.g., Bohrson, 2007 and references therein). Small-scale heterogeneities may be obscured in erupted lavas, because discrete melt batches with distinct compositions may be mixed and homogenized during magma ponding. In addition, the composition of erupted lavas may have been overprinted as the result of assimilating Pacific lithosphere that is isotopically distinct from Hawaiian magmas. Therefore, in order to make proper interpretation of the compositional variations of Hawaiian lavas, it is necessary to evaluate the effects of crustal storage and melt-crust interaction on Hawaiian magmas.

The majority of Hualalai xenoliths are cumulates formed by fractional crystallization of Hualalai magmas during ponding within crustal reservoirs (e.g., Clague, 1987). Hualalai cumulate xenoliths include a variety of lithologies, which likely result from crystallization of different magma types at various depths. These cumulate xenoliths thus can provide more information on the compositional variability of discrete melt batches than erupted lavas. The significance of magma mixing and homogenization may be constrained by comparing the compositional variability of cumulate xenoliths with that of erupted lavas. In addition, if Hualalai melts have assimilated wall materials during

magma ponding and fractional crystallization, signatures of coupled assimilation and fractional crystallization (AFC) should be recorded in cumulate xenoliths. In the following discussion, we first discussed the origins (parental magma and depth of fractionation) of Hualalai cumulate xenoliths. The geochemical variations of these cumulate xenoliths are then used to evaluate the role of magma mixing and crustal assimilation in the evolution of Hualalai melt compositions.

2.4.1.1 Origins of Hualalai xenoliths

Hualalai volcano has evolved through a shield stage that is dominated by tholeiitic basalt eruption, and a post-shield stage characterized by alkali basalt eruption. The magma plumbing systems of Hawaiian volcanoes also evolve over time. A shallow-level reservoir within the volcanic edifice has been detected by seismic imaging at Hawaiian shield-stage volcanoes (e.g., Mauna Loa and Kilauea; Okubo et al., 1997). Some studies argue that a deep magma reservoir also exists during the shield stage (e.g., Clague, 1987; Vazquez et al., 2007; Gao et al., 2016a), whereas other studies suggest that there is only one shallow reservoir (e.g., Frey et al., 1990; Shamberger and Hammer, 2006). During the post-shield stage, decreasing magma supply leads to solidification of the shallow reservoir. The presence of LOC gabbroic xenoliths in post-shield-stage lavas suggests deep magma reservoirs exist within or at the base of LOC during the post-shield stage (e.g., Bohrson, 2007 and references therein). Therefore, Hualalai cumulate xenoliths may be crystallized from either shield-stage tholeiitic magma or post-shield-stage alkalic magma at a range of depths. Here we discuss the origins of Hualalai xenoliths by combining (1) xenolith composition and lithology; (2) MELTS thermodynamic models (Ghiorso and Sack, 1995); and (3) comparison with previous interpretations of the origins of Hualalai mafic and ultramafic xenoliths (Table 2.3).

Lithology	Shield stage?	Post-shield stage?	P/T constraints
1-pyx gabbros		Lack orthopyroxene High clinopyroxene TiO2 contents (e.g., B&C, 1988; F&G, 1997)	
2-pyx gabbros	Presence of orthopyroxene Low clinopyroxene TiO_2 contents (e.g., B&C, 1988; F&G, 1997)		1007 – 1069°C; ~1 – 5, mostly ~3 kbar (S&H, 2006) 942 – 1075°C, ~2.5 – 5 kbar (Gao, 2016)
Websterites	Presence of orthopyroxene Low clinopyroxene TiO_2 contents (e.g., B&C, 1988; F&G, 1997)		1225 – 1350°C, 4.5 – 9 kbar (B&C, 1988)
Dunite	Presence of orthopyroxene MELTS modeling: major liquidus phase Cross-cutting by websterite vein	Spinel Cr#, clinopyroxene $^{87}Sr/^{86}Sr$ and whole-rock $^{3}He/^{4}He$ similar to post-shield lavas (Chen, 1992)	<2.8 kbar (Roedder, 1965; C&B, 1991) <2 kbar (this study)

Table 2.3: Origins of Hualalai cumulate xenoliths.

Summary of interpretations of the parental magmas and fractional crystallization depths of Hualalai cumulate xenolith.

The majority of xenoliths from the c.a. 1800-1801 Kaupulehu flow are cumulates derived from Hualalai magmas, except that a small subset represents fragments of ancient Pacific LOC gabbro layer (e.g., Clague, 1987; Lassiter and Hauri, 1998; Gao et al., 2016a). Sixteen of the 2-pyroxene gabbros examined in this study are characterized by depleted Sr-Nd isotope compositions and depleted light rare earth element (LREE) patterns that are similar to oceanic crust cumulate, but distinct from Hawaiian lavas (Gao et al., 2016a). These gabbros also have highly radiogenic Os isotope compositions ($^{187}Os/^{188}Os$ = 0.212-0.634) that are positively correlated with $^{187}Re/^{188}Os$. This is consistent with ingrowth of ^{187}Os through radiogenic decay of ^{187}Re over time. All these features indicate that these 2-pyroxene gabbros derive from ancient Pacific LOC beneath the Hawaiian Islands. In contrast, all the other 2-pyroxene gabbros, 1-pyroxene gabbros, dunites, and websterites examined have Sr, Nd and Os isotope compositions similar to Hawaiian lavas (Gao et al., 2016a and this study). In addition, clinopyroxene from these gabbros have rare earth element concentrations that are in equilibrium with Hualalai-lava-like melts (Gao et al., 2016a). These xenoliths are therefore most likely cumulates derived from Hualalai magmas. In this section, we will only concentrate on discussing the origins of the cumulate xenoliths. Therefore, the depleted 2-pyroxene gabbros will be referred to as LOC-derived gabbros, whereas 2-pyxroxene gabbros only refer to Hualalai-derived cumulate gabbros in the following discussion.

The shield- versus post-shield-stage origins of Hualalai cumulate xenoliths can be inferred from their petrology and mineral compositions. Presence of orthopyroxene suggests that the parental magma is silica-saturated, and therefore indicates tholeiitic origin (e.g., Bohrson and Clague, 1988; Fodor and Galar, 1997; Shamberger and Hammer, 2006). In addition, silica-saturated tholeiitic magma-derived clinopyroxene is characterized by lower TiO_2 contents at a given Mg# than alkalic magma-derived

clinopyroxene (e.g., Clague and Bohrson, 1991; Fodro and Galar, 1997). Therefore, 2-pyroxene gabbros and websterites that contain orthopyroxene and have relatively low TiO_2 content most likely derive from tholeiitic shield-stage magmas (Fig. 2.3).

Websterites appear to derive from greater depths than 2-pyroxene gabbros. Bohrson and Clague (1988) examined the textures of websterite xenoliths to extract information of mineral crystallization sequence, which was compared to the results of fractional crystallization experiments conducted at a range of pressures. They argued that first crystallization of olivine followed by orthopyroxene is consistent with fractionation of websterites between ~4.5-9 kbar (Bohrson and Clague, 1988). Shamberger and Hammer (2006) suggested 2-pyroxene gabbros were crystallized at lower pressures (~1-5 kbar, mostly 3 kbar) based on clinopyroxene geobarometry (Nimis, 1999). Gao et al (2016a) also suggested similar crystallization depths (~2.5 – 5 kbar) for 2-pyroxene gabbros based on comparing the mineral compositions of 2-pyroxene gabbros with MELTS models.

The higher inferred crystallization pressures of websterites compared to those gabbros indicate that websterites may crystallize earlier and cumulate deeper than 2-pyroxene gabbros. This is consistent with 2-pyrxoene gabbros extending to lower Mg#(78-83; Gao et al., 2016a) than websterites (Mg# = 83-87). This is also in agreement with the higher sub-solidus equilibrium temperatures recorded in websterites. Two-pyroxene thermometer suggests websterite xenoliths were last equilibrated at temperatures of ~1045-1090 °C (Bohrson and Clague, 1988). Two-pyroxene gabbros record subsolidus 2-pyroxene equilibration temperatures of ~942–1075°C (Gao et al., 2016a). QUIF thermometry (Lindsley and Frost, 1992; Andersen et al., 1993) also suggested similar equilibrium temperature of ~1007 – 1069°C for 2-pyroxene gabbros (Shamberger and Hammer, 2006).

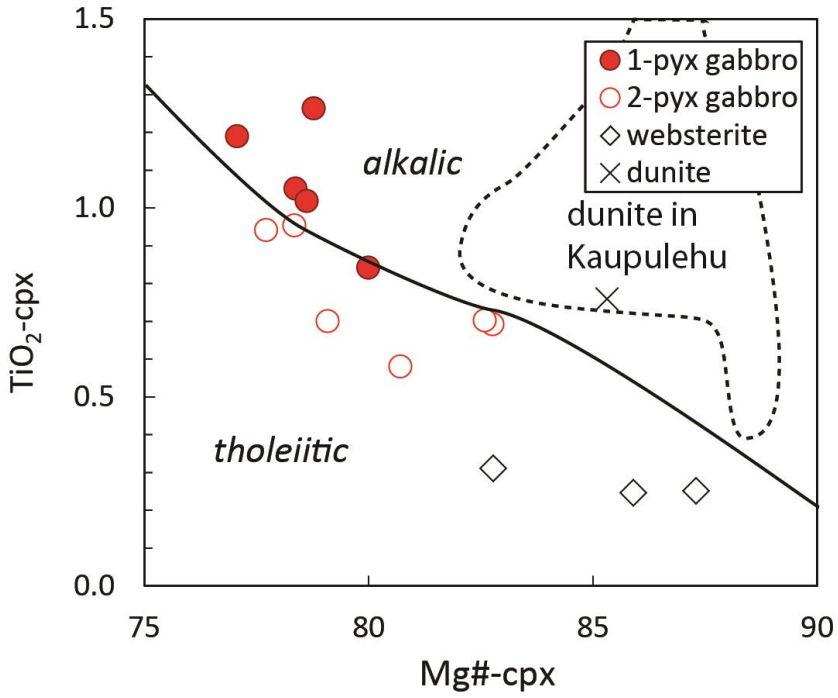

Figure 2.3: Mg# versus TiO_2 content of clinopyroxene.

The alkali versus tholeiitic divide is based on the compositions of clinopyroxene phenocryst in Hualalai tholeiitic shild-stage and alkalic post-shield-stage lavas following Clague and Bohrson (1991). Dashed line marks the range of clinopyroxene composition of dunite xenoliths in the Kaupulehu flow (Clague and Bohrson, 1991).

In contrast, 1-pyroxene gabbros most likely derive from fractional crystallization of post-shield-stage alkalic magmas within LOC reservoirs. One-pyroxene gabbros lack orthopyroxene, and have relatively high clinopyroxene TiO_2 content. These features are consistent with derivation from alkalic magmas (Gao et al., 2016a). During the post-shield stage, the shallow edifice reservoir existed during shield-stage is solidified, as the result of decreasing magma supply rate. Only the deep, LOC reservoir maintains. Therefore, 1-pyroxene gabbros are most likely crystallized at LOC depths.

The parental magma of dunite xenoliths is less straightforward. Chen et al (1992) suggested that dunites derive from alkalic post-shield-stage magmas. This interpretation was based on dunite xenoliths have similar spinel Cr# (molar 100*Cr/(Cr+Al), ~20-70) as phenocrysts in post-shield-stage lavas (~30 – 60). In addition, dunite whole rock $^{3}He/^{4}He$ values (8.6 – 9.6 Ra) are consistent with post-shield-stage lavas (7.84 – 9.84 Ra), but significantly lower than shield-stage lavas (14.4 – 17.6 Ra). Finally, clinopyroxene separates of dunites have $^{87}Sr/^{86}Sr$ (0.70348 – 0.70361) within the range of post-shield-stage lavas (0.70351 – 0.70366) (Chen et al., 1992). Our measurements of dunite whole-rock $^{87}Sr/^{86}Sr$ (0.70355 - 0.70361) are also consistent with post-shield-stage lavas.

However, Chen et al (1992) also documented a dunite xenolith containing orthopyroxene, which would suggest derivation from tholeiitic magma. In addition, the wide range of forsterite content (Fo = 83 – 90) observed in the dunite xenoliths suggests protracted fractional crystallization of mainly olivine over a wide temperature range. This is consistent with fractionation of tholeiitic magmas at relatively low pressure as suggested by MELTS thermodynamic models (Ghioro and Sack, 1995). In order to constrain the origin of dunite xenoliths, we modeled fractional crystallization of Hualalai tholeiitic and alkali magmas using MELTS. Hualalai tholeiite KK-14-5 and average 1800 alkalic basalt are used as start melts (Bohrson and Clague, 1988). Water content was

initiated at 0.4 wt.%. Oxygen buffer was initiated at NNO and allowed to proceed unbuffered. Isobaric fractional crystallization of the primitive melts was modeled over a pressure range of 1-8 kbar. MELTS modeling results suggest fractional crystallization of primary olivine over an extended range of temperature only occurs for tholeiite at relatively low pressures (<2 kabr; Fig. 2.4). Moreover, Hualalai dunites are more likely formed during shield-stage based on the field observation that some dunites are cut orthopyroxenite veins (personal conversation with Clague). Such crosscutting relationship indicates that formation of these dunites preceded the formation of the orthopyroxenite veins, which most likely derived from shield-stage tholeiitic magmas. Therefore, dunites are also likely formed during shield stage.

Combined together, these approaches provide constraints on the origins (parental magmas and formation depths) of Hualalai cumulate xenoliths. One-pyroxene gabbros most likely derive from fractional crystallization of post-shield-stage magmas at LOC depths (e.g., Gao et al., 2016a). Dunites, 2-pyroxene gabbros and websterites are likely cumulates crystallized from shiled-stage magmas at various depths, and therefore provide us a slice through the plumbing system during the shield stage. The following discussion is based on the xenolith classification described here.

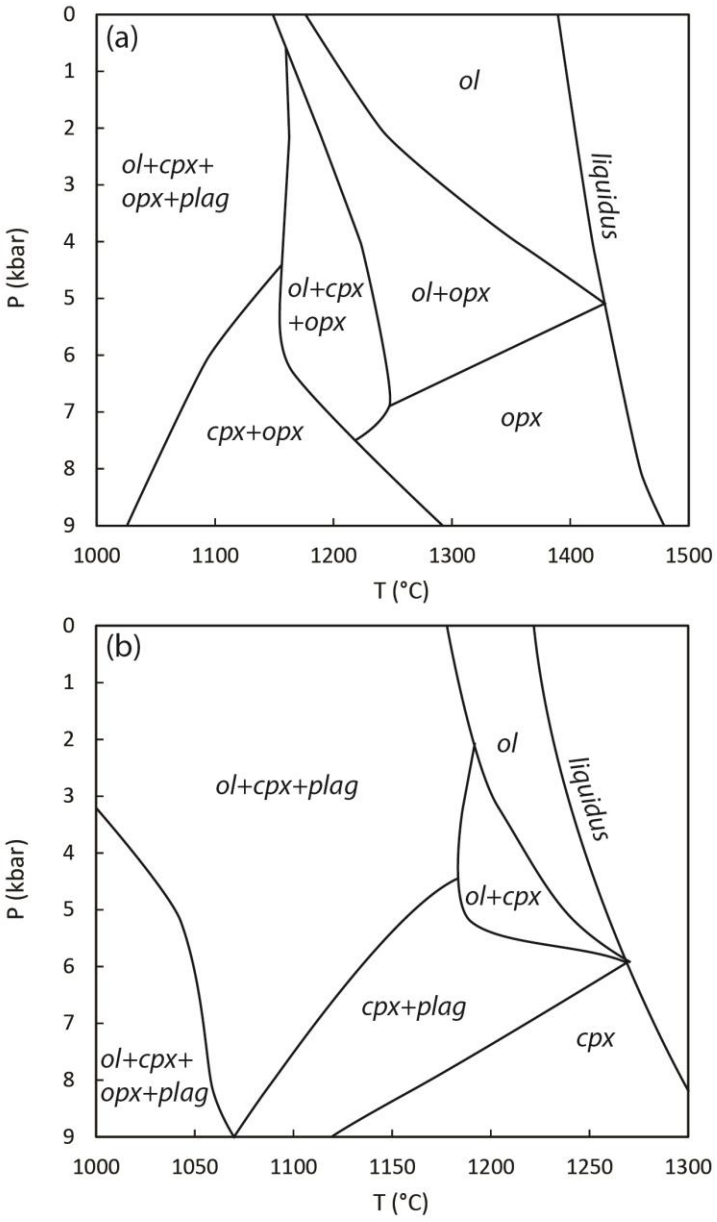

Figure 2.4: MELTS modeling results – phase diagrams.

2.4.1.2 Hualalai magma mixing and crustal contamination?

Hualalai cumulates show a range of isotope compositions that are similar but not identical to Hualalai lavas. Hualalai lavas show temporal variations of isotopic compositions. Shield-stage lavas are characterized by systematically more enriched Sr-Nd isotope compositions than post-shield-stage lavas (e.g., Yokose et al., 2005; Yamasaki et al., 2009). Post-shield stage cumulates (1-pyroxene gabbros) have Sr-Nd isotope compositions within the range of post-shield-stage lavas (Gao et al., 2016a). In contrast, shield-stage cumulates span a wider range of Sr-Nd isotope compositions compared to shield-stage lavas. For example, webseterites have $^{87}Sr/^{86}Sr$ extending to as low as 0.70331, whereas Hualalai shield-stage lavas have $^{87}Sr/^{86}Sr$ ranging between 0.70366 and 0.70380.

The greater isotopic variability in cumulates may reflect either better preservation of primitive, small-scale heterogeneities of Hawaiian plume-derived melts, or higher degree of crustal contamination recorded. In the first case, because magma mixing and homogenization usually couple with protracted fractional crystallization within magma reservoirs, more evolved lavas/cumulates (lower Mg#) are expected to display less isotopic variations (e.g., Rubin et al., 2010). In contrast, in the second case, higher degree of crustal contamination is expected to be observed in more evolved lavas and cumulates. Therefore, examining the correlations between the index of fractionation and isotopic compositions in lavas and cumulates can help constrain the significance of magma mixing and crustal contamination. Neither shield-stage nor post-shield-stage Hualalai lavas show any systematic variations in Sr-Nd isotope compositions correlated with whole rock Mg#. Therefore, in the discussion below, we will focus on examining the compositional variations in cumulate xenoliths, which provides snapshot of Hualalai

magma compositions at different stages and depths, to place constraints on the evolution of Hualalai magmas.

Different types of Hualalai cumulate xenoliths have different characteristics of isotopic compositions. As mentioned above, 1-pyroxene gabbros have relatively uniform isotope compositions: $^{87}Sr/^{86}Sr_{cpx}$ = 0.70357 – 0.70364, $^{143}Nd/^{144}Nd_{cpx}$ = 0.51290 – 0.51294 and $\delta^{18}O_{plag}$ = +6.1 to +6.2‰ (Gao et al., 2016a). Their compositions are consistent with post-shield stage lavas ($^{87}Sr/^{86}Sr$ = 0.70351 – 0.70366, $^{143}Nd/^{144}Nd$ = 0.51290 – 0.51296; $\delta^{18}O_{ol}$ = +5.3 to +5.4‰; e.g., Hanano et al., 2010; Eiler et al., 1996). Dunites also have similar uniform isotope compositions ($^{87}Sr/^{86}Sr_{cpx}$ = 0.70348 – 0.70361, $^{87}Sr/^{86}Sr_{wr}$ = 0.70355 - 0.70361, $^{143}Nd/^{144}Nd_{cpx}$ = 0.51293 – 0.51298, and $\delta^{18}O_{ol}$ = +5.2 to +5.4‰; Chen et al., 1992 and this study). In contrast, websterites are characterized by heterogeneous Sr isotope compositions extending to lower $^{87}Sr/^{86}Sr$ than any Hualalai lavas, but relatively uniform Nd and O isotope compositions ($^{87}Sr/^{86}Sr_{cpx}$ = 0.70331 – 0.70358, $^{143}Nd/^{144}Nd_{cpx}$ = 0.51289 – 0.51296, and $\delta^{18}O_{ol}$ = +5.3 to +5.6‰). Finally, 2-pyroxene gabbros extend to higher $^{87}Sr/^{86}Sr_{cpx}$ (0.70359 – 0.70376; Gao et al., 2016a) than websterites and dunite, and have heterogeneous Nd isotope compositions ($^{143}Nd/^{144}Nd_{cpx}$ = 0.51285 – 0.51306; Fig. 2.5). Both the Sr and Nd isotope compositions of 2-pyroxene gabbros are more heterogeneous than Hualalai shield-stage lavas. Given Hualalai volcano is a "Loa-trend" volcano, the most striking feature of 2-pyroxene gabbros is that they possess low $\delta^{18}O$ values ($\delta^{18}O_{cpx}$ = +4.9 to +5.4‰, $\delta^{18}O_{plag}$ = +5.2 to +6.3‰) that are a characteristic of Hawaiian "Kea-trend" lavas (Fig. 2.6). The Os isotope compositions of 2-pyroxene ($^{187}Os/^{188}Os$ = 0.132 – 0.136) and websterites ($^{187}Os/^{188}Os$ = 0.134 – 0.139) are also more heterogeneous than dunites ($^{187}Os/^{188}Os$ = 0.133 – 0.135; Fig. 2.7).

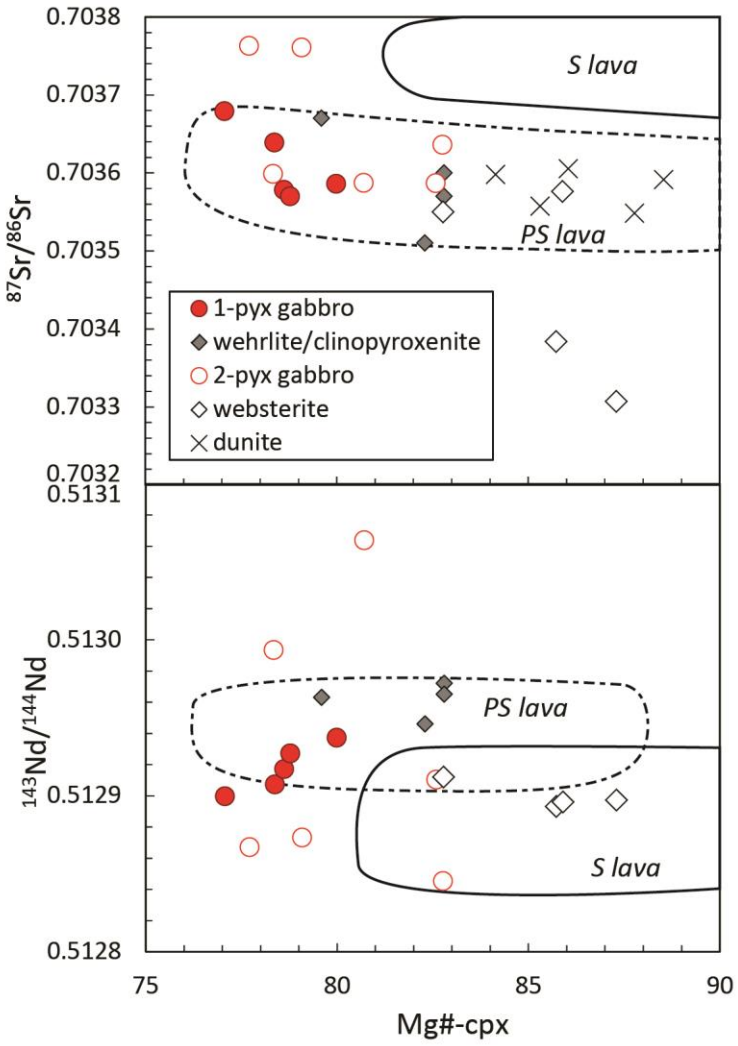

Figure 2.5: Sr-Nd isotope compositions versus Mg#.

Gabbro data is from Gao et al. (2016a), wehrlite and clinopyroxenite data is from Chen et al. (1992). The compositional ranges of Hualalai shield- and post-shield-stage lavas are also plotted for comparison (data compiled from GeoRoc database).

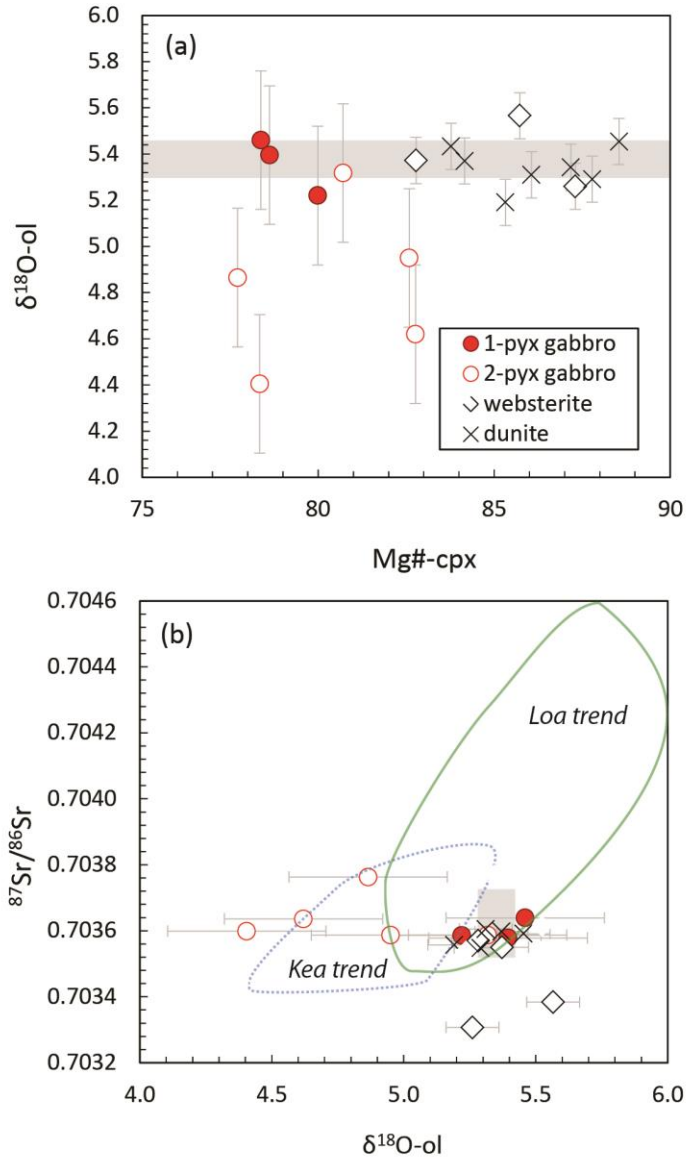

Figure 2.6: Oxygen isotope systematics of Hualalai xenoliths.

The compositional range of Loa-trend lavas, Kea-trend lavas and Hualalai shield stage lavas (grey field) are also shown for comparison (data compiled from GeoRoc database).

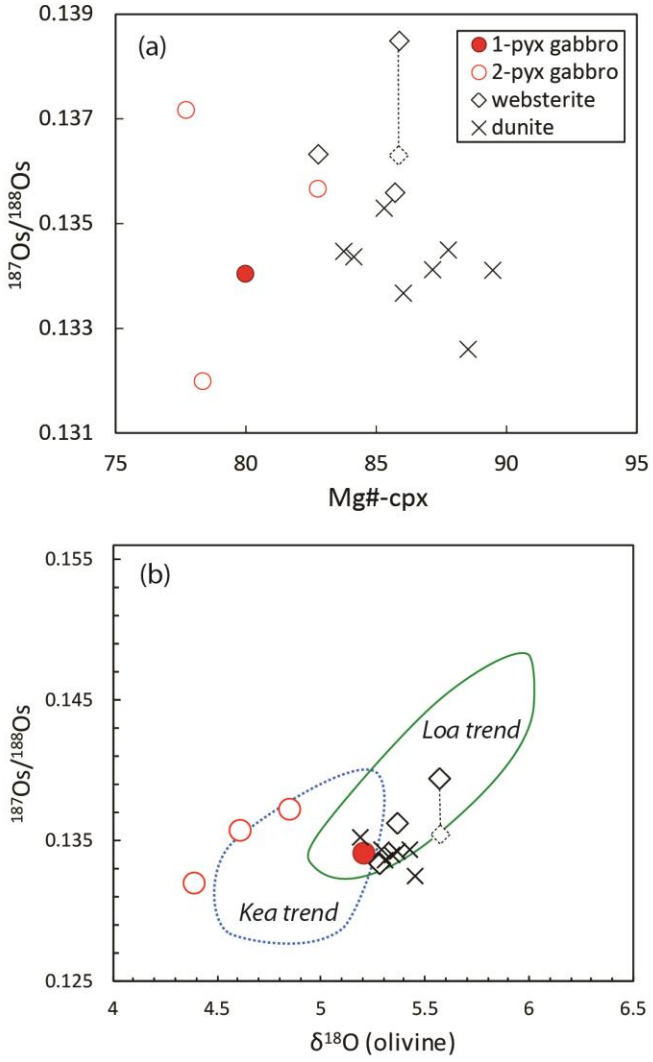

Figure 2.7: Osmium isotope systematics of Hualalai xenoliths.

Dashed diamond shows that age corrected Os isotope composition (assuming an age of ~500 kyr for shield-stage xenolith fractionation). Age correction has minor effect on most samples except on websterites with high Re/Os ratio. The compositional range of Loa-trend and Kea-trend lavas are also shown for comparison (data compiled from GeoRoc database).

Post-shield-stage xenoliths show evidence of AFC processes. We compiled literature data of post-shield-stage gabbro, wehrlite and clinopyroxenite xenoliths, which are mostly likely post-shield-stage xenoliths because of lacking orthopyroxene (Chen et al., 1992; Gao et al., 2016a). These xenoliths show negative correlation between clinopyroxene $^{87}Sr/^{86}Sr$ and Mg#, and positive correlation between $^{144}Nd/^{143}Nd$ and Mg# (Fig. 2.5). These correlations suggest that post-shield stage magmas fractionated while assimilating materials with higher $^{87}Sr/^{86}Sr$ and lower $^{144}Nd/^{143}Nd$. This is consistent with assimilating earlier Hualalai shield-stage produces that have more enriched Sr-Nd isotope compositions than post-shield-stage magmas (e.g., Yamasaki et al., 2009).

The relatively homogeneous isotope compositions of dunite xenoliths may be the result of magma mixing. As discussed in previous section, Hualalai shield-stage cumulates may be formed at a range of different depths. Dunites are most likely formed at shallow depths (<2 kbar), whereas 2-pyroxene gabbros appear to have crystallized within oceanic crust (~2.5 – 5 kbar; Gao et al., 2016a), and webseterites likely derived from the greatest depths (~4.5 – 9 kbar; Bohrson and Clauge, 1988). Therefore, it is reasonable to postulate that dunites are cumulates formed in a shallow reservoir within volcano edifice, whereas 2-pyroxene gabbros and websterites are cumulates formed with a deep reservoir within oceanic crust. If magmas ponded in the shallow reservoir were fed from the deep reservoir, longer history of mixing and homogenization of discrete magma batches would result in more homogenized magma compositions in the shallower reservoir. Then the more homogeneous compositions of dunite xenoliths compared 2-pyroxene gabbros and websterites are consistent with this scenario.

The more heterogeneous isotope compositions of 2-pyroxene gabbros and websterites compared to shield-stage lavas may be due to greater degrees of crustal contamination recorded in the cumulates. Websterites have systematically higher Mg#,

and lower $^{87}Sr/^{86}Sr$ than 2-pyroxene gabbros. Therefore, overall there appear to be a negative correlation between the Mg# and Sr isotope compositions of these cumulates (n = 10, r = 0.83; Fig. 2.5a). This is consistent with fractional crystallization while assimilating materials with higher $^{87}Sr/^{86}Sr$ than shield-stage magmas.

In addition, 2-pyroxene gabbros have lower $\delta^{18}O$ values than websterites. Gao et al. (2016a) reported $\delta^{18}O$ values of clinopyroxene and plagioclase from the shield-stage gabbros ($\delta^{18}O_{plag}$ = +5.2 to +6.3‰, $\delta^{18}O_{cpx}$ = +4.9 to +5.4‰). In this study, the oxygen isotope compositions of websterites are measured on olivine separates ($\delta^{18}O_{ol}$ = +5.3 to +5.6‰). In order to compare the oxygen isotope compositions of the gabbros and websterites, we assume $\Delta_{cpx\text{-}ol}$ = +0.3‰ and $\Delta_{plag\text{-}ol}$ = +0.8‰ (Mattey et al., 1994; Eiler et al., 2001). When only clinopyroxene or plagioclase $\delta^{18}O$ values are available, the equilibrium olivine $\delta^{18}O$ values are calculated using the assumed $\Delta_{cpx\text{-}ol}$ and $\Delta_{plag\text{-}ol}$. When both clinopyroxene and plagioclase $\delta^{18}O$ values are available are available, the average of calculated olivine $\delta^{18}O$ values using $\Delta_{cpx\text{-}ol}$ and $\Delta_{plag\text{-}ol}$ is used for comparison. Under this assumption, the shield-stage gabbros have equilibrium olivine $\delta^{18}O$ values ranging from +4.4 to +5.3‰. Then the oxygen isotope compositions of 2-pyroxene gabbros and websterites show broad positive correlation with clinopyroxene Mg# (n = 8, r = 0.61; Fig. 2.6a), and negative correlation with clinopyroxene $^{87}Sr/^{86}Sr$ (n = 7, r = 0.57; Fig. 2.6b).

Combined together, these correlations appear to be consistent with an AFC process where the contaminant is characterized by lower $\delta^{18}O$ values and higher $^{87}Sr/^{86}Sr$ than Hualalai shield-stage magmas. These features would be consistent with hydrothermally altered lower oceanic crust. However, all LOC xenoliths discovered at the Hualalai volcano have fresh MORB-like Sr and O isotope compositions, which indicate minimal hydrothermal alteration. Therefore, it is difficult to explain the

compositional variations in the 2-pyroxene gabbros and websterites as the result of assimilating *in situ* Pacific LOC.

Alternatively, the different isotope compositions of different xenolith types may be primitive, and reflect evolution of primary Hualalai magma compositions at different times and/or conditions. During the evolution of Hualalai volcanism, magma supply rates and degrees of partial melting of the Hawaiian plume source vary over time (e.g., Clague, 1987). It is widely accepted that the Hawaiian plume is highly heterogeneous in turns of both isotopic compositions and lithologies (e.g., Lassiter and Hauri, 1998; Huang et al., 2013; Hoffman et al., 2013). Varied degrees of partial melting can result in changing melt compositions. Meanwhile, coupled variations in magma supply rates can lead to structural transform of magma plumbing system and fractional crystallization of different type of cumulates at different P/T conditions. In this case, the various isotope compositions and degrees of fractionation observed in different xenolith types is just the coincidental result of such processes. This is highly possible because correlations between Mg# and isotope ratios are not observed in any of the individual xenolith types. If this is true, the wide range of isotopic compositions observed in 2-pyroxene gabbros and websterites indicates that the heterogeneities of Hualalai magma compositions have been damped out in erupted lavas, but preserved in cumulate xenoliths.

2.4.3 Effects of crustal storage and melt-crust interaction on Pacific lithosphere: Implications for the origin of Hawaiian rejuvenated-stage lavas

Small volumes of rejuvenated-stage lavas erupted semi-synchronously (within the last 1 Myr) at six older Hawaiian volcanoes and the North Arch volcanic field (Kaula, Niihau, Kauai, Oahu, east Molokai and west Maui; e.g., Ozawa et al., 2005). The high MgO contents of these lavas (>10%; Clague & Frey, 1982) and the high forsterite contents of their olivines (86-89) indicate that rejuvenated-stage magmas are relatively

primitive (Maaløe et al., 1992). Rejuvenated-stage lavas span a relatively restricted range of Sr-Nd-Hf isotope compositions that are more depleted compared to the underlying shield and post-shield lavas (e.g., Lassiter et al., 2000; Frey et al., 2005; Fekiacova et al., 2007). In contrast, they are more enriched in incompatible trace elements than shield and post-shield lavas (e.g., Clague & Dalrymple, 1988; Garcia et al., 2010). Rejuvenated-stage lavas are also characterized by radiogenic Os isotope compositions (e.g., Lassiter et al., 2000).

The origin of Hawaiian rejuvenated volcanism has long been debated. Many early studies related the depleted Sr-Nd-Hf isotope compositions of rejuvenated-stage lavas to reflect partial melting of oceanic lithosphere that has been heated from below by the Hawaiian plume (e.g., Chen & Frey, 1985; Lassiter et al., 2000; Yang et al., 2003). For example, Lassiter et al. (2000) suggested that rejuvenated-stage lavas derive from melting of petrologically heterogeneous Pacific lithospheric mantle that contains high-$^{187}Os/^{188}Os$ pyroxenite veins. Alternatively, Yang et al. (2003) proposed that the enriched trace element and depleted Sr-Nd isotope compositions of rejuvenated-stage lavas are best explained by derivation from depleted lithosphere that has been recently metasomatized by incipient low-degree melt from the Hawaiian plume.

In contrast, many recent studies argue that there are systematic differences between the isotopic compositions of Hawaiian rejuvenated-stage magmas and Pacific lithosphere, based on the isotopic compositions of basalts from EPR and ODP Site 843 (e.g., Fekiacova et al., 2007; Bizimis et al., 2013). Overall, at a given $^{206}Pb/^{204}Pb$, rejuvenated-stage lavas have higher $^{87}Sr/^{86}Sr$ and $^{208}Pb/^{204}Pb$ but lower $^{143}Nd/^{144}Nd$ and $^{207}Pb/^{204}Pb$ than both EPR MORBs and ODP 843 basalts (e.g., Fekiacova et al., 2007; Garcia et al., 2010). In addition, the $^{206}Pb/^{204}Pb$-$^{207}Pb/^{204}Pb$ array defined by rejuvenated-stage lavas does not intersect with the field of ODP 843 (e.g., Fekiacova et al., 2007).

Therefore, it was argued that Pacific lithosphere could be neither the source nor one endmember component of Hawaiian rejuvenated-stage lavas, and that the depleted source of rejuvenated-stage lavas is intrinsic to the Hawaiian plume (e.g., Frey et al., 2005; Garcia et al., 2010; Bizimis et al., 2013). Here we examine the Sr-Nd-Hf-Pb-Os isotope compositions of *in situ* LOC gabbros to compare the compositions of the *in situ* Pacific lithosphere to Hawaiian rejuvenated-stage lavas.

Clinopyroxenes in some LOC gabbros have higher $^{87}Sr/^{86}Sr$ than co-existing plagioclase ($\Delta^{87}Sr/^{86}Sr_{cpx\text{-}plag}$ up to 0.0008; Gao et al., 2016a). One LOC gabbro even has clinopyroxene Sr-Nd isotope compositions ($^{87}Sr/^{86}Sr_{cpx}$ = 0.7036, $^{143}Nd/^{144}Nd_{cpx}$ = 0.5130) similar to the most enriched rejuvenated-stage lavas (Fig. 2.1). Previous study interpreted the Sr isotope disequilibrium between clinopyroxene and plagioclase in LOC gabbros as results of interaction with Hawaiian plume magmas (Gao et al., 2016a). A simple binary mixing model suggested the range of Sr-Nd isotope compositions observed in Hualalai LOC gabbros may be accounted for by mixing with up to ~10% Hualalai melts (Gao et al., 2016a). Therefore, the compositions of *in situ* Pacific lithospheric LOC may have been modified by Hawaiian shield- and post-shield-stage melts percolating through the Pacific lithosphere.

As to LOC, this process has significant affected the Sr-Nd isotope compositions of clinopyroxene, but has minor effect on the Sr isotope composition of plagioclase. This is because plagioclase has high Sr concentrations, and therefore is more resistant to modification by melt-crust interaction. Depleted MORB mantle (DMM) on average has Sr concentration of 7.66 ppm and Nd concentration of 0.58 ppm (Walkman & Hart, 2005). These concentrations are similar to the Sr and Nd concentrations in clinopyroxenes from LOC gabbros. Therefore, similar to the clinopyroxenes that have been modified by melt-crust interaction, melt-metasomatized lithospheric mantle beneath

the Hawaiian Islands may also have Sr-Nd isotope compositions similar to rejuvenated-stage lavas.

One of the main pieces of evidence against derivation of Hawaiian rejuvenated volcanism from Pacific lithosphere is the Pb isotope systematics of basalts from EPR and ODP Site 843 (e.g., Fekiacova et al., 2007; Garcia et al., 2010; Bizimis et al., 2013). For example, ODP 843 basalts have more radiogenic Pb isotope compositions than Hawaiian rejuvenated-stage lavas (e.g., King et al., 1999; Fekiacova et al., 2007; Fig. 2.2). In addition, rejuvenated-stage lavas have higher $^{208}Pb/^{204}Pb$ and lower $^{207}Pb/^{204}Pb$ at a given $^{206}Pb/^{204}Pb$ than EPR and ODP 843 basalts (e.g., Fekiacova et al., 2007; Garcia et al., 2010; Fig. 2.2). However, plagioclases from *in situ* LOC gabbros have systematically less radiogenic Pb isotope compositions than ODP 843 basalts. Moreover, compared to EPR MORBs and ODP 843 basalts, many Hualalai LOC gabbros have higher $^{208}Pb/^{204}Pb$ and lower $^{207}Pb/^{204}Pb$ at a given $^{206}Pb/^{204}Pb$, which is consistent with Hawaiian Rejuvenated lavas (Fig. 2.2).

The Pb isotope compositions of Hualalai LOC gabbros may also reflect melt-crust interaction between the local oceanic crust and Hualalai magmas. These LOC gabbros have plagioclase Pb isotope compositions intermediate between EPR MORBs and Hualalai lavas. High precision (double spike) plagioclase Δ8/4 of these gabbros positively correlate with clinopyroxene $^{87}Sr/^{86}Sr$ and La/Sm ratios (Δ8/4 measures deviation from the Northern Hemisphere Reference Line; Hart, 1984) (Fig. 2.8). Hawaiian lavas have higher Δ8/4, $^{87}Sr/^{86}Sr$, and La/Sm than EPR MORBs. Therefore, the positive correlations between plagioclase Δ8/4 and clinopyroxene $^{87}Sr/^{86}Sr$ and La/Sm likely reflect interaction with Hawaiian melts. Pacific lithospheric mantle beneath the Hawaiian Islands may have similar Pb isotope compositions as these LOC gabbros, as the result of metasomatism by Hawaiian plume-derived melts (e.g., Yang et al., 2003).

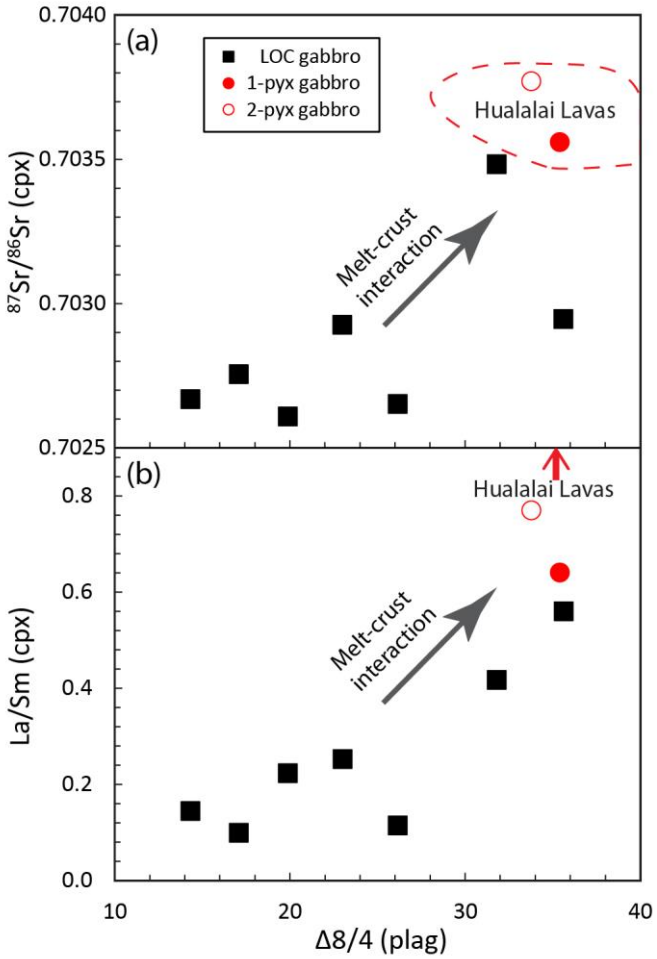

Figure 2.8: Plagioclase Δ8/4 of LOC gabbros reflects melt-crust interaction.

Gao et al. (2016a) suggested that the positive correlation between clinopyroxene $^{87}Sr/^{86}Sr$ and La/Sm are results of melt-crust interaction between Hawaiian lavas and Pacific crust. Plagioclase Δ8/4 values of LOC gabbros show correlation with these indicators of melt-crust interaction. Only double spike Pb data are included in this plot. (a) Plagioclase Δ8/4 versus clinopyroxene $^{87}Sr/^{86}Sr$. (b) Plagioclase Δ8/4 versus clinopyroxene La/Sm.

The radiogenic Hf isotope compositions of Hualalai LOC gabbros are also similar to Hawaiian rejuvenated-stage lavas. In the Nd-Hf isotope space, Hawaiian rejuvenated-stage lavas have high $^{176}Hf/^{177}Hf$, and plot above the array defined by Hawaiian shield and post-shield lavas, and EPR MORBs (Fig. 2.9). The radiogenic Hf isotope compositions of rejuvenated-stage lavas are also evident in $^{176}Hf/^{177}Hf$ versus $^{206}Pb/^{204}Pb$ plot, where they extend to highly radiogenic $^{176}Hf/^{177}Hf$ values at relatively constant $^{206}Pb/^{204}Pb$ (Fig. 2.10). Although Hualalai LOC gabbros show significant scatter in the Hf-Nd and Hf-Pb isotope plots, they again largely overlap with the range of Hawaiian rejuvenated-stage lavas.

Overall, Hualalai LOC xenoliths have Pb-Hf isotope compositions, and clinopyroxene Sr-Nd isotope compositions overlapping the range of compositions of Hawaiian rejuvenated stage lavas. The compositions of these LOC gabbros appear to have been modified by interaction with Hawaiian magmas. The *in situ* Pacific lithospheric mantle may also have been overprinted by Hawaiian shield- and post-shield-stage melts percolating through the Pacific lithosphere, and therefore has isotope compositions similar to the LOC. If this were the case, partial melting of this metasomatised lithospheric mantle would be able to produce Hawaiian rejuvenated-stage lavas.

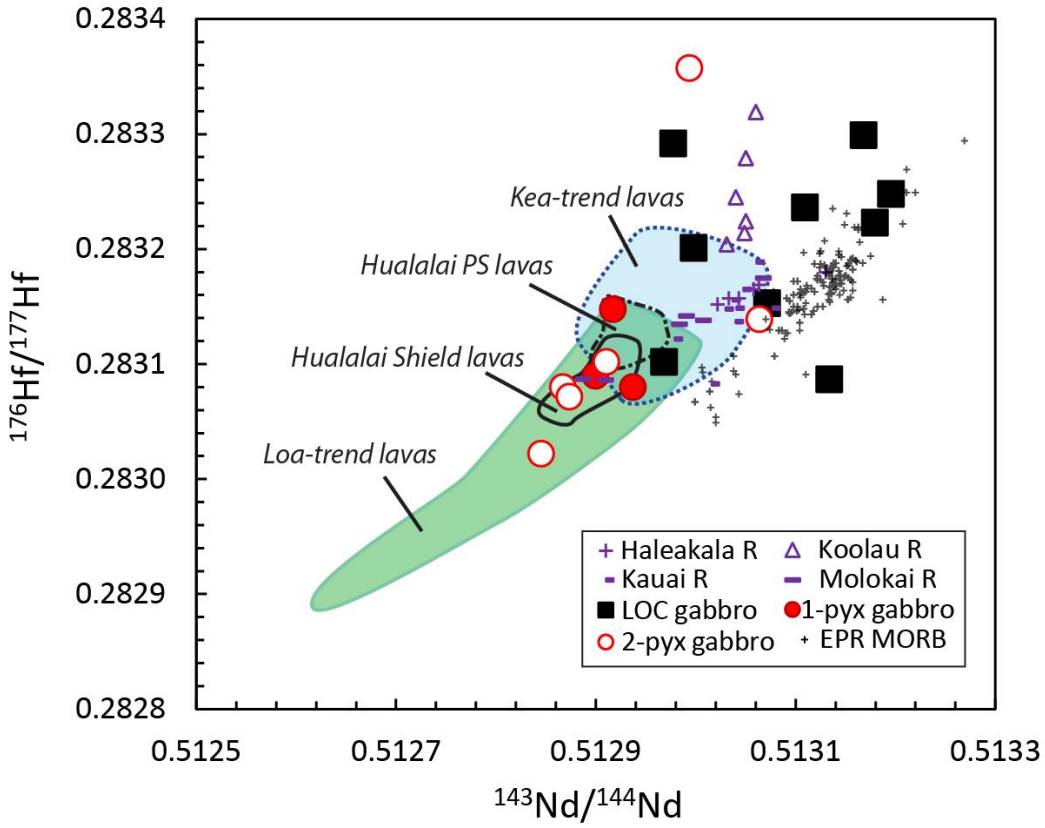

Figure 2.8: Nd-Hf isotope plot.

The clinopyroxene Nd-Hf isotope compositions of Hualalai gabbroic xenoliths are plotted in comparison with Hawaiian lavas and EPR MORBs (data compiled from GeoRoc and PetDB). Hawaiian shield and post-shield stage lavas are shown as Kea-trend and Loa-trend fields. The fields of Hualalai shield and post-shield stage lavas are also drawn for comparison. Available literature Nd-Hf isotope data from rejuvenated volcano Haleakala, Kauai, Molokai, and Koolau are shown with purple symbols.

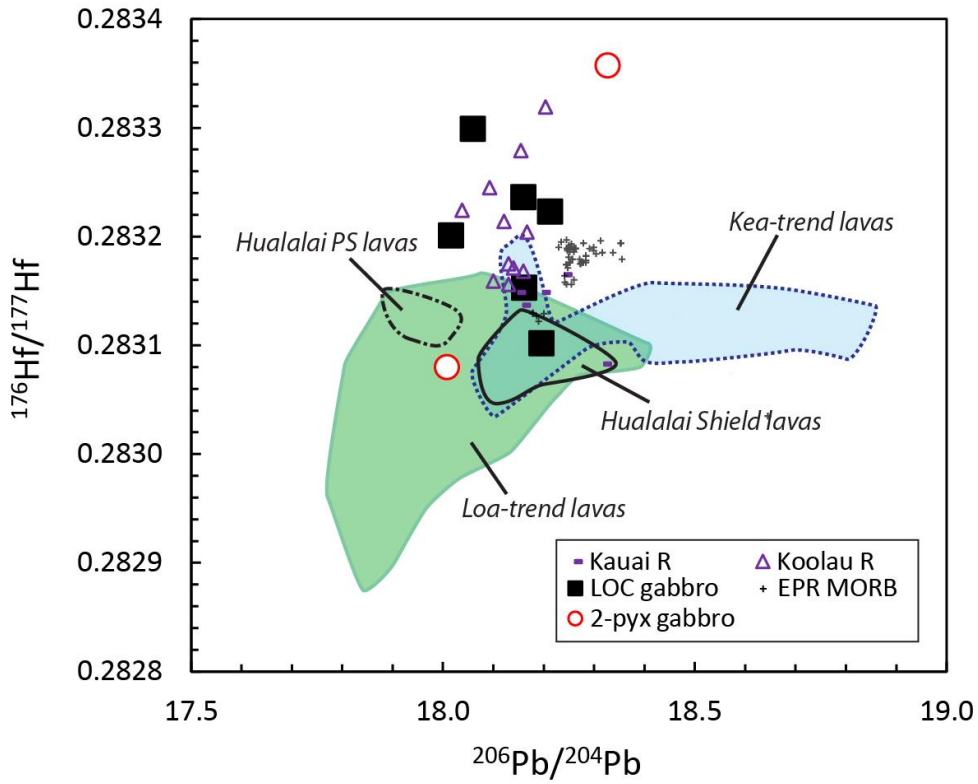

Figure 2.9: Pb-Hf isotope plot.

Plagioclase $^{206}Pb/^{204}Pb$ of Hualalai gabbroic xenoliths are plotted versus clinopyroxene $^{176}Hf/^{177}Hf$. The Pb-Hf isotope compositions of Hawaiian lavas and EPR MORBs are also plotted for comparison (data compiled from GeoRoc and PetDB). Hawaiian shield and post-shield stage lavas are shown as Kea-trend and Loa-trend fields. The fields of Hualalai shield and post-shield stage lavas are also drawn for comparison. Available literature Pb-Hf isotope data from rejuvenated volcano Kauai and Koolau are shown with purple symbols.

Another important feature of Hawaiian rejuvenated lavas is their radiogenic Os isotope compositions ($^{187}Os/^{188}Os$ = 0.138-0.160). Lassiter et al. (2000) showed that the Os isotope compositions of rejuvenated lavas display no correlation with Sr, Nd or Pb isotopes, but positively correlate with major and trace elements (e.g., Al_2O_3, SiO_2, Sr). These features were interpreted as reflecting melting and mixing of low-$^{187}Os/^{188}Os$ peridotite and high-$^{187}Os/^{188}Os$ pyroxenite veins within lithospheric mantle (Lassiter et al., 2000). Alternatively, the radiogenic Os isotope compositions of Hawaiian rejuvenated-stage lavas may be generated by assimilating or partial melting of the *in situ* LOC gabbros that have highly radiogenic $^{187}Os/^{188}Os$ (0.212-0.634). Because plagioclase in gabbros have high Al_2O_3 content, assimilation of gabbros then is consistent with the observed positive correlation between $^{187}Os/^{188}Os$ and Al_2O_3. Although Hawaiian rejuvenated-stage lavas have high MgO content (>10 wt.%) and appear to be primitive, high-MgO lavas still may have incorporated an evolved and contaminated component (e.g., Gao et al., 2016b). This is because erupted lavas usually represent a mixture of different magma batches, where one magma batch may be primitive with high MgO content, but mixed with magmas batches that are evolved and crustally contaminated. This can be tested by examining phenocryst compositions within rejuvenated-stage lavas. If rejuvenated-stage lavas are hybrid, their crystal phases are expected to be out of equilibrium with the host lavas (Gao et al., 2016b).

All together, Hualalai LOC gabbros provide additional constraints on the isotopic compositions of the *in situ* Pacific lithosphere beneath the Hawaiian Islands, other than previous constraints from EPR MORBs and ODP Site 843 basalts (e.g., Fekiacova et al., 2007). As the result of melt-crust interaction between Hawaiian melt and the *in situ* Pacific crust, the Pb-Hf isotope compositions of LOC gabbros (in particular Pb) are consistent with the isotopic characteristics of Hawaiian rejuvenated-stage lavas.

Therefore, the Pacific lithosphere beneath the Hawaiian Islands, which has seen a large amount of Hawaiian-plume-derived melts, possibly has been metasomatised and thus has isotopic compositions similar to Hualalai LOC gabbros. If this is the case, partial melting of metasomatised Pacific lithosphere is capable of generating the range of isotopic compositions observed in Hawaiian rejuvenated-stage lavas. The role of Pacific lithosphere in generating Hawaiian rejuvenated-stage lavas needs to be re-evaluated.

2.5 CONCLUSION

Hualalai magma-derived cumulates (gabbros, websterites and dunites) display variations in Sr, Nd, and Os isotope compositions that are correlated with clinopyroxene/olivine Mg#. These correlations are consistent with coupled fractional crystallization and assimilation of LOC or volcano edifice materials. These observations suggest that the compositions of Hawaiian melts may have been partially overprinted during magma storage, fractionation, and assimilation prior to eruption.

Lower oceanic crust (LOC) gabbroic xenoliths from Hualalai Volcano have Sr-Nd-Pb-Hf isotope compositions (in particular Pb) that are more similar to Hawaiian rejuvenated-stage lavas than EPR and ODP 843 basalts. The isotopic compositions of these LOC gabbros are likely the result of melt-crust interaction between Hualalai magmas and the *in situ* Pacific crust. Therefore, the Pacific lithosphere beneath the Hawaiian Islands, which has seen large amount of Hawaiian plume-derived melts, may have been metasomatised and have isotopic compositions similar to Hualalai LOC gabbros. If this is the case, a metasomatised Pacific lithosphere is a likely source for Hawaiian rejuvenated-stage volcanism.

A few LOC gabbroic xenoliths contain plagioclase with high An and clinopyroxene with low incompatible trace element abundances and MREE/HREE ratios.

These gabbros are also characterized by high Re concentration, high $^{187}Re/^{188}Os$, and high $^{187}Os/^{188}Os$. The correlations between Os isotope ratios, clinopyroxene MREE/HREE ratios and plagioclase An contents indicate these features are primary and derive from processes occurred at mid-ocean ridges.

The Sr and O isotope compositions suggest the high-An plagioclase in these gabbros unlikely derive from hydrous melting or hydrothermal plagioclase replacement. Both melt-crust interaction and high Ca/Na parental melt composition may be the origin of high-An plagioclase at mid-ocean ridges. However, the strong positive correlation between whole rock Re concentration and plagioclase An content observed in Hualalai LOC gabbros is mysterious, and may place further constraints on the origin of high-An gabbros at mid-ocean ridges.

ACKNOWLEDGEMENTS

This work was supported in part by NSF grant EAR-1321937 and by the Jackson School of Geosciences, University of Texas at Austin. We thank J.D. Barnes, T.E. Larson, E.M. Marshall, A.M. Koleszar, S. Loewy, B.L. Byerly, and R. Chatterjee for laboratory assistance. Some of the xenoliths studied here were collected when DAC were employed by the U.S. Geological Survey, which supported his fieldwork. DAC is supported through a grant from the David and Lucile Packard Foundation to the Monterey Bay Aquarium Research Institute.

Chapter 3: Crustal or Mantle Origin of Temporal Compositional Trends in Monogenetic Vent Eruptions? Insights from the Crystal Cargo in the Papoose Canyon Sequence, Big Pine Volcanic Field, CA[2]

ABSTRACT

The Papoose Canyon (PC) monogenetic vent eruption sequence in the Big Pine Volcanic Field, California records systematic stratigraphic variations in whole rock chemical and Sr-Nd-Pb isotope compositions (e.g., trace element concentrations decreased by up to a factor of 2 during the course of the eruption). Correlations between trace element concentrations and isotopic ratios indicate these temporal variations reflect binary mixing of two distinct melts, one of which is chemically and isotopically more enriched than the other. This mixing process may reflect crustal assimilation, or melting and mixing of heterogeneous mantle source(s). We examine major and trace element and Sr-Nd-Pb-O isotopic variations in the crystal cargo (phenocrysts and xenoliths) in PC lavas to constrain the history of pre-eruption magma storage and the nature of the two mixing endmembers.

PC olivine and clinopyroxene phenocrysts span a wide range of Mg# (olivine Fo = 77-89, cpx Mg# = 81-89), and the majority of phenocrysts are more evolved than their host lavas (equilibrium Mg# ~85-89). In addition, olivine and clinopyroxene from ultramafic xenoliths within the early sequence have similar Mg# (73-87) to the phenocrysts, and lower than typical mantle peridotites. Sr-Nd-Pb isotope compositions of clinopyroxene from the xenoliths are similar to early PC lavas. Finally, many clinopyroxene phenocrysts and clinopyroxene in xenoliths have trace element abundances that indicate derivation from melts with higher trace element abundances

[2]The content of this chapter was submitted to *Earth and Planetary Science Letters*.

than the most enriched PC lavas. These features suggest that the phenocrysts and xenoliths derive from melt that is more fractionated and enriched than PC lavas.

Pressure constraints suggest PC phenocrysts and ultramafic xenoliths crystallized at ~5-7 kbar, corresponding to mid-crust depths. Correlations between HFSE depletion and Sr-Nd-Pb isotopic compositions, high $\delta^{18}O$ values in olivines, and radiogenic Os isotopic compositions in whole rocks also suggest PC lavas have incorporated a crustally contaminated component. In conjunction, we propose that PC phenocrysts and ultramafic xenoliths derive from early PC melts that ponded and fractionated and assimilated continental crust, possibly in mid-crustal sills. These melts were drained and mixed with more primitive melts as the eruption began, and the temporal-compositional trends therefore reflect gradual deflation and exhaustion of these sills as the eruption progressed. These results indicate that even "primitive" melts may contain a significant signature of crustal contamination.

3.1 INTRODUCTION

Geochemical variations in basalts from different regions and tectonic settings have provided invaluable insight into the composition and evolution of Earth's mantle (e.g., Hart, 1988; Sun & McDonough, 1989). However, basalts represent only indirect probes of mantle composition. Processes such as melt generation, migration, and melt-crust interaction all can affect the compositions of erupted lavas, making it difficult to discriminate mantle source signatures. For example, mantle signals can be overprinted and obscured by crustal contamination at continental settings (e.g., Glazner, 1991). Therefore, accurate inferences regarding mantle composition or melting processes using basalt probes require an understanding of melt generation and migration processes from source to surface.

Many ocean island volcanoes and continental monogenetic vents display significant chemical and isotopic variations during a single eruptive cycle, which can mimic compositional variations observed in entire volcanoes or regions over longer timescales (e.g., Garcia et al., 2000; Blondes et al., 2008; Erlund et al., 2010). Given the short timescales of single eruptive cycles, melt generation conditions and source characteristics are expected to be relatively invariant. The compositional variations observed in single eruption sequences therefore may provide valuable insight into the processes of magma generation and migration that are not possible from studies conducted over broader areas and larger timescales (e.g., Reiners, 2002). In some cases these short-term variations are proposed to reflect melt generation and extraction from heterogeneous mantle sources (e.g., Reiners et al., 2002; Blondes et al., 2008; Rasoazanamparany et al., 2015). In other cases, these temporal variations appear related to temporally varying degrees of crustal contamination (e.g., McBirney et al., 1987; Erlund et al., 2010; Needham et al., 2011). Distinguishing between these two mechanisms is particularly difficult for continental settings, because crustally contaminated melts may have qualitatively similar chemical and isotopic signatures as melts from metasomatized continental lithospheric mantle (e.g., Hildreth et al., 1991; Glazner, 1991).

Several recent studies indicate that erupted lavas are often hybrid mixtures of multiple discrete magma batches (e.g., Andrews et al., 2008; Moune et al., 2012). Temporal-compositional variations at monogenetic vents may reflect variable mixing of different magma batches. Understanding the history and location (crust vs. mantle) of magma storage and mixing can therefore help constrain the origins of the compositional variations in monogenetic vents. This history is often difficult to constrain from bulk lavas because of the mixing and homogenization processes described above. Instead,

crystal cargos (phenocrysts and xenoliths) often contain more information about the magma storage and mixing history than bulk lavas (e.g., Rankenburg et al., 2004; Andrews et al., 2008). In this study, we examine the crystal cargo of the Papoose Canyon (PC) monogenetic vent sequence in Big Pine Volcanic Field (BPVF), California, a well-documented monogenetic vent with clear temporal-compositional trends (Blondes et al., 2008). Major and trace element and isotope variations in olivine and clinopyroxene phenocrysts and ultramafic xenoliths provide new constraints on the pre-eruptive magma storage and mixing history at PC vent, and allow us to test crust versus mantle origins for the observed temporal-compositional trends.

3.2 BACKGROUND

The BPVF is a monogenetic volcano field situated in Owens Valley, California, bounded to the east and west by the Inyo-White Mountains and the Sierra Nevada. With the exception of one silicic vent, lavas erupted at the BPVF are primarily mafic in composition, ranging from basanites to alkalic and sub-alkalic basalts (Bierman et al., 1991). Most vents erupted between 0.1 and 0.8 Ma, with the oldest documented eruption at ~1.2 Ma (Gillespie, 1984; Bierman, 1991; Blondes et al., 2008). The origin of BPVF volcanism is commonly attributed to Basin-and-Range regional extension and associated lithosphere thinning and/or delamination (e.g., Beard & Glazner, 1995; Lee et al., 2001).

Basalts erupted at the BPVF span a range of major and trace element and isotope compositions. For example, whole rock SiO_2 abundances vary from 44.1 to 53.0 wt.%, olivine-fractionation-corrected Sr concentrations vary from ~900 to 2300 ppm and $^{87}Sr/^{86}Sr$ ranges from 0.70534 to 0.70648. (Ormerod et al., 1988 & 1991; Rogers et al., 1995; Beard & Glazner, 1995; Mordick & Glazner, 2006; Blondes et al., 2008). Ormerod et al. (1991) suggested that the variations in trace element abundances reflect different

degrees of partial melting of a relatively homogeneous mantle source. However, this cannot account for observed isotopic variations. Beard and Glazner (1995) proposed that the observed compositional variations reflect melt generation from heterogeneous metasomatized continental lithospheric mantle. More recently, Gazel et al. (2012) suggested that melt generation depths of BPVF lavas have shifted from asthenospheric mantle to the lithosphere-asthenosphere boundary over time, resulting in increased incorporation of lithospheric mantle components in younger BPVF lavas.

Several individual monogenetic vents in the BPVF display significant temporal compositional variations (Blondes et al., 2008). For example, trace element and isotope compositions of the PC sequence (760.8 ± 22.8 ka) span much of the range defined by the BPVF as a whole. Over the course of the PC eruption, the concentrations of highly incompatible trace elements decreased by up to a factor of ~2 (e.g., La concentrations decreased from 66 to 33 ppm). This decrease in trace element concentrations was accompanied by decreasing $^{87}Sr/^{86}Sr$ (0.7063 – 0.7055) and increasing ε_{Nd} (-3.5 – -1.1). SiO_2 (43.5 – 47.7 wt.%) and Al_2O_3 (15.6 – 16.5 wt.%) abundances and compatible element (e.g., Cr and Ni) concentrations increased slightly over time, whereas MgO (9.8 ± 0.3 wt.%) remained roughly constant (Blondes et al., 2008, Gazel et al., 2012).

3.3 SAMPLES AND METHODS

3.3.1 Field observations and samples

The Papoose Canyon valley cuts and exposes a stacked basaltic eruption sequence derived from a cinder cone at the easternmost part of the BPVF. The PC vent is in contact with dolomite country rock. The PC sequence contains both massive lava and vesicular scoria layers. Massive lavas appear mostly fresh, with scattered secondary zeolite/calcite minerals filling vesicles. Cinders and scorias are generally more altered and oxidized.

Overall, PC lavas have low phenocryst abundances, with phenocryst mineralogy dominated by olivine and clinopyroxene (cpx). Abundant pyroxene-rich ultramafic xenoliths (70-90 % modal cpx and 10-30 % modal olivine) and some carbonate crustal xenoliths are present in the early eruption sequence. Both ultramafic and carbonate xenoliths are sub-rounded to rounded. We collected stratigraphically-controlled samples from the massive flows during two field trips in 2012 and 2014. Pyroxene-rich ultramafic xenoliths and carbonate crustal xenoliths contained in the PC flows were also collected with host lavas when possible. Sample location and approximate stratigraphic position are reported in Appendix Table A1. Relative stratigraphic positions were calculated assuming an overall bedding dip similar to the angle of repose for most cinder cones (~30^{o}), consistent with measured bedding angles. See Appendix Fig. S3.1 for details.

3.3.2 Methods

3.3.2.1 Point counting

Olivine phenocryst abundance was determined by point counting of 6 stratigraphically controlled samples spanning the eruption sequence. Each sample was cut into flat slabs of ~5 × 8 cm and polished. Point counting was done under an optical microscope using a transparent 2 × 2 mm grid sheet overlay. More than 500 points were counted for each sample. Olivine phenocrysts are classified into 3 populations based on size: small phenocrysts (0.5-1 mm), large phenocrysts (1-3.5 mm) and megacrysts (> 3.5 mm).

3.3.2.2 Major element, trace element, and isotope composition

Whole rock major and trace elements were analyzed using standard XRF and LA-ICP-MS techniques at Washington State University. Olivine and cpx major element abundances were measured by EMPA at the University of Texas at Austin (UT Austin).

Clinopyroxene trace element compositions were measured by LA-ICP-MS (UT Austin). Strontium, Nd and Pb isotopes were measured by TIMS. Osmium isotopes were measured by N-TIMS, and Os concentrations were measured by isotope dilution. Oxygen isotope ratios were measured by laser fluorination. All isotopic analyses were performed at UT Austin. Further discussion of analytical methods is provided in the Appendix.

3.4 RESULTS

3.4.1 Point counting

Point counting results are presented in Appendix Table A2. PC lavas contain 2-7% olivine and < 0.5% cpx phenocrysts, as well as rare olivine and cpx megacrysts (<0.1%). The modal abundance of large olivine phenocrysts (1-3.5 mm) decreases gradually from 4.1% in the early-sequence sample to 0.6% in the late-sequence sample (Fig. 3.1). In contrast, the modal abundance of small olivine phenocrysts (0.5-1 mm, 0.7-3.9% modal abundance) does not change systematically over time. Megacryst abundances in most samples are too low to be determined by point counting in this study.

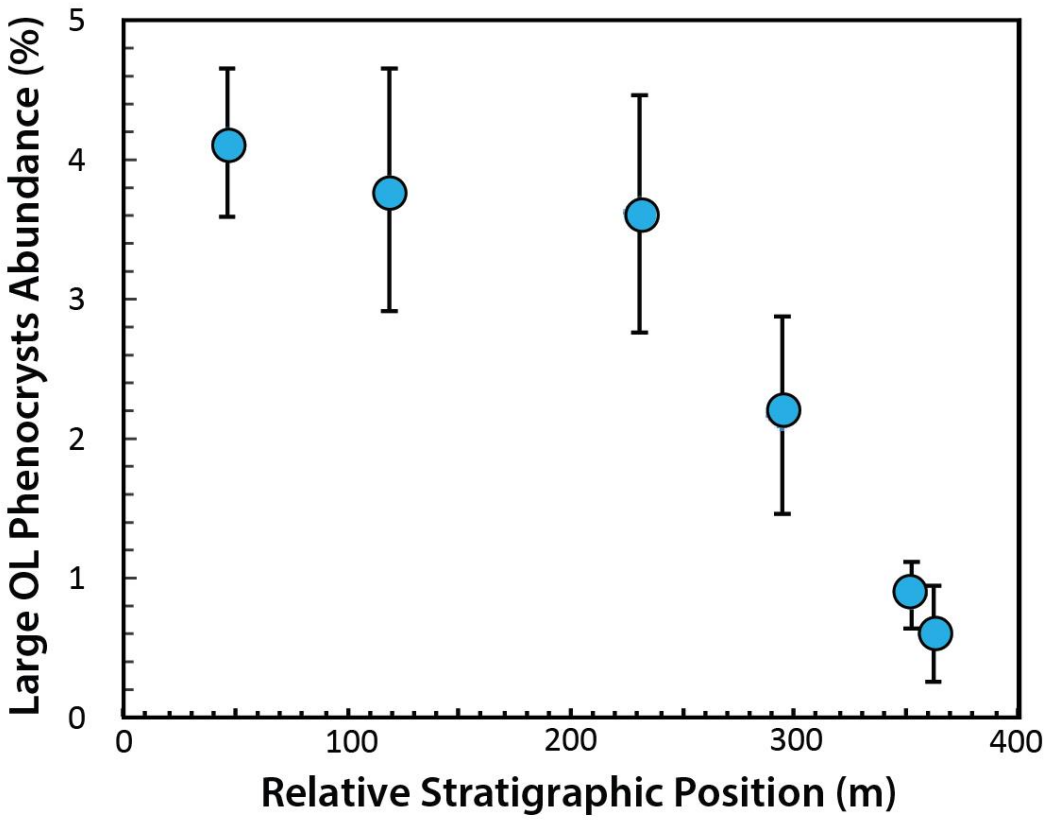

Figure 3.1 Modal abundance of large olivine phenocrysts.

The modal abundance of large olivine phenocryst (1-3.5 mm) in PC lavas decreases over the course of eruption.

3.4.2 Major and trace elements

3.4.2.1 Whole-rock major and trace elements

The major and trace element compositions of PC lavas are presented in Appendix Table A3. PC lavas have relatively high and uniform Mg# (69-70). SiO_2 (45.7-47.4 wt.%) and Al_2O_3 (15.8-16.3 wt.%) increase over the course of eruption, whereas CaO (10.2-9.6 wt.%), TiO_2 (2.1-1.9 wt.%), K_2O (2.0-1.4 wt.%) and P_2O_5 (1.1-0.7 wt.%) decrease. FeO_{total} (8.8-9.1 wt.%), Na_2O (3.6-3.9 wt.%), and MgO (9.3-9.8 wt.%) do not show systematic temporal trends. Our data are generally consistent with previous studies (Blondes et al., 2008; Gazel et al., 2012; Fig. S3.2).

PC lavas show Ti and HFSE depletions, slight positive Sr anomalies and no Eu anomalies. Incompatible trace element concentrations (e.g., Sr, Ba, and LREE) decrease significantly over the course of eruption. LREE and large ion lithosphere elements (LILE, e.g., Sr, Ba) show greater variation than high field strength elements (HFSE, e.g., Nb, Ta) and HREE, with the former varying by about a factor of 2 while the latter vary by ~20-30% (e.g., Fig. 3.2b). The concentrations of moderately incompatible trace elements (e.g., HREE) remain nearly constant, whereas those of compatible elements (Cr = 185-384 ppm; Ni = 151-226 ppm) increase over the course of eruption. The concentrations of highly incompatible trace elements show linear correlations with those of moderately incompatible trace elements (e.g., La vs. Sm; Fig. 3.3a).

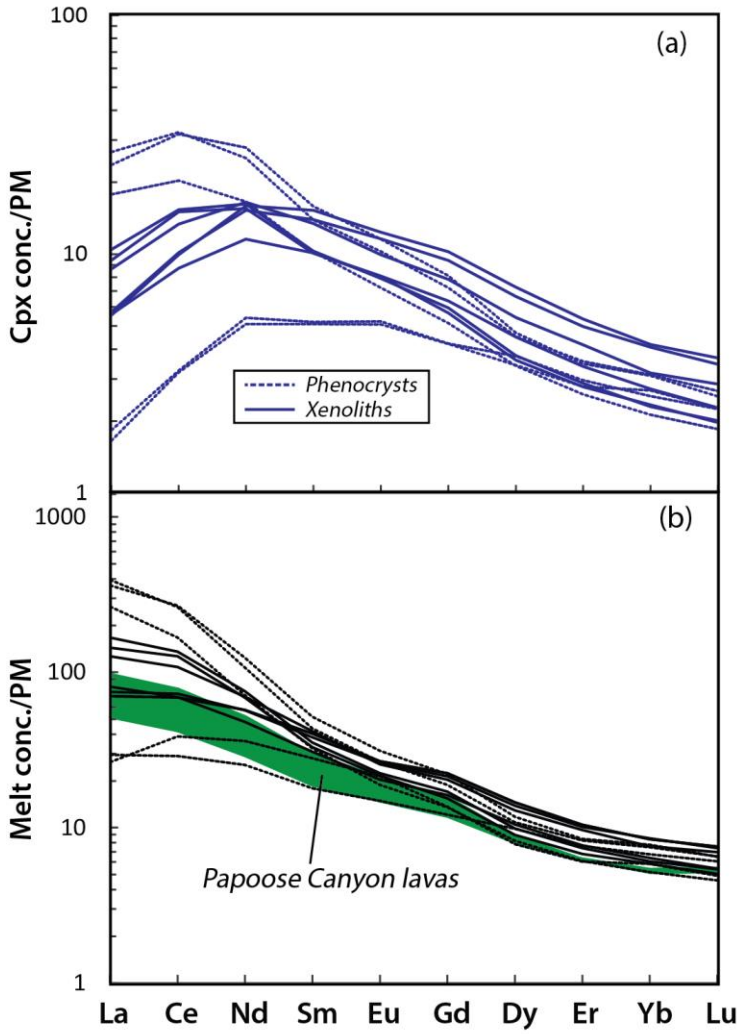

Figure 3.2 REE patterns of cpx and equilibrium melts.

(a) Measured clinopyroxene REE concentrations of PC phenocrysts and xenoliths (normalized to primitive mantle; McDonough and Sun, 1995). (b) Calculated melt REE concentrations in equilibrium with the clinopyroxene assuming no trapped melt in the xenoliths. See Appendix for more details about K_d value estimation. Green field shows the compositional variations of bulk PC lavas.

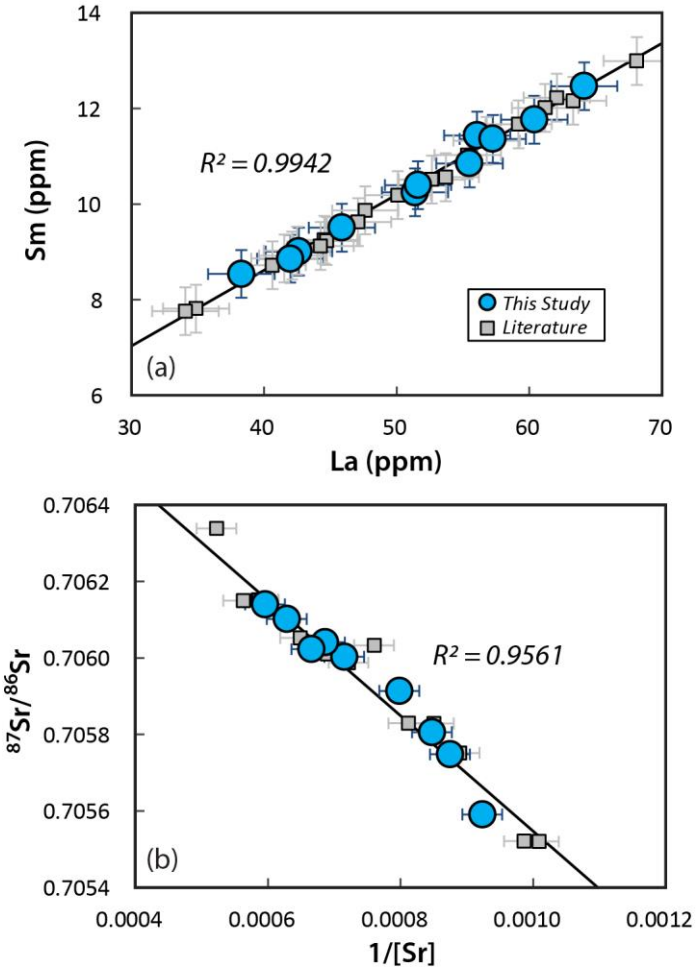

Figure 3.3 Geochemical trends suggestive of binary mixing.

Correlations between trace element concentrations and isotopic ratios of PC lavas suggest binary mixing of two distinct components. (a) La and Sm concentrations are linearly correlated, which cannot be explained by variations in the degree of partial melting because of differences in D_{La} and D_{Sm}. (b) $^{87}Sr/^{86}Sr$ is linearly correlated with the inverse of Sr concentration, which is consistent with binary mixing of two isotopically distinct components. Literature data from Blondes et al. (2008).

3.4.2.2 Mineral major and trace elements

Major element compositions of 215 olivine phenocryst grains from 8 samples spanning the entire stratigraphy are reported in Appendix Table A4. Olivine phenocrysts have Mg#s ranging from 77 to 89, with an average Mg# ≈ 84 (Fig. S3.3a). Several individual samples contain olivines spanning a wide range of composition, which is nearly as great as the range defined by PC olivine phenocrysts as a whole (Fig. 3.4a). 37 cpx phenocryst grains from 4 samples were also analyzed (Table A5). These cpx phenocrysts have Mg#s ranging from 81 to 87, with an average of 84 (Fig. S3.3a). Again, individual samples contain cpx spanning a range in composition (Fig. 3.4b).

Olivine and cpx from PC ultramafic xenoliths have major element compositions largely consistent with PC phenocrysts (Table A4 and A5). Olivines from PC ultramafic xenoliths have Mg#s ranging from 73-87, whereas cpx from these xenoliths have Mg#s ranging from 73-88 (Fig. S3.3b). Olivine and cpx from individual xenoliths have relatively uniform Mg#s, and the Mg# of olivine and cpx are also similar to each other in a given xenolith. The range of Mg#s observed in the ultramafic xenoliths extends to lower values than observed in PC phenocrysts. However, the Mg# distribution and average are similar (Fig. S3.3).

Clinopyroxene trace element abundances in PC phenocrysts and ultramafic xenoliths are presented in Table A6. Phenocryst cpx and xenolith cpx have similar trace element patterns, with depleted HFSE (Fig. 3.2a). These cpx also show greater variations in highly incompatible trace element concentrations (e.g., [La] = 1.1-17.3 ppm) than in moderately incompatible trace element concentrations (e.g., [Lu] = 0.1-0.4 ppm).

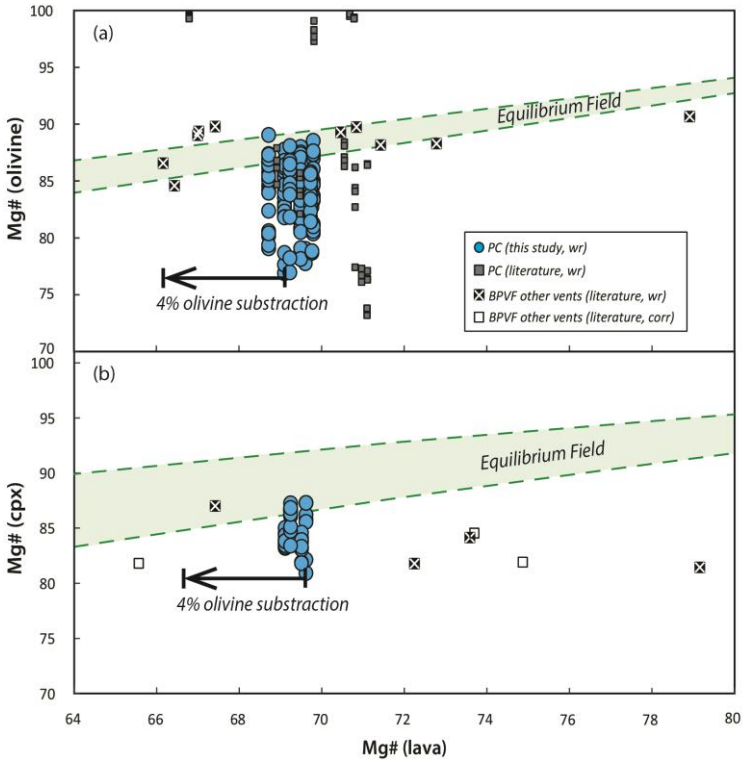

Figure 3.4 PC phenocrysts are out of equilibrium with their host lavas.

Figure 4. Measured Mg# of PC phenocrysts are plotted versus whole rock Mg# of their host lavas. Equilibrium fields are calculated from Fe^{2+}/Mg partition coefficient between olivine or cpx and melt. (a) Olivine phenocrysts versus host lavas, (b) cpx phenocrysts versus host lavas. PC literature data are from Blondes et al. (2008 and 2012) and Gazel et al. (2012). BPVF literature data are from Mordick & Glazner (2006) and Gazel et al. (2012). Open squares show wholerock data from Mordick & Glazner (2006) that are corrected for olivine addition. Some olivine phenocrysts from Blondes et al. (2012) have extremely high Mg# (>95), which they interpreted as the result of subsolidus oxidation after eruption, and are therefore not relevant to this study.

3.4.3 Radiogenic and oxygen isotopes

Strontium, Nd, Pb, Os and O isotope compositions are reported in Table 1. $^{87}Sr/^{86}Sr$ decreases from 0.7061 to 0.7058, and ε_{Nd} increases from -2.7 to -1.4 over the course of the eruption. Pb isotopic compositions also evolve toward less enriched compositions over time (e.g., $^{206}Pb/^{204}Pb$ varies from 19.11 to 18.99). The Sr, Nd, and Pb isotopic ratios are linearly correlated with the inverse of trace element concentrations (e.g., $^{87}Sr/^{86}Sr$ vs. 1/[Sr]; $^{143}Nd/^{144}Nd$ vs. 1/[Nd]; Fig. 3.3b).

Five middle-sequence samples were measured for $^{187}Os/^{188}Os$ to fill the gap of the Os-isotope data set previously reported by Blondes et al. (2008). The Os isotopic compositions of PC lavas ($^{187}Os/^{188}Os$ = 0.183-0.287) are more radiogenic than depleted MORB mantle or primitive upper mantle ($^{187}Os/^{188}Os < 0.130$; Shirey & Walker, 1998). However, Os isotopic ratios do not correlate with Sr-Nd-Pb isotopes or relative stratigraphic position.

Five pyroxene-rich ultramafic xenoliths have Sr, Nd, and Pb isotopic compositions falling on the trend defined by PC lavas (e.g., these xenoliths have $^{87}Sr/^{86}Sr$ = 0.7059 – 0.7063, ε_{Nd} = -2.5 – -3.3, $^{206}Pb/^{204}Pb$ = 19.08 – 19.14). However, all of the xenoliths are isotopically more enriched than their host lavas, with higher $^{87}Sr/^{86}Sr$ and $^{206}Pb/^{204}Pb$ (Fig. 3.5).

Olivine phenocryst separates from PC flows have $\delta^{18}O$ values ranging from +5.4‰ to +5.8‰, slightly higher than the $\delta^{18}O$ value of olivine from fresh NMORB and mantle peridotite (+5.2±0.2‰; Eiler, 2001; Mattey et al., 1994). No temporal trend was observed. The $\delta^{18}O$ values of olivine mineral separates from PC ultramafic xenoliths range from +5.5‰ to +5.7‰.

	Mg# (wr)	Mg#** (ol corr.)	Mg# (ol, ave.)	Mg# (cpx, ave.)	$^{87}Sr/^{86}Sr$	$^{143}Nd/^{144}Nd$	$^{206}Pb/^{204}Pb$	$^{207}Pb/^{204}Pb$	$^{208}Pb/^{204}Pb$	$^{187}Os/^{188}Os$	Os (ppt)	$\delta^{18}O$ (ol)
Lavas												
14PC-2	68.7	65.5	84.2		0.70614	0.51250	19.11	15.66	38.86	0.183	39	5.6
14PC-4	69.2	66.2	83.9	86.0	0.70610	0.51249	19.11	15.66	38.86	0.190	38	
14PC-5	69.8	67.2	83.4		0.70604		19.08	15.65	38.84	0.287	55	
PC-1	69.6	67.4	83.1	85.0	0.70600	0.51249	19.06	15.65	38.85	0.261	20	5.4, 5.6
PC-2	69.5	67.7	84.0	83.3	0.70591	0.51251	19.03	15.65	38.85			5.7
14PC-12	69.8	69.3	84.5		0.70575	0.51254	18.98	15.63	38.80	0.207	37	5.4
14PC-13	69.7	69.4	84.6		0.70559	0.51257	18.99	15.64	38.79			
PC-3	69.1	68.7	84.3	83.9	0.70581	0.51252	18.99	15.64	38.83			5.6, 5.8
14PCX-3 host lava					0.70596		19.07	15.65	38.83			5.5
14PCX-6 host lava					0.70600		19.09	15.66	38.85			5.5
14PCX-9 host lava					0.70602		19.12	15.67	38.89			
14PCX-17 host lava					0.70606		19.12	15.67	38.89			
Xenoliths												
14PCX-3			83.9	84.0	0.70625*	0.51248*	19.11*	15.66*	38.86*			5.7
14PCX-6			84.5	83.4	0.70606*	0.51248*	19.08*	15.66*	38.85*			5.5
14PCX-9				85.1	0.70629*	0.51247*	19.16*	15.68*	38.91*			
14PCX-15			84.4	85.6	0.70591*	0.51251*	19.12*	15.67*	38.88*			5.6
14PCX-17			86.3	85.3	0.70613*	0.51248*	19.14*	15.68*	38.93*			

Table 3.1: Compositions of PC lavas, phenocrysts, and xenoliths.

* Radiogenic isotopic compositions measured on clinopyroxene separates from ultramafic xenoliths. ** Mg# of PC melts are calculated by subtract cumulate olivine from whole rock. The average composition of PC olivine phenocrysts was

used. The amount of olivine cumulate subtracted is determined based on the least squares regression between large olivine phenocryst abundance and relative stratigraphic position of samples (Fig. 1).

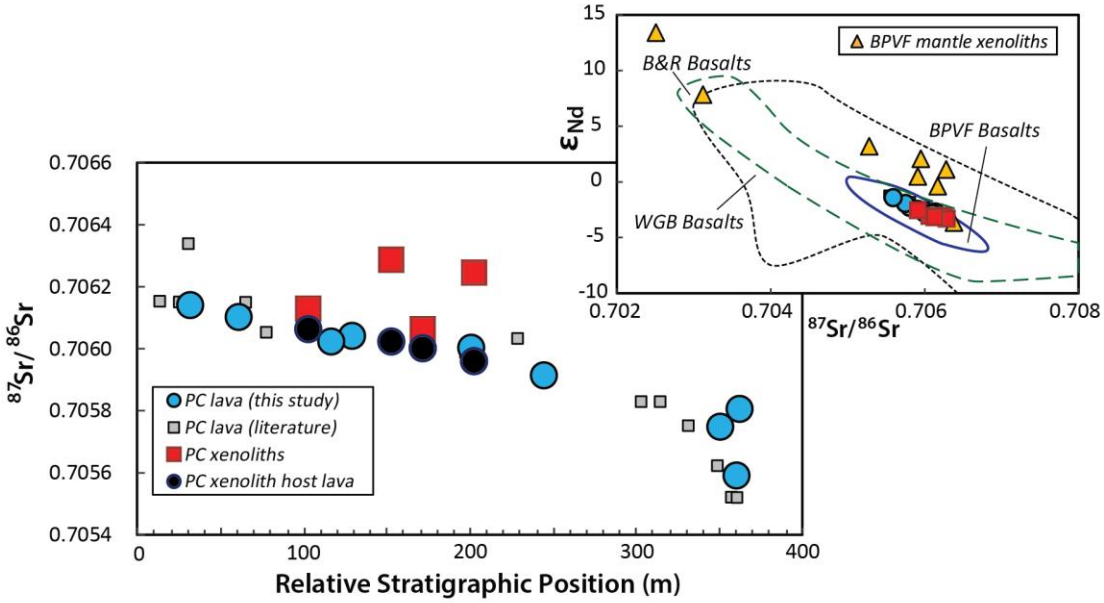

Figure 3.5 PC ultramafic xenoliths are more enriched than their host lavas.

The ultramafic xenoliths in early PC sequence have isotopic compositions overlapping but extending to more enriched compositions compared to PC lavas. Individual xenoliths are systematically more enriched than their host lavas. WGB – western great basin, B&R – basin and range, BPVF – Big Pine volcanic field (Rogers et al., 1995; Beard & Glazner, 1995; Reid & Ramos, 1996; Beard & Johnson, 1997; Kempton et al., 1991; Blondes et al., 2008).

3.5 DISCUSSION

3.5.1 Temporal compositional variations reflect two-component mixing

Lavas from the PC monogenetic vent display significant temporal variations in major and trace element and isotope composition. Over the course of the PC eruption, incompatible trace element concentrations decreased, whereas Sr, Nd and Pb isotopes evolved to less enriched compositions. Several lines of evidence suggest these compositional variations primarily reflect mixing of two distinct melt components. For example, PC lavas show linear correlations between highly and moderately incompatible trace elements (e.g., La vs. Sm, Nb vs. Zr; Fig. 3.3a). Although variations in degree of partial melting may generate variations in trace element concentrations (e.g., Ormerod et al., 1991), curved correlations are expected for elements with different partition coefficients (e.g., Reiners, 2002). In contrast, two-component mixing will generate linear correlations between different elements regardless of their compatibility (e.g., Reiners, 2002). Sr, Nd and Pb isotopic ratios are also linearly correlated with inverse trace element concentration (e.g., $^{87}Sr/^{86}Sr$ vs. 1/[Sr]; Fig. 3.3b), which is again consistent with binary mixing (e.g., Glazner et al., 1991; Reiners, 2002). Overall, the compositional variations suggest mixing of one melt characterized by high incompatible trace element concentrations and enriched isotopic signatures, and another melt that is chemically and isotopically less enriched. PC lavas show greater compositional variation in LILE and LREE (~2x) than in HFSE and HREE (~1-1.2x). LREE/HFSE ratios in PC lavas also correlate with Sr-Nd-Pb isotope compositions. This suggests that the enriched melt is preferentially enriched in LILE and LREE relative to HFSE and HREE. The observed stratigraphic variations indicate that the proportion of the enriched component contained in the erupted hybrid melt decreased over time.

Several different models have been proposed for these two melt components, which have different implications for melt generation and transportation. For example, partial melting of a lithologically heterogeneous mantle source (e.g., pyroxenite and peridotite) may produce melts with distinct chemical and isotopic compositions (e.g., Reiners, 2002; Blondes et al., 2008). Alternatively, the compositional trends could reflect mixing of lithosphere- and asthenosphere- derived melts, possibly as asthenosphere-derived melts ponded at the asthenosphere/lithosphere boundary (Blondes et al., 2008). Finally, if PC magmas ponded within the continental crust prior to eruption, the compositional trends could reflect variable degrees of crustal contamination. Therefore, when and where melt mixing occurred has important implications for the origin of the observed compositional trends. In the following section, we evaluate the record of magma storage contained within PC phenocrysts and ultramafic xenoliths.

3.5.2 Magma storage and fractionation

Previous studies have proposed rapid magma ascent from source to surface with limited shallow storage for many monogenetic volcanoes (e.g., Mattsson, 2012; McGee et al., 2013). PC whole rocks have relatively high and uniform MgO contents (8.7-10.5 wt.%) and Mg# (69-70), indicating they have undergone limited fractional crystallization (Blondes et al., 2008). In addition, early PC sequence lavas contain abundant ultramafic xenoliths that were previously interpreted as mantle xenoliths (Blondes et al., 2008). These features would seem to indicate PC lavas have experienced limited crustal ponding and fractionation, which would suggest the melt mixing described above occurred within the mantle (Reiner, 2002; Blondes et al., 2008). However, as discussed below, the compositions of PC phenocrysts and xenoliths suggest a more complicated history of

magma storage, fractionation and mixing than suggested by whole rock compositional variations.

PC whole rocks span a narrow range of Mg# (69-70, assuming $Fe^{2+}/Fe_T \approx 85\%$). In contrast, olivine phenocrysts in PC lavas span a wide range of composition (Fo = 77-89, with an average of 84). Large variations are observed among olivine grains from individual samples (Fig. 3.4a). In addition, the majority of olivine phenocrysts appear to be more evolved than olivine in equilibrium with their host lavas. Assuming a $K_D^{\text{ol-melt}}$ $(Fe^{2+}/Mg) = 0.3\pm0.03$ (Roeder & Emslie, 1970), olivine phenocrysts in equilibrium with PC lavas should have Fo ≈ 87-89, but the majority of phenocrysts have significantly lower Fo (Fig. 3.4a). Clinopyroxene phenocrysts span a slightly narrower range of Mg# than olivines (Mg# = 81-87, with average of 84), but for the most part also have Mg#s lower than in equilibrium with their host lavas ($K_D^{\text{cpx-melt}}$ $(Fe^{2+}/Mg) = 0.28\pm0.08$; Putirka, 2008; Fig. 3.4b).

One possible explanation for the apparent disequilibrium between phenocrysts and whole rocks is that the whole rocks contain cumulate olivine and cpx, which may result in overestimation of melt Mg# from whole rock compositions. PC lavas contain up to ~4% large olivine (1-3.5 mm), ~1-4% small olivine (0.5-1 mm), and trace amounts of cpx phenocrysts (<0.5 %). If we assume the majority of large phenocrysts are cumulate and take this effect into account, the melt composition estimated from cumulate subtraction is still not in equilibrium with the phenocryst phases (Fig. 3.4). Alternatively, the melt Fe^{2+}/Fe_T ratio may be higher than the value we chose (0.85). This Fe^{2+}/Fe_T ratio corresponds to melt oxygen fugacity of ~FMQ+1, which was estimated by Gazel et al. (2012) for BPVF lavas based on V partitioning between olivine and melt inclusions. High oxygen fugacity of BPVF lavas is also suggested by high sulfur contents of the least degassed melt inclusions (Gazel et al., 2012; Jugo et al., 2010). In addition, few melts

from the Great Basin have oxygen fugacities lower than FMQ (e.g., Christiansen & McCurry, 2008). A Fe^{2+}/Fe_T ratio of 0.9, which would correspond to ~FMQ (Botcharnikov et al., 2005), would shift the calculated melt Mg# by only ~1 unit, too little to bring the melt and phenocrysts into equilibrium. Therefore, the phenocrysts appear to derive primarily from melts that have lower Mg# and thus experienced greater fractionation than their host lavas.

Ultramafic xenoliths in early PC lavas were previously described as likely derived from the mantle (Blondes et al., 2008), which would indicate rapid magma ascent from mantle depths. However, the xenoliths we investigated all lack orthopyroxene and no true 4-phase peridotites were identified. Most mantle-derived xenolith suites contain peridotite even if pyroxenite is also present. In addition, xenolith olivine and cpx Mg#s range from 73 to 87, extending well below the range of Mg# (88-90) reported from BPVF mantle xenoliths from other localities (Beard & Glazner, 1995; Lee et al., 2001 & 2002). Instead, the range of Mg#s are similar to the range defined by PC phenocrysts. These xenoliths therefore most likely formed as cumulates from the same melts that generated the phenocrysts.

Overall, both the phenocrysts and ultramafic xenoliths appear to derive from melts that on average are more evolved and have lower Mg# than PC lavas. This suggests that PC lavas represent mixtures of a primitive melt component with high Mg# and a more evolved, low-Mg# melt containing these phenocrysts and xenoliths. Over the course of the eruption, abundances of both large olivine phenocrysts and ultramafic xenoliths decrease, which may indicate that the large olivine phenocrysts are cumulates derived from the more evolved magma, whereas smaller olivines represent true phenocrysts formed during rapid near-surface cooling. In this case, decreasing abundances of large phenocrysts and ultramafic xenoliths indicate that the proportion of the evolved melt

component in the erupted lavas decreased over time. As discussed in section 5.1, the compositional variations in PC lavas likely reflect mixing of two melt components. Given the discussion above, the mixing between a primitive melt and a more evolved melt suggested by the observed phenocryst-host-rock disequilibrium may account for these compositional trends. In the following discussion, we examine the likely depths of magma storage and fractional crystallization.

Previous studies have estimated the storage depths of younger (< 500 ka) BPVF lavas using phenocryst-melt thermobarometers and the volatile contents in phenocryst-hosted melt inclusions to constrain phenocryst crystallization depths. Mordick & Glazner (2006) suggested deep cpx crystallization using the cpx-melt thermobarometer of Putirka et al. (1996). They examined four samples from younger BPVF vents, and suggested cpx phenocryst growth at ~1.4±0.3 GPa and ~1250±100 °C (Mordick & Glazner, 2006). In contrast, Gazel et al. (2012) suggested shallow fractionation (~5 kbar) of olivine phenocrysts, based on volatile contents (CO_2 and H_2O) of melt inclusions trapped in the phenocrysts. These pressure constraints would seem to indicate that cpx and olivine phenocrysts in BPVF lavas formed at very different depths. However, coexisting olivine and cpx in PC ultramafic xenoliths have similar Mg#, and olivine and cpx phenocrysts in PC lavas span similar ranges of Mg# and have the same average Mg#. These features indicate concurrent crystallization of olivine and cpx.

The use of the cpx-melt thermobarometer to calculate crystallization pressures presupposes that phenocrysts and host lavas are in chemical equilibrium. However, as is true for the majority of PC phenocrysts, most of the samples investigated by Mordick & Glazner (2006) contain cpx that are out of equilibrium with their host lavas, even after whole rock compositions are corrected for phenocryst accumulation to estimate melt compositions (Fig. 3.4). The only cpx/melt pair examined by Mordick & Glazner (2006)

that is close to equilibrium (sample B-1) resulted in the lowest estimated pressure (~1 GPa). In addition, the Putirka et al. (1996) thermobarometer is calibrated for anhydrous melts, whereas BPVF magmas have relatively high water contents (1.5-3.0 wt.%; Gazel et al., 2012). Because water can lower the liquidus temperature of melts, failing to take into consideration of the effects of water may lead to overestimation of crystallization temperatures. This in turn will result in overestimation of pressure, because temperature is an input in the Putirka (1996) cpx-melt barometer. Therefore, the estimated cpx crystallization pressures of Mordick & Glazner (2006) may be systematically too high.

Fractionation at >1 GPa would appear to be inconsistent with abundant olivine phenocrysts in BPVF lavas. Many experimental studies show that olivine fractionation in alkalic basalts primarily occurs at pressures <1 GPa (e.g., Green & Ringwood, 1967; Nekvasil et al., 2004). As pressure increases, the stability field of clinopyroxene expands at the expense of olivine and plagioclase (e.g., O'Hara, 1968). Olivine is the dominant phenocryst phase in PC lavas. Clinopyroxene is less abundant, whereas plagioclase is absent. Olivine and cpx are both present in PC ultramafic xenoliths.

We further constrained the potential pressure range of PC magma crystallization by modeling fractional crystallization over a range of pressures (1-11 kbar) using the MELTS thermodynamic model (Ghiorso & Sack, 1995). The crystallization pressures of PC phenocrysts and ultramafic xenoliths were then constrained by comparing the model-predicted crystallization phases and mineral compositions with observations. We also evaluated the effects of initial melt composition, water content, oxygen fugacity, and crystallization style (fractional versus batch) on modeling results by varying these parameters over reasonable ranges. The compositions of both the earliest and the latest PC lavas were used as the initial model melt compositions. Initial water contents of 1.5 and 3.0 wt.% were used, consistent with the estimated water contents for primitive BPVF

melts (Gazal et al., 2012). Oxygen fugacity was initiated at FMQ and FMQ+1, and allowed to proceed unbuffered in MELTS modeling.

All models produced similar crystallization trends. One representive set of modeling results is shown in Fig. 3.6, and additional information is presented in Appendix Fig. S3.4. Over the range of pressures investigated, the stability field of olivine shrinks with increasing pressure, and olivine is not crystallized at pressures >10 kbar. In contrast, the onset of cpx fractionation occurs at higher temperature with increasing pressure, resulting in higher Mg# of the first-crystallized cpx. These results are consistent with experimental observations (e.g., Green & Ringwood, 1987; Nekvasil et al., 2004). Olivine and cpx in PC phenocrysts and xenoliths span a wide range of Mg# (73-89, Fig. S3.4). The MELTS modeling results suggest that at pressures greater than ~7 kbar, olivine fractionation will be suppressed and olivine with low Mg# (< 73) will not be formed because olivine is replaced by cpx on the liquidus. On the other hand, at pressures < ~5kbar, the onset of cpx fractionation will be too late to produce cpx with Mg# up to 88. Therefore, MELTS modeling suggest the phenocrysts and xenoliths crystallized at pressures of ~5-7 kbar, assuming isobaric rather than polybaric fractionation (Fig. 3.6). This pressure estimate is consistent with the pressure estimates derived from BPVF melt inclusions (Gazel et al., 2012).

Taken collectively, we suggest the phenocrysts contained in PC lavas most likely formed at ~5-7 kbar. Using an average crustal density of 2,750 kg/m^3 (Wang et al. 2002), the estimated depth of magma fractionation is ~19-26 km. Given a local crustal thickness of ~36 km (Wang et al., 2002), the magmas parental to the PC phenocrysts and ultramafic xenoliths therefore likely ponded within the middle to lower crust prior to eruption. Gazel et al. (2012) suggested that magmas may have stalled and ponded near the brittle-ductile transition (~20 km) within the crust, due to this rheological contrast.

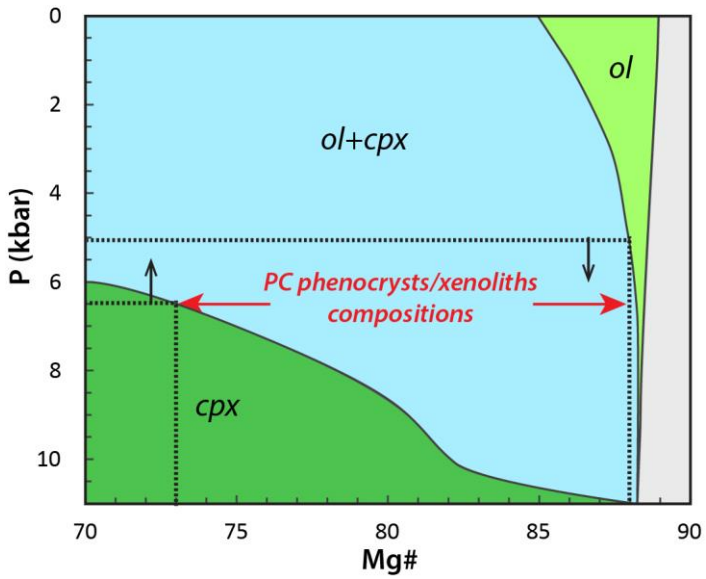

Figure 3.6 Pressure constraints based on MELTS modeling results.

MELTS modeling results of fractional crystallization using 14PC-2 as the starting melt composition, 1.5 wt.% initial water content, and oxygen buffer initiated at FMQ+1. The range of crystallized mineral compositions (Mg#) varies with pressure. The range of olivine and clinopyroxene Mg# observed in PC phenocrysts and xenoliths suggests they were crystallized at ~5-6.5 kbar. See text for discussion.

3.5.3 Crustal contamination

Paragraphs with the style *Heading 4,h4* applied can be extracted to appear in the table of contents with the style *TOC 4*. The above discussion suggests mixing of a primitive melt and an evolved melt occurred within the crust to generate the observed compositional variations in PC lavas. The trace element concentrations in cpx phenocrysts and cpx in xenoliths vary by up to a factor of 15. We calculated the REE concentrations of the melts from which these cpx formed using estimated cpx-melt partition coefficients (see Appendix for more details). Most of the calculated melts have incompatible trace element concentrations that are higher than any PC lavas (Fig. 3.2b). Clinopyroxene HFSE and HREE concentrations are well correlated with cpx Mg#. These correlations are generally consistent with compositional variations derived from fractional crystallization in conjunction with increasing K_D values with decreasing Mg# (e.g., Lu, Fig. 3.7a). In contrast, LILE and LREE concentrations do not correlate with Mg#, and pyroxenes spanning a narrow range in Mg# show much larger variations in the concentrations of these elements than can be explained by the effects of fractional crystallization alone (Fig. 3.7b). The LILE and LREE variations observed in these pyroxenes require pyroxene crystallization from melts with highly variable LILE and LREE concentrations and LILE/HFSE fractionation (Fig. 3.7b).

In addition, although ultramafic xenoliths have Sr, Nd, and Pb isotopic compositions overlapping the range of PC lavas, these xenoliths extend to (and beyond in the case of Pb) the most enriched compositions defined by PC lavas. In every sample analyzed, individual xenoliths have isotopic compositions that are more enriched than their host lava (Fig. 3.5). Overall, PC phenocrysts and xenoliths appear to derive from melts that are isotopically more enriched than their host lavas, and characterized by LILE and LREE enrichment relative to HFSE and HREE. Therefore, the parental melt of PC

phenocrysts and xenoliths resembles the "enriched" mixing component discussed in Section 5.1.

In principle, it is possible that the primitive and evolved melts derived from distinct mantle sources, and the chemically and isotopically more enriched compositions of the evolved melts are a mantle-derived primary feature. For example, the "enriched" melts may derive from partial melting of enriched mantle domains (e.g., pyroxenite veins; Reiners, 2002; Blondes et al., 2008). In this case, the fact that the more enriched melt is also more evolved is coincidental. However, as discussed below, several lines of chemical and isotopic evidence suggest that crustal contamination may have played an important role in modifying the composition of the evolved melt that is the source of PC phenocrysts and ultramafic xenoliths.

Average continental crust has radiogenic $^{87}Sr/^{86}Sr$ and unradiogenic $^{143}Nd/^{144}Nd$ compared to both convecting upper mantle and primitive mantle. Continental crust is also characterized by significant HFSE depletion. For example, average continental crust has La/Nb of ~2.5, N-MORB has La/Nb of ~1.0, and ocean island basalts have La/Nb $\leq$1.2 (Rudnick & Gao, 2003; McDonough & Sun, 1995). Assimilation of continental crust therefore is expected to generate correlations between isotopic compositions and LILE/HFSE ratios, as has been observed in several previous studies (e.g., Davies & Macdonald, 1987; Rowe et al., 2011). PC lavas are variably depleted in HFSE, with La/Nb ranging from ~2 to 3.6. In addition, La/Nb ratios strongly correlate with $^{87}Sr/^{86}Sr$, $^{206}Pb/^{204}Pb$ and $^{143}Nd/^{144}Nd$ (e.g., Fig. 3.8). These features are consistent with crustal contamination, although melt generation from subduction-modified mantle (especially if rutile is present as a trace phase) could also potentially produce isotopically enriched, HFSE-depleted melts.

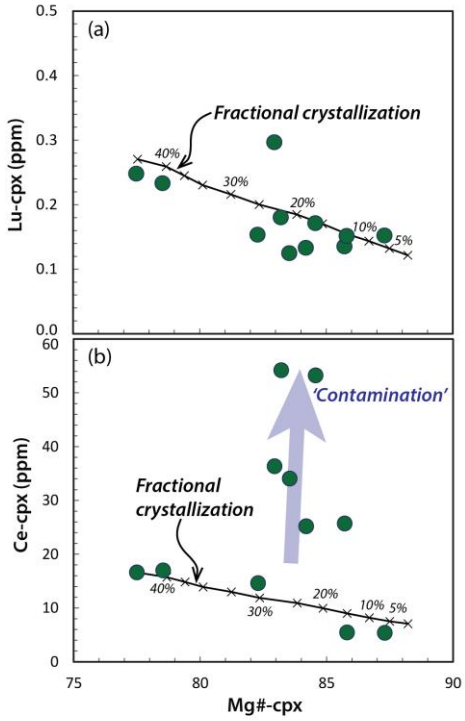

Figure 3.7 Clinopyroxene Mg# versus trace element concentrations.

(a) Lu concentrations in clinopyroxene from PC phenocrysts and xenoliths are negatively correlated with cpx Mg#. This trend is largely consistent with fractional crystallization. (b) Ce concentrations in these cpx show large variations that cannot be explained by fractional crystallization alone. The fractional crystallization curves are modeled assuming the initial melt has a composition resembling the least enriched (latest) PC lava ([Lu] = 0.38 ppm, [Ce] = 71 ppm). The mass fraction and Mg# of fractional crystallization products of this initial melt was modeled using the MELTS software at 6 kbar, with an initial water content of 1.5 wt.%, initial oxygen buffer of QFM+1, and temperature steps of 10°C. Partition coefficients between cpx and melt was varied corresponding to the crystallization temperature of each step (K_d^{Lu} = 0.32-0.49, K_d^{Ce} = 0.100-0.144, see appendix for more information on K_d selection).

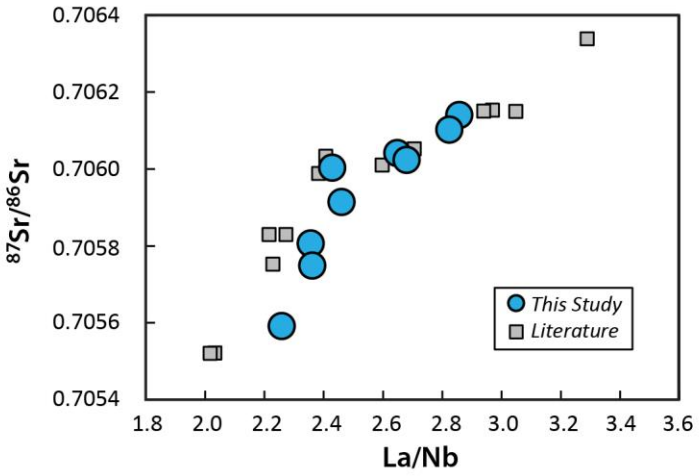

Figure 3.8 Correlation between La/Nb ratios and Sr isotopes in PC lavas.

The oxygen isotope compositions of PC phenocrysts and cumulate xenoliths are also consistent with crustal contamination. Olivine phenocrysts from PC lavas have $\delta^{18}O$ values ranging from +5.4 to +5.8 ‰. Olivines from PC cumulate xenoliths display a similar range of oxygen isotope compositions ($\delta^{18}O$ = +5.5 to +5.7 ‰). These values are slightly but consistently higher than normal mantle olivine ($\delta^{18}O$ = +5.0 to +5.4 ‰, Mattey et al., 1994) or olivine from most uncontaminated MORB or ocean island basalts (Eiler, 2001). Continental crust typically has higher than mantle $\delta^{18}O$ values (e.g., Taylor et al., 1968; Kempton & Harmon, 1992). Positively correlated $\delta^{18}O$ values and radiogenic $^{87}Sr/^{86}Sr$ in many basalt suites has been attributed to crustal contamination (e.g., Puricutin, McBirney et al., 1987; Aeolian arc, Peccerillo et al., 2004). Although PC lavas and ultramafic xenoliths contain olivines with $\delta^{18}O$ values higher than typical MORB, no correlation between olivine $\delta^{18}O$ and whole rock $^{87}Sr/^{86}Sr$ is observed. This may reflect derivation of the olivines from the evolved (and contaminated) melt, whereas the whole rocks represent mixtures of evolved, contaminated melt and primitive, uncontaminated melt. As a result, the Sr isotope composition of the melt mixture is dependent on the ratio of contaminated and primitive melt in the hybrid melt, but $\delta^{18}O$ values of the olivines, which formed from the contaminated melt prior to mixing, are not.

PC lavas also have radiogenic Os isotopic compositions ($^{187}Os/^{188}Os$ = 0.183-0.310) compared to normal mantle peridotite ($^{187}Os/^{188}Os < 0.130$; e.g., Shirey & Walker, 1998; Lassiter et al., 2014) and most unmodified mantle-derived magmas ($^{187}Os/^{188}Os <$ 0.150; e.g., Hauri & Hart, 1993; Lassiter & Hauri, 1998). Continental crust has high Re/Os ratios and therefore variable but high $^{187}Os/^{188}Os$ (e.g. Esser & Turekian, 1993). Although the highly radiogenic Os isotope compositions in PC lavas are suggestive of crustal contamination, wholerock Os isotope ratios do not systematically vary with stratigraphic position or correlate with other chemical and isotopic systems. Because PC

lavas have very low Os concentrations ([Os]<60 ppt), their Os isotopic compositions may be largely controlled by the composition of trace phases such as sulfide inclusions within olivine phenocrysts. Sulfides may have grown from either primitive melt or contaminated melt. A mixture of different sulfide populations could result in whole rock Os isotopic compositions becoming decoupled from other isotope systems.

Taken collectively, all of the features described above are consistent with crustal contamination. Therefore, although we cannot exclude the possibility that the evolved melt derives from a distinct subduction-modified mantle source, it appears more likely that the evolved melt fractionated and assimilated continental crust during magma storage. The compositional variations in PC lavas therefore likely reflect varying degrees of crustal contamination, as is suggested for many other monogenetic vents (e.g., McBirney et al., 1987; Schaaf et al., 2005; Erlund et al., 2010; Rowe et al., 2011).

3.5.4 Sills model

The above discussion indicates that the PC lavas contain a melt component that has experienced significant crustal storage and fractional crystallization and that therefore the observed compositional variations in PC lavas are most readily explained by mixing of an evolved and crustally-contaminated melt with a more primitive melt. Signatures of the enriched, evolved component decrease over the course of the PC eruption, as suggested by decreasing incompatible trace element concentrations and the decreasing abundance of large olivine phenocrysts and cumulate xenoliths. A model is needed to explain this temporal trend. Here we propose a two-stage eruption model, where an initial melt pulse stalls and fractionates in the crust, and the eruption is triggered by arrival of a later melt pulse which then mixes with the earlier component (Fig. 3.9).

In this model, an initial melt pulse stalled and formed one or more sills within the crust. According to pressure constraints, these sills most likely formed at ~20 km, near the brittle-ductile transition within the crust (Gazel et al., 2012). Magmas within the crustal sills fractionated and assimilated crustal materials while cooling via coupled assimilation and fractional crystallization (DePaolo, 1981; Spera & Bohrson, 2001). Therefore, these magmas are characterized by high incompatible trace element concentrations and enriched isotopic compositions, and contain significant amounts of phenocrysts and cumulates. A later melt pulse that broke to the surface then triggered the eruption. As the eruption began, the pressures within the crustal sills shifted from lithostatic to magmatic, and as a result the sills collapsed and magma from the sills was forced into the main conduit and mixed with the later, more primitive magmas from depth. Over the course of eruption, the sill component was gradually exhausted. As a result, the sill-component signatures decreased over time, which is reflected in decreasing incompatible trace element concentrations, less enriched isotopic compositions and lower phenocryst and cumulate xenolith abundances in later PC lavas.

The limited major element variation recorded in PC lavas places constraints on the extent of mixing of evolved (low Mg#) and primitive (high Mg#) melts. After correcting for olivine phenocrysts, the Mg# of erupted PC melts varied from ~66 in the earliest PC melt to ~70 at the end of the eruption. We estimated the potential composition of the evolved sill component by calculating the liquid line of descent of primitive PC lavas using the MELTS program. Trace element abundances were estimated from the most enriched cpx, which has a Ce concentration of ~54 ppm, and is estimated to derive from a melt with ~420 ppm Ce (K_d = 0.13). Modeling details are given in the appendix. A simple binary mixing model suggests addition of up to ~20% of the sill component could generate the relatively small variations in Mg# and large variations in incompatible trace

element concentrations in the erupted melts (Fig. S3.5). This mixing process can also explain the variations in Sr-Nd-Pb isotopic compositions in PC lavas. However, we note that the modest increase in SiO_2 content over the course of eruption would appear to be inconsistent with the sills model, because fractional crystallization and assimilation of silicic crust usually increases the SiO_2 content of evolved and contaminated melts. One possibility is that the parental melt to the sill component initially had lower SiO_2 than the second melt pulse. Alternatively, the sill component may have assimilated crustal rocks with low SiO_2 abundance (e.g., carbonate or skarn).

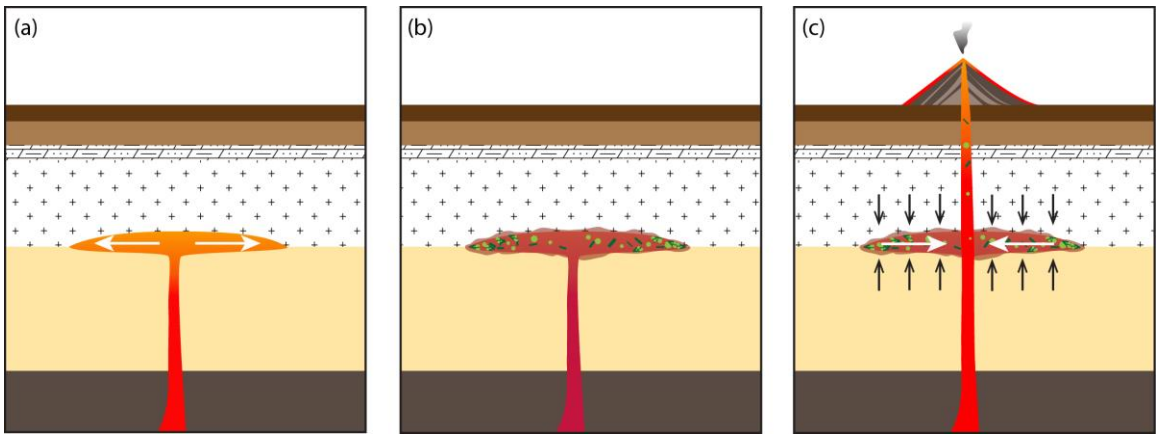

Figure 3.9 Deflating sills model.

(a) One or more sills are created through a magmatic pulse some time prior to eruption; (b) Melts ponding in the sills undergo fractional crystallization and assimilate crustal rocks; (c) A second magma pulse triggers eruption. As the eruption progresses, the sills deflate due to dropping pressure, which forces the evolved and contaminated magma with phenocrysts and xenoliths to mix back into the feeder conduit with more primitive melt.

3.6 CONCLUSIONS

- Lavas from the Papoose Canyon (PC) monogenetic vent sequence display significant temporal variations in major and trace element abundances and Sr, Nd, and Pb isotope compositions.
- Correlations between trace element concentrations and isotopic ratios indicate the observed temporal variations reflect binary mixing of two distinct melts, where the proportion of the chemically and isotopically more enriched component decreases over time.
- The major and trace element compositions of PC phenocrysts and ultramafic xenoliths suggest they derive from a melt that is more evolved and chemically more enriched than PC lavas.
- Pressure constraints suggest PC phenocrysts and ultramafic xenoliths fractionated at pressures of ~5-7 kbar, which corresponds to the middle crust, possibly near the brittle-ductile transition.
- Correlations between HFSE depletions and Sr-Nd-Pb isotopic compositions, high $\delta^{18}O$ in olivines, and radiogenic Os isotopic compositions in wholerocks suggest PC lavas have likely experienced crustal contamination.
- A deflating sills model is proposed to explain the observations and implications described above. An initial melt pulse stalled and formed one or more sills within the crust, where melt fractionated and assimilated crustal material. The eruption was triggered by the arrival of a later melt pulse, and the early, evolved melts were drained and mixed with the later, more primitive melts. The temporal-compositional trends therefore reflect exhaustion of the sill component over time.

- These results indicate that even “primitive” lavas may contain a significant signature of magma ponding, fractionation, and crustal contamination that is obscured within the bulk lava but is recorded in the melt “crystal cargo”.

ACKNOWLEDGEMENTS

This work was supported in part by NSF grant EAR-1301621 and by the Jackson School of Geosciences, University of Texas at Austin. We thank T.E. Larson, E.M. Marshall, J.D. Barnes, and R. Chatterjee for laboratory assistance. We also thank J.T. Cullen, J.S. Jordan, and J.D. Barnes for help in the field.

Appendices

APPENDIX A1: SUPPLEMENTARY FILE FOR CHAPTER 1

Appendix A1.1 Analytical Methods

Xenoliths were crushed by hand and then placed in deionized water and ultrasonicated for 15 minutes, after which cleaned grains were dried and sieved. Grains of 250-850 microns in diameter were picked under a binocular microscope to prepare clinopyroxene and plagioclase separates. Care was taken to avoid any grains with visible alteration or adhered melt. Epoxy grain mounts were then made and polished for mineral major and trace element analyses of 2-3 grains from each sample.

Mineral compositions of most samples were analyzed at the USGS on polished thin sections using standards, procedures, and equipment and yielding analytical accuracy and precision outlined in Bohrson and Clague (1988) and Davis et al. (1994). Each analysis in the table is an average of the number of points indicated in Supplemental Tables S1.1 through S1.3. Additional major elements on some of the clinopyroxene and plagioclase separated for other chemical analyses were measured using a JEOL JXA-8200 EPMA at UT Austin at 15kV accelerating voltage, with a 10nA beam current, and a defocused beam of 10μm diameter. Measurements of secondary standards were accurate to within 5%, and are generally reproducible within 5% (1 s.d.) except MnO (20%). Some samples were analyzed at both the USGS and UTA to evaluate any potential inter-laboratory bias and these replicates are presented in Supplemental Tables S1.1 through S1.3. The differences between the two labs are smaller than the compositional variation observed between grains of individual samples, so no systematic inter-laboratory differences were detected.

Clinopyroxene trace element concentrations were measured by LA-ICP-MS using an Agilent 7500ce quadrupole with a New Wave UP-193FX laser system using methods described in Byerly and Lassiter (2012). 75 μm spots were pre-ablated and dwell time was 60s with 50s washout time. Analyses of most elements for secondary standard BCR-2g were accurate to within 5% of the accepted values. Gadolinium and Hf were accurate to within 7%, and Y was accurate to within 10%. Repeat analyses of BCR-2g were reproducible to within 3% (1 s.d.). In most cases 3 spots per sample were analyzed and average concentrations are reported.

For Sr and Sm-Nd isotopes, 100-150 mg plagioclase and/or clinopyroxene separates were digested following procedures described in Byerly & Lassiter (2012) and Connelly et al. (2006). Before digestion, samples for Sr and Sm-Nd analysis were leached in 2.5 N HCl for 30 min, and then washed and ultra-sonicated in deionized water. Sr-Spec and REE-spec/HDEHP resins were used to separate Sr and Sm/Nd, respectively. Strontium and Sm/Nd were run on a Triton TIMS. Strontium was run as metal on single Re filaments loaded with Ta_2O_5. Neodymium and Sm were run as metals on double Re filaments. NBS 987 and UT Ames Nd standards were measured regularly during the course of this study. The average NBS 987 $^{87}Sr/^{86}Sr$ for the TIMS lab over the period during which analyses were performed was 0.710273±0.000015 (2 s.d.), similar to the value reported by Thirlwall (1991) (0.710248±0.000015). The average $^{143}Nd/^{144}Nd$ of UT Ames Nd was 0.512072±0.000010 (2 s.d.), and is consistent with the values reported by Scher & Delaney (2010) (0.512069±0.000014). During the period of analytical work, replacement of one faraday cup resulted in a slight shift of measured standard $^{87}Sr/^{86}Sr$ and $^{143}Nd/^{144}Nd$ ratios. Therefore the sample ratios reported in this study are standard corrected (Sr standard corrected to 0.710250 and Nd standard corrected to 0.512070 using average measured standard values from before and after faraday cup replacement).

Five duplicates were measured and the standard deviations (2 s.d.) for $^{87}Sr/^{86}Sr$ and $^{143}Nd/^{144}Nd$ were 12ppm and 5ppm, respectively. Strontium total procedure blanks were less than 150pg, and Nd blanks were less than 75pg. The impact from blanks was negligible for the sample sizes analyzed, and no blank correction was applied to the reported data.

For oxygen analyses, under a binocular microscope plagioclase and clinopyroxene crystals are carefully picked to avoid visible melt infiltration, inclusions or surface alteration. Oxygen isotope ratios were measured on ~2 mg of optically pure clinopyroxene and plagioclase separates by laser fluorination (Sharp, 1990). Each sample was heated with a CO_2 laser in the presence of BrF_5. The extracted O2 was cryogenically purified prior to introduction into a ThermoElectron MAT253 isotope ratio mass spectrometer. In house quartz standard Lausanne-1 ($\delta^{18}O$ = 18.1‰), garnet standard UWG-2 ($\delta^{18}O$ = 5.8‰) (Valley et al., 1995) and olivine standard San Carlos ($\delta^{18}O$ = 5.2‰) were measured to ensure accuracy and precision. $\delta^{18}O$ values are reported relative to SMOW, where the $\delta^{18}O$ value of NSB-28 is +9.65‰. Duplicates were measured on different days, and duplicate data are reported in Supplemental Table S1.6. Precision based on replicates of the standards is ±0.1 (1 s.d.).

Appendix A1.2 Melt REE Concentrations Calculation

We calculated the REE concentrations of melts in equilibrium with clinopyroxene from Hualalai gabbros, assuming no trapped melt. The Kd values used were obtained using the empirical program BIGD (Nielsen, 1992). The input parameters for the program are Xmelt – average Hualalai melt composition (data from GeoRoc), Xmineral – average measured clinopyroxene composition, and T – average temperature (1100 °C) of clinopyroxene fractionation. The Kd values are listed in the following Table S1.7. If

trapped melts were present, this melt would increase REE concentrations in clinopyroxene following sub-solidus re-equilibration, which will result in overestimation of REE abundances in calculated equilibrium melts. This cannot account for the LREE-depleted, MORB-like patterns calculated for the melts in equilibrium with group-1 gabbros. In addition, the similarity of the calculated melts in equilibrium with group-2 and -3 gabbros with Hualalai lavas suggests little sub-solidus reequilibration with trapped melt components.

Appendix A1.3 MELTS Modeling

The crystallization products of primitive Hualalai tholeiitic melt KK-14-5 (Table. S1.8; Bohrson & Clague, 1988) were modeled using MELTS (Ghiorso & Sack, 1995). Water content measured for KK-14-5 is 0.39 wt. % (Bohrson & Clauge, 1988), and water content estimates for primitive Hawaiian range up to 0.6 wt. % (Hauri, 2002). We investigated the effect of varying water content by using 0.4-0.7 wt. % initial water content for MELTS models. Oxygen buffer suggested for Hawaiian melts is between NNO and QFM (e.g. Gerlach, 1993). MELTS models initiated at the NNO buffer and QFM buffer were investigated in this study. The model-predicted crystallization sequences at different pressures are presented in Figure A3.3 (using initial 0.4 wt. % water content and NNO oxygen buffur).

Appendix A1.4 MORB Nd Isotopic Heterogeneity

We compiled Nd isotope data of MORB at ocean spreading centers using the PetDB database. In order to investigate the correlation between MORB Nd isotopic heterogeneity and ridge spreading rates, ten mid-ocean ridge segments with different spreading rates (Press et al., 2004) were selected (listed in Table. S1.9). We excluded segments previously found to be influenced by hotspot inputs (Steinberger, 2000). The

degree of Nd isotope heterogeneity along individual ridge segments was quantified by calculating the standard deviation of ε_{Nd} in ~50 km long sections with rolling bins, and then averaging the standard deviations of the bins from each ridge segment. The 50 km bin size was chosen to ensure sufficient analyses within most bins to allow calculation of the standard deviation. The ridge segments used and the number of Nd-isotope analyses included for each segment are listed in Table S1.9.

Appendix A1.5 Figures

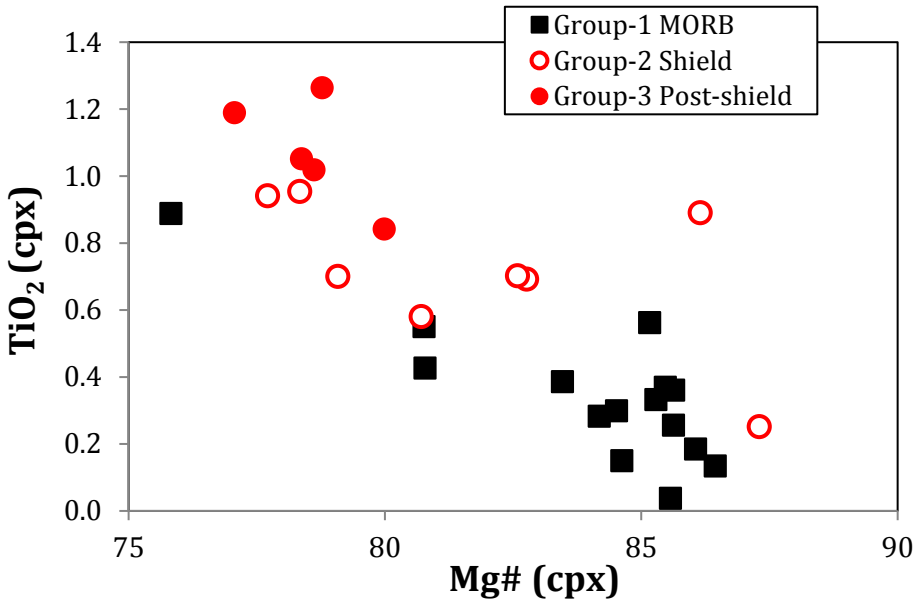

Figure S1.1: Clinopyroxene T_iO_2 vs. clinopyroxene Mg# of Hualalai gabbroic xenoliths.

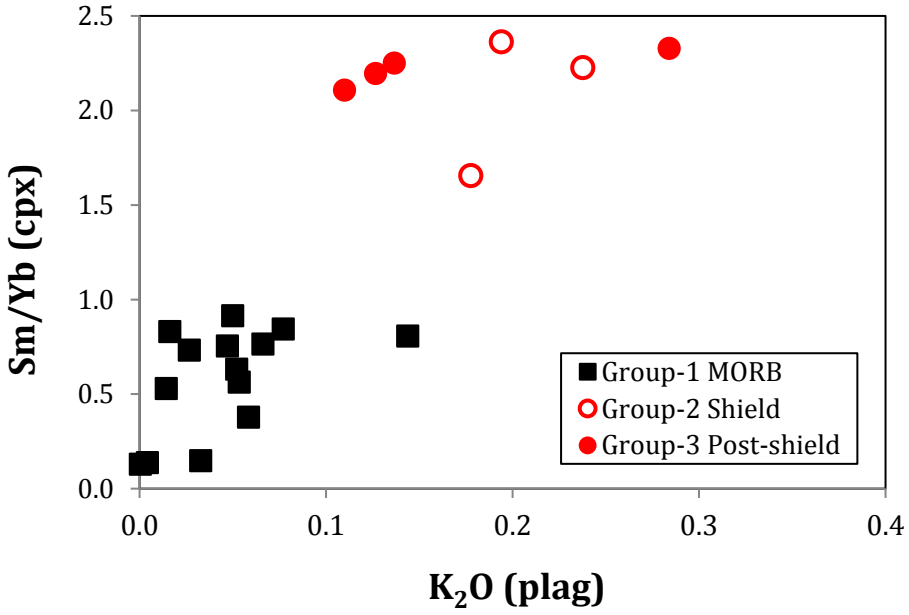

Figure S1.2: Plagioclase K_2O vs. clinopyroxene Sm/Yb of Hualalai gabbroic xenoliths.

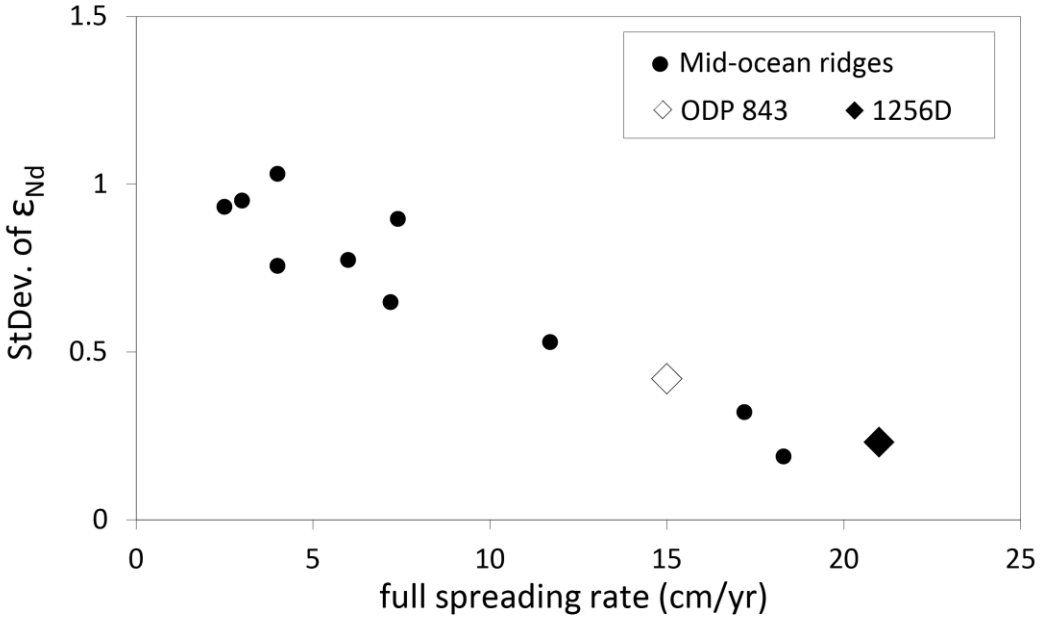

Figure S1.3: Nd isotope heterogeneity versus spreading rate.

Nd isotope heterogeneity (calculated as 1 s.d. of the population) of Hualalai group-3 gabbros compared with mid-ocean ridge basalts sampled from ~50 km rolling bins along different ridge segments. Data for ODP 843 basalts are from King et al. (1991); data for ODP 1256D are from Höfig et al. (2014); data for other mid-ocean ridges are compiled from PetDB (more detailed information is provided in supplement text).

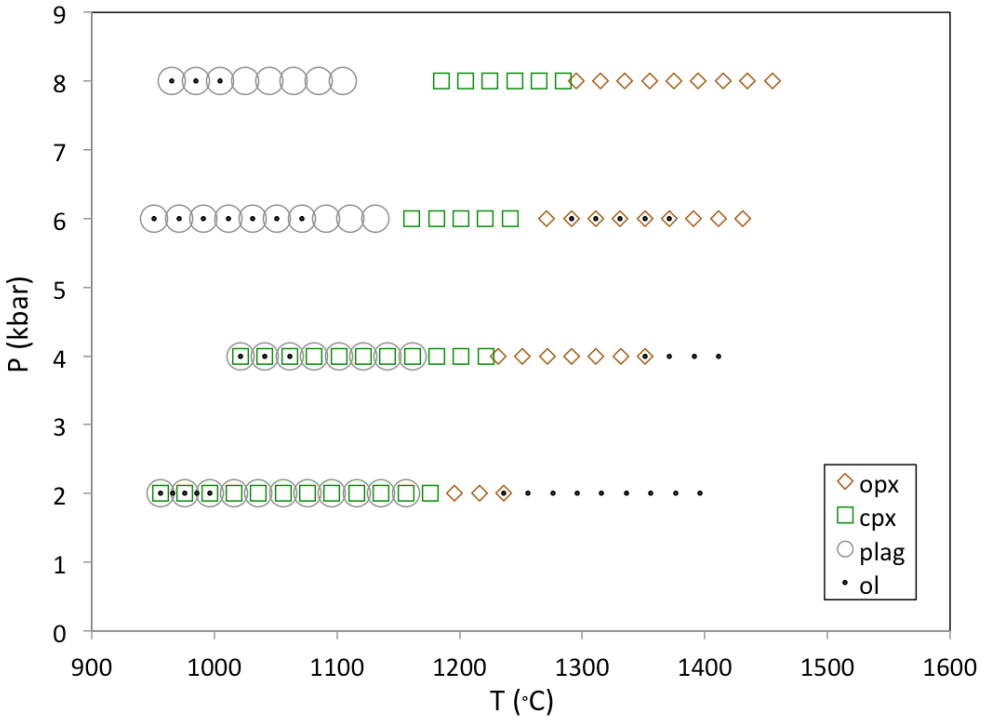

Figure S1.4: Crystallization sequence of the MELTS model results.

Crystallization sequence of the MELTS model results with 0.4 wt.% initial water content and NNO oxygen buffer.

Appendix A1.6 Tables

Sample	n	SiO_2	Al_2O_3	Na_2O	MgO	CaO	MnO	FeO	TiO_2	Cr_2O_3	Total	Mg#
Group-1 MORB												
63Kap-3[b]	3	52.01 (.66)	2.39 (.33)	0.36 (.03)	17.74 (.73)	20.85 (.12)	0.20 (.02)	5.01 (.06)	0.13 (.02)	0.20 (.01)	98.94 (1.74)	86.4 (.4)
65-Kap-14d[a]	3	52.13 (.21)	3.12 (.18)	0.18 (.01)	16.53 (.21)	21.53 (.31)	0.13 (.02)	5.48 (.23)	0.21 (.06)	0.19 (.10)	99.50 (.17)	84.3 (.7)
65Kap-14d rep[b]	*3*	*52.88 (.69)*	*2.57 (.03)*	*0.05 (.02)*	*18.81 (1.79)*	*20.51 (2.01)*	*0.13 (.02)*	*5.71 (.52)*	*0.04 (.04)*	*0.43 (.04)*	*101.15 (.85)*	*85.6 (.1)*
63Kap-13[a]	6	52.35 (.80)	3.64 (.58)	0.51 (.04)	16.58 (1.02)	20.68 (1.11)	0.15 (.01)	5.58 (.24)	0.33 (.04)	0.72 (.14)	100.57 (.58)	84.1 (.5)
63Kap-13 rep[b]	*6*	*52.51 (.52)*	*3.08 (.22)*	*0.46 (.03)*	*16.83 (.25)*	*21.29 (.25)*	*0.16 (.03)*	*5.68 (.07)*	*0.27 (.03)*	*0.68 (.07)*	*101.00 (.74)*	*84.2 (.2)*
65Kap-13[a]	6	51.72 (.52)	3.58 (.83)	0.66 (.05)	16.47 (.49)	20.55 (.23)	0.14 (.01)	5.12 (.14)	0.43 (.07)	0.58 (.05)	99.23 (.34)	85.1 (.6)
65Kap-13 rep[b]	*3*	*52.99 (.46)*	*2.74 (.05)*	*0.49 (.03)*	*17.07 (.09)*	*21.37 (.04)*	*0.15 (.01)*	*5.30 (.04)*	*0.33 (.03)*	*0.69 (.03)*	*101.12 (.47)*	*85.3 (.1)*
65Kap-14a[b]	5	51.31 (.41)	2.40 (.04)	0.08 (.03)	17.27 (.28)	21.83 (.31)	0.14 (.03)	5.58 (.23)	0.09 (.05)	0.34 (.09)	99.08 (.57)	84.8 (.4)
65-61-26[b]	4	49.72 (.74)	4.11 (.69)	0.61 (.02)	15.82 (.33)	20.85 (.08)	0.18 (.03)	4.96 (.16)	0.37 (.06)	0.64 (.03)	97.30 (.88)	85.1 (.7)
65-60-32[a]	5	49.74 (.87)	4.33 (1.04)	0.68 (.02)	14.76 (.61)	19.94 (.59)	0.22 (.01)	8.45 (.28)	0.96 (.21)	0.20 (.08)	99.24 (.35)	75.7 (1)
65-60-32 rep[b]	*2*	*50.00 (.15)*	*4.13 (.40)*	*0.58 (.02)*	*14.69 (.23)*	*19.75 (.20)*	*0.26 (.01)*	*8.43 (.25)*	*0.89 (.04)*	*0.19 (.02)*	*98.94 (.04)*	*75.8 (.3)*
65-7-133[a]	5	51.70 (.53)	4.05 (.93)	0.55 (.09)	16.56 (.58)	20.46 (.76)	0.14 (.01)	4.83 (.31)	0.47 (.08)	0.84 (.21)	99.60 (.29)	85.9 (1.1)
65-7-133 rep[b]	*6*	*51.77 (.57)*	*2.99 (.11)*	*0.52 (.01)*	*16.83 (.27)*	*21.53 (.17)*	*0.15 (.01)*	*5.07 (.06)*	*0.41 (.06)*	*0.76 (.05)*	*100.04 (.76)*	*85.7 (.1)*
65-86-64[a]	5	51.50 (.66)	3.61 (.58)	0.62 (.04)	15.70 (.27)	20.50 (.38)	0.19 (.02)	6.79 (.19)	0.48 (.05)	0.28 (.03)	99.64 (.32)	80.5 (.6)
65-86-64 rep[b]	*4*	*51.21 (1.19)*	*4.24 (.85)*	*0.61(.04)*	*14.72 (1.26)*	*20.61 (.39)*	*0.23 (.06)*	*7.16 (.19)*	*0.53 (.06)*	*0.21 (.06)*	*99.54 (1.60)*	*78.7 (1.5)*
83Kap-8[a]	4	51.39 (.50)	3.69 (.79)	0.55 (.03)	15.93 (.29)	20.78 (.16)	0.16 (.01)	5.25 (.16)	0.30 (.07)	0.46 (.18)	98.5 (.53)	84.4 (.6)
83Kap-8 rep[b]	*2*	*52.75 (.36)*	*2.94 (.01)*	*0.49 (.03)*	*16.74 (.17)*	*21.00 (.36)*	*0.18 (.04)*	*5.52 (.12)*	*0.21 (.01)*	*0.70 (.00)*	*100.57 (.28)*	*84.5 (.2)*
83Kap-9[a]	6	51.63 (.38)	3.52 (.49)	0.52 (.02)	16.03 (.36)	20.91 (.25)	0.13 (.03)	4.84 (.19)	0.26 (.05)	0.69 (.08)	98.53 (.30)	85.5 (.7)
83-Kap-9 rep[b]	*3*	*51.55 (.23)*	*2.95 (.15)*	*0.49 (.00)*	*16.16 (.12)*	*20.97 (.36)*	*0.17 (.01)*	*5.44 (.07)*	*0.21 (.00)*	*0.71 (.03)*	*98.69 (.35)*	*84.2 (.2)*
87Kap-10[a]	9	50.13 (.80)	5.73 (.92)	0.35 (.02)	15.49 (.47)	21.58 (.19)	0.13 (.01)	5.52 (.18)	0.39 (.28)	0.14 (.08)	99.41 (.24)	83.3 (.9)
94Kap-7[a]	7	52.48 (.36)	2.51 (.32)	0.09 (.02)	16.75 (.22)	21.52 (.27)	0.12 (.01)	4.88 (.35)	0.18 (.13)	0.18 (.13)	98.71 (.27)	86.0 (1.0)
96Kap-7[a]	6	50.90 (.31)	3.89 (.59)	0.64 (.05)	15.48 (.33)	20.28 (.27)	0.19 (.03)	6.63 (.23)	0.55 (.09)	0.23 (.02)	98.78 (.60)	80.6 (.5)

88Kap-2[a]	15	50.62 (.88)	4.23 (.71)	0.64 (.06)	15.58 (.81)	20.56 (.67)	0.16 (.01)	6.24 (.33)	0.60 (.33)	0.38 (.04)	99.00 (.69)	81.6 (1.3)
87Kap-14[a]	5	51.22 (.94)	4.55 (.84)	0.61 (.03)	15.82 (.59)	21.50 (.24)	0.14 (.02)	4.96 (.28)	0.56 (.14)	0.70 (.06)	100.14 (.87)	85.0 (.9)
Group-2 Shield												
63Kap-15[b]	3	50.68 (.09)	2.49 (.06)	0.37 (.01)	15.12 (.08)	22.00 (.05)	0.19 (.02)	7.53 (.12)	0.95 (.03)	0.21 (.02)	99.55 (.26)	78.2 (.3)
65-115-10[b]	6	50.80 (.45)	3.21 (.35)	0.46 (.03)	15.39 (.15)	21.44 (.29)	0.21 (.03)	7.77 (.18)	1.02 (.13)	0.11 (.03)	100.42 (.87)	78.1 (.5)
65-60-17[b]	4	49.73 (.53)	5.69 (.19)	0.52 (.04)	15.27 (.20)	21.00 (.25)	0.14 (.03)	6.53 (.14)	0.70 (.25)	0.67 (.11)	100.31 (.72)	80.8 (.3)
84-1801-5[a]	4	50.42 (.42)	4.54 (.36)	0.64 (.09)	15.64 (1.04)	19.46 (1.12)	0.16 (.02)	7.45 (.20)	0.70 (.08)	0.45 (.04)	99.42 (.22)	78.9 (.8)
87Kap-11[a]	5	51.06 (.83)	4.85 (.51)	0.83 (.04)	15.34 (.36)	21.10 (.43)	0.15 (.01)	5.75 (.12)	0.69 (.22)	0.62 (.11)	100.40 (.91)	82.6 (.6)
92Kap-1[a]	5	51.25 (.41)	4.33 (.29)	0.58 (.03)	16.06 (.17)	20.85 (.37)	0.10 (.01)	4.20 (.21)	0.25 (.04)	1.05 (.14)	98.67 (.29)	87.2 (.6)
92Kap-3[a]	5	50.02 (.98)	4.99 (1.12)	0.74 (.06)	15.31 (.36)	19.74 (.31)	0.14 (.03)	5.81 (.32)	0.70 (.29)	0.91 (.29)	98.36 (.28)	82.4 (1.1)
Group-3 Post-shield												
63Kap-7[a]	8	49.93 (.26)	5.75 (.17)	0.61 (.03)	15.18 (.13)	19.83 (.23)	0.16 (.01)	7.46 (.18)	1.05 (.07)	0.33 (.05)	100.26 (.41)	78.4 (.3)
63Kap-7 rep[b]	*3*	*48.49 (.28)*	*5.62 (.04)*	*0.54 (.04)*	*15.35 (.06)*	*19.18 (.03)*	*0.20 (.02)*	*7.62 (.11)*	*1.05 (.02)*	*0.31 (.02)*	*98.39 (.36)*	*78.4 (.3)*
65-86-92[a]	5	49.10 (.37)	6.34 (.18)	0.49 (.04)	14.82 (.19)	20.44 (.17)	0.14 (.01)	6.68 (.08)	0.95 (.18)	0.51 (.05)	99.46 (.21)	79.8 (.4)
65-86-92 rep[b]	*4*	*48.85 (.44)*	*5.54 (.23)*	*0.43 (.02)*	*15.24 (.15)*	*19.94 (.13)*	*0.17 (.01)*	*6.90 (.09)*	*0.82 (.04)*	*0.53 (.03)*	*98.46 (.39)*	*79.9 (.3)*
65-109-146abc[b]	2	49.44 (.39)	5.84 (.42)	0.49 (.01)	15.11 (.30)	20.88 (.03)	0.19 (.02)	7.40 (.12)	1.02 (.06)	0.66 (.06)	101.02 (.05)	78.6 (.6)
65-100-110[b]	2	48.84 (.49)	4.73 (.29)	0.55 (.05)	15.14 (.29)	21.11 (.05)	0.16 (.02)	7.34 (.03)	1.26 (.15)	0.49 (.03)	99.66 (.45)	78.8 (.3)
65-60-221[a]	6	49.70 (.30)	3.88 (.23)	0.57 (.01)	14.68 (.15)	21.40 (.28)	0.24 (.03)	7.70 (.14)	1.32 (.18)	0.02 (.01)	99.47 (.26)	77.3 (.4)
65-60-221 rep[b]	*3*	*49.53 (.47)*	*4.09 (.20)*	*0.53 (.02)*	*14.43 (.21)*	*21.16 (.12)*	*0.27 (.01)*	*7.73 (.07)*	*1.19 (.02)*	*0.11 (.02)*	*99.04 (.63)*	*77.1 (.4)*

Table S1.1: Clinopyroxene major element compositions (wt. %).

[a]Analyses performed at USGS. [b]Analyses preformed at UT Austin. Major element contents reported are average of multiple analyses. N indicates numbers of measurements for given sample. Digits in brackets after concentrations are 1 s.d. of the mineral population for each sample.

Sample	n	SiO_2	Al_2O_3	Na_2O	MgO	CaO	MnO	FeO	TiO_2	Cr_2O_3	Total	Mg#
Group-1 MORB												
65Kap-14d[a]	2	53.95 (.35)	3.24 (.23)	0.05 (.02)	29.15 (.35)	1.29 (.21)	0.22 (.02)	11.30 (.71)	0.16 (.01)	0.09 (.01)	99.40 (.71)	82.1 (1.1)
65Kap-14d rep[b]	*3*	*54.37 (.21)*	*3.22 (.14)*	*0.00 (.01)*	*31.11 (.12)*	*1.06 (.02)*	*0.19 (.02)*	*10.51 (.15)*	*0.07 (.01)*	*0.09 (.02)*	*100.69 (.36)*	*84.2 (.2)*
63Kap-13[a]	7	54.81 (1.03)	2.97 (.80)	0.05 (.01)	30.14 (.42)	1.09 (.13)	0.24 (.01)	10.63 (.24)	0.14 (.01)	0.39 (.04)	100.47 (.88)	83.5 (.5)
65Kap-13[a]	2	53.65 (.07)	3.84 (.08)	0.07 (.01)	30.05 (.07)	0.95 (.05)	0.23 (.01)	10.15 (.07)	0.17 (.02)	0.32 (.04)	99.40 (.14)	84.1 (.1)
65-60-32[a]	3	52.13 (.06)	3.29 (.10)	0.04 (.01)	26.43 (.15)	1.19 (.12)	0.33 (.02)	15.23 (.15)	0.35 (.02)	0.07 (.01)	99.03 (.04)	75.6 (.2)
65-60-32 rep[b]	*3*	*51.78 (.15)*	*3.54 (.06)*	*0.04 (.02)*	*26.54 (.09)*	*1.16 (.11)*	*0.38 (.02)*	*15.42 (.11)*	*0.33 (.02)*	*0.05 (.00)*	*99.25 (.36)*	*75.6 (.2)*
65-7-133[a]	3	53.83 (.35)	3.8 (.07)	0.07 (.02)	30.23 (.15)	1.01 (.06)	0.22 (.01)	9.80 (.06)	0.28 (.02)	0.35 (.02)	99.6 (.17)	84.6 (.0)
65-86-64[a]	3	53.97 (.49)	2.51 (.45)	0.04 (.01)	28.73 (.29)	1.08 (.07)	0.30 (.01)	12.80 (.17)	0.17 (.02)	0.18 (.02)	99.70 (.20)	80.0 (.4)
83Kap-8[a]	5	53.51 (.30)	3.19 (.53)	0.06 (.03)	29.50 (.16)	0.99 (.08)	0.24 (.01)	10.35 (.34)	0.13 (.04)	0.30 (.07)	98.28 (.61)	83.6 (.5)
83Kap-9[a]	6	53.74 (.51)	3.49 (.45)	0.07 (.04)	29.83 (.27)	1.00 (.10)	0.22 (.02)	9.90 (.08)	0.11 (.02)	0.39 (.04)	98.75 (.60)	84.3 (.1)
87Kap-10[a]	4	53.98 (.58)	3.45 (.76)	0.02 (.01)	30.13 (.45)	1.04 (.06)	0.21 (.01)	10.53 (.26)	0.10 (.01)	0.10 (.01)	99.50 (.24)	83.6 (.6)
94Kap-7[a]	5	55.08 (.23)	2.03 (.09)	0.02 (.02)	30.12 (.46)	1.26 (.35)	0.22 (.04)	9.81 (.72)	0.06 (.04)	0.15 (.06)	98.75 (.53)	84.6 (1.1)
96Kap-7[a]	6	53.35 (.23)	2.89 (.43)	0.04 (.01)	28.02 (.31)	1.10 (.08)	0.28 (.03)	12.87 (.30)	0.21 (.02)	0.13 (.01)	98.90 (.57)	79.5 (.4)
88Kap-2[a]	13	53.58 (.61)	3.11 (.35)	0.05 (.01)	29.10 (.34)	1.04 (.08)	0.26 (.02)	11.82 (.29)	0.17 (.04)	0.25 (.02)	99.39 (.80)	81.5 (.4)
87Kap-14[a]	5	54.72 (.37)	3.49 (.62)	0.04 (.01)	30.54 (.27)	1.00 (.08)	0.22 (.01)	9.85 (.23)	0.20 (.06)	0.36 (.05)	100.40 (.58)	84.7 (.4)
Group-2 Shield												
84-1801-5[a]	5	53.16 (.44)	3.40 (.32)	0.06 (.01)	28.16 (.35)	1.27 (.05)	0.25 (.01)	12.86 (.43)	0.27 (.02)	0.28 (.02)	99.68 (.22)	79.6 (.7)
84-1801-5 rep[b]	*3*	*53.43 (.41)*	*3.45 (.17)*	*0.07 (.05)*	*28.41 (1.09)*	*2.15 (1.62)*	*0.24 (.01)*	*12.10 (.49)*	*0.24 (.03)*	*0.26 (.05)*	*100.39 (.34)*	*80.9 (.2)*
87Kap-11[a]	5	54.42 (.15)	3.04 (.27)	0.05 (.00)	29.80 (.22)	1.07 (.05)	0.24 (.01)	10.72 (.22)	0.24 (.05)	0.33 (.04)	99.92 (.48)	83.2 (.4)
92Kap-1[a]	5	54.47 (.22)	3.26 (.25)	0.06 (.01)	30.92 (.16)	1.01 (.02)	0.18 (.01)	8.20 (.34)	0.09 (.02)	0.47 (.04)	98.65 (.23)	87.0 (.5)
92Kap-3[a]	6	53.99 (.53)	2.78 (.60)	0.11 (.02)	29.36 (.39)	1.85 (.62)	0.20 (.02)	9.84 (.74)	0.16 (.10)	0.60 (.18)	98.88 (.18)	84.2 (1.1)

Table S1.2: Orthopyroxene major element compositions (wt. %).

Sample	n	SiO_2	Al_2O_3	Na_2O	MgO	CaO	FeO	K_2O	Total	An
Group-1 MORB										
63Kap-3[b]	5	45.92 (.47)	34.14 (.19)	1.53 (.12)	0.08 (.01)	17.52 (.17)	0.33 (.05)	0.06 (.02)	99.58 (.41)	86.4 (1.0)
65Kap-14d[a]	4	43.68 (.15)	35.28 (.36)	0.42 (.05)	0.10 (.01)	19.70 (.16)	0.35 (.02)	0.00 (.01)	99.51 (.48)	96.3 (.4)
65Kap-14d rep[b]	*4*	*43.65 (.43)*	*34.97 (.39)*	*0.26 (.06)*	*1.07 (.13)*	*19.62 (.22)*	*0.44 (.06)*	*0.00 (.01)*	*100.01 (.74)*	*97.7 (.5)*
63Kap-13[a]	5	46.66 (.58)	33.62 (.33)	1.77 (.19)	0.11 (.02)	17.22 (.33)	0.30 (.03)	0.02 (.01)	99.69 (.32)	84.3 (1.7)
63Kap-13 rep[b]	*5*	*47.07 (.48)*	*33.97 (.21)*	*1.64 (.27)*	*0.26 (.23)*	*17.30 (.37)*	*0.37 (.05)*	*0.01 (.01)*	*100.62 (.41)*	*85.4 (2.2)*
65Kap-13[a]	5	48.02 (.08)	32.02 (.19)	2.43 (.05)	0.09 (.02)	15.86 (.15)	0.25 (.01)	0.04 (.02)	98.71 (.19)	78.2 (.5)
65Kap-13 rep[b]	*8*	*48.64 (.62)*	*32.81 (.29)*	*2.61 (.16)*	*0.10 (.02)*	*15.70 (.29)*	*0.25 (.04)*	*0.02 (.01)*	*100.12 (.38)*	*76.9 (1.3)*
65Kap-14a[b]	5	43.77 (.34)	35.65 (.43)	0.25 (.05)	0.66 (.26)	19.67 (.04)	0.46 (.10)	0.00 (.01)	100.47 (.38)	97.7 (.5)
65-61-26[b]	8	48.11 (.49)	33.07 (.24)	2.29 (.20)	0.14 (.09)	15.84 (.19)	0.29 (.07)	0.14 (.09)	99.89 (.44)	79.3 (1.6)
65-60-32[a]	7	51.79 (.68)	30.50 (.43)	4.45 (.18)	0.07 (.02)	12.94 (.36)	0.37 (.04)	0.08 (.01)	100.19 (.77)	61.7 (1.6)
65-7-133[a]	5	47.62 (.30)	33.18 (.26)	2.13 (.03)	0.10 (.02)	16.32 (.08)	0.28 (.03)	0.04 (.01)	99.68 (.57)	80.9 (.3)
65-7-133 rep[b]	*7*	*48.08 (.47)*	*32.98 (.49)*	*2.40 (.18)*	*0.12 (.05)*	*15.96 (.45)*	*0.28 (.04)*	*0.05 (.01)*	*99.86 (.52)*	*78.6 (1.6)*
65-86-64[a]	6	51.40 (.45)	31.38 (.27)	3.85 (.16)	0.08 (.02)	13.85 (.32)	0.31 (.02)	0.05 (.01)	100.92 (.31)	66.6 (1.4)
65-86-64 rep[b]	*3*	*51.23 (.51)*	*30.77 (.13)*	*3.86 (.11)*	*0.05 (.07)*	*13.30 (.09)*	*0.33 (.06)*	*0.28 (.02)*	*99.82 (.41)*	*65.6 (.5)*
83Kap-8[a]	9	47.16 (.68)	33.52 (.49)	1.80 (.35)	0.05 (.01)	16.71 (.56)	0.28 (.02)	0.05 (.01)	99.57 (.36)	83.7 (3.1)
83Kap-9[a]	8	47.24 (.24)	33.31 (.27)	1.86 (.09)	0.08 (.07)	16.67 (.14)	0.26 (.05)	0.05 (.02)	99.48 (.30)	83.2 (.7)
87Kap-10[a]	6	44.55 (.11)	34.95 (.28)	0.72 (.06)	0.09 (.02)	19.41 (.28)	0.29 (.02)	0.03 (.01)	100.04 (.56)	93.7 (.6)
94Kap-7[a]	9	43.86 (.21)	35.29 (.30)	0.38 (.06)	0.07 (.01)	19.23 (.15)	0.29 (.03)	0.03 (.03)	99.16 (.27)	96.6 (.5)
96Kap-7[a]	4	52.11 (.22)	29.92 (.37)	3.95 (.14)	0.06 (.02)	12.98 (.15)	0.31 (.00)	0.07 (.00)	99.39 (.33)	64.5 (1.0)
88Kap-2[a]	4	50.56 (1.98)	30.93 (1.43)	3.29 (.80)	0.10 (.01)	14.01 (1.41)	0.33 (.02)	0.14 (1.41)	99.37 (.15)	70.2 (7.2)
87Kap-14[a]	14	47.48 (.71)	33.04 (.36)	2.26 (.27)	0.08 (.02)	16.83 (.40)	0.28 (.02)	0.03 (.01)	100.00 (.72)	80.5 (2.2)
Group-2 Shield										
63Kap-15[a]	4	52.50 (.16)	29.70 (.26)	4.33 (.03)	0.06 (.01)	12.60 (.00)	0.34 (.02)	0.18 (.00)	99.69 (.24)	61.7 (.2)
63Kap-15 rep[b]	*6*	*52.80 (.30)*	*29.95 (.19)*	*4.34 (.14)*	*0.05 (.02)*	*12.50 (.05)*	*0.34 (.05)*	*0.19 (.02)*	*100.18 (.05)*	*61.4 (.7)*
65-115-10[b]	9	50.46 (.48)	31.43 (.52)	3.18 (.30)	0.10 (.04)	14.36 (.39)	0.70 (.30)	0.24 (.04)	100.47 (.32)	70.4 (2.5)

84-1801-5[a]	6	51.17 (1.04)	31.00 (.61)	3.61 (.41)	0.14 (.02)	13.80 (.70)	0.29 (.04)	0.18 (.05)	100.19 (.33)	67.9 (3.6)
87Kap-11[a]	6	51.51 (2.03)	30.16 (1.17)	3.97 (.83)	0.07 (.01)	13.58 (1.39)	0.25 (.02)	0.18 (.06)	99.72 (.57)	65.4 (7.0)
92Kap-1[a]	6	51.20 (1.41)	30.75 (.98)	3.26 (.56)	0.07 (.01)	13.60 (1.14)	0.24 (.03)	0.65 (.15)	99.77 (.08)	69.7 (5.4)
92Kap-3[a]	4	52.16 (.63)	29.99 (.40)	3.98 (.22)	0.07 (.01)	12.71 (.40)	0.29 (.02)	0.32 (.04)	99.51 (.20)	63.8 (2.0)
Group-3 Post-shield										
63Kap-7[a]	5	49.96 (.18)	31.22 (.13)	2.92 (.03)	0.11 (.01)	15.04 (.09)	0.45 (.05)	0.15 (.01)	99.84 (.19)	74.0 (.3)
63Kap-7 rep[b]	*5*	*49.67 (.25)*	*31.85 (.29)*	*2.97 (.04)*	*0.09 (.02)*	*14.73 (.14)*	*0.41 (.03)*	*0.13 (.02)*	*99.84 (.54)*	*73.3 (.2)*
65-86-92[a]	5	47.40 (.22)	32.88 (.18)	1.96 (.08)	0.12 (.01)	16.70 (.16)	0.46 (.02)	0.12 (.01)	99.63 (.35)	82.5 (.7)
65-86-92 rep[b]	*6*	*47.27 (.53)*	*33.36 (.11)*	*1.89 (.10)*	*0.14 (.04)*	*16.76 (.10)*	*0.44 (.06)*	*0.11 (.01)*	*99.97 (.62)*	*83.1 (.8)*
65-109-146abc[b]	4	47.75 (.28)	32.67 (.21)	2.31 (.24)	0.16 (.04)	15.72 (.20)	0.53 (.06)	0.14 (.02)	99.27 (.30)	79.0 (1.9)
65-60-221[a]	8	53.95 (.81)	29.20 (.64)	4.85 (.45)	0.07 (.01)	11.69 (.79)	0.42 (.02)	0.39 (.06)	100.56 (.44)	57.1 (3.9)
65-100-110[b]	7	51.31 (.58)	30.82 (.32)	3.59 (.25)	0.13 (.04)	13.52 (.34)	0.52 (.03)	0.28 (.03)	100.17 (.35)	67.5 (2.0)

Table S1.3: Plagioclase major element compositions (wt. %).

Sample	La	Ce	Pb	Sr	Nd	Sm	Zr	Hf	Eu	Gd	Dy	Y	Er	Yb
Group-1 MORB														
63Kap-3	0.03	0.24	0.007	3.51	0.46	0.28	1.8	0.08	0.14	0.57	1.09	5.96	0.71	0.74
65Kap-14d	0.01	0.07	0.0001	2.1	0.09	0.07	0.42	0.01	0.02	0.16	0.42	2.78	0.4	0.54
63Kap-13	0.11	0.67	0.004	3.75	1.18	0.59	7.56	0.25	0.24	1.12	1.61	8.84	1.05	1.11
65Kap-13	0.21	1.31	0.009	5.75	1.88	0.95	9.52	0.3	0.39	1.39	1.92	10.1	1.16	1.15
65Kap-14a	0.03	0.14	0.002	1.28	0.21	0.10	1.54	0.04	0.03	0.28	0.66	4.62	0.6	0.76
65-61-26	1.00	4.21	0.07	7.10	4.19	1.48	22.5	0.64	0.56	1.88	2.33	11.27	1.40	1.29
65-60-32	0.46	2.81	0.02	8.05	4.09	1.99	18.9	0.68	0.85	2.95	3.88	21.1	2.41	2.36
65-7-133	0.26	1.41	0.009	5.32	2.13	1.04	13.8	0.35	0.37	1.62	2.28	12.4	1.4	1.38
65-86-64	0.50	2.33	0.05	7.12	2.63	1.20	6.14	0.32	0.55	1.82	2.41	12.90	1.45	1.31
83Kap-8	0.12	0.64	0.01	4.56	0.93	0.49	3.64	0.15	0.21	0.79	1.21	6.64	0.78	0.78
83Kap-9	0.06	0.41	0.002	3.64	0.71	0.43	3.01	0.12	0.18	0.70	1.12	6.12	0.73	0.78
94Kap-7	0.01	0.09	0.009	1.39	0.14	0.10	0.74	0.04	0.04	0.26	0.66	4.54	0.56	0.71
96Kap-7	0.09	0.66	0.008	6.52	1.50	0.92	4.16	0.28	0.38	1.55	2.23	11.25	1.28	1.20
88Kap-2	0.23	1.07	0.003	6.28	1.51	0.83	3.47	0.21	0.41	1.40	1.94	10.12	1.17	1.08
87Kap-14	0.11	0.63	0.05	5.12	1.07	0.59	3.81	0.16	0.24	0.90	1.32	7.39	0.82	0.85
Group-2 Shield														
63Kap-15	1.21	5.94	0.04	25.00	8.67	3.61	32.60	1.24	1.10	4.63	4.69	20.40	2.17	1.53
65-115-10	2.20	9.51	0.09	36.40	8.76	2.85	30.80	0.99	0.94	3.17	3.15	14.00	1.58	1.28
65-60-17	1.26	4.58	0.08	36.72	4.56	1.56	16.73	0.67	0.60	1.85	2.02	9.03	0.95	0.72
87Kap-11	0.89	3.83	0.01	19.09	3.34	1.18	7.67	0.28	0.48	1.37	1.70	8.06	0.86	0.71
Group-3 Post-shield														
63Kap-7	1.01	4.39	0.01	41.20	5.18	1.95	16.90	0.79	0.76	2.47	2.48	11.40	1.15	0.89
65-86-92	1.16	4.81	0.08	37.20	5.18	1.83	20.90	0.90	0.67	2.18	2.19	9.98	1.09	0.87
65-109-146abc	1.50	5.92	0.03	45.80	6.35	2.33	25.90	1.24	0.82	2.83	2.83	12.40	1.32	1.04
65-100-110	1.91	7.32	0.04	46.50	8.29	2.98	33.60	1.60	1.04	3.42	3.46	15.10	1.63	1.28

Table S1.4: Clinopyroxene trace element concentrations (ppm).

Sample	T_{BNK} (°C)	*Sample*	T_{BNK} (°C)
Group-1 MORB		***Group-2 Shield***	
65Kap-14d	1065	83Kap-7	1075
63Kap-13	971	84-1801-5	1030
65Kap-13	988	87Kap-11	942
65-60-32	975	92Kap-1	1006
65-7-133	955	92Kap-3	1041
65-86-64	983	94Kap-14	1033
83Kap-8	1014	65-68-46	991
83Kap-9	982	65Kap-4	957
87Kap-10	954	82-1800-32	922
94Kap-7	997	82-1800-29	962
96Kap-7	974	65-7-195	1003
88Kap-2	971	83Kap-2	1029
87Kap-14	1022	94Kap-3	954

Table S1.5: Equilibrium temperatures.

Equilibrium temperature calculated using two-pyroxene geothermometer (Brey&Kohler, 1990).

Sample	*Clinopyroxene*		*Plagioclase*	
	$\delta^{18}O$ - 1	$\delta^{18}O$ - 2	$\delta^{18}O$ - 1	$\delta^{18}O$ – 2
Group-1 MORB				
63Kap-3	5.02	5.24	5.65	5.65
65Kap-14d	5.27		5.67	5.58
63Kap-13	5.10	4.99	5.79	5.95
65Kap-13	5.41	5.20	5.79	6.11
65Kap-14a	5.25	5.34	5.76	5.71
65-61-26	4.93		5.65	5.86
65-60-32	5.75		6.02	6.38
65-7-133	5.11		5.76	5.81
65-86-64	5.23	5.05	5.56	5.73
83Kap-8			5.34	5.35
83Kap-9			5.61	5.88
87Kap-10			5.69	5.67
94Kap-7			5.53	5.81
96Kap-7			6.06	5.61
88Kap-2			5.93	5.59
87Kap-14			5.71	5.91
Group-2 Shield				
63Kap-15			5.07	5.34
65-115-10			5.74	5.59
65-60-17	5.47	5.34	6.45	6.21
87Kap-11	4.92			
92Kap-1			6.06	
92Kap-3	5.25			
Group-3 Post-shield				
63Kap-7	5.56		6.02	6.17
65-86-92	5.43		6.03	6.01
65-109-146abc	5.23		6.02	6.17

Table S1.6: Oxygen isotope duplicate measurements.

	La	Ce	Nd	Sm	Eu	Gd	Dy	Er	Yb
K_d	0.05	0.11	0.20	0.27	0.31	0.33	0.36	0.36	0.35

Table S1.7: K_d value used for melt composition calculation.

SiO_2	Al_2O_3	Fe_2O_3	FeO	MgO	CaO	Na_2O	K_2O	TiO_2	MnO	H_2O	CO_2	Total	Mg#
47.90	10.40	1.30	10.44	16.50	8.23	1.64	0.22	1.52	0.18	0.50	0.01	98.87	73.8

Table S1.8: Start melt composition for MELTS models (wt. %).

Ridge	Latitude Range	Longitude Range	Spreading Rate (cm/yr)	# of Data Points	# of bins
Chile Rise	36.839° S – 46.0405° S	75.8967° W – 97.1675° W	7.4	23	7
EPR	31.377° S – 49.733° S	109.232° W – 113.783° W	18.3	33	14
EPR	2.5° S - 20.5965° S	103.017° W – 114.035° W	17.2	63	24
EPR	6.225° N – 27.253° N	102.525° W – 113.712° W	11.7	388	65
Juan de Fuca	40.38° N – 50.89° N	127.98° W – 130.55° W	6	73	19
SE Indian Ridge	41.098° S – 50.3475° S	86.23° E – 118° E	7.2	71	33
C. India Ridge	1.32° S – 24.98° S	62.47° E – 70.045° E	4	92	22
MAR	10.071° S – 30.98° S	13.198° W – 13.46° W	4	40	13
MAR	0.037° E – 13.9025° E	24.872° W – 45.0305 W	2.5	82	9
MAR	14.085° E – 35.9447° E	34.1667° W – 45.0207° W	3	262	70

Table S1.9: Summary of ridge segments compiled for MORB Nd isotopic heterogeneity evaluation.

APPENDIX A2: SUPPLEMENTARY FILE FOR CHAPTER 2

Appendix A2.1 Figures

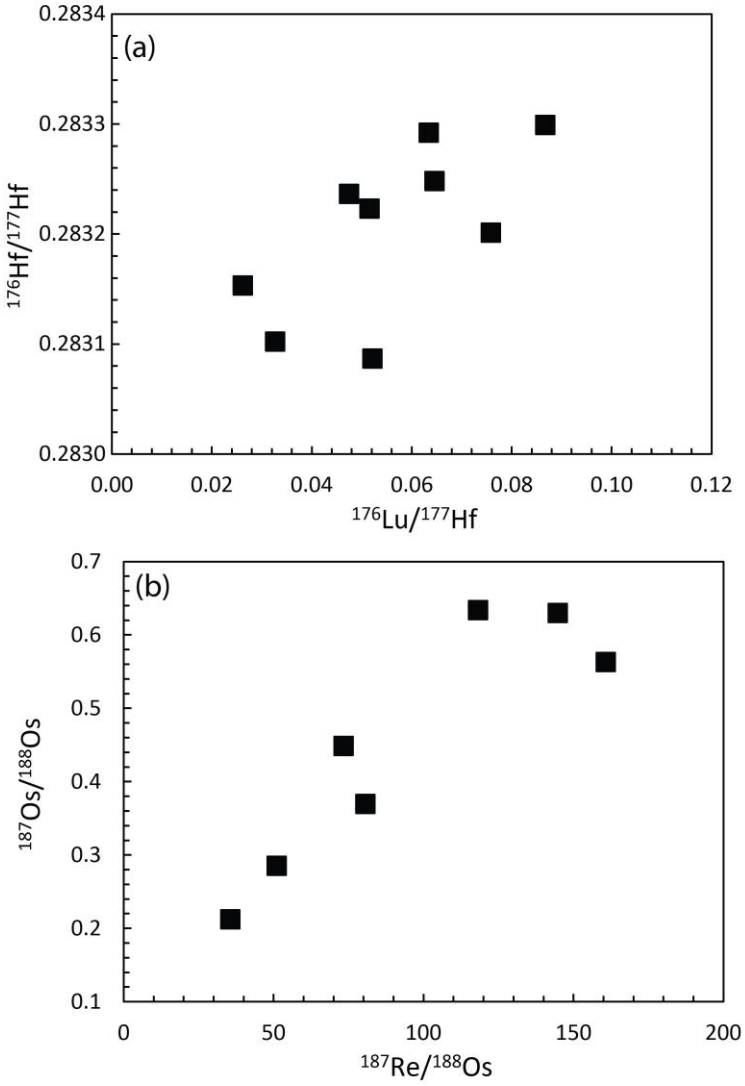

Figure S2.1: Correlations of parent-daughter isotopes in LOC gabbros.

(a) $^{176}Hf/^{177}Hf$ versus $^{176}Hf/^{177}Hf$. (b) $^{187}Re/^{188}Os$ versus $^{187}Os/^{188}Os$.

Appendix A2.2 Tables

	$^{206}Pb/^{204}Pb$	$^{207}Pb/^{204}Pb$	$^{208}Pb/^{204}Pb$
63kap-3	18.115	15.500	37.788
63kap-13	18.408	15.522	37.958
65kap-13	18.249	15.512	37.867
83kap-8	18.194	15.480	37.869
94kap-7*	*18.355*	*15.597*	*38.039*
96kap-7*	*18.202*	*15.545*	*37.952*
65kap-14a	17.932	15.551	37.742
65kap-14d	18.625	15.605	38.217
83kap-9	18.446	15.583	38.077
63kap-15	18.414	15.478	37.923
63kap-7	18.443	15.591	38.092
65-100-110	18.489	15.568	38.139

Table S2.1: Pb isotope compositions of leachates.

*Standard corrected Pb isotope data.

APPENDIX A3: SUPPLEMENTARY FILE FOR CHAPTER 3

Appendix A3.1 Methods

A3.1.1 Whole rock major and trace elements

Major and trace elements were analyzed on fresh whole rock samples using standard XRF and solution ICP-MS techniques at Washington State University. Duplicate measurements of major elements by XRF are reproducible within 1% (1 s.d.). Trace elements measured by ICP-MS are reproducible within 3% (1 s.d.). The secondary standard BHVO-2 is accurate within 1% for major elements, within 5% for most trace elements except Nb, Hf, Rb (10%) and Tb, Ta (15%).

A3.1.2 Mineral major and trace elements

Olivine and clinopyroxene major element abundances were measured by EMPA on a JEOL-8200 microprobe at the University of Texas at Austin (UT Austin) using methods outlined in Gao et al. (2016). Fresh samples were crushed, and olivine and clinopyroxene grains with no visible alteration were handpicked under a binocular microscope and mounted in epoxy. A focused beam was used for olivine analyses, whereas a defocused beam (10μm) was used for cpx to reduce Na migration. Initial analyses demonstrated only minor core-rim variations [e.g. within-grain variation in Mg# ($100*Mg/(Mg+Fe^{2+})$) < 1]. Therefore, only core analyses were performed for remaining grains. Measurements of secondary standards were accurate to within 5% for Na, Ni and Cr, within 3% for Al, Si and Fe, within 1% for Mg and Ca, and 18% for MnO. Duplicates are reproducible within 5% (1 s.d.) for Fe and Al, within 2% for Na, Cr, Ca, Mg, Mn and Ni, within 1% for Si, and 10% for MnO.

Clinopyroxene trace element concentrations were measured via an Agilent 7500ce quadrupole with a New Wave UP-193FX laser system at UT Austin using methods outlined in Gao et al. (2016). BCR-2g was measured as a secondary standard, based on which all elements

are accurate to within 10% and reproducible within 5% (1 s.d.). Three spots were analyzed for most grains, and the average of the analyses from a single grain are reported in Table A6.

A3.1.3 Radiogenic and oxygen isotopes

For Sr, Nd, and Pb isotopes, ~100-150 mg cpx separates or ~20 mg phenocryst-free matrix chips were digested following the procedures outlined in Byerly & Lassiter (2012). AG1-X8, Sr-Spec and REE-spec/HDEHP resins were used to separate Pb, Sr and Nd, respectively. Sr, Nd, and Pb isotopes were analyzed on a TE Triton TIMS using methods outlined in Gao et al. (2016) and Byerly & Lassiter (2012). NBS 987, UT Ames Nd and NBS 981 standards were measured regularly during the course of this study. The average NBS 987 $^{87}Sr/^{86}Sr$ for the TIMS lab over the period during which analyses were performed was 0.710253±15 (2 s.d.), consistent with previously reported values (e.g., 0.710248±15; Thirlwall, 1991). The average $^{143}Nd/^{144}Nd$ of UT Ames Nd was 0.512072±10 (2 s.d.), comparable to previously reported values (e.g., 0.512069±14; Scher & Delaney, 2010). For Pb isotopes, instrumental mass fractionation was corrected using a Pb double spike. NBS 981 measured by the double spike method during the course of this study has average $^{206}Pb/^{204}Pb$=16.933±3, $^{207}Pb/^{204}Pb$=15.488±3, and $^{208}Pb/^{204}Pb$=36.688±11 (2 s.d.). For comparison, the values reported by Todt et al. (1996) are $^{206}Pb/^{204}Pb$=16.9356±7, $^{207}Pb/^{204}Pb$=15.4891±9, and $^{208}Pb/^{204}Pb$=36.7006±34 (2 s.d.). Total procedure blanks were less than 150 pg, 75 pg and 15 pg for Sr, Nd and Pb, respectively. No standard or blank correction was applied to the reported data.

Osmium concentrations and Os isotopes were measured on whole rock powders of 5 samples. Fresh samples were cut with a diamond saw, and then carefully polished with aluminum oxide sandpaper to remove any saw marks. Samples were rinsed with DI water and dried before being wrapped in plastic (to avoid contact with metal) and crushed by hammer.

Lava chips were then powdered in an alumina ball mill. Rhenium and osmium were separated from whole rock powders following the procedures of Byerly & Lassiter (2012). Osmium concentrations were measured via isotope dilution using a mixed ^{185}Re-^{190}Os spike. Osmium isotopes were measured with the TE Triton TIMS in negative ion mode. The UMD Os standard was measured regularly and the average measured ^{187}Os/^{188}Os was 0.11382±0.00003 (2 s.d.), consistent with the value (0.1137920±0.0000024) reported by Walker et al. (2005). Osmium blanks were ~0.3 pg/g.

Oxygen isotope compositions were measured on ~2 mg of olivine separates by laser fluorination following the methods of Sharp (1995) using a ThermoElectron MAT253 mass spectrometer. In-house quartz standard Lausanne-1 (δ^{18}O = 18.1‰), garnet standard UWG-2 (δ^{18}O = 5.8‰) (Valley et al., 1995), and olivine standard San Carlos (δ^{18}O = 5.2‰) were measured to ensure accuracy and precision. δ^{18}O values are reported relative to SMOW, where the δ^{18}O value of NBS-28 is +9.65‰. Precision based on replicates of the standards is ±0.1‰ (1 s.d.). All the isotope analyses described above were performed at UT Austin.

Appendix A3.2 MELTS modeling

The crystallization products of PC magma were modeled using MELTS (Ghiorso & Sack, 1995). The effects of initial melt composition, water content, oxygen fugacity, and crystallization style (fractional versus batch) on modeling results were evaluated by varying one parameter at a time compared to the set of parameters reported in the main text. When using 14PC-13 as the initial melt, the Mg# of the first clinopyroxene decrease more significantly with decreasing pressure, compared to using 14PC-2 as initial melt. As a result, there is no single pressure range where clinopyroxene with high Mg# and olivine with low Fo can be both formed (Fig. S4a). When 3 wt.% initial water content was used instead of 1.5 wt.% water, clinopyroxene

crystallization at relatively low pressures is further suppressed, and the MELTS modeling results suggest crystallization of PC phenocrysts and xenoliths at ~7-7.5 kbar (Fig. S4b). Batch crystallization of 14PC-2 with initial water content of 1.5 wt.% and oxygen fugacity of FMQ+1 suggests crystallization pressures of 5-7.5 kbar (Fig. S4c). Finally, when initial oxygen buffer was set at FMQ, MELTS modeling suggests crystallization of PC magmas at ~7.5-8 kbar (Fig. S4d). Therefore, although the fields of olivine and clinopyroxene compositions shift slightly with different input parameters, all MELTS models suggest significant olivine crystallization (with Fo extending to 73) only occurs at crustal depths (<8 kbar).

Appendix A3.3 Clinopyroxene-melt partition coefficients

Clinopyroxene-melt partition coefficients (K_d) are a function of melt composition, mineral composition, temperature and pressure. Therefore, choosing appropriate K_d values is important for modeling melting and crystallization processes. In general, K_d values for Sr increase and K_d values for HFSE decrease with increasing pressure. K_d values of most incompatible elements increase as temperature, melt Mg# and cpx Mg# decreases (e.g., Adam & Green, 2003; Bédard, 2014). K_d values of REE and HFSE also increase with increasing TiO_2 content in cpx (e.g., Adam & Green, 1994; Bédard, 2014).

Clinopyroxenes in PC lavas and ultramafic xenoliths span a range of compositions, which is consistent with progressive fractional crystallization (Mg# negatively correlates with TiO_2 contents). We assume that all PC phenocrysts and xenoliths were crystallized at relatively uniform pressures (5-7 kbar). MELTS modeling suggest that the majority of PC phenocrysts and ultramafic xenoliths crystallized at temperatures of 1090-1200°C (assuming 1.5 wt.% initial water content). The K_d values for high-Mg# cpx (88), which we estimate formed at ~1200 °C, were calculated using the BIGD program (Nielsen, 1992). The major element compositions of

PC sample 14PC-2 and of the most magnesian clinopyroxene were used as inputs to the BigD model. The composition of the youngest PC lava was assumed as melt composition, which has Mg# in chemical equilibrium with the high-Mg# cpx. Estimated K_d values for high-Mg# cpx calculated using BigD are largely consistent with published K_d values for cpx in equilibrium with alkali basalt (e.g., Zack & Brumm, 1998), as well as with experimentally determined partition coefficients for cpx crystallized at similar pressure and temperature (Adam & Green, 1994; Green et al., 2000; Adam & Green, 2003).

Estimation of partition coefficients for more evolved cpx (Mg# = 78) is subject to greater uncertainty because the composition of the melt from which these cpx grew is more uncertain. Equilibrium crystallization of the more evolved cpx (Mg# = 78) requires a parental melt Mg# ≈ 42. A possible parental melt composition was estimated by calculating effects of fractional crystallization of 14PC-2 using the MELTs program as described above. When using compositions of this evolved melt, BIGD gives unreasonably high K_d values, e.g., $K_d^{HREE} > 2$. However, experiments run at similar pressure (5 kbar), temperature (1070 °C), cpx (Mg# = 74, TiO_2 = 1.25) and melt compositions (Mg# = 44) suggests $K_d^{La} = 0.1$, $K_d^{ce} = 0.16$, $K_d^{Nd} = 0.29$, $K_d^{Dy} = 0.51$, $K_d^{Er} = 0.58$, and $K_d^{Yb} = 0.69$ (Mercer & Johnston, 2008). These partition coefficients were utilized for the low-Mg# cpx. For cpx with intermediate Mg# and estimated crystallization temperatures, we interpolated between the high-Mg# and low-Mg# K_d estimates. Estimated K_D values utilized in Figures 2 and 7 are reported in Table A7. Uncertainties in calculated K_d values may effect the exact position and slope of the calculated parental melt REE patterns shown in Figure 2. However, regardless of K_d value, the large variation in LREE abundance at roughly constant Mg# illustrated in Figure 7 requires cpx to crystallize from a range of melts variably enriched in LREE and LILE.

Appendix A3.4 Binary mixing model

In order to constrain the proportion of the sill component mixed with primitive melts in the erupted PC lavas, we modeled binary mixing of a primitive melt and an evolved melt. The primitive melt is assumed to have a composition similar to the least enriched PC lavas (MgO = 9.32, FeO = 7.14 assuming FeO/FeO_T = 0.85, [Ce] = 71 ppm). To estimate the major element composition of the evolved sill component, we used the MELTS model to estimate the composition melt generated by fractional crystallization, using a "primitive" melt (14PC-2) as the starting composition, using the same model parameters as above (P = 6 kbar, 1.5 wt.% H2O, initial oxygen fugacity = FMQ). The melt composition in equilibrium with cpx with Mg# = 73 (the most evolved cpx phenocryst measured) was used to estimate the composition of the sill component (MgO = 2.31, FeO = 7.37). The most enriched cpx observed has Ce concentration of ~54 ppm, and therefore is in equilibrium with a melt having Ce concentration of ~420 ppm (using a K_d = 0.13, corresponding to the Mg# of this particular cpx). Binary mixing of this evolved, enriched melt and the primitive melt can generate the observed correlation between melt Mg# and Ce concentration by mixing a maximum of ~20% of the sill component with the primitive melt (Fig. S5).

Although this mixing model can account for the large variations in incompatible trace element abundance and modest variations in Mg# observed in the PC lavas, our estimated evolved melt component has higher SiO_2 than the primitive melt, and therefore this model predicts that SiO_2 should decrease rather than increase during the course of eruption (as the ratio of sill melt/primitive melt decreases with time). In addition, the model does not explain the slightly higher CaO in the early (more contaminated) melts. This suggests either that the first melt pulse that ponded and fractionated within the crust initially had a lower SiO_2 content than the later pulse that triggered eruption, or that the process of assimilation caused SiO_2 to decrease

rather than increase. The coupled low SiO_2 and high CaO required of the sill component based on the temporal major element trends may indicate assimilation of high-Ca, low-Si skarn material rather than more typical lower crust.

Appendix A3.5 Figures

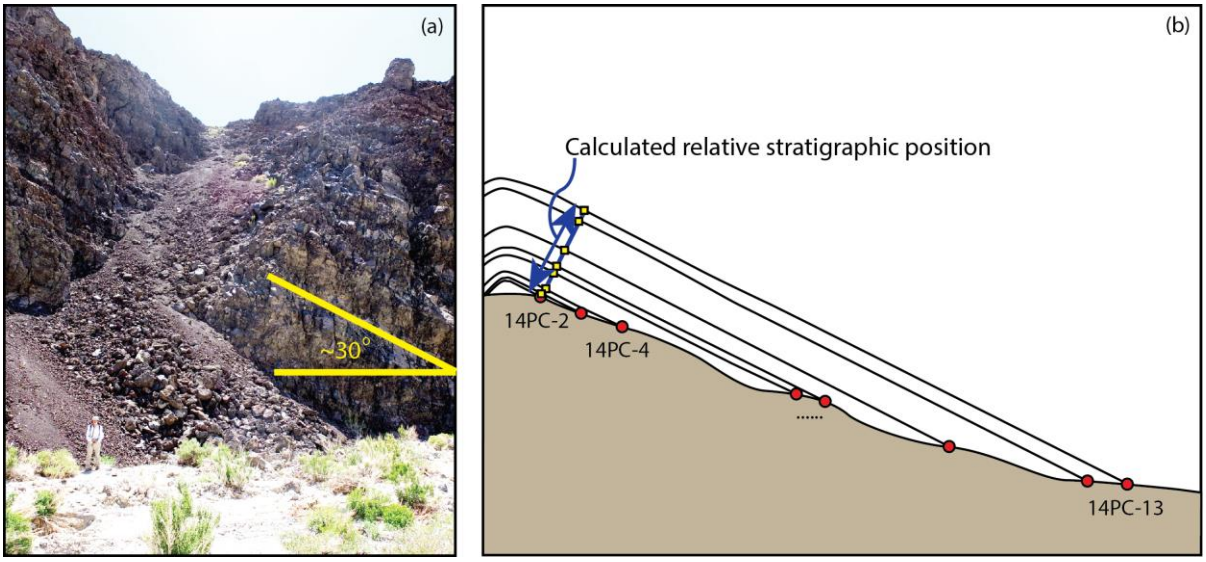

Figure S3.1: Sampling strategy.

(a) Stacked basaltic eruption sequence was cut and exposed at the Papoose Canyon. (b) Schematic diagram showing our sampling strategy. We walked down the canyon valley, and collected lava flow samples from earlier to later Papoose Canyon eruption sequence. The dipping angle of actual PC lava strata varies from ~30° in the earliest strata to shallower angle in later strata. We calculated the relative stratigraphic height of each sample assuming a uniform dipping angle of 30°, which is also the typical static angle of repose for scoria cone (Carrigy, 1970). Given the fact that the dipping angle of actual PC lava strata appear to be shallower in later strata, the calculated stratigraphic thickness may be slightly overestimated, but the relative stratigraphic positions are still robust. Calculated relative stratigraphic positions are reported in Table A1.

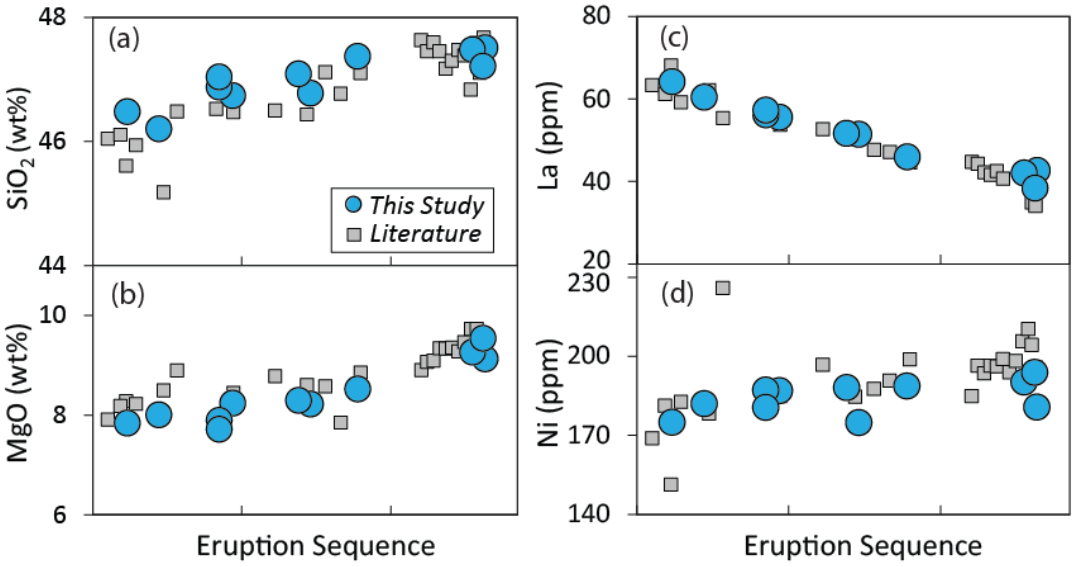

Figure S3.2: Temporal-compositional variations of major and trace elements.

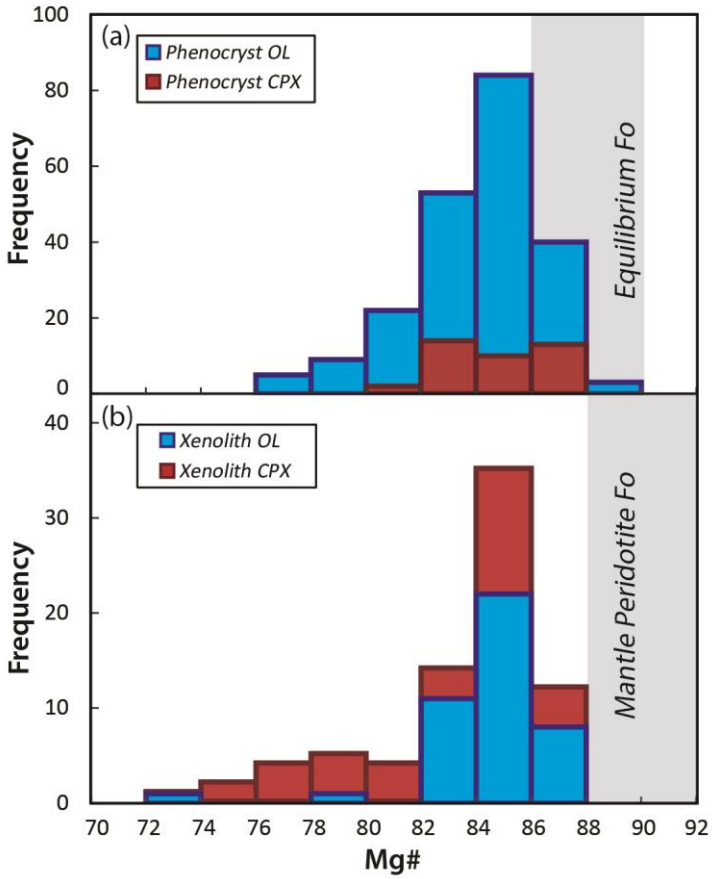

Figure S3.3: Distribution of mineral Mg#.

(a) Olivine and clinopyroxene phenocrysts in PC lavas span a wide range of Mg#, and are mostly out of equilibrium with their host lavas. (b) Olivine and clinopyroxene from PC ultramafic xenoliths span a similar range of Mg# as PC phenocrysts, which is lower than typical mantle peridotites.

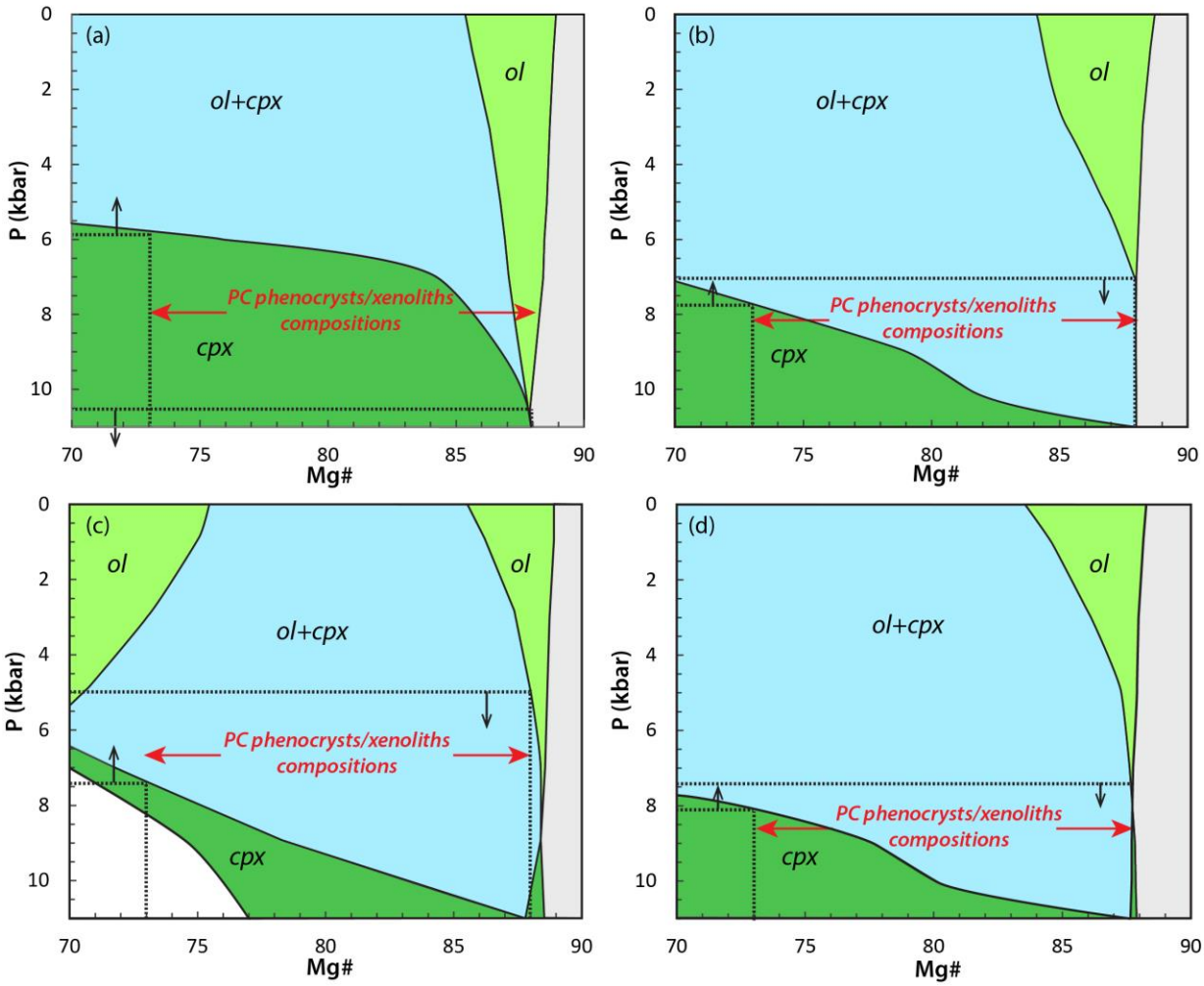

Figure S3.4: MELTS modeling results.

(a) Fractional crystallization of 14PC-13 with initial water content of 1.5 wt.% and FMQ+1 oxygen buffer. (b) Fractional crystallization of 14PC-2 with initial water content of 3.0 wt.% and FMQ+1 oxygen buffer. (c) Batch fractional crystallization of 14PC-2 with initial water content of 1.5 wt.% and FMQ+1 oxygen buffer. (d) Fractional crystallization of 14PC-2 with initial water content of 1.5 wt.% and FMQ oxygen buffer.

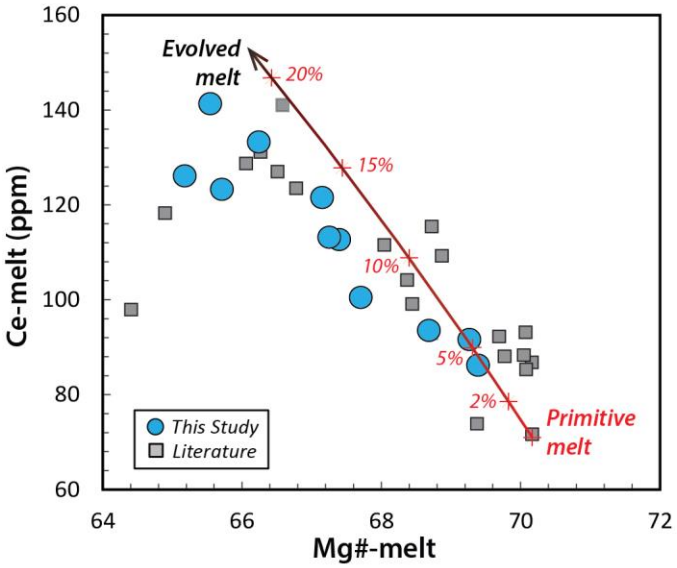

Figure S3.5: Binary mixing model.

Binary mixing model suggests that mixing up to ~20% evolved melt into primitive melt can produce the observed compositional variations in PC lavas. Mg# of the modeled melt is calculated from the MgO and FeO contents of mixed melt. Mg# of PC samples are melt Mg# calculated from whole rock composition by subtracting cumulate olivine.

Appendix A3.5 Tables

	N	W	ELE (m)	STRAT (m)		N	W	ELE (m)
PC-1	37.01492	118.1684	1588.3	204	14PCX-6	37.01515	118.1615	1652.0
PC-2	37.01512	118.1697	1563.0	242	14PCX-7	37.01515	118.1615	1652.0
PC-3	37.01545	118.1731	1521.0	364	14PCX-8	37.01515	118.1615	1652.0
14PC-2	37.01515	118.1636	1638.0	18	14PCX-9	37.01592	118.1619	1676.4
14PC-4	37.01526	118.1645	1617.0	46	14PCX-10	37.01592	118.1619	1676.4
14PC-5	37.01528	118.1664	1597.2	119	14PCX-11	37.01592	118.1619	1676.4
14PC-8A	37.01478	118.1690	1586.5	231	14PCX-12	37.01658	118.1619	1676.4
14PC-9	37.01549	118.1703	1589.0	295	14PCX-13	37.01522	118.1629	1639.5
14PC-12	37.01537	118.1728	1527.0	353	14PCX-15	37.01522	118.1629	1639.5
14PC-13	37.01547	118.1731	1521.0	362	14PCX-16	37.01518	118.1635	1635.3
14QC-2	37.01493	118.1680	1596.2	193	14PCX-17	37.01510	118.1635	1636.2
14PCX-5	37.01515	118.1615	1652.0		14PCX-18	37.01493	118.1680	1596.2

Table S3.1: Coordinates of samples.

ELE – elevation, STRAT – calculated relative stratigraphic position.

	14PC-4	14PC-5	14PC-8a	14PC-9	14PC-12	14PC-13
1-3.5mm (%)	4.1	3.8	3.4	2.2	0.9	0.6
<1mm (%)	0.7	2.8	1.6	3.9	1.8	1.2
Total (%)	4.8	6.5	4.0	6.1	2.7	1.8

Table S3.2: Olivine phenocryst point counting results.

	14PC-2	14PC-4	14PC-5	14PCX-9L	14QC-2	PC-1	PC-2	14PC-12	14PC-13	PC-3	BHVO-2
SiO_2	45.83	45.66	46.17	46.48	46.58	46.60	47.00	47.42	46.96	47.20	49.88
TiO_2	2.14	2.09	2.09	2.03	2.01	2.06	1.97	1.95	1.94	1.97	2.76
Al_2O_3	15.76	15.83	15.82	15.91	16.09	16.33	16.10	16.24	16.18	16.29	13.61
FeO*	9.11	9.05	9.07	8.97	8.87	8.80	8.87	8.80	8.94	8.83	11.18
MnO	0.15	0.15	0.15	0.15	0.15	0.15	0.15	0.15	0.15	0.15	0.17
MgO	9.46	9.62	9.39	9.78	9.57	9.52	9.55	9.62	9.73	9.34	7.30
CaO	9.92	10.21	9.79	10.05	9.65	9.95	9.66	9.62	9.76	9.69	11.42
Na_2O	3.72	3.72	3.75	3.81	3.95	3.94	3.74	3.83	3.82	3.59	2.23
K_2O	2.04	2.09	1.95	1.95	1.75	1.89	1.85	1.68	1.40	1.68	0.52
P_2O_5	1.10	1.02	0.94	0.93	0.86	0.89	0.77	0.71	0.69	0.73	0.26
Sum	99.23	99.44	99.12	100.05	99.47	100.13	99.67	100.03	99.58	99.47	99.32
LOI (%)	0.19	0.44	0.25	0.28	0.02	-0.17	-0.19	0.16	0.54	-0.02	0.00
Cs	0.28	0.27	0.28	0.29	0.34	0.31	0.31	0.28	0.25	0.28	0.10
Rb	28.5	24.8	22.7	27.1	26.4	24.3	23.6	26.9	20.2	23.0	8.9
Ba	1329.7	1230.7	1117.8	1102.6	1038.2	1064.7	927.9	842.8	780.8	866.3	128.2
Th	4.3	4.1	3.8	3.9	3.7	3.7	3.3	3.1	2.7	3.0	1.24
U	1.2	1.1	1.1	1.1	1.1	1.1	0.9	0.8	0.8	0.9	0.42
Ta	1.4	1.3	1.3	1.3	1.3	1.3	1.1	1.2	1.1	1.1	1.17
Nb	22.4	21.4	20.9	20.9	20.7	21.1	18.6	17.8	16.9	18.1	16.8
La	64.1	60.4	56.1	55.5	51.6	51.4	45.9	42.0	38.3	42.6	15.3
Ce	141.3	133.3	123.3	121.6	113.2	112.7	100.5	91.6	86.2	93.5	36.9
Pb	7.9	7.2	6.6	7.1	6.4	6.8	6.0	5.4	5.3	5.6	1.6
Pr	18.4	17.2	16.0	15.7	14.5	14.6	13.1	11.9	11.2	12.2	5.26
Sr	1678.9	1591.7	1503.5	1457.8	1371.0	1398.9	1253.3	1143.3	1083.2	1180.3	395.9
Nd	71.8	68.0	63.6	61.5	57.8	57.8	51.9	47.9	45.0	49.0	24.1
Hf	5.9	5.6	5.6	5.7	5.8	5.9	5.5	5.2	5.1	5.4	4.4
Zr	271.7	263.8	263.6	266.3	268.2	271.6	258.2	247.1	238.2	252.0	166.2
Sm	12.5	11.8	11.4	10.9	10.4	10.2	9.5	8.9	8.5	9.0	6.4
Eu	3.5	3.3	3.2	3.1	3.0	3.0	2.8	2.6	2.5	2.7	2.2
Gd	8.9	8.5	8.4	8.0	8.0	7.9	7.6	7.1	7.0	7.3	6.4
Tb	1.2	1.2	1.2	1.1	1.1	1.1	1.1	1.0	1.0	1.1	1.0
Dy	6.5	6.5	6.3	6.3	6.4	6.3	6.1	5.9	6.0	6.0	5.7
Ho	1.2	1.2	1.2	1.2	1.2	1.2	1.2	1.2	1.1	1.2	1.1
Er	3.1	3.0	3.0	3.0	3.1	3.1	3.0	3.1	3.0	3.0	2.6
Tm	0.42	0.41	0.41	0.40	0.43	0.44	0.42	0.42	0.41	0.42	0.35
Y	30.1	29.8	29.7	29.5	30.5	30.4	29.9	29.2	28.7	29.4	25.6
Yb	2.5	2.5	2.5	2.5	2.6	2.6	2.6	2.6	2.6	2.6	1.9
Lu	0.37	0.37	0.38	0.37	0.40	0.42	0.39	0.39	0.38	0.40	0.28
Sc	22.4	23.5	24.0	23.1	23.8	24.3	25.8	25.5	25.7	26.0	31.9
Ni	174.8	181.9	187.2	186.9	187.8	174.7	188.6	190.1	193.8	180.6	115.0
Cr	237.0	260.0	268.2	250.7	264.1	267.5	273.4	287.2	299.1	280.3	280.3
V	188.4	189.7	183.9	186.3	187.8	189.5	188.4	186.7	176.7	190.6	312.5
Ga	15.4	15.7	14.5	16.2	15.4	16.5	15.4	16.5	17.2	16.4	20.8
Cu	44.2	39.2	52.1	40.1	34.0	45.9	48.2	52.7	42.5	35.1	126.9
Zn	74.1	74.5	71.5	72.6	70.6	93.2	72.8	69.5	70.3	73.1	99.3

Table S3.3: Major and trace element compositions of PC lavas.

Major element concentrations are in wt.%. Trace element concentrations are in ppm. The measured composition of secondary standard BHVO-2 is also reported.

	SiO2	FeO	MnO	MgO	NiO	CaO	Totals	Mg#		SiO2	FeO	MnO	MgO	NiO	CaO	Totals	Mg#
Phenocrysts									12PC-2-O13	40.27	14.63	0.22	46.45	0.24	0.08	101.88	85.1
PC-1-O1	39.41	16.70	0.22	45.10	0.30	0.09	101.82	82.9	12PC-2-O14	40.15	13.19	0.16	47.13	0.24	0.08	100.95	86.5
PC-1-O2	39.97	13.49	0.19	46.83	0.32	0.10	100.89	86.2	12PC-2-O15	39.04	19.58	0.30	41.83	0.26	0.11	101.11	79.4
PC-1-O3	38.95	20.59	0.35	40.32	0.10	0.11	100.42	77.9	12PC-2-O16	39.74	14.24	0.22	46.38	0.22	0.09	100.89	85.4
PC-1-O4	38.86	21.05	0.31	40.90	0.08	0.12	101.32	77.8	12PC-2-O17	39.94	12.91	0.20	46.97	0.19	0.09	100.31	86.8
PC-1-O5	40.12	16.20	0.23	44.59	0.26	0.08	101.49	83.2	12PC-2-O18	40.12	13.53	0.20	47.76	0.26	0.08	101.95	86.4
PC-1-O6	39.59	13.30	0.22	46.67	0.18	0.12	100.07	86.3	12PC-2-O19	39.07	18.69	0.30	42.58	0.15	0.09	100.88	80.4
PC-1-O7	39.79	14.04	0.24	45.81	0.27	0.11	100.26	85.4	12PC-2-O20	40.34	12.79	0.20	47.26	0.49	0.12	101.20	86.9
PC-1-O8	40.14	15.77	0.20	45.65	0.18	0.12	102.05	83.9	14PC-4-O1	40.09	14.38	0.21	46.71	0.25	0.08	101.71	85.4
PC-1-O9	40.11	16.14	0.23	46.10	0.25	0.09	102.92	83.7	14PC-4-O2	40.44	13.05	0.16	47.53	0.28	0.09	101.55	86.8
PC-1-O10	40.51	14.01	0.23	47.03	0.25	0.09	102.12	85.8	14PC-4-O3	39.77	17.68	0.32	44.22	0.20	0.15	102.34	81.8
PC-1-O11	40.13	16.16	0.19	45.15	0.26	0.07	101.97	83.4	14PC-4-O4	38.64	21.89	0.35	40.63	0.05	0.10	101.67	77.0
PC-1-O12	38.83	20.00	0.27	41.87	0.07	0.17	101.22	79.0	14PC-4-O5	40.46	14.20	0.19	46.93	0.26	0.08	102.12	85.6
PC-1-O13	40.48	14.55	0.17	45.88	0.25	0.09	101.43	85.0	14PC-4-O6	40.14	13.77	0.19	47.08	0.28	0.09	101.55	86.0
PC-1-O14	39.74	16.59	0.21	45.14	0.14	0.10	101.92	83.0	14PC-4-O7	40.45	13.79	0.18	47.11	0.22	0.08	101.82	86.0
PC-2-O1	39.70	14.14	0.22	46.15	0.25	0.12	100.58	85.4	14PC-4-O8	40.44	13.28	0.22	47.23	0.25	0.10	101.53	86.5
PC-2-O2	39.25	18.49	0.27	43.20	0.15	0.20	101.56	80.8	14PC-4-O9	39.14	20.98	0.48	41.81	0.19	0.16	102.76	78.2
PC-2-O3	39.44	15.85	0.23	45.18	0.30	0.12	101.13	83.7	14PC-4-O10	39.98	15.11	0.22	45.74	0.16	0.08	101.29	84.5
PC-2-O4	39.24	18.41	0.43	42.90	0.22	0.25	101.45	80.7	14PC-4-O11	40.00	14.83	0.21	45.92	0.18	0.09	101.23	84.8
PC-2-O5	39.70	15.07	0.27	45.48	0.28	0.21	101.02	84.5	14PC-4-O12	39.78	15.30	0.27	45.40	0.25	0.07	101.08	84.2
PC-2-O6	39.37	18.55	0.35	43.34	0.16	0.11	101.88	80.8	14PC-4-O13	39.85	15.98	0.26	45.94	0.24	0.09	102.36	83.8
PC-2-O7	40.00	15.14	0.22	46.06	0.28	0.10	101.80	84.6	14PC-5-O1	39.37	16.58	0.25	44.43	0.18	0.10	100.91	82.8
PC-2-O8	39.99	14.47	0.24	46.55	0.27	0.12	101.63	85.3	14PC-5-O2	39.41	15.51	0.21	45.76	0.25	0.10	101.25	84.2
PC-2-O9	39.93	14.23	0.19	46.42	0.29	0.10	101.16	85.5	14PC-5-O3	40.57	14.89	0.21	45.89	0.17	0.10	101.83	84.7
PC-2-O10	40.20	14.61	0.22	46.59	0.24	0.11	101.96	85.2	14PC-5-O4	39.99	14.88	0.23	46.12	0.21	0.08	101.51	84.8
PC-2-O11	39.02	15.36	0.23	45.01	0.31	0.08	100.00	84.1	14PC-5-O5	39.86	16.63	0.26	45.21	0.18	0.10	102.24	83.0
PC-2-O12	40.02	14.96	0.20	45.01	0.29	0.08	100.57	84.4	14PC-5-O6	39.57	16.63	0.21	44.82	0.17	0.11	101.51	82.9
PC-2-O13	39.80	13.50	0.22	45.64	0.20	0.10	99.46	85.9	14PC-5-O7	39.83	16.87	0.25	44.88	0.24	0.11	102.19	82.7
PC-2-O14	39.06	18.08	0.24	43.93	0.14	0.10	101.54	81.4	14PC-5-O8	39.73	15.29	0.21	45.73	0.22	0.09	101.28	84.3
PC-2-O15	39.04	19.59	0.31	41.16	0.18	0.07	100.34	79.1	14PC-5-O9	38.95	20.42	0.25	41.90	0.18	0.15	101.85	78.7
PC-2-O16	39.53	18.42	0.25	42.69	0.25	0.11	101.26	80.7	14PC-5-O10	39.91	16.40	0.25	44.87	0.27	0.10	101.81	83.1

PC-2-O17	39.56	13.69	0.20	45.48	0.25	0.08	99.26	85.7	14PC-5-O11	40.13	16.23	0.22	44.60	0.12	0.11	101.41	83.2
PC-2-O18	39.28	15.73	0.22	45.46	0.19	0.11	101.00	83.9	14PC-5-O12	40.01	15.00	0.20	46.20	0.27	0.09	101.76	84.7
PC-2-O19	40.22	15.03	0.22	46.87	0.29	0.09	102.72	84.9	14PC-5-O13	40.20	15.07	0.22	45.83	0.14	0.10	101.57	84.6
PC-2-O20	39.76	16.24	0.22	45.27	0.24	0.07	101.79	83.4	14PC-5-O14	39.33	16.58	0.25	45.12	0.23	0.12	101.63	83.0
PC-2-O21	39.85	15.58	0.22	45.22	0.19	0.11	101.18	83.9	14PC-5-O15	39.61	16.68	0.22	45.21	0.28	0.09	102.08	83.0
PC-2-O22	38.69	18.56	0.27	43.55	0.05	0.14	101.25	80.9	14PC-5-O16	38.89	20.39	0.28	42.17	0.08	0.14	101.95	78.8
PC-2-O23	39.36	16.84	0.28	44.33	0.27	0.04	101.13	82.6	14PC-5-O17	39.77	15.43	0.25	45.56	0.17	0.10	101.29	84.2
PC-2-O24	40.14	15.21	0.22	46.36	0.25	0.07	102.25	84.6	14PC-5-O18	39.63	16.94	0.28	45.25	0.19	0.11	102.39	82.8
PC-2-O25	39.95	13.56	0.21	47.46	0.28	0.08	101.54	86.3	14PC-5-O19	40.54	13.28	0.22	47.58	0.20	0.08	101.90	86.6
PC-2-O26	40.27	14.07	0.21	46.64	0.25	0.14	101.58	85.6	14PC-5-O20	39.88	14.35	0.23	46.78	0.24	0.09	101.56	85.4
PC-2-O27	39.95	14.99	0.24	46.05	0.29	0.09	101.62	84.7	14PC-12-O1	40.10	12.91	0.17	47.91	0.34	0.13	101.55	87.0
PC-2-O28	38.81	20.89	0.38	41.47	0.28	0.06	101.88	78.1	14PC-12-O2	39.53	15.75	0.25	44.96	0.19	0.09	100.77	83.7
PC-2-O29	39.70	14.70	0.21	46.25	0.18	0.09	101.12	85.0	14PC-12-O3	40.20	12.47	0.21	47.83	0.27	0.08	101.07	87.3
PC-2-O30	39.10	17.01	0.33	43.32	0.15	0.21	100.12	82.1	14PC-12-O4	39.02	17.95	0.28	43.20	0.11	0.13	100.69	81.2
PC-2-O31	40.72	11.99	0.20	48.77	0.35	0.22	102.24	88.0	14PC-12-O5	39.44	16.10	0.23	45.06	0.23	0.09	101.15	83.4
PC-2-O32	40.33	13.68	0.21	46.29	0.21	0.10	100.83	85.9	14PC-12-O6	39.45	15.88	0.25	44.99	0.18	0.11	100.85	83.6
PC-2-O33	40.18	15.87	0.24	45.47	0.25	0.10	102.12	83.8	14PC-12-O7	39.06	18.64	0.29	42.43	0.17	0.12	100.71	80.4
PC-2-O34	39.68	14.55	0.19	46.24	0.19	0.09	100.94	85.1	14PC-12-O8	39.99	14.52	0.23	45.87	0.27	0.10	100.98	85.0
PC-2-O35	39.75	14.43	0.25	46.27	0.24	0.09	101.01	85.2	14PC-12-O9	39.85	14.79	0.21	45.90	0.29	0.10	101.14	84.8
PC-2-O36	39.74	14.51	0.25	46.10	0.24	0.12	100.95	85.1	14PC-12-O10	39.75	13.60	0.18	46.69	0.25	0.09	100.57	86.1
PC-2-O37	39.24	17.45	0.26	44.37	0.16	0.09	101.56	82.1	14PC-12-O11	40.12	12.50	0.18	47.98	0.35	0.09	101.20	87.4
PC-2-O38	39.55	18.43	0.30	43.22	0.26	0.14	101.89	80.8	14PC-12-O12	39.80	16.01	0.22	45.14	0.25	0.10	101.52	83.5
PC-2-O39	40.78	12.68	0.20	47.94	0.23	0.22	102.04	87.2	14PC-12-O13	39.78	15.74	0.24	44.73	0.19	0.10	100.79	83.6
PC-2-O40	40.26	14.14	0.25	46.69	0.22	0.10	101.65	85.6	14PC-12-O14	38.72	16.02	0.21	44.29	0.17	0.09	99.51	83.3
PC-2-O41	39.31	12.56	0.20	47.24	0.22	0.09	99.64	87.1	14PC-12-O15	40.23	12.29	0.19	47.78	0.24	0.12	100.86	87.5
PC-2-O42	40.58	12.24	0.18	47.61	0.25	0.09	100.94	87.5	14PC-12-O16	39.02	18.69	0.28	43.17	0.16	0.12	101.44	80.6
PC-2-O43	39.70	12.30	0.16	47.26	0.27	0.12	99.81	87.4	14PC-12-O17	39.14	16.06	0.25	44.82	0.16	0.10	100.53	83.4
PC-2-O44	39.04	16.97	0.20	44.20	0.11	0.09	100.62	82.4	14PC-12-O18	39.99	12.40	0.18	47.70	0.23	0.10	100.60	87.4
PC-2-O45	40.48	14.77	0.24	45.91	0.30	0.08	101.78	84.8	14PC-12-O19	40.23	11.29	0.17	48.42	0.27	0.24	100.61	88.5
PC-2-O46	40.48	14.92	0.23	46.78	0.22	0.09	102.72	85.0	14PC-12-O20	39.77	15.01	0.21	45.92	0.27	0.09	101.27	84.6
PC-2-O47	39.21	17.69	0.31	43.87	0.22	0.15	101.44	81.7	14PC-12-O21	40.59	12.27	0.23	48.25	0.22	0.07	101.64	87.6
PC-2-O48	39.99	16.15	0.26	45.61	0.19	0.15	102.36	83.6	14PC-12-O22	39.45	18.28	0.28	43.36	0.13	0.12	101.63	81.0
PC-2-O49	40.21	16.32	0.22	45.89	0.17	0.11	102.92	83.5	14PC-12-O23	39.87	14.92	0.22	45.83	0.21	0.12	101.17	84.7

PC-2-O50	39.28	18.89	0.27	43.39	0.10	0.09	102.02	80.5	14PC-13-O1	40.30	14.41	0.22	46.89	0.22	0.09	102.14	85.4
PC-2-O51	39.83	12.89	0.20	48.19	0.30	0.11	101.52	87.1	14PC-13-O2	39.99	17.65	0.27	44.03	0.18	0.11	102.23	81.8
PC-2-O52	39.71	16.55	0.21	45.44	0.23	0.10	102.23	83.2	14PC-13-O3	40.31	15.57	0.25	46.46	0.29	0.09	102.97	84.3
PC-2-O53	39.55	16.89	0.24	44.90	0.15	0.10	101.83	82.7	14PC-13-O4	40.50	14.07	0.24	47.01	0.25	0.09	102.16	85.7
PC-2-O54	40.37	16.42	0.28	45.62	0.32	0.08	103.08	83.3	14PC-13-O5	40.03	13.97	0.20	46.86	0.25	0.10	101.40	85.8
PC-2-O55	39.92	13.83	0.27	47.02	0.29	0.22	101.55	86.0	14PC-13-O6	39.75	18.04	0.25	44.32	0.11	0.11	102.58	81.6
PC-3-O1	39.53	14.47	0.20	46.31	0.23	0.07	100.81	85.2	14PC-13-O7	40.25	14.20	0.24	46.82	0.22	0.08	101.81	85.6
PC-3-O2	38.83	17.02	0.25	44.48	0.23	0.16	100.98	82.5	14PC-13-O8	39.72	16.64	0.27	44.83	0.18	0.07	101.70	82.9
PC-3-O3	39.95	14.44	0.24	46.35	0.32	0.10	101.40	85.2	14PC-13-O9	40.12	15.32	0.20	45.72	0.31	0.09	101.76	84.3
PC-3-O4	39.86	14.07	0.25	46.57	0.29	0.13	101.17	85.6	14PC-13-O10	40.72	14.37	0.21	46.86	0.19	0.09	102.43	85.4
PC-3-O5	38.38	21.66	0.55	40.03	0.17	0.29	101.07	76.9	14PC-13-O11	40.54	14.14	0.23	47.13	0.27	0.10	102.41	85.7
PC-3-O6	39.90	14.29	0.22	46.16	0.28	0.11	100.97	85.3	14PC-13-O12	39.82	17.23	0.28	44.67	0.24	0.11	102.35	82.3
PC-3-O7	40.33	13.20	0.20	47.23	0.29	0.12	101.38	86.6	14PC-13-O13	40.67	14.35	0.21	47.09	0.22	0.09	102.62	85.5
PC-3-O8	39.83	13.01	0.21	46.60	0.24	0.19	100.08	86.6	14PC-13-O14	39.85	15.30	0.24	46.05	0.24	0.09	101.77	84.4
PC-3-O9	39.17	13.88	0.18	47.35	0.23	0.09	100.90	86.0	14PC-13-O15	39.58	17.92	0.29	43.62	0.19	0.11	101.71	81.4
PC-3-O10	38.76	12.78	0.18	46.92	0.25	0.09	98.99	86.9	14PC-13-O16	39.87	15.94	0.26	45.64	0.18	0.11	102.01	83.7
PC-3-O11	39.30	13.96	0.19	46.97	0.18	0.09	100.69	85.8	14PC-13-O17	40.38	14.00	0.20	46.87	0.30	0.09	101.83	85.8
PC-3-O12	40.14	13.00	0.19	46.93	0.23	0.09	100.57	86.7	14PC-13-O18	39.31	16.04	0.22	44.74	0.17	0.11	100.59	83.4
PC-3-O13	39.54	13.77	0.16	46.98	0.19	0.08	100.71	86.0	14PC-13-O19	40.16	14.96	0.22	46.45	0.26	0.10	102.15	84.8
PC-3-O14	40.01	14.26	0.17	47.39	0.27	0.08	102.17	85.7	14PC-13-O20	39.57	14.15	0.17	46.76	0.31	0.07	101.03	85.6
PC-3-O15	39.31	15.94	0.20	44.88	0.14	0.06	100.52	83.5									
PC-3-O16	39.75	15.61	0.22	45.80	0.24	0.11	101.74	84.1	***Xenoliths***								
PC-3-O17	39.44	16.46	0.26	44.83	0.22	0.11	101.32	83.1	14PCX-1-O1	39.84	13.05	0.21	46.80	0.28	0.12	100.30	86.6
PC-3-O18	39.23	17.19	0.37	43.57	0.15	0.10	100.61	82.0	14PCX-2-O1	37.42	16.13	0.22	45.30	0.16	0.10	99.34	83.5
PC-3-O19	39.49	15.99	0.27	45.12	0.26	0.15	101.27	83.6	14PCX-2-O2	37.32	16.44	0.23	45.26	0.12	0.10	99.48	83.2
PC-3-O20	39.67	13.78	0.16	46.53	0.29	0.09	100.52	85.9	14PCX-2-O3	37.85	16.26	0.21	45.35	0.22	0.10	99.99	83.4
PC-3-O21	39.29	13.04	0.18	47.11	0.29	0.12	100.02	86.7	14PCX-2-O4	38.04	16.01	0.23	45.36	0.12	0.08	99.84	83.6
PC-3-O22	39.74	11.91	0.18	47.46	0.25	0.10	99.64	87.8	14PCX-3-O1	37.86	15.56	0.23	45.71	0.23	0.08	99.66	84.1
PC-3-O23	39.63	14.38	0.17	46.82	0.20	0.09	101.28	85.4	14PCX-3-O2	37.42	15.85	0.23	45.66	0.23	0.09	99.48	83.8
PC-3-O24	39.38	13.70	0.26	46.26	0.22	0.08	99.90	85.9	14PCX-3-O3	37.66	15.65	0.22	45.32	0.21	0.10	99.16	83.9
PC-3-O25	39.85	16.60	0.30	44.27	0.17	0.06	101.26	82.8	14PCX-4-O1	37.75	15.98	0.22	45.32	0.10	0.11	99.49	83.6
PC-3-O26	39.56	13.84	0.26	46.50	0.27	0.17	100.60	85.8	14PCX-4-O2	37.77	15.78	0.26	46.20	0.17	0.09	100.27	84.1
PC-3-O27	39.23	13.65	0.22	46.48	0.28	0.08	99.94	86.0	14PCX-4-O3	38.27	16.05	0.24	45.21	0.13	0.10	100.01	83.5

PC-3-O28	39.47	15.23	0.23	45.97	0.17	0.10	101.18	84.5	14PCX-5-O1	39.79	14.25	0.19	46.15	0.24	0.10	100.71	85.4
PC-3-O29	39.68	14.25	0.22	46.55	0.32	0.13	101.15	85.5	14PCX-5-O2	39.62	14.46	0.22	45.40	0.20	0.08	99.98	85.0
PC-3-O30	40.22	17.39	0.25	44.50	0.22	0.10	102.68	82.2	14PCX-5-O3	39.83	14.20	0.21	45.88	0.18	0.09	100.39	85.3
PC-3-O31	38.90	17.16	0.26	44.40	0.15	0.10	100.97	82.3	14PCX-6-O1	37.55	15.09	0.23	45.97	0.11	0.08	99.02	84.6
PC-3-O32	39.34	17.75	0.29	44.43	0.23	0.07	102.12	81.8	14PCX-6-O2	37.54	15.35	0.22	45.64	0.18	0.07	99.00	84.3
PC-3-O33	39.87	15.24	0.21	46.07	0.20	0.10	101.71	84.5	14PCX-6-O3	37.89	14.94	0.21	45.76	0.22	0.10	99.12	84.6
PC-3-O34	39.90	13.10	0.18	47.74	0.25	0.07	101.23	86.8	14PCX-7-O1	38.19	14.92	0.22	45.83	0.19	0.08	99.44	84.7
PC-3-O35	40.49	14.35	0.22	46.92	0.29	0.09	102.36	85.5	14PCX-7-O2	38.69	15.29	0.20	45.51	0.17	0.08	99.94	84.3
PC-3-O36	40.70	14.97	0.18	46.63	0.18	0.09	102.75	84.9	14PCX-7-O3	38.82	14.46	0.19	46.37	0.20	0.09	100.13	85.2
PC-3-O37	40.04	17.89	0.24	44.67	0.16	0.09	103.09	81.8	14PCX-7-O4	37.76	14.34	0.19	46.01	0.18	0.10	98.58	85.2
PC-3-O38	40.65	14.61	0.26	47.20	0.25	0.09	103.06	85.3	14PCX-8-1-O1	38.53	14.69	0.20	46.36	0.21	0.10	100.09	85.0
PC-3-O39	39.96	13.53	0.19	47.26	0.23	0.09	101.27	86.3	14PCX-8-1-O2	38.54	14.58	0.21	46.16	0.22	0.07	99.78	85.1
PC-3-O40	39.86	15.88	0.21	46.02	0.21	0.07	102.25	83.9	14PCX-8-1-O3	37.47	14.42	0.20	45.86	0.14	0.08	98.17	85.1
PC-3-O41	40.15	13.99	0.18	47.76	0.17	0.09	102.34	86.0	14PCX-8-1-O4	38.92	14.41	0.22	46.30	0.13	0.09	100.06	85.3
PC-3-O42	40.51	15.19	0.23	46.52	0.23	0.09	102.78	84.6	14PCX-10-O1	38.13	13.36	0.20	47.63	0.23	0.10	99.66	86.5
PC-3-O43	38.66	21.36	0.27	41.24	0.08	0.16	101.77	77.7	14PCX-10-O2	38.87	13.48	0.19	47.60	0.21	0.10	100.45	86.4
PC-3-O44	39.28	20.45	0.42	41.89	0.13	0.15	102.32	78.7	14PCX-10-O3	38.59	13.09	0.18	47.91	0.20	0.10	100.07	86.8
PC-3-O45	40.17	14.05	0.22	47.41	0.33	0.08	102.26	85.9	14PCX-10-O4	38.53	13.26	0.20	47.63	0.24	0.10	99.96	86.6
PC-3-O46	39.90	13.70	0.19	47.45	0.28	0.09	101.61	86.2	14PCX-11	37.89	20.33	0.27	42.61	0.14	0.12	101.36	79.0
PC-3-O47	40.64	13.63	0.18	48.02	0.28	0.09	102.84	86.4	14PCX-13-1-O1	36.14	16.42	0.23	44.72	0.17	0.09	97.76	83.1
12PC-2-O1	40.51	13.27	0.19	47.54	0.31	0.10	101.93	86.6	14PCX-13-1-O2	37.81	16.55	0.22	45.45	0.20	0.08	100.32	83.2
12PC-2-O2	39.90	17.17	0.22	44.63	0.20	0.08	102.20	82.4	14PCX-13-2-O1	37.86	15.32	0.24	46.16	0.21	0.07	99.86	84.4
12PC-2-O3	38.90	18.63	0.26	42.99	0.14	0.10	101.03	80.6	14PCX-15-O1	37.94	15.21	0.24	46.15	0.24	0.09	99.86	84.5
12PC-2-O4	39.76	13.93	0.19	46.68	0.22	0.09	100.87	85.8	14PCX-15-O2	38.55	15.55	0.22	46.72	0.27	0.08	101.40	84.4
12PC-2-O5	39.60	15.04	0.21	45.96	0.20	0.10	101.12	84.6	14PCX-15-O3	37.97	15.38	0.23	46.35	0.26	0.09	100.30	84.4
12PC-2-O6	39.82	15.59	0.20	45.58	0.23	0.13	101.55	84.0	14PCX-15-O4	37.77	15.45	0.21	46.20	0.24	0.08	99.96	84.3
12PC-2-O7	40.40	10.91	0.16	49.36	0.23	0.09	101.16	89.1	14PCX-16-O1	34.93	24.45	0.42	38.11	0.04	0.12	98.07	73.7
12PC-2-O8	39.45	20.01	0.27	42.01	0.18	0.10	102.02	79.1	14PCX-17-O1	38.07	14.16	0.20	47.09	0.22	0.08	99.82	85.7
12PC-2-O9	39.79	15.48	0.23	45.73	0.23	0.08	101.54	84.2	14PCX-17-O2	38.69	13.22	0.20	47.64	0.16	0.07	99.99	86.6
12PC-2-O10	40.37	13.56	0.20	47.08	0.33	0.08	101.63	86.2	14PCX-17-O3	40.35	12.79	0.21	47.31	0.17	0.07	101.06	86.9
12PC-2-O11	39.29	18.98	0.28	42.58	0.16	0.10	101.39	80.2	14PCX-17-O4	40.17	13.78	0.22	46.76	0.19	0.09	101.37	85.9
12PC-2-O12	39.92	15.61	0.22	45.45	0.24	0.09	101.53	84.0	14PCX-17-O5	39.91	13.42	0.20	46.89	0.20	0.04	100.72	86.3

Table S3.4: Major element compositions of olivine (wt.%).

Olivine grains from individual samples are numbered in order. For example, PC-1-O1 stands for the first olivine grain from sample PC-1.

	SiO2	TiO2	Al2O3	FeO	Cr2O3	MnO	MgO	CaO	Na2O	Totals	Mg#		SiO2	TiO2	Al2O3	FeO	Cr2O3	MnO	MgO	CaO	Na2O	Totals	Mg#
Phenocrysts												14PCX-4-P4	51.46	0.69	5.57	5.76	0.83	0.14	17.52	17.69	1.07	100.77	84.6
PC-1-P1	50.10	0.73	7.23	4.55	0.73	0.16	15.28	20.57	1.02	100.38	85.8	14PCX-5-P1	49.51	0.75	6.89	4.67	0.70	0.12	15.55	19.96	0.82	99.08	85.7
PC-1-P2	49.98	0.70	6.78	4.52	0.79	0.12	15.70	18.53	0.77	97.89	86.2	14PCX-5-P2	50.83	0.68	6.49	4.76	0.60	0.14	15.91	19.89	0.99	100.27	85.8
PC-1-P3	50.22	0.56	6.80	5.07	0.83	0.11	19.38	16.16	0.67	99.79	87.3	14PCX-5-P3	50.21	0.70	6.33	4.75	0.61	0.16	15.66	19.98	0.85	99.30	85.6
PC-1-P4	50.54	0.65	6.92	4.49	0.87	0.10	17.14	18.09	0.68	99.48	87.3	14PCX-5-P4	49.93	0.82	6.69	4.46	0.72	0.13	15.21	20.65	0.91	99.60	86.0
PC-1-P5	51.72	0.59	5.50	4.88	0.94	0.15	16.07	20.24	0.82	100.96	85.6	14PCX-6-P1	49.66	0.97	7.55	5.93	0.44	0.15	15.13	20.16	0.85	100.84	82.1
PC-1-P6	51.58	0.35	5.79	6.21	0.17	0.19	14.64	21.11	1.00	101.03	80.9	14PCX-6-P2	49.86	0.80	7.26	6.14	0.28	0.12	15.68	19.87	0.72	100.75	82.1
PC-1-P7	51.44	0.45	5.45	5.69	0.13	0.16	14.54	19.74	0.96	98.55	82.1	14PCX-6-P3	49.51	1.01	7.66	4.90	0.63	0.12	15.20	19.69	0.77	99.48	84.8
PC-2-P1	52.31	0.56	5.39	5.18	0.76	0.15	15.24	21.59	1.00	102.21	84.1	14PCX-6-P4	48.92	0.90	7.63	4.99	0.50	0.15	15.13	19.69	0.96	98.87	84.5
PC-2-P2	51.99	0.39	5.05	5.44	0.63	0.16	15.00	21.52	0.94	101.13	83.2	14PCX-7-P1	50.38	0.72	6.50	5.79	0.34	0.14	15.91	19.97	0.74	100.51	83.2
PC-2-P3	51.83	0.49	5.12	5.27	0.96	0.16	15.09	21.26	1.04	101.20	83.8	14PCX-7-P2	50.17	0.77	6.92	5.67	0.38	0.13	15.74	19.97	0.85	100.61	83.3
PC-2-P4	50.81	0.54	6.45	5.79	0.50	0.17	14.55	20.96	1.07	100.87	81.9	14PCX-7-P3	50.32	0.63	6.25	5.15	0.34	0.11	16.04	19.60	0.78	99.29	84.9
PC-2-P5	51.71	0.54	5.48	5.48	0.70	0.16	14.94	21.29	0.94	101.23	83.1	14PCX-7-P4	49.96	0.72	6.70	4.81	0.29	0.13	15.49	19.24	0.80	98.22	85.3
PC-2-P6	51.69	0.52	5.14	5.01	0.67	0.13	15.29	21.39	0.91	100.75	84.6	14PCX-8-1-P1	49.92	0.65	6.99	5.18	0.73	0.13	15.81	19.55	0.61	99.54	84.6
PC-2-P7	53.44	0.36	4.68	6.36	0.55	0.19	18.45	16.97	0.84	101.90	83.9	14PCX-8-1-P2	49.03	0.99	7.21	4.57	0.86	0.11	15.41	20.26	0.87	99.28	85.9
PC-2-P8	52.78	0.44	5.32	5.45	0.72	0.18	15.12	21.41	0.98	102.38	83.3	14PCX-8-1-P3	49.61	0.73	7.25	5.22	0.50	0.12	15.68	20.02	0.71	99.86	84.4
PC-2-P9	52.40	0.51	5.67	6.66	1.03	0.15	16.66	18.66	0.81	102.58	81.8	14PCX-8-1-P4	49.86	0.68	6.23	5.41	1.01	0.13	15.62	19.77	0.99	99.76	83.9
PC-3-P1	49.85	0.48	5.64	5.48	0.48	0.17	15.10	20.89	0.97	99.05	83.2	14PCX-8-2-P1	47.62	1.74	8.06	7.78	0.02	0.14	15.24	17.70	0.86	99.18	77.9
PC-3-P2	51.46	0.31	4.57	5.13	0.69	0.13	15.62	20.99	0.96	99.86	84.6	14PCX-8-2-P2	46.86	1.91	9.00	7.45	0.01	0.16	13.89	18.88	0.98	99.13	77.0
PC-3-P3	51.46	0.45	5.16	5.49	0.55	0.15	15.49	21.12	0.97	100.84	83.5	14PCX-8-2-P3	47.47	1.79	8.74	6.84	0.01	0.17	14.01	18.63	1.06	98.66	78.7
PC-3-P4	51.33	0.53	5.12	5.36	0.90	0.16	15.25	21.32	0.83	100.81	83.7	14PCX-9-P1	51.36	0.73	6.07	4.80	0.24	0.13	16.45	19.95	0.76	100.52	86.0
PC-3-P5	51.20	0.34	4.61	5.54	0.52	0.18	15.35	20.84	0.95	99.53	83.3	14PCX-9-P2	51.54	0.68	5.71	5.48	0.25	0.12	17.00	18.83	0.89	100.55	84.8
PC-3-P6	51.74	0.53	5.54	5.33	0.49	0.17	14.95	21.16	0.95	100.87	83.5	14PCX-9-P3	50.64	0.85	6.09	5.25	0.28	0.12	15.90	19.89	0.84	99.89	84.5
PC-3-P7	50.97	0.57	5.48	4.70	0.56	0.17	14.84	21.28	0.90	99.46	85.0	14PCX-10-P1	50.37	0.60	5.64	4.13	1.15	0.14	16.56	19.62	0.80	99.04	87.8
PC-3-P8	51.85	0.44	4.99	6.38	0.55	0.19	18.59	17.54	0.68	101.22	84.0	14PCX-10-P2	50.44	0.47	5.20	4.29	1.29	0.10	16.19	19.77	1.07	98.84	87.2
PC-3-P9	50.40	0.56	5.18	5.00	0.71	0.11	15.01	21.56	0.88	99.42	84.4	14PCX-11-P1	48.50	1.52	8.34	6.90	0.04	0.16	14.43	18.41	1.02	99.28	79.0
PC-3-P10	51.35	0.37	4.94	5.33	0.42	0.16	15.35	21.01	0.93	99.86	83.8	14PCX-12-1-P1	50.82	0.59	5.93	4.95	0.53	0.14	16.22	19.84	1.23	100.27	85.5
PC-3-P11	50.54	0.53	4.89	5.29	0.36	0.09	15.22	21.14	0.85	98.92	83.8	14PCX-12-1-P2	51.29	0.54	8.91	4.53	0.53	0.13	13.25	18.87	1.44	99.50	84.1
14PC-4-P1	51.54	0.67	6.17	4.52	1.09	0.12	16.21	20.28	0.75	101.34	86.6	14PCX-12-2-P1	50.70	0.74	7.30	4.78	0.77	0.15	16.65	19.31	0.78	101.19	86.3
14PC-4-P2	49.92	1.00	8.61	4.75	0.59	0.14	14.66	20.72	0.93	101.35	84.8	14PCX-12-2-P2	49.55	0.87	8.21	4.77	0.76	0.12	14.89	20.17	0.90	100.28	84.9
14PC-4-P3	50.69	1.24	5.35	5.41	0.21	0.12	15.11	22.88	0.57	101.58	83.4	14PCX-12-2-P3	49.85	0.85	7.34	4.91	0.42	0.14	16.22	19.16	0.68	99.60	85.6
14PC-4-P4	50.20	0.76	7.22	4.61	0.75	0.09	15.85	20.35	0.74	100.60	86.1	14PCX-12-2-P4	50.24	0.78	7.12	5.02	0.87	0.13	15.73	19.09	1.02	100.06	84.9

14PC-4-P5	52.05	0.52	5.51	4.36	1.17	0.13	16.59	20.53	0.68	101.58	87.3	14PCX-13-1-P1	50.77	0.57	5.77	4.80	0.93	0.13	16.42	20.02	0.70	100.11	86.0
14PC-4-P6	51.09	0.77	6.87	4.55	1.02	0.12	16.47	19.93	0.69	101.51	86.7	14PCX-13-1-P2	51.68	0.45	4.92	4.24	0.86	0.14	15.82	20.89	0.90	99.98	87.0
14PC-4-P7	51.57	0.57	6.14	4.38	1.04	0.10	15.84	20.96	0.75	101.37	86.7	14PCX-13-1-P3	49.80	1.09	6.41	4.86	0.90	0.11	15.11	22.34	0.47	101.10	84.8
14PC-4-P8	51.03	0.64	6.01	4.99	0.97	0.13	15.90	19.42	0.90	100.13	85.1	14PCX-13-2-P1	50.17	0.86	6.84	4.73	0.81	0.12	15.55	19.52	1.08	99.67	85.5
14PC-4-P9	51.89	0.56	5.57	4.77	1.18	0.14	17.31	18.83	0.76	101.04	86.7	14PCX-13-2-P2	51.12	0.60	6.05	4.56	0.97	0.13	15.41	19.96	1.05	99.83	85.9
14PC-4-P10	51.41	0.67	6.52	4.87	0.78	0.15	17.03	19.41	0.72	101.62	86.3	14PCX-13-2-P3	48.62	1.51	8.25	5.59	0.23	0.13	14.38	19.63	1.08	99.43	82.3
14PC-4-P11	52.85	0.46	5.39	4.80	1.06	0.13	17.57	19.16	0.82	102.24	86.8	14PCX-13-2-P4	49.60	1.02	7.60	4.76	0.60	0.10	15.32	20.20	0.94	100.22	85.3
Xenoliths												14PCX-15-P1	50.03	0.71	6.67	4.83	1.06	0.12	15.77	20.40	0.97	100.52	85.5
14PCX-1-P1	50.23	0.82	6.76	5.01	0.85	0.10	16.84	17.90	0.80	99.43	85.8	14PCX-15-P2	48.61	1.44	5.92	5.12	0.57	0.12	15.06	22.19	0.37	99.47	84.1
14PCX-2-P1	49.16	1.12	8.41	6.30	0.27	0.16	14.87	19.81	0.86	100.97	80.9	14PCX-15-P3	50.12	0.54	6.45	4.64	1.07	0.12	16.86	19.08	0.64	99.57	86.7
14PCX-2-P2	48.71	1.27	8.05	5.67	0.24	0.14	14.37	19.58	0.90	99.00	82.0	14PCX-15-P4	49.85	0.66	6.20	4.73	1.03	0.11	16.20	19.82	0.66	99.31	86.0
14PCX-2-P3	49.91	1.01	7.55	6.55	0.09	0.14	15.30	19.52	0.93	101.09	80.8	14PCX-16-P1	47.31	2.00	9.47	7.40	0.02	0.22	12.87	19.24	1.22	99.69	75.8
14PCX-2-P4	49.05	0.93	8.31	7.02	0.16	0.15	15.11	19.59	0.69	101.04	79.5	14PCX-16-P2	48.63	1.02	12.12	6.29	0.02	0.16	11.05	16.15	4.25	99.75	76.0
14PCX-3-P1	49.12	1.09	8.16	5.40	0.35	0.14	14.43	20.13	0.96	99.84	82.8	14PCX-16-P3	46.96	1.86	9.72	8.33	0.00	0.23	12.21	19.37	1.20	99.83	72.5
14PCX-3-P2	49.85	0.97	5.92	4.96	0.42	0.12	15.68	21.76	0.53	100.26	85.0	14PCX-17-P1	50.75	0.60	5.77	4.58	1.03	0.10	15.59	20.87	0.89	100.19	86.0
14PCX-3-P3	48.89	0.91	7.97	5.32	0.25	0.13	15.14	20.33	0.83	99.81	83.7	14PCX-17-P2	51.12	0.53	5.06	4.96	0.88	0.11	16.17	19.88	0.90	99.57	85.4
14PCX-3-P4	49.08	1.05	6.36	5.23	0.52	0.13	15.62	20.34	0.78	99.18	84.3	14PCX-18-P1	51.35	0.48	5.29	4.60	1.01	0.12	16.37	20.42	0.80	100.51	86.5
14PCX-4-P1	49.14	1.17	8.22	6.23	0.11	0.17	15.39	18.98	0.84	100.24	81.6	14PCX-18-P2	50.19	0.75	7.33	5.43	0.44	0.10	15.63	19.45	0.78	100.14	83.8
14PCX-4-P2	48.80	1.35	8.00	5.54	0.20	0.16	14.71	19.24	0.95	99.06	82.7	14PCX-18-P3	50.78	0.63	6.44	5.65	0.85	0.13	18.40	16.36	0.67	99.97	85.4
14PCX-4-P3	48.45	1.73	8.11	6.16	0.24	0.15	14.87	19.58	0.93	100.30	81.3	14PCX-18-P4	49.65	1.15	8.27	5.49	0.46	0.14	14.94	20.02	1.06	101.22	83.0

Table S3.5: Major element compositions of clinopyroxene (wt.%).

	PC-1-1	PC-1-4	PC-3-1	PC-3-2	PC-3-3	14PCX-6-1	14PCX-6-2	14PCX-8-2-1	14PCX-8-2-2	14PCX-9-1	14PCX-9-2	BCR-2
Nb	0.0	0.0	0.4	0.1	0.3	0.2	0.2	0.2	0.2	0.1	0.2	11.7
La	1.2	1.1	17.3	15.3	11.5	8.4	3.6	3.7	3.6	6.8	6.1	23.1
Ce	5.4	5.4	54.2	53.2	34.1	36.3	14.6	17.0	16.6	25.7	25.2	50.4
Pb	0.0	0.0	0.7	0.5	0.6	0.3	0.3	0.2	0.2	0.2	0.2	10.3
Sr	64.5	65.0	228.9	209.0	208.2	163.4	110.2	136.1	140.8	235.0	205.5	321.3
Nd	6.8	6.4	31.5	34.9	20.8	34.5	14.4	19.1	19.9	20.3	19.4	26.6
Hf	0.8	0.8	1.1	1.5	0.8	4.5	1.2	1.8	1.9	1.4	1.3	4.3
Zr	22.6	22.8	47.5	54.6	28.0	126.1	30.3	40.4	44.7	46.9	44.3	169.0
Sm	2.1	2.1	5.6	6.4	4.2	8.0	4.1	5.7	6.2	4.2	4.1	6.2
Eu	0.8	0.8	1.6	1.8	1.1	2.2	1.2	1.8	1.9	1.2	1.2	1.8
Gd	2.3	2.3	3.9	4.4	2.8	6.2	3.5	5.1	5.6	3.2	3.1	6.0
Dy	2.5	2.3	3.1	3.2	2.3	5.0	3.0	4.5	4.9	2.5	2.4	6.0
Er	1.3	1.2	1.6	1.5	1.1	2.5	1.5	2.2	2.3	1.3	1.2	3.4
Y	12.3	11.7	14.6	14.9	10.5	22.7	13.3	20.0	21.5	11.5	11.0	31.0
Yb	1.1	1.2	1.4	1.4	0.9	2.1	1.2	1.8	1.8	1.0	1.0	3.1
Lu	0.2	0.2	0.2	0.2	0.1	0.3	0.2	0.2	0.2	0.1	0.1	0.5

Table S3.6: Clinopyroxene trace element compositions of PC phenocrysts and xenoliths (ppm).

The sample averages of multiple spot analyses are reported. The average of repeatedly measured secondary standard BCR-2 is also reported.

cpx Mg#	T (°C)	La	Ce	Nd	Sm	Eu	Gd	Dy	Er	Yb	Lu
77	1090	0.080	0.146	0.282	0.384	0.466	0.463	0.507	0.520	0.504	0.493
79	1110	0.076	0.139	0.268	0.365	0.444	0.440	0.481	0.494	0.478	0.468
81	1130	0.069	0.126	0.241	0.328	0.398	0.394	0.430	0.441	0.428	0.419
84	1150	0.068	0.123	0.235	0.319	0.388	0.384	0.419	0.430	0.417	0.408
86	1170	0.062	0.112	0.214	0.290	0.352	0.348	0.380	0.390	0.378	0.371
87.5	1190	0.060	0.108	0.205	0.277	0.337	0.333	0.363	0.372	0.362	0.355
88	1200	0.058	0.106	0.201	0.271	0.329	0.325	0.355	0.364	0.354	0.347

Table S3.7: K_d value used for melt composition calculation.

Conclusion

Mafic and ultramafic xenoliths from Hualalai Volcano Gabbroic xenoliths from Hualalai Volcano contains gabbroic lower oceanic crust (LOC) fragments, and cumulates derived from Hualalai shield- and post-shield-stage magmas. Strontium and O isotope compositions of LOC gabbros are within the range of fresh NMORB, and therefore indicate minimal hydrothermal alteration of *in situ* LOC beneath the Hawaii Island. The minimal hydrothermal alteration recorded in Hualalai LOC xenoliths is in contrast with pervasive alteration recorded in ophiolitic gabbros and LOC xenoliths from the Canary Islands. Combined with other lines of geochemical and geophysical evidence (e.g., shallow magma fractionation depths, seismic evidence for shallow melt lenses), I propose a long-lived, shallow melt lens at fast ridges restricts deep penetration of on-axis hydrothermal circulation. Magmas pass through and fractionate within the long-lived, shallow melt lens to produce LOC at fast ridges.

Melt-crust interaction between Hawaiian magmas and Pacific LOC has partially overprinted the trace element and isotopic compositions of *in situ* LOC. Hualalai LOC gabbros have Sr-Nd-Pb-Hf isotope compositions similar to Hawaiian rejuvenated-stage lavas. The *in situ* Pacific lithospheric mantle may have similar isotopic composition as LOC gabbros, as the result of metasomatism by Hawaiian-plume derived melts. If this is the case, Pacific lithosphere is a likely source for Hawaiian rejuvenated-stage volcanism.

Most Hualalai xenoliths are cumulates derived from Hualalai shield-stage and post-shield-stage cumulates, which provide information on the evolution of Hawaiian magmas and magma storage systems. MELTS modeling and equilibration temperatures suggest Hualalai shield-stage gabbros are formed in a magma reservoir within or at the base of local LOC. Gabbro and websterites derived from Hualalai shield-stage magmas

display more variations in Sr-Nd-Pb-Hf isotopic compositions than shield-stage lavas. Dunites derived from Hualalai post-shield-stage magmas have Os isotope composition indicating coupled fractional crystallization and assimilation. Therefore, magmas storage, fractionation, and crustal assimilation appear to have partially homogenized and overprinted Hawaiian melt compositions. However, the range of oxygen isotope compositions recorded in Hawaiian melts cannot be generated by assimilation of the *in situ* LOC, which have relatively uniform and MORB-like $\delta^{18}O$ values.

The Papoose Canyon (PC) monogenetic vent eruption records temporal compositional variations that reflect binary mixing of two distinct melts, one of which is chemically and isotopically more enriched than the other. Although PC lavas have high MgO content and appear to be primitive, PC phenocrysts and ultramafic xenoliths derive from a melt that is more evolved and chemically more enriched than their host lavas. Pressure constraints suggest PC phenocrysts and ultramafic xenoliths fractionated at middle-crust depths. Typical crustal contamination signatures such as correlations between HFSE depletions and Sr-Nd-Pb isotopic compositions, radiogenic Os isotopic compositions, and high $\delta^{18}O$ in olivines are also observed in PC lavas. Therefore, a deflating sill model is proposed to explain the temporal trends observed. PC phenocrysts and xenoliths fractionated and assimilated crustal materials in crustal sill(s) formed by early melt pulse. The eruption was triggered by the arrival of a later melt pulse. Then the early, evolved melts were drained and mixed with the later, more primitive melts. The temporal-compositional trends reflect exhaustion of the sill component over time, which is consistent with the decreasing phenocryst and xenolith abundances in PC lavas. These results indicate that even "primitive" lavas may contain a significant signature of magma ponding, fractionation, and crustal contamination that is obscured within the bulk lava but is evident in the melt "crystal cargo".

References

Abouchami, W., Hofmann, A. W., Galer, S. J. G., Frey, F. A., Eisele, J., & Feigenson, M. (2005). Lead isotopes reveal bilateral asymmetry and vertical continuity in the Hawaiian mantle plume. Nature, 434(7035), 851-856.

Adam, J., & Green, T. (2003). The influence of pressure, mineral composition and water on trace element partitioning between clinopyroxene, amphibole and basanitic melts. European Journal of Mineralogy, 15(5), 831-841.

Adam, J., & Green, T. H. (1994). The effects of pressure and temperature on the partitioning of Ti, Sr and REE between amphibole, clinopyroxene and basanitic melts. Chemical Geology, 117(1), 219-233.

Allan, J.F., Baptize, R., Permit, M.R., Fernery, D.J., Sack, R.O., 1989.Petrology of lavas from the Lamont seamount chain and adjacent East Pacific Rise, 10°N. J. Petrol. 30, 1245–1298.

Alt, J. C., & Teagle, D. A. (2000). Hydrothermal alteration and fluid fluxes in ophiolites and oceanic crust. Special Papers-Geological Society of America, 273-282.

Alt, J. C., Laverne, C., Coggon, R. M., Teagle, D. A., Banerjee, N. R., Morgan, S., Smith‐Duque, C. E., Harris M. & Galli, L. (2010). Subsurface structure of a submarine hydrothermal system in ocean crust formed at the East Pacific Rise, ODP/IODP Site 1256. Geochemistry, Geophysics, Geosystems, 11(10).

Andrews, B. J., Gardner, J. E., & Housh, T. B. (2008). Repeated recharge, assimilation, and hybridization in magmas erupted from El Chichón as recorded by plagioclase and amphibole phenocrysts. Journal of Volcanology and Geothermal Research, 175(4), 415-426.

Baker, J. A., Thirlwall, M. F., & Menzies, M. A. (1996). Sr-Nd-Pb isotopic and trace element evidence for crustal contamination of plume-derived flood basalts: Oligocene flood volcanism in western Yemen. Geochimica et Cosmochimica Acta, 60(14), 2559-2581.

Beard, B.L., Glazner, A.F., 1995. Trace element and Sr and Nd isotopic composition of mantle xenoliths from the Big Pine volcanic field, California. J. Geophys. Res. 100, 4169–4179.

Beard, J. S., & Borgia, A. (1989). Temporal variation of mineralogy and petrology in cognate gabbroic enclaves at Arenal volcano, Costa Rica.Contributions to Mineralogy and Petrology, 103(1), 110-122.

Bédard, J. H. (2014). Parameterizations of calcic clinopyroxene—Melt trace element partition coefficients. Geochemistry, Geophysics, Geosystems,15(2), 303-336.

Bierman, P., Gillespie, A., Whipple, K., & Clark, D. (1991). Quaternary geomorphology and geochronology of Owens Valley, California: Geological Society of America

field trip. In Geological excursions in southern California and Mexico: guidebook for the 1991 annual meeting. Geological Society of America, San Diego (pp. 199-223).

Bizimis, M., Salters, V. J., Garcia, M. O., & Norman, M. D. (2013). The composition and distribution of the rejuvenated component across the Hawaiian plume: Hf-Nd-Sr-Pb isotope systematics of Kaula lavas and pyroxenite xenoliths. Geochemistry, Geophysics, Geosystems, 14(10), 4458-4478.

Blondes, M. S., Brandon, M. T., Reiners, P. W., Page, F. Z., & Kita, N. T. (2012). Generation of forsteritic olivine (Fo99· 8) by subsolidus oxidation in basaltic Flows. Journal of Petrology, 53(5), 971-984.

Blondes, M. S., Reiners, P. W., Ducea, M. N., Singer, B. S., & Chesley, J. (2008). Temporal–compositional trends over short and long time-scales in basalts of the Big Pine Volcanic Field, California. Earth and Planetary Science Letters, 269(1), 140-154.

Bohrson, W. A. (2007). Insight into subvolcanic magma plumbing systems. Geology, 35(8), 767-768.

Bohrson, W. A., & Clague, D. A. (1988). Origin of ultramafic xenoliths containing exsolved pyroxenes from Hualalai Volcano, Hawaii. Contributions to Mineralogy and Petrology, 100(2), 139-155.

Bosch, D., Jamais, M., Boudier, F., Nicolas, A., Dautria, J. M., & Agrinier, P. (2004). Deep and high-temperature hydrothermal circulation in the Oman ophiolite—petrological and isotopic evidence. Journal of Petrology, 45(6), 1181-1208.

Botcharnikov, R. E., Koepke, J., Holtz, F., McCammon, C., & Wilke, M. (2005). The effect of water activity on the oxidation and structural state of Fe in a ferro-basaltic melt. Geochimica et Cosmochimica Acta, 69(21), 5071-5085.

Brey, G. P., & Köhler, T. (1990). Geothermobarometry in four-phase lherzolites II. New thermobarometers, and practical assessment of existing thermobarometers. Journal of Petrology, 31(6), 1353-1378.

Burke, W. H., Denison, R. E., Hetherington, E. A., Koepnick, R. B., Nelson, H. F., & Otto, J. B. (1982). Variation of seawater 87Sr/86Sr throughout Phanerozoic time. Geology, 10(10), 516-519.

Byerly, B. L., & Lassiter, J. C. (2012). Evidence from mantle xenoliths for lithosphere removal beneath the central Rio Grande Rift. Earth and Planetary Science Letters, 355, 82-93.

Carlson, R. W., Lugmair, G. W., & Macdougall, J. D. (1981). Columbia River volcanism: the question of mantle heterogeneity or crustal contamination.Geochimica et Cosmochimica Acta, 45(12), 2483-2499.

Carrigy, M. A. (1970). Experiments on the angles of repose of granular materials1. Sedimentology, 14(3‐4), 147-158.

Chen, C. Y., & Frey, F. A. (1985). Trace element and isotopic geochemistry of lavas from Haleakala volcano, East Maui, Hawaii: implications for the origin of Hawaiian basalts. Journal of Geophysical Research: Solid Earth (1978–2012), 90(B10), 8743-8768.

Chen, C. H., Presnall, D. C., & Stern, R. J. (1992). Petrogenesis of ultramafic xenoliths from the 1800 Kaupulehu flow, Hualalai volcano, Hawaii.Journal of Petrology, 33(1), 163-202.

Christiansen, E. H., & McCurry, M. (2008). Contrasting origins of Cenozoic silicic volcanic rocks from the western Cordillera of the United States. Bulletin of Volcanology, 70(3), 251-267.

Clague, D. A., & Frey, F. A. (1982). Petrology and trace element geochemistry of the Honolulu Volcanics, Oahu: implications for the oceanic mantle below Hawaii. Journal of Petrology, 23(3), 447-504.

Clague, D. A. (1987). Hawaiian xenolith populations, magma supply rates, and development of magma chambers. Bulletin of Volcanology, 49(4), 577-587.

Clague, D. A., & Dalrymple, G. B. (1987). The Hawaiian-Emperor volcanic chain. Part I. Geologic evolution. Volcanism in Hawaii, 1, 5-54.

Clague, D. A., & Bohrson, W. A. (1991). Origin of xenoliths in the trachyte at Puu Waawaa, Hualalai Volcano, Hawaii. Contributions to mineralogy and petrology, 108(4), 439-452.

Connelly, J. N., Ulfbeck, D. G., Thrane, K., Bizzarro, M., & Housh, T. (2006). A method for purifying Lu and Hf for analyses by MC-ICP-MS using TODGA resin. Chemical Geology, 233(1), 126-136.

Coogan, L. A., Howard, K. A., Gillis, K. M., Bickle, M. J., Chapman, H., Boyce, A. J., Jenkin, G.R.T. & Wilson, R. N. (2006). Chemical and thermal constraints on focussed fluid flow in the lower oceanic crust. American Journal of Science, 306(6), 389-427.

Coogan, L. A., Jenkin, G. R. T., & Wilson, R. N. (2007). Contrasting cooling rates in the lower oceanic crust at fast-and slow-spreading ridges revealed by geospeedometry. Journal of Petrology, 48(11), 2211-2231.

Davies, G. R., & Macdonald, R. (1987). Crustal Influences in the petrogenesis of the Naivasha basalt—comendite complex: Combined trace element and Sr-Nd-Pb isotope constraints. Journal of Petrology, 28(6), 1009-1031.

Davis, A. S., Clague, D. A., & Friesen, W. B. (1994). Petrology and mineral chemistry of basalt from Escanaba Trough. US Geological Survey Bulletin, Report: B, 2022, 153-170.

Davis, A. S., Clague, D. A., & Paduan, J. B. (2007). Diverse origins of xenoliths from seamounts at the continental margin, offshore central California. Journal of Petrology, 48(5), 829-852.

DePAOLO, D. J. (1981). Trace element and isotopic effects of combined wallrock assimilation and fractional crystallization. Earth and planetary science letters, 53(2), 189-202.

Dixon, J., Clague, D. A., Cousens, B., Monsalve, M. L., & Uhl, J. (2008). Carbonatite and silicate melt metasomatism of the mantle surrounding the Hawaiian plume: Evidence from volatiles, trace elements, and radiogenic isotopes in rejuvenated‐stage lavas from Niihau, Hawaii. Geochemistry, Geophysics, Geosystems, 9(9).

Duncan, R. A., & Green, D. H. (1987). The genesis of refractory melts in the formation of oceanic crust. Contributions to Mineralogy and Petrology, 96(3), 326-342.

Eiler, J. M. (2001). Oxygen isotope variations of basaltic lavas and upper mantle rocks. Reviews in Mineralogy and geochemistry, 43(1), 319-364.

Eiler, J. M., Farley, K. A., Valley, J. W., Hofmann, A. W., & Stolper, E. M. (1996). Oxygen isotope constraints on the sources of Hawaiian volcanism. Earth and Planetary Science Letters, 144(3), 453-467.

Eiler, J. M., Schiano, P., Kitchen, N., & Stolper, E. M. (2000). Oxygen-isotope evidence for recycled crust in the sources of mid-ocean-ridge basalts. Nature,403(6769), 530-534.

Erlund, E. J., Cashman, K. V., Wallace, P. J., Pioli, L., Rosi, M., Johnson, E., & Granados, H. D. (2010). Compositional evolution of magma from Parícutin Volcano, Mexico: the tephra record. Journal of Volcanology and Geothermal Research, 197(1), 167-187.

Esser, B. K., & Turekian, K. K. (1993). The osmium isotopic composition of the continental crust. Geochimica et Cosmochimica Acta, 57(13), 3093-3104.

Fekiacova, Z., Abouchami, W., Galer, S. J. G., Garcia, M. O., & Hofmann, A. W. (2007). Origin and temporal evolution of Koʻolau Volcano, Hawaiʻi: Inferences from isotope data on the Koʻolau Scientific Drilling Project (KSDP), the Honolulu Volcanics and ODP Site 843. Earth and Planetary Science Letters, 261(1), 65-83.

Fodor, R. V., & Galar, P. (1997). A view into the subsurface of Mauna Kea volcano, Hawaii: crystallization processes interpreted through the petrology and petrography of gabbroic and ultramafic xenoliths. Journal of Petrology, 38(5), 581-624.

França, Z., Lago, M., Gale, C., Ubide, T., Widom, E., Arranz, E., & Forjaz, V.H. (2008). Composition of gabbroic xenoliths in Flores Island (Azores, Portugal). Revista de la Sociedad Espanola de Mineralog| a, 9, 103-104.

Frey, F. A., Wise, W. S., Garcia, M. O., West, H., Kwon, S. T., & Kennedy, A. (1990). Evolution of Mauna Kea Volcano, Hawaii: Petrologic and geochemical constraints on postshield volcanism. Journal of Geophysical Research: Solid Earth (1978–2012), 95(B2), 1271-1300.

Gaffney, A. M. (2002). Environments of crystallization and compositional diversity of Mauna Loa xenoliths. Journal of Petrology, 43(6), 963-981.

Gao, R., Lassiter, J. C., Barnes, J. D., Clague, D. A., & Bohrson, W. A. (2016a). Geochemical investigation of Gabbroic Xenoliths from Hualalai Volcano: Implications for lower oceanic crust accretion and Hualalai Volcano magma storage system. Earth and Planetary Science Letters, 442, 162-172.

Gao, R., Lassiter, J.C., Ramirez, G. (2016b). Crustal or mantle origin of temporal compositional trends in monogenetic vent eruption? Insight from the crystal cargo in the Papoose Canyon sequence, Big Pine volcanic field, CA. Earth and Planetary Science Letters (in review).

Gao, Y., Vils, F., Cooper, K. M., Banerjee, N., Harris, M., Hoefs, J., Teagle., D. A. H., Casey, J. F., Laverne, C., Alt, J. C. & Muehlenbachs, K. (2012). Downhole variation of lithium and oxygen isotopic compositions of oceanic crust at East Pacific Rise, ODP Site 1256. Geochemistry, Geophysics, Geosystems, 13(10).

Garcia, M. O., Pietruszka, A. J., Rhodes, J. M., & Swanson, K. (2000). Magmatic processes during the prolonged Pu'u'O'o eruption of Kilauea Volcano, Hawaii. Journal of Petrology, 41(7), 967-990.

Garcia, M. O., Swinnard, L., Weis, D., Greene, A. R., Tagami, T., Sano, H., & Gandy, C. E. (2010). Petrology, geochemistry and geochronology of Kaua 'i lavas over 4· 5 Myr: Implications for the origin of rejuvenated volcanism and the evolution of the Hawaiian plume. Journal of Petrology, 51(7), 1507-1540.

Gazel, E., Plank, T., Forsyth, D. W., Bendersky, C., Lee, C. T. A., & Hauri, E. H. (2012). Lithosphere versus asthenosphere mantle sources at the Big Pine Volcanic Field, California. Geochemistry, Geophysics, Geosystems, 13(6).

Gee, J., Staudigel, H., & Natland, J. H. (1991). Geology and petrology of Jasper Seamount. Journal of Geophysical Research: Solid Earth (1978–2012), 96(B3), 4083-4105.

Gerlach, T. M. (1993). Oxygen buffering of Kilauea volcanic gases and the oxygen fugacity of Kilauea basalt. Geochimica et Cosmochimica Acta, 57(4), 795-814.

Ghiorso, M. S., & Sack, R. O. (1995). Chemical mass transfer in magmatic processes IV. A revised and internally consistent thermodynamic model for the interpolation and extrapolation of liquid-solid equilibria in magmatic systems at elevated temperatures and pressures. Contributions to Mineralogy and Petrology, 119(2-3), 197-212.

Gillespie, A. R., Huneke, J. C., & Wasserburg, G. J. (1984). Eruption Age of a~ 100,000-Year-Old Basalt From^(40) Ar-^(39) Ar Analysis of Partially Degassed Xenoliths. Journal of Geophysical Research B, 89(B2), 1033-1048.

Glazner, A. F., Farmer, G. L., Hughes, W. T., Wooden, J., & Pickthorn, W. (1991). Contamination of basaltic magma by mafic crust at Amboy and Pisgah Craters, Mojave Desert, California. Journal of Geophysical Research: Solid Earth, 96(B8), 13673-13691.

Green, D. H., & Ringwood, A. E. (1967). The genesis of basaltic magmas. Contributions to Mineralogy and Petrology, 15(2), 103-190.

Green, T. H., Blundy, J. D., Adam, J., & Yaxley, G. M. (2000). SIMS determination of trace element partition coefficients between garnet, clinopyroxene and hydrous basaltic liquids at 2–7.5 GPa and 1080–1200 C. Lithos, 53(3), 165-187.

Gregory, R. T., & Taylor, H. P. (1981). An oxygen isotope profile in a section of Cretaceous oceanic crust, Samail Ophiolite, Oman: Evidence for δ 18O buffering of the oceans by deep (> 5 km) seawater - hydrothermal circulation at mid - ocean ridges. Journal of Geophysical Research: Solid Earth, 86(B4), 2737-2755.

Hanano, D., Weis, D., Scoates, J. S., Aciego, S., & DePaolo, D. J. (2010). Horizontal and vertical zoning of heterogeneities in the Hawaiian mantle plume from the geochemistry of consecutive postshield volcano pairs: Kohala - Mahukona and Mauna Kea – Hualalai. Geochemistry, Geophysics, Geosystems, 11(1).

Hansteen, T. H., & Troll, V. R. (2003). Oxygen isotope composition of xenoliths from the oceanic crust and volcanic edifice beneath Gran Canaria (Canary Islands): consequences for crustal contamination of ascending magmas. Chemical Geology, 193(3), 181-193.

Hart, S. R. (1984). A large-scale isotope anomaly in the Southern Hemisphere mantle. Nature, 309, 753-757.

Hart, S. R. (1988). Heterogeneous mantle domains: signatures, genesis and mixing chronologies. *Earth and Planetary Science Letters*, *90*(3), 273-296.

Hart, S. R., & Dunn, T. (1993). Experimental cpx/melt partitioning of 24 trace elements. Contributions to Mineralogy and Petrology, 113(1), 1-8.

Hart, S. R., Blusztajn, J., Dick, H. J., Meyer, P. S., & Muehlenbachs, K. (1999). The fingerprint of seawater circulation in a 500-meter section of ocean crust gabbros. Geochimica et Cosmochimica Acta, 63(23), 4059-4080.

Hauri, E. (2002). SIMS analysis of volatiles in silicate glasses, 2: isotopes and abundances in Hawaiian melt inclusions. Chemical Geology, 183(1), 115-141.

Hauri, E. H. (1996). Major-element variability in the Hawaiian mantle plume. Nature, 382(6590), 415-419.

Hauri, E. H., & Hart, S. R. (1993). Re Os isotope systematics of HIMU and EMII oceanic island basalts from the South Pacific Ocean. Earth and Planetary Science Letters, 114(2), 353-371.

Hildreth, W. E. S., HALLIDAY, A. N., & CHRISTIANSEN, R. L. (1991). Isotopic and chemical evidence concerning the genesis and contamination of basaltic and rhyolitic magma beneath the Yellowstone Plateau volcanic field. Journal of Petrology, 32(1), 63-138.

Hoernle, K. A. J. (1998). Geochemistry of Jurassic oceanic crust beneath Gran Canaria (Canary Islands): implications for crustal recycling and assimilation. Journal of Petrology, 39(5), 859-880.

Höfig, T. W., Geldmacher, J., Hoernle, K., Hauff, F., Duggen, S., & Garbe-Schönberg, D. (2014). From the lavas to the gabbros: 1.25 km of geochemical characterization of upper oceanic crust at ODP/IODP Site 1256, eastern equatorial Pacific. Lithos, 210, 289-312.

Hooft, E. E., Detrick, R. S., & Kent, G. M. (1997). Seismic structure and indicators of magma budget along the southern East Pacific Rise. Journal of Geophysical Research: Solid Earth (1978–2012), 102(B12), 27319-27340.

Jackson, E. D., Clague, D. A., Engleman, E., Friesen, W. F. and Norton, D. (1981). Xenoliths in the alkalic basalt flows from Hualalai volcano, Hawaii. USGS Open-File Rep 81-1031.

Jamais, M., Lassiter, J. C., & Brügmann, G. (2008). PGE and Os-isotopic variations in lavas from Kohala Volcano, Hawaii: constraints on PGE behavior and melt/crust interaction. Chemical Geology, 250(1), 16-28.

Jones, C. E., Tarney, J., Baker, J. H., & Gerouki, F. (1992). Tertiary granitoids of Rhodope, northern Greece: Magmatism related to extensional collapse of the Hellenic Orogen?. Tectonophysics, 210(3), 295-314.

Jugo, P. J., Wilke, M., & Botcharnikov, R. E. (2010). Sulfur K-edge XANES analysis of natural and synthetic basaltic glasses: Implications for S speciation and S content as function of oxygen fugacity. Geochimica et Cosmochimica Acta, 74(20), 5926-5938.

Kauahikaua, J., Cashman, K., Clague, D., Champion, D., & Hagstrum, J. (2002). Emplacement of the most recent lava flows on Hualālai Volcano, Hawai ‘i. Bulletin of volcanology, 64(3-4), 229-253.

Kawahata, H., Nohara, M., Ishizuka, H., Hasebe, S., & Chiba, H. (2001). Sr isotope geochemistry and hydrothermal alteration of the Oman ophiolite. Journal of Geophysical Research: Solid Earth (1978–2012), 106(B6), 11083-11099.

Kelemen, P. B., Koga, K., & Shimizu, N. (1997). Geochemistry of gabbro sills in the crust-mantle transition zone of the Oman ophiolite: Implications for the origin of the oceanic lower crust. Earth and Planetary Science Letters, 146(3), 475-488.

Kempton, P. D., & Harmon, R. S. (1992). Oxygen isotope evidence for large-scale hybridization of the lower crust during magmatic underplating. Geochimica et Cosmochimica Acta, 56(3), 971-986.

King, A. J., Waggoner, D. G., & Garcia, M. O. (1991). Geochemistry and petrology of basalts from Leg 136, Central Pacific Ocean. In Proceedings of the Ocean Drilling Program. Scientific results (Vol. 136, pp. 107-118). Ocean Drilling Program.

Kyser, T. K., O'Neil, J. R., & Carmichael, I. S. (1981). Oxygen isotope thermometry of basic lavas and mantle nodules. Contributions to Mineralogy and Petrology, 77(1), 11-23.

Lanphere, M. A. (1981). K‐Ar ages of metamorphic rocks at the base of the Samail Ophiolite, Oman. Journal of Geophysical Research: Solid Earth (1978–2012), 86(B4), 2777-2782.

Lassiter, J. C., & Hauri, E. H. (1998). Osmium-isotope variations in Hawaiian lavas: evidence for recycled oceanic lithosphere in the Hawaiian plume. Earth and Planetary Science Letters, 164(3), 483-496.

Lassiter, J. C., Hauri, E. H., Reiners, P. W., & Garcia, M. O. (2000). Generation of Hawaiian post-erosional lavas by melting of a mixed lherzolite/pyroxenite source. Earth and Planetary Science Letters, 178(3), 269-284.

Lassiter, J. C., Byerly, B. L., Snow, J. E., & Hellebrand, E. (2014). Constraints from Os-isotope variations on the origin of Lena Trough abyssal peridotites and implications for the composition and evolution of the depleted upper mantle. Earth and Planetary Science Letters, 403, 178-187.

Lee, C. T. A. (2002). Platinum-group element geochemistry of peridotite xenoliths from the Sierra Nevada and the Basin and Range, California. Geochimica et Cosmochimica Acta, 66(22), 3987-4005.

Lee, C. T., Rudnick, R. L., & Brimhall, G. H. (2001). Deep lithospheric dynamics beneath the Sierra Nevada during the Mesozoic and Cenozoic as inferred from xenolith petrology. Geochemistry, Geophysics, Geosystems, 2(12).

Maaløe, S., James, D., Smedley, P., Petersen, S., & Garmann, L. B. (1992). The Koloa volcanic suite of Kauai, Hawaii. Journal of Petrology, 33(4), 761-784.

Maclennan, J. (2008). Concurrent mixing and cooling of melts under Iceland. Journal of Petrology, 49(11), 1931-1953.

Maclennan, J., Hulme, T., & Singh, S. C. (2004). Thermal models of oceanic crustal accretion: linking geophysical, geological and petrological observations. Geochemistry, Geophysics, Geosystems, 5(2).

Maclennan, J., Hulme, T., & Singh, S. C. (2005). Cooling of the lower oceanic crust. Geology, 33(5), 357-366.

Manning, C. E., & MacLeod, C. (1996). Fracture-controlled metamorphism of Hess Deep gabbros, Site 894: constraints on the roots of mid-ocean-ridge hydrothermal systems at fast-spreading centers. Ocean Drilling Program.

Mattey, D., Lowry, D., & Macpherson, C. (1994). Oxygen isotope composition of mantle peridotite. Earth and Planetary Science Letters, 128(3), 231-241.

Mattsson, H. B. (2012). Rapid magma ascent and short eruption durations in the Lake Natron–Engaruka monogenetic volcanic field (Tanzania): a case study of the olivine melilititic Pello Hill scoria cone. Journal of Volcanology and Geothermal Research, 247, 16-25.

McBirney, A. R., Taylor, H. P., & Armstrong, R. L. (1987). Paricutin re-examined: a classic example of crustal assimilation in calc-alkaline magma. Contributions to Mineralogy and Petrology, 95(1), 4-20.

McCulloch, M. T., Gregory, R. T., Wasserburg, G. J., & Taylor, H. P. (1980). A neodymium, strontium, and oxygen isotopic study of the Cretaceous Samail ophiolite and implications for the petrogenesis and seawater-hydrothermal alteration of oceanic crust. Earth and Planetary Science Letters, 46(2), 201-211.

McDonough, W. F., & Sun, S. S. (1995). The composition of the Earth. Chemical geology, 120(3), 223-253.

McGee, L. E., Smith, I. E., Millet, M. A., Handley, H. K., & Lindsay, J. M. (2013). Asthenospheric control of melting processes in a monogenetic basaltic system: a case study of the Auckland Volcanic Field, New Zealand. Journal of Petrology, egt043.

Mercer, C. N., & Johnston, A. D. (2008). Experimental studies of the P–T–H2O near-liquidus phase relations of basaltic andesite from North Sister Volcano, High Oregon Cascades: constraints on lower-crustal mineral assemblages. Contributions to Mineralogy and Petrology, 155(5), 571-592.

Michael, P. J., & Cornell, W. C. (1998). Influence of spreading rate and magma supply on crystallization and assimilation beneath mid‐ocean ridges: Evidence from chlorine and major element chemistry of mid‐ocean ridge basalts. Journal of Geophysical Research: Solid Earth (1978–2012), 103(B8), 18325-18356.

Mitra, S., Princivalle, F., Samanta, A. K., & Moon, H. S. (1999). Geothermometry and mineralogy of two-pyroxene granulites: Evaluation from Mossbauer and X-ray single crystal cation partitioning of Ca-poor and Ca-rich pyroxenes. Geological Society of India, 53(5), 537-548.

Moore, J. G. (1987). Subsidence of the Hawaiian Ridge. US Geol Sur Prof Pap 1350: 85-100.

Mordick, B. E., & Glazner, A. F. (2006). Cpx thermobarometry of basalts from the Coso and Big Pine volcanic fields, California. Contributions to Mineralogy and Petrology, 152(1), 111-124.

Moune, S., Sigmarsson, O., Schiano, P., Thordarson, T., & Keiding, J. K. (2012). Melt inclusion constraints on the magma source of Eyjafjallajökull 2010 flank eruption. Journal of Geophysical Research: Solid Earth, 117(B9).

Müller, R. D., Sdrolias, M., Gaina, C., & Roest, W. R. (2008). Age, spreading rates, and spreading asymmetry of the world's ocean crust. Geochemistry, Geophysics, Geosystems, 9(4).

Needham, A. J., Lindsay, J. M., Smith, I. E. M., Augustinus, P., & Shane, P. A. (2011). Sequential eruption of alkaline and sub-alkaline magmas from a small monogenetic volcano in the Auckland Volcanic Field, New Zealand. Journal of Volcanology and Geothermal Research, 201(1), 126-142.

Nekvasil, H., Dondolini, A., Horn, J., Filiberto, J., Long, H., & Lindsley, D. H. (2004). The origin and evolution of silica-saturated alkalic suites: an experimental study. Journal of Petrology, 45(4), 693-721.

Nielsen, R. L. (1992). BIGD. FOR: a fortran program to calculate trace-element partition coefficients for natural mafic and intermediate composition magmas. Computers & Geosciences, 18(7), 773-788.

O'hara, M. J. (1968). The bearing of phase equilibria studies in synthetic and natural systems on the origin and evolution of basic and ultrabasic rocks. Earth-Science Reviews, 4, 69-133.

Ormerod, D. S., Hawkesworth, C. J., Rogers, N. W., Leeman, W. P., & Menzies, M. A. (1988). Tectonic and magmatic transitions in the Western Great Basin, USA.

Ormerod, D. S., Rogers, N. W., & Hawkesworth, C. J. (1991). Melting in the lithospheric mantle: Inverse modelling of alkali-olivine basalts from the Big Pine Volcanic Field, California. Contributions to Mineralogy and Petrology,108(3), 305-317.

Ozawa, A., Tagami, T., & Garcia, M. O. (2005). Unspiked K–Ar dating of the Honolulu rejuvenated and Ko ‘olau shield volcanism on O ‘ahu, Hawai ‘i. Earth and Planetary Science Letters, 232(1), 1-11.

Panjasawatwong, Y., Danyushevsky, L. V., Crawford, A. J., & Harris, K. L. (1995). An experimental study of the effects of melt composition on plagioclase-melt equilibria at 5 and 10 kbar: implications for the origin of magmatic high-An plagioclase. Contributions to Mineralogy and Petrology,118(4), 420-432.

Peccerillo, A., Dallai, L., Frezzotti, M. L., & Kempton, P. D. (2004). Sr–Nd–Pb–O isotopic evidence for decreasing crustal contamination with ongoing magma evolution at Alicudi volcano (Aeolian arc, Italy): implications for style of magma-crust interaction and for mantle source compositions. Lithos, 78(1), 217-233.

Peucker‐Ehrenbrink, B., & Jahn, B. M. (2001). Rhenium‐osmium isotope systematics and platinum group element concentrations: Loess and the upper continental crust. Geochemistry, Geophysics, Geosystems, 2(10).

Phipps Morgan, J., & Chen, Y. J. (1993). The genesis of oceanic crust: Magma injection, hydrothermal circulation, and crustal flow. Journal of Geophysical Research: Solid Earth (1978–2012), 98(B4), 6283-6297.

Phipps Morgan, J., Parmentier, E. M., & Lin, J. (1987). Mechanisms for the origin of mid‐ocean ridge axial topography: Implications for the thermal and mechanical structure of accreting plate boundaries. Journal of Geophysical Research: Solid Earth (1978‐2012), 92(B12), 12823-12836.

Pietruszka, A. J., Hauri, E. H., Carlson, R. W., & Garcia, M. O. (2006). Remelting of recently depleted mantle within the Hawaiian plume inferred from the 226 Ra–230 Th–238 U disequilibria of Puʻu ʻŌʻō eruption lavas.Earth and Planetary Science Letters, 244(1), 155-169.

Pollack, H. N., Hurter, S. J., & Johnson, J. R. (1993). Heat flow from the Earth's interior: analysis of the global data set. Reviews of Geophysics, 31(3), 267-280.

Press, F. (2004). Understanding earth. Macmillan.

Putirka, K. D. (2008). Thermometers and barometers for volcanic systems. Reviews in Mineralogy and Geochemistry, 69(1), 61-120.

Putirka, K., Johnson, M., Kinzler, R., Longhi, J., & Walker, D. (1996). Thermobarometry of mafic igneous rocks based on clinopyroxene-liquid equilibria, 0–30 kbar. Contributions to Mineralogy and Petrology, 123(1), 92-108.

Quick, J. E., & Denlinger, R. P. (1993). Ductile deformation and the origin of layered gabbro in ophiolites. Journal of Geophysical Research: Solid Earth (1978–2012), 98(B8), 14015-14027.

Rankenburg, K., Lassiter, J. C., & Brey, G. (2004). Origin of megacrysts in volcanic rocks of the Cameroon volcanic chain–constraints on magma genesis and crustal contamination. Contributions to Mineralogy and Petrology, 147(2), 129-144.

Rasoazanamparany, C., Widom, E., Valentine, G. A., Smith, E. I., Cortés, J. A., Kuentz, D., & Johnsen, R. (2015). Origin of chemical and isotopic heterogeneity in a mafic, monogenetic volcanic field: A case study of the Lunar Crater Volcanic Field, Nevada. Chemical Geology, 397, 76-93.

Reiners, P. W. (2002). Temporal‐compositional trends in intraplate basalt eruptions: Implications for mantle heterogeneity and melting processes.Geochemistry, Geophysics, Geosystems, 3(2), 1-30.

Roeder, P. L., & Emslie, R. (1970). Olivine-liquid equilibrium. Contributions to mineralogy and petrology, 29(4), 275-289.

Rogers, N. W., Hawkesworth, C. J., & Ormerod, D. S. (1995). Late Cenozoic basaltic magmatism in the western Great Basin, California and Nevada.Journal of Geophysical Research: Solid Earth (1978–2012), 100(B6), 10287-10301.

Rowe, M. C., Peate, D. W., & Peate, I. U. (2011). An investigation into the nature of the magmatic plumbing system at Paricutin Volcano, Mexico.Journal of Petrology, 52(11), 2187-2220.

Rubin, K. H., Sinton, J. M., Maclennan, J., & Hellebrand, E. (2009). Magmatic filtering of mantle compositions at mid-ocean-ridge volcanoes. Nature Geoscience, 2(5), 321-328.

Rudnick, R. L., & Gao, S. X. (2003). Composition of the continental crust. Treatise on geochemistry, 3, 1-64.

Schaaf, P., Stimac, J. I. M., Siebe, C., & Macías, J. L. (2005). Geochemical evidence for mantle origin and crustal processes in volcanic rocks from Popocatépetl and surrounding monogenetic volcanoes, central Mexico. Journal of Petrology, 46(6), 1243-1282.

Scher, H. D., & Delaney, M. L. (2010). Breaking the glass ceiling for high resolution Nd isotope records in early Cenozoic paleoceanography. Chemical Geology, 269(3), 329-338.

Schmincke, H. U., Klügel, A., Hansteen, T. H., Hoernle, K., & van den Bogaard, P. (1998). Samples from the Jurassic ocean crust beneath Gran Canaria, La Palma and Lanzarote (Canary Islands). Earth and Planetary Science Letters, 163(1), 343-360.

Shamberger, P. J., & Hammer, J. E. (2006). Leucocratic and gabbroic xenoliths from Hualalai Volcano, Hawai'i. Journal of Petrology, 47(9), 1785-1808.

Sharp, Z. D. (1990). A laser-based microanalytical method for the in situ determination of oxygen isotope ratios of silicates and oxides. Geochimica et Cosmochimica Acta, 54(5), 1353-1357.

Sharp, Z. D. (1995). Oxygen isotope geochemistry of the Al 2 SiO 5 polymorphs. American Journal

Shirey, S. B., & Walker, R. J. (1998). The Re-Os isotope system in cosmochemistry and high-temperature geochemistry. Annual Review of Earth and Planetary Sciences, 26(1), 423-500.

Singh, S. C., Crawford, W. C., Carton, H., Seher, T., Combier, V., Cannat, M., Canales, J. P., Dusunur, D., Escartin, J. & Miranda, J. M. (2006). Discovery of a magma chamber and faults beneath a Mid-Atlantic Ridge hydrothermal field. Nature, 442(7106), 1029-1032.

Smith, I. E. M., Blake, S., Wilson, C. J. N., & Houghton, B. F. (2008). Deep-seated fractionation during the rise of a small-volume basalt magma batch: Crater Hill,

Auckland, New Zealand. Contributions to Mineralogy and Petrology, 155(4), 511-527.

Spera, F. J., & Bohrson, W. A. (2001). Energy-constrained open-system magmatic processes I: general model and energy-constrained assimilation and fractional crystallization (EC-AFC) formulation. Journal of Petrology, 42(5), 999-1018.

Stakes, D. S., & Taylor, H. P. (1992). The northern Samail ophiolite: an oxygen isotope, microprobe, and field study. Journal of Geophysical Research: Solid Earth, 97(B5), 7043-7080.

Steinberger, B. (2000). Plumes in a convecting mantle- Models and observations for individual hotspots. Journal of Geophysical Research, 105(B5), 11-127

Strong, M., & Wolff, J. (2003). Compositional variations within scoria cones.Geology, 31(2), 143-146.

Sun, S. S., & McDonough, W. F. (1989). Chemical and isotopic systematics of oceanic basalts: implications for mantle composition and processes. Geological Society, London, Special Publications, 42(1), 313-345.

Taylor Jr, H. P. (1968). The oxygen isotope geochemistry of igneous rocks. Contributions to Mineralogy and Petrology, 19(1), 1-71.

Theissen-Krah, S., Iyer, K., Rüpke, L. H., & Morgan, J. P. (2011). Coupled mechanical and hydrothermal modeling of crustal accretion at intermediate to fast spreading ridges. Earth and Planetary Science Letters, 311(3), 275-286.

Thirlwall, M. F. (1991). Long-term reproducibility of multicollector Sr and Nd isotope ratio analysis. Chemical Geology, 94(2), 85-104.

Thirlwall, M. F. (1991). Long-term reproducibility of multicollector Sr and Nd isotope ratio analysis. Chemical Geology: Isotope Geoscience section, 94(2), 85-104.

Todt, W., Cliff, R. A., Hanser, A., & Hofmann, A. W. (1996). Evaluation of a 202Pb‐205Pb Double Spike for High‐Precision Lead Isotope Analysis.*. Earth processes: reading the isotopic code, 429-437.

Valley, J. W., Kitchen, N., Kohn, M. J., Niendorf, C. R., & Spicuzza, M. J. (1995). UWG-2, a garnet standard for oxygen isotope ratios: strategies for high precision and accuracy with laser heating. Geochimica et Cosmochimica.

Vance, D., Stone, J. O. H., & O'Nions, R. K. (1989). He, Sr and Nd isotopes in xenoliths from Hawaii and other oceanic islands. Earth and Planetary Science Letters, 96(1), 147-160.

Vazquez, J. A., Shamberger, P. J., & Hammer, J. E. (2007). Plutonic xenoliths reveal the timing of magma evolution at Hualalai and Mauna Kea, Hawaii. Geology, 35(8), 695-698.

Waggoner, D.G., 1993. The age and alteration of central Pacific oceanic crust near Hawaii, Site 843. In Wilkens, R.H., Firth, J.V., Bender, J., et al., Proc. ODP, Sci. Results, 136: College Station, TX (Ocean Drilling Program), 119–132.

Walker, R. J., Brandon, A. D., Bird, J. M., Piccoli, P. M., McDonough, W. F., & Ash, R. D. (2005). 187 Os–186 Os systematics of Os–Ir–Ru alloy grains from southwestern Oregon. Earth and Planetary Science Letters, 230(1), 211-226.

Wang, K., Plank, T., Walker, J.D., Smith, E.I., 2002. A mantle melting profile across the Basin and Range, SW USA. J. Geophys. Res. 107 (B1). doi:10.1029/2001JB000209.

Wang, Z., & Eiler, J. M. (2008). Insights into the origin of low-δ18O basaltic magmas in Hawaii revealed from in situ measurements of oxygen isotope compositions of olivines. Earth and Planetary Science Letters, 269(3), 377-387.

Wang, Z., Kitchen, N. E., & Eiler, J. M. (2003). Oxygen isotope geochemistry of the second HSDP core. Geochemistry, Geophysics, Geosystems, 4(8).

Weaver, B. L. (1991). The origin of ocean island basalt end-member compositions: trace element and isotopic constraints. Earth and Planetary Science Letters, 104(2), 381-397.

Waggoner, D.G., 1993. The age and alteration of central Pacific oceanic crust near Hawaii, Site 843. In Wilkens, R.H., Firth, J.V., Bender, J., et al., Proc. ODP, Sci. Results, 136: College Station, TX (Ocean Drilling Program), 119–132.

Yamasaki, S., Kani, T., Hanan, B. B., & Tagami, T. (2009). Isotopic geochemistry of Hualalai shield-stage tholeiitic basalts from submarine North Kona region, Hawaii. Journal of Volcanology and Geothermal Research, 185(3), 223-230.

Yang, H. J., Frey, F. A., & Clague, D. A. (2003). Constraints on the source components of lavas forming the Hawaiian North Arch and Honolulu Volcanics. Journal of Petrology, 44(4), 603-627.

Yoder, H. S., & Tilley, C. E. (1962). Origin of basalt magmas: an experimental study of natural and synthetic rock systems. Journal of Petrology, 3(3), 342-532.

Yokose, H., Lipman, P. W., & Kanamatsu, T. (2005). Physical and chemical properties of submarine basaltic rocks from the submarine flanks of the Hawaiian Islands. Marine geology, 219(2), 173-193.

Vita

Ruohan Gao was born in Nanchong, Sichuan, China in February 1990. She graduated from Baita High School in Nanchong, Sichuan in June 2006. She received a Bachelor of Science in geochemistry from the University of Science and Technology of China in June 2010. In August 2010 she enrolled in the Graduate School at the University of Texas at Austin. By far Ruohan's best achievement while in Austin was meeting her husband, Jie Xu. They got married in December 2015.

Permanent email: ruohan.gao@gmail.com

This dissertation was typed by the author.